Head Office: Università degli Studi di Padova
Department of: Physics and Astronomy *Galileo Galilei*
Coordinator: Prof. Franco Simonetto

Ph.D. COURSE IN PHYSICS, 34th CYCLE

The importance of clustering analysis in future Gravitational Wave surveys

Ph.D. student: Sarah Libanore

Supervisor: Prof. Michele Liguori
Co-Supervisor: Dr. Alvise Raccanelli

Abstract

The question at the backbone of the work presented in this thesis is: *Will future gravitational wave surveys be an effective tool to constrain cosmology?* To answer this question, we will focus on the analysis of the clustering properties of binary mergers as mapped by future gravitational wave detectors in luminosity distance space.

After an initial overview dedicated to cosmology, to the study of large scale structures and to the main features of gravitational wave science, we will show that the tomographic analysis of angular power spectra of binary mergers will provide important information on parameters related with both cosmology and the formation channels of the merger themselves. We will then investigate how clustering properties can help us disentangling the astrophysical and primordial origin of binary black hole mergers, by applying Bayesian model selection techniques. Finally, we will deal with simulations in order to test our results and starting building a tool devoted to the analysis of future datasets.

Contents

Contents ii

1 Introduction **1**
  1.1 Main goal of the thesis 1
  1.2 Summary 2

BACKGROUND MATERIAL 6

2 A quick glance at cosmology **7**
  2.1 The standard cosmological model 7
    2.1.1 Universe components and cosmological parameters 10
    2.1.2 Distance measurements 11
    2.1.3 Thermal history and Universe epochs 12
  2.2 Cosmological Perturbations 15
    2.2.1 Evolution 15
    2.2.2 Statistics 16
    2.2.3 Evolution in Fourier space 19
  2.3 The primordial Universe 21
    2.3.1 Primordial black holes 22

3 Tracers of the dark **26**
  3.1 Large scale structures 26
    3.1.1 Dark matter halos 29
    3.1.2 Clustering and bias 32
  3.2 Number counts angular power spectrum 34
    3.2.1 Redshift space distortions 37
  3.3 Tracers 44
    3.3.1 Galaxies 44
    3.3.2 Supernovae IA 47
    3.3.3 Binary mergers 49

4 The era of gravitational wave science **54**
  4.1 GW theory 54
    4.1.1 GW propagation 55
    4.1.2 GW sources 57

4.2 GW detectors 61
4.2.1 Present: second generation detectors 64
4.2.2 Future from the ground: ET 65
4.2.3 Future from the space: LISA, BBO 65
4.3 GW and cosmology 66
4.3.1 Binary mergers 66

RESEARCH WORK 70

5 Forecasts for future GW surveys 71
5.1 The dark sirens problem 72
5.2 Modelling observational effects 73
5.2.1 Peculiar velocities 74
5.2.2 Lensing 77
5.2.3 Numerical implementation 78
5.3 Modelling source distribution and bias 80
5.3.1 Merger distribution 80
5.3.2 Merger clustering 82
5.3.3 Supernovae distribution and bias 86
5.4 Forecast analysis 88
5.4.1 Survey specifications 88
5.4.2 Fisher matrix formalism 90
5.4.3 Multi-tracer technique 93
5.4.4 Analysis set-up 94
5.5 Results: First analysis 95
5.5.1 Cosmological parameter constraints 96
5.5.2 Bias parameter constraints 96
5.6 Results: Follow-up analysis 98
5.6.1 Single-tracer analysis 99
5.6.2 Multi-tracer analysis 100
5.6.3 Effects of using a prior on bias parameters 103

6 Model selection for PBH scenarios 106
6.1 Bayesian statistics 108
6.1.1 Model selection and Bayes factor 108
6.1.2 Laplace approximation and Gaussian prior 109
6.2 Merger distribution and clustering 112
6.2.1 ABH 112
6.2.2 PBH 113
6.2.3 Blind survey 115
6.3 Results 116

7 Analysis of ABH simulations **124**
7.1 Simulations and catalogues 124
7.1.1 N-body simulations 125
7.1.2 Hydrodynamical simulations 127
7.1.3 The population-synthesis code MOBSE 129
7.2 Power spectrum estimator 130
7.2.1 Interlacing 133
7.2.2 FKP 134
7.3 Bias estimator 135
7.4 Results 137

8 Conclusions **148**
8.1 Future prospects 149

Bibliography **151**

Introduction 1

> *The immense distances to the stars and the galaxies mean that we see everything in space in the past, some as they were before the Earth came to be. Telescopes are time machines. Long ago, when an early galaxy began to pour light out into the surrounding darkness, no witness could have known that billions of years later some remote clumps of rock and metal, ice and organic molecules would fall together to make a place called Earth; or that life would arise and thinking beings evolve who would one day capture a little of that galactic light, and try to puzzle out what had sent it on its way.*
>
> Carl Sagan
> *A Pale Blue Dot* [1]

Cosmology is a wide field of research, the aim of which is to understand how the Universe is made, how it originated and how it evolved across cosmic time. A large number of theoretical models, numerical simulations and observational campaigns devoted to the **analysis of both the early and the late Universe** arose in the last decades, alongside with a larger and larger dedicated scientific community. The use of different points of view and perspectives became fundamental to develop innovative strategies to deal with novel and sometimes unexpected challenges.

The study of the Universe as a whole, however, can not disregard the understanding of how astrophysical objects form and behave. They constitute the sources through which we can **trace the large scale structure** of the cosmos: the statistical analysis of their distribution carries information about their past history and can be used as tool to look into the unknown.

The synergies between cosmology and astrophysics have always been many, but their interconnection was even more enhanced by the birth of **gravitational wave science**. This new field of study represents an unprecedented occasion for researchers in all fields, pledging to provide an incredible amount of data, information and results in the years to come. To deal with them, it will be necessary to further develop theoretical models of the astrophysical gravitational wave sources and of their interplay with the underlying cosmological scenario. At the same times, a large numerical and data analysis effort will be required.

1.1 Main goal of the thesis

The question at the backbone of the work presented in this thesis is:

> *Will future gravitational wave surveys be an effective tool to constrain cosmology?*

The short answer is: yes, they will. Of course, this will be detailed and justified throughout the text.

Indeed, it is already well known that, thanks to their standard siren property, gravitational waves will be able to provide powerful constraints on dark energy and accurate measurements of the Hubble parameter. In our work we will focus instead on a different, less explored aspect, namely the **clustering properties of**

binary mergers from which gravitational waves are produced. These are the only resolved sources we observed until now and they will dominate future observational campaigns as well. Catalogues provided by future detectors will map them in the full sky and to very high distances, up to the edge of the cosmic dark ages, when the first stars began to form.

We will show that the **tomographic analysis of the angular power spectrum** estimated from the distribution of such sources will provide important information on parameters related with both cosmology and the formation channels of the sources themselves. Throughout the thesis, we will derive forecasts mainly for the Einstein Telescope, a third generation ground−based gravitational wave detector that will become operational in the mid 2030s. The reason for this is that clustering studies require a large number of sources, at least $10^3 - 10^4$, which will be achievable with this kind of detectors.

The techniques we will adopt present **similarities** with the methods currently used in the literature for **galaxy survey analyses**. There will be however also significant differences and new technical challenges to address. We will look deeply into two main topics: how the clustering of the sources can be modelled and how their observed positions in the sky can be affected by large scale structures.

To **model the clustering** of binary mergers, we will rely on state−of−the art hydrodynamical simulations. These take into account astrophysical processes that lead to binary formation and connect them with the distribution and characteristics of their host galaxies. We will first of all model the clustering through a semi−analytical approach. We will then test our results thanks to direct estimates performed on the catalogues extracted from the simulations themselves.

In the computation of the angular power spectrum, we will also pay specific attention to the **deformation effects** induced by gravitational lensing and peculiar velocities of the source host galaxies. In galaxy surveys, where the distance indicator is the redshift, the latter are known as redshift space distortions. However, for gravitational waves signals we will only directly measure the luminosity distance: to obtain redshifts also for gravitational wave events, we will need electromagnetic counterparts or cross−correlations with external datasets. We want however to avoid this in our work and rely on gravitational wave observations alone. For this reason, space distortion effects will have to be recomputed in **luminosity distance space**. In this thesis, we will describe in detail the main reasons behind this choice and discuss its implications.

The work we will present collects the analyses and the results we developed in the published papers [2, 3] and in the forthcoming ones [4, 5].

1.2 Summary

This thesis is organized as follows. At the end of this chapter, we provide a summary of the abbreviations adopted throughout the text.

In the first part, **BACKGROUND MATERIAL**, we will summarize the state−of−the−art of the cosmological model, of the techniques used to trace and analyse large scale structures and of gravitational wave science.

In particular, **chapter 2**, **A quick glance at cosmology**, is dedicated to the standard cosmological model.

- In section 2.1 we will describe the geometry and evolution of the Universe, together with its main properties and components.
- In section 2.2 we will introduce the cosmological perturbations and we will define the statistical tools required to analyse them.
- In section 2.3 we will discuss the primordial Universe and the hypothesis of the existence of primordial black holes.

In **chapter 3**, **Tracers of the dark**, we will deal with large scale structures.

- In section 3.1 we will describe large scale structures, with particular reference to the distribution and clustering of dark matter halos.
- In section 3.2 we will derive the characteristics and the functional expression of the angular power spectrum for discrete tracers in redshift space.
- In section 3.3 we will summarize the formation, distribution and clustering of galaxies, supernovae IA and compact object binary mergers, both of astrophysical and primordial origin, as tracers of large scale structures.

In **chapter 4**, **The era of gravitational wave science**, we will revise the main features of the theory that describes gravitational waves and we will summarize how they are detected and analysed.

- In section 4.1 we will present the general relativistic description of gravitational wave generation and propagation, together with their different kinds of sources.
- In section 4.2 we will characterize the gravitational wave detectors and we will describe current and future instruments.
- In section 4.3 we will describe two applications of gravitational waves to cosmological studies.

The second part, **RESEARCH WORK**, will deal with the original work we developed in the context of this thesis and with the results we obtained.

In **chapter 5**, **Forecasts for future GW survey**, we will compute the Einstein Telescope forecasts for cosmological and bias parameters, using the clustering of astrophysical binary mergers.

- In section 5.1 we will introduce dark sirens i.e., binary mergers without electromagnetic counterpart, for which the redshift can not be measured.
- In section 5.2 we will describe the luminosity distance space and we will compute a first approximated expression for angular power spectrum corrections due to space distortions.
- In section 5.3 we will model the number distribution and the clustering of binary mergers we adopted in our analysis.
- In section 5.4 we will summarize how forecasts can be obtained through the Fisher matrix technique.
- In section 5.5 we will present our results on the capability of Einstein Telescope and other, more advanced, detector configurations in constraining both cosmological parameters and clustering properties of the sources.
- In section 5.6 we will improve on the previous analysis under several points, the most important of which will be the implementation of a multi−tracer technique involving supernovae IA.

Results from this chapter were published in [2, 3].

In **chapter 6**, **Model selection for PBH scenarios**, we will perform model selection forecasts to verify whether the clustering of mergers will have the potential to discriminate between scenarios in which some of the gravitational waves are produced by primordial black hole mergers and scenarios in which only astrophysical sources exist.

- In section 6.1 we will revise Bayesian statistics and we will introduce the Bayes factor, which is the key ingredient for the model selection that will be performed.
- In section 6.2 we will model the number distribution and clustering properties of both astrophysical and primordial black hole mergers.
- In section 6.3, we will discuss the analysis set−up and we will present the results obtained.

The analysis developed in this chapter will soon be published in [4].

In **chapter 7**, **Analysis of ABH simulations**, we will perform a direct estimate of both the power spectrum and the clustering using simulated data, made by sets of astrophysical black hole mergers. We will exploit this analysis both to characterize the properties of hydrodynamical simulations that are currently used to study the binary formation channels and to test our semi−analytical model developed in chapter 5.

- In section 7.1 we will give a brief review of different kinds of simulations, namely collision−less N−body, hydrodynamical and population−synthesis based.
- In section 7.2 we will describe the power spectrum estimators implemented for the analysis.
- In section 7.3 we will characterize the techniques used to study clustering in a simulated dataset.
- In section 7.4, we will summarize how we implemented the analysis and we will present our results, highlighting the differences that can arise when performing studies on the different types of simulations.

The results summarized here will soon be published in [5].

Finally in **chapter 8** we will draw our conclusions and summarize our main results. We will also describe the future prospects and the possible follow−up applications of our analysis.

Abbreviations

In the following table we summarize the abbreviations used throughout the text and the chapters where they can be found.

Symbol	Name	Chapters
ABH	astrophysical black hole (mergers)	[3, 6, 7]
BBH	binary black hole mergers	[4,5, 7]
BNS	binary neutron star mergers	[4, 5, 7]
BHNS	black hole−neutron star mergers	[5, 7]
CIC	cloud−in−cell (GAS)	[7]
CDM	cold dark matter	[2]
CMB	cosmic microwave background	[2, 3, 4, 5]
CPL	Chevallier−Polarski−Linder DE parametrization	[2, 5]
DE	dark energy	[2, 3, 5]
DM	dark matter	[2, 3, 5, 6, 7]
EM	electromagnetic	[3, 4, 5]
EoS	equation of state	[2, 3]
EFT	effective field theory	[2]
ET	Einstein Telescope	[4, 5, 6]
FKP	Feldman−Kaiser−Peackock estimator	[7]
FLRW	Friedmann−Lemaître−Robertson−Walker metric	[2, 3, 5]
FoF	friends−of−friends (algorithm)	[7]
FFT	fast Fourier transform	[7]
GAS	grid assignment scheme	[7]
GR	general relativity	[2, 3, 4, 5]
GUT	grand unified theory	[2]
GW	gravitational waves	[3, 4, 5, 6, 7]
HOD	halo occupation distribution	[3, 5, 6, 7]
HOD/GOD	galaxy occupation distribution	[5, 6, 7]
IM	intensity mapping	[3]
ΛCDM	standard cosmological model	[2]
LDS	luminosity distance space	[5]
LoS	line of sight	[3, 4, 5]
LSS	large scale structure	[3, 5, 6, 7]
MG	modified gravity	[2]
NS	neutron star	[3]
PBH	primordial black hole (mergers)	[2, 3, 4, 6]
SFR	star formation rate	[3, 5, 7]
SPT	standard perturbation theory	[3]
SMF	stellar mass function	[5]
SNR	signal−to−noise ratio	[3, 4, 5, 7]
VRO	Vera Rubin observatory	[5]
WIMP	weakly interacting massive particles	[2]
WD	white dwarf	[3]

BACKGROUND MATERIAL

2

A quick glance at cosmology

2.1 The standard cosmological model . . 7
Universe components and cosmological parameters 10
Distance measurements 11
Thermal history and Universe epochs 12
2.2 Cosmological Perturbations 15
Evolution 15
Statistics 16
Evolution in Fourier space 19
2.3 The primordial Universe 21
Primordial black holes . 22

Cosmology is a wide research field, which deals with the study of the Universe as a whole: from its initial condition and early stages, following the structure formation and evolution up to the present times. In this chapter, we briefly summarize the standard cosmological model and we introduce the main observables that are used to probe it. The review presented in this chapter does not pretend to be at all exhaustive: since its main goal is to be functional to the study performed in the next chapters, we limit ourselves to describe some essential elements of cosmological theory. When limitations are present, we highlight them, referring the reader to specific literature where to learn more about it.

In particular, in section 2.1 we summarize the main equations required to describe the geometry and evolution of the Universe and we introduce the cosmological parameters that describe them. We characterize the matter and energy components and we discuss how distances are measured in cosmology. We also give a brief overview of the thermal history of the Universe and of the different epochs that this defines. In section 2.2 we introduce the cosmological perturbations, we describe their evolution both in real and in Fourier space, and we define the statistical tools required to analyse them, namely the spatial correlation function, the power spectrum and the angular power spectrum. Finally, in section 2.3 we briefly discuss how the primordial Universe can be described, giving particular attention to the hypothesis of the existence of primordial black holes. We discuss how they could form and we summarize the constraints that today exist on their abundance in the different mass ranges.

2.1 The standard cosmological model

The current standard cosmological model can also be referred to as ΛCDM, from the names of its main components: the cosmological constant (or dark energy) Λ and the Cold Dark Matter (CDM). These make up more of 90% of the Universe density content, the rest being split between baryonic matter, radiation and neutrinos [6]. In this framework, the Universe is well described by a geometrically flat spacetime and General Relativity (GR) is used to describe its dynamical behaviour. Moreover, the **cosmological principle**, firstly introduced by Einstein and Milne in the 1930s [7], holds: on large scales i.e., above 100 Mpc, isotropy and homogeneity assure rotational and translation invariance.

Under these conditions, the background metric i.e., the average geometry of the spacetime, is described by the Friedmann−Lemaître−Roberson−Walker (FLRW, see [8] and references therein) metric:

$$ds^2 = g_{\mu\nu}dx^{\mu}dx^{\nu} = -c^2dt^2 + a^2(t)\left(\frac{dr^2}{1-\Bbbk r^2} + r^2 d\theta^2 + r^2 d\sin^2\theta\, d\varphi^2\right), \qquad (2.1)$$

where s is the line element and $[t, \boldsymbol{x}] = [t, r, \theta, \varphi]$ are the time and space comoving coordinates,[1] c is the speed of light in the vacuum and $\Bbbk = 0$ is the spatial

[1] We use the convention that Greek letters (e.g., $\mu\nu$) express spacetime coordinates, roman letters (e.g., ij) indicate their spatial components.

curvature in the flat Universe.[2] $a(t)$ instead is called the **scale factor**: it describes the expansion rate of the Universe; its local value is $a(t=0) = a_0 = 1$. In the local Universe $a(t) > 0$, meaning that the expansion is accelerated; this however only acts on the large scales, while bound systems such as clusters or galaxies are not affected by it [9]. While we indicate with r the comoving radial coordinate, we use χ to indicate the comoving distance; this is related with the proper distance by $d(t) = a(t)\chi$, as section 2.1.2 shows in detail.

The scale factor can be related to the wavelength variation a light−ray (or a gravitational wave) undergoes because of the expansion itself. In fact, considering a light−ray (gravitational wave) having wavelength λ_e at the emission time t_e, this is observed with $\lambda_0 = \lambda_e a(t_0)/a(t_e)$ at the present time t_0 because of the Doppler effect caused by the relative motion between the source and the observer; this relation can be described through the **redshift**:

$$z = \frac{\lambda_0 - \lambda_e}{\lambda_e} \;\longrightarrow\; 1 + z = \frac{a(t_0)}{a(t_e)} = \frac{1}{a(t_e)} \;. \tag{2.2}$$

The relation between redshift and distance was firstly found out by Hubble in 1929 [10]. Locally, this is expressed through the Hubble law:

$$cz \sim H_0 d \tag{2.3}$$

where H_0 is called the **Hubble constant**[3] . Hubble's studies on the recession velocity of distance galaxies were the first probe of the cosmic expansion.

The **Einstein gravitational field equations** characterize the relation between the spacetime and its components:

$$G^{\mu\nu} + \Lambda g^{\mu\nu} = \frac{8\pi G}{c^4} T^{\mu\nu} \;, \tag{2.4}$$

$g^{\mu\nu} = \mathrm{diag}\big(1\, a^2(t)\, a^2(t)\, a^2(t)\big)$ being the FLRW metric defined in eq. (2.1), G the gravitational constant, Λ the cosmological constant defined in section 2.1.1 and $G^{\mu\nu}$, $T^{\mu\nu}$ the Einstein tensor and the covariant stress−energy−momentum tensor respectively. The first encodes the information on the geometry of spacetime, being defined by the mean of the Ricci tensor $R^{\mu\nu}$ (i.e., the contraction through the metric of the Riemann tensor in eq. (4.2)) and the Ricci scalar R as:

$$G^{\mu\nu} = R^{\mu\nu} + \frac{1}{2} g^{\mu\nu} R \;. \tag{2.5}$$

The stress−energy−momentum tensor instead depends on the content of the Universe, being related to the rest−mass energy density[4] ρ, the pressure p and the 4−velocity u^μ of its constituents. Assuming the Universe behaves as a perfect fluid (see e.g., [11] and references therein), $T^{\mu\nu}$ is defined as:

$$T^{\mu\nu} = \left(\rho + \frac{p}{c^2}\right) u^\mu u^\nu + p g^{\mu\nu} \;. \tag{2.6}$$

In the case of an imperfect fluid, the anisotropic stress tensor $\Pi^{\mu\nu}$ would also be included: this is required to study a Universe filled with several uncoupled components. The **Friedmann equations** are obtained by solving eq. (2.4) for an

[2] The value of $\Bbbk$ would be +1 in a closed Universe, −1 in an open one.

[3] It is usual to adopt the dimensionless factor $h = H_0/(100\,\mathrm{km\,s^{-1}Mpc^{-1}})$ as a rescaling factor to make the values of cosmological parameters independent from H_0 uncertainties (see section 2.1.1)

[4] When referring to the density ρ, we implicitly assume ρc^2.

homogeneous and isotropic fluid [12]:

$$3\left(\frac{\dot{a}}{a}\right)^2 = 8\pi G\rho - 3\frac{3{\mkern3mu\mathchar'26\mkern-12mu k}c^2}{a^2} + \Lambda\,, \tag{2.7}$$

$$\frac{\ddot{a}}{a} = -\frac{4\pi G}{3}\left(\rho + 3\frac{p}{c^2}\right) + \frac{\Lambda}{3}\,, \tag{2.8}$$

where we neglected the time dependence for clarity. Through the Friedmann equations it is possible to characterize the dynamics of the Universe and to study the scale factor evolution across cosmic time. In eq. (2.7), the term $H(t) = \dot{a}/a$ is defined[5] as the **Hubble parameter**. The Hubble parameter is shown in figure 2.1, where the conversion between redshift and cosmic time is made by assuming:

$$\int_0^t \frac{dt}{a(t)} = \frac{c}{a_0}\int_0^z \frac{dz}{H(z)}\,. \tag{2.9}$$

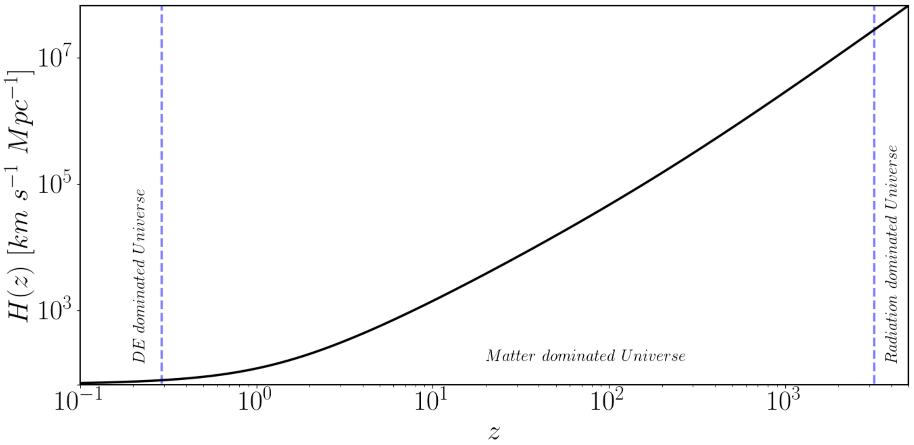

Figure 2.1: Hubble parameter $H(z)$ depending on z. This trend is obtained from eq. (2.10) in a ΛCDM Universe, assuming for the cosmological parameters the estimates of *Planck 2018* [13]. Vertical lines indicate when relevant events in the history of the Universe took place, which are describe in section 2.1.3.

Being strictly related to the evolution of the scale factor, the Hubble parameter is particularly relevant for cosmology. In an isotropic Universe, by using the conservation of the stress−energy−momentum $\nabla_\nu T^{\mu\nu} = 0$,[6] from which the continuity eq. (2.29) is found, eq. (2.7) can be rewritten such that the Hubble parameter is:

$$H(z) = H_0\sqrt{\sum_i \Omega_i(1+z)^{3(2+\omega_i)}} \tag{2.10}$$

where for each component i the dimensionless density parameter is defined as $\Omega_i = \rho_i/\rho_c = 8\pi G\rho_i/3H_0^2$, $\rho_c = 8\pi G/3H_0^2$ being the critical density required to get ${\mkern3mu\mathchar'26\mkern-12mu k} = 0$ i.e., a flat Universe today, from eq. (2.7). The redshift dependence is obtained by knowing the Equations of State (EoS) $\omega_i = p_i/\rho_i$ (see eq. (2.25)). Eq. (2.9) in this case can be rewritten in terms of the $i-$th dominant component as:

$$\frac{1}{1+z} \sim t^{2/3(1+\omega_i)}\,. \tag{2.11}$$

In eq. (2.10), $H_0 = H(0)$ is the Hubble constant already defined in eq. (2.3). Its measurement represents one of the challenges of modern cosmology: high redshift (i.e., estimates on the Cosmic Microwave Background, see section 2.1.3 and [13, 14]) and low redshift probes (e.g, the standard candles described in section 3.3.2

[5] $\dot{}$ indicates the derivative with respect to t. This can be related to the conformal time τ through $dt = a d\tau$.

[6] ∇_ν is the covariant derivative.

[15–17]), in fact, provide values that are discrepant at more than 4σ (see e.g., [18, 19]). This so called **Hubble tension** highlights the presence of an internal inconsistency that could be both related to systematics in the local measurement (e.g., [20, 21]) or due to the inaccuracy of the models we use to describe the early or late Universe (e.g., [22, 23]). The latest release of the SHOES and *Pantheon+* enhanced this tension up to 5σ, pointing to the fact that no indications arise of measurement errors or analysis variations: the tension therefore seems to be intrinsic and its nature is still unknown [24]. Further measurements of H_0 with different probes will help shed light on this problem: gravitational waves from binary mergers and their standard siren behaviour, which are described in section 4.3, represent one possible way to deal with this [25–27].

2.1.1 Universe components and cosmological parameters

In the ΛCDM model, four are the species that represent the main energy content of the Universe: matter, radiation (i.e., photons and neutrinos) and dark energy. Their existence is assumed as an hypothesis in the model, together with the definition of the cosmological parameters required by the model itself [6]. Consequently, measurements of the Cosmic Microwave Background (CMB, see section 2.1.3) power spectrum and models of structure formation (see chapter 3) are used to constrain their densities and properties.

Two types of matter exist: the **baryonic matter**, made of atoms that were firstly created during the primordial nucleosynthesis [28–30] or made up through nuclear fusion in stars [31, 32] and other astrophysical processes [33], and the **Dark Matter** (DM). This is a pressure−less, stable (at least over tens of billions of years) component, that weakly interacts with baryonic matter, mainly gravitationally. It was firstly theorised by Zwicky in the 1930s to explain the velocities of galaxies in clusters [34] and then adopted by Rubin and others in the 1980s [35] to describe the behaviour of the galaxy rotational curves in their outer parts. Constraints provided by structure formation require DM to become non−relativistic before decoupling from the other species: for this reason, it is referred as **cold DM**. Its nature is still unclear and many hypothesis exist to explain it, generally through particles beyond the standard model (see e.g., [36]); the favourite candidates in this case are Weakly Interacting Massive Particles (WIMP, see e.g., [37]) and axions (see e.g., [38]). Also other hypothesis about the nature of DM exist e.g., primordial black holes [39] (see section 2.3). Both baryonic and dark matter, being pressure−less, are described by the EoS $\omega = 0$.

Relativistic species represent today a subdominant fraction of the Universe content. While constraints on the photon densities are clearly set by the CMB [6], cosmological neutrinos are still an open research field, particularly when referring to their masses [40]. Photons and mass−less neutrinos are described by the EoS $\omega = 1/3$.

Dark Energy (DE) is the great unknown of modern cosmology. It can be referred also as the cosmological constant: firstly introduced by Einstein in his equations to keep the Universe static, it was then reinterpreted in light of the discovery of its accelerated expansion thanks to supernova observations [41, 42]. Its nature and behaviour are still under debate, both regarding its physical explanation and its possible dynamical evolution [43, 44]. Its EoS is usually described through the Chevallier−Polarski−Linder (CPL) parametrization [45, 46]:

$$w(a(t)) = w_0 + w_a(1 - a(t)) \, . \tag{2.12}$$

In the case DE is constant over cosmic time, $w = w_0 = -1,\ w_a = 0$. From eq. (2.4), it is evident that Λ could be interpreted not only as an energy contribution, but also as a modification of the Einstein tensor. In this case, the accelerated expansion of the Universe would be explained as gravity behaving differently on the largest cosmological scales with respect to GR. Many of such models exists, generically referred to as **Modified Gravity** (MG) [47]: any departure from GR would introduce new degrees of freedom in the theory, defined as scalar, vector or tensor fields. The simplest case assumes to introduce a single scalar field: to describe this framework while remaining model independent, an Effective Field Theory (EFT, see [48] and references therein) formalism can be applied. Whether the Universe expansion is due to DE, MG or both of them is still an open issue (see e.g., [49] for a review).

Results from the *Planck* satellite [13] constrain the densities of these components, as well as the other cosmological parameters characterising the ΛCDM model. Among these, there are the amplitude A_s and spectral index n_s of the primordial power spectrum of adiabatic perturbations (see section 2.3) and the curvature density $\Omega_{\mathchar'26\mkern-9mu k}$. Derived parameters are constrained as well, such as H_0 and the DE EoS parameters $w_0,\ w_a$ defined in eq. (2.12). Table 2.1 reports the fiducial values of the cosmological parameters that will enter our analysis in chapter 5; note that the densities are expressed as $\Omega_i h^2$. In a flat Universe, $\Omega_{\mathchar'26\mkern-9mu k} = 0$ and by considering dark matter and baryons ($DM,\ b$), dark energy (Λ), photons and neutrinos ($\gamma,\ \nu$), it holds:

$$\Omega_{TOT} = \Omega_{\mathchar'26\mkern-9mu k} + (\Omega_{DM} + \Omega_b) + \Omega_\Lambda + \Omega_\gamma + \Omega_\nu \sim \Omega_{m=DM+b} + \Omega_\Lambda = 1\ . \tag{2.13}$$

Fiducial Cosmology			
H_0	67.66 ± 0.42	Ω_Λ	0.6889 ± 0.0056
$\Omega_b h^2$	0.02242	$\Omega_c h^2$	0.11933 ± 0.00091
w_0	-1 ± 0.13	w_a	0 ± 0.55
A_s	$2.105 \cdot 10^{-9}$	n_s	0.9665

Table 2.1: Fiducial values from *Planck 2018* TT, TE, EE+lowE+lensing+BAO [13] with their 68% confidence interval. The errors for the DE EoS parameters w_0 and w_a have been estimated by symmetrizing the ones from Planck+SNe+BAO [13].

2.1.2 Distance measurements

Distance in an expanding Universe is not uniquely defined. In the FLRW metric in eq. (2.1), coordinates are comoving with the scale factor i.e., they are fixed inside the evolving Universe. The **comoving distance** χ they define between two points is linked to their physical proper distance $d(t)$ through $a(t)$:

$$d(t) = a(t)\chi \quad \text{where } \chi = \begin{cases} |\mathchar'26\mkern-9mu k|^{-1/2}\sinh^{-1}\sqrt{|\mathchar'26\mkern-9mu k|}r & \text{if } \mathchar'26\mkern-9mu k < 0 \\ r & \text{if } \mathchar'26\mkern-9mu k = 0 \\ |\mathchar'26\mkern-9mu k|^{-1/2}\sin^{-1}\sqrt{|\mathchar'26\mkern-9mu k|}r & \text{if } \mathchar'26\mkern-9mu k > 0 \end{cases}\ . \tag{2.14}$$

As e.g., [12] shows, from eq. (2.9) the comoving distance of a light source from the observer can be computed as:

$$\chi_{source} = \int_{t(a_{source})}^{t_0} \frac{dt}{a(t)} = \int_{a_{source}}^{1} \frac{da}{a^2 H(a)} = \int_0^{z_{source}} \frac{c^2}{H(z)}\, dz\ . \tag{2.15}$$

Alternatively, its **luminosity distance** D_L is defined as:

$$F = \frac{L}{4\pi D_L^2} \,, \tag{2.16}$$

where L denotes the luminosity i.e., the power emitted at time t, and F the flux i.e., the power received per unit area.[7] F depends on the number of photons received and on their energy. At the observer location, the photon number is smaller by a factor $a(t_{source})$ than it was at the emission, because of the expansion of the Universe; similarly, the energy decreases by a factor $a(t_{source})$ (see [12] for details). Therefore, the observed flux is smaller by a factor $a(t_{source})^2$ than the intrinsic luminosity L. The flux that crosses the spherical shell $4\pi\chi^2_{source}$ seen by the observer is then:

$$F = \frac{L}{4\pi}\frac{a(t_{source})^2}{\chi^2_{source}} \,. \tag{2.17}$$

By equating eq. (2.16) and eq. (2.17), the luminosity distance is found to be:

$$D_L = \frac{\chi}{a(t)} = (1+z)\,c^2 \int_0^z \frac{dz'}{H(z')} \,. \tag{2.18}$$

A third way to measure distances exists, which is linked with the apparent angular size ϑ of an extended source. Defined as d the physical size of the source itself, from eq. (2.14) its comoving size is computed as $d/a(t)$. The subtended angle appears to be $\vartheta = [d/a(t)]/\chi$ (see [12] for details); consequently the **angular diameter distance** D_A is defined as:

$$D_A = \frac{d}{\vartheta} = a(t)\chi = \frac{D_L}{(1+z)^2} \,. \tag{2.19}$$

The difference between χ, D_L and D_A in the ΛCDM Universe is showed in figure 2.2.

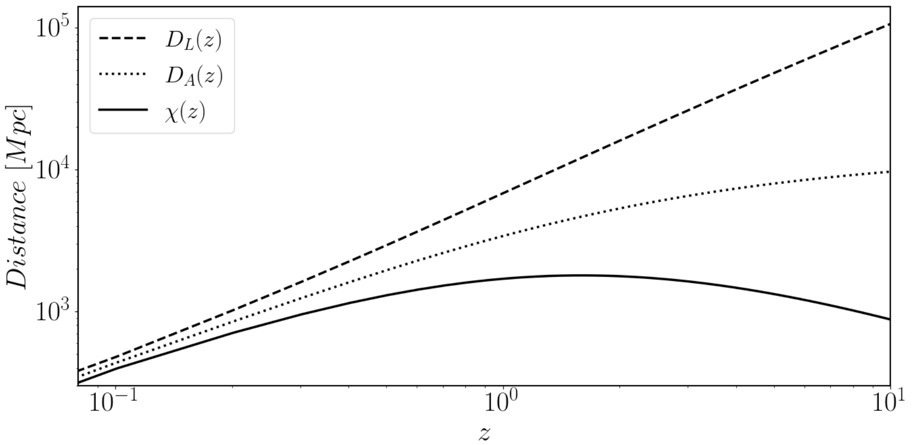

Figure 2.2: Comoving distance χ (continuous line), luminosity distance D_L (dashed line) and angular diameter distance D_A (dotted line) as function of redshift z in the ΛCDM cosmology described by [13].

2.1.3 Thermal history and Universe epochs

Observations today give good evidence that the Universe is flat and expanding in an accelerated manner, which is compatible with an EoS dominated by DE. However, this has not always been the case.

[7] For gravitational waves, D_L is defined analogously by referring to the emitted and received gravitational energy, see section 4.3.

To study the different phases of the evolution history, one needs to look at the particle content of Universe itself: baryons, photons, neutrinos and even DM if it is made by particles, can interact together. Let the interaction rate at a given time be:

$$\Xi = n\sigma v_{rel} \; , \tag{2.20}$$

$n, \; \sigma, \; v_{rel}$ being respectively the particle number density, the process cross−section and the relative velocity between the two interacting particles. If Ξ is much larger than the Hubble parameter $H(t)$ in eq. (2.10) at a certain time, the particles are in **thermal equilibrium** [50]. In this condition, the mean free path between the particles is way smaller than the **Hubble radius**,[8] which is defined as:

$$d_H(t) = \frac{c}{H(t)} \; , \tag{2.21}$$

and it contains the regions that are in causal contact with one another at time t. Therefore, particles interact so frequently that they are *unaware* of the cosmic expansion and whatever fluctuation in their energy density would be rapidly smoothed out. Eq. (2.20) can be applied to each particle species: the condition $\Xi >> H(t)$ turns out to be satisfied only up to a certain t, whose value is different for each species depending on its own number density and distribution and on the cross−section of the processes through which it can interact with the other species. When a certain species reach the condition $\Xi \simeq H(t)$, it **decouples** from the thermal equilibrium and its distribution starts evolving according only to gravitational instability and cosmic expansion [50].

To study whether the thermal equilibrium condition holds or not, the **Boltzmann equation** is required. This links the distribution function $f(t, \boldsymbol{x}, \boldsymbol{p})$ ($\boldsymbol{x}$ and $\boldsymbol{p}$ being respectively the position and the proper momentum) to the collisional term $C[f]$ i.e., the functional describing the interactions between all the particles included in the system. The relation between the two is simply:

$$\frac{df}{dt} = \frac{\partial f}{\partial t} + \frac{d\boldsymbol{x}}{dt} \cdot \nabla_{\boldsymbol{x}} f + \frac{d\boldsymbol{p}}{dt} \cdot \nabla_{\boldsymbol{p}} f = C[f] \, . \tag{2.22}$$

The study of eq. (2.22) in an expanding and cooling Universe, combined with the standard particle model hypothesis [52], allows us to understand the different phases the Universe went into. Briefly,[9] our description of the Universe can be pushed back to $t = 10^{-43}$ s after the Big Bang, when the energy reached the **Planck scale** $c^2 m_{pl} = 10^{19}$ GeV; before this moment, quantum gravity would be needed. At a certain time, when energy was still at the **Grand Unified Theory**[10] scale ($\simeq 10^{16}$ GeV), inflation occurred (see section 2.3) and the Universe expanded on cosmological scales. Afterwards, **baryogenesis** and **leptogenesis** occurred, producing a still unexplained excess of matter above antimatter, which brought to the creation of bounded quark states at the **QCD phase transition** ($\simeq 150$ MeV, $t \simeq 20\,\mu$s).

At this stage, the Universe was filled with a hot plasma where all the species were in thermal equilibrium. The first to decouple were neutrinos: the energy scale was around 1MeV ($t \simeq 1$ s), its exact value depending on the neutrino mass. After that, the electron−positron annihilation stopped at $\simeq 0.5$ MeV and, at $\simeq 0.1$ MeV, the first nuclei[11] formed. Here, after $\simeq 3$ minutes after the Big Bang, the **primordial nucleosynthesis** finally took place. As for particle DM, the moment of the decoupling depends on the model adopted to describe it.

It is important to note that, across this thermal history of the Universe, particle

[8] The Hubble radius $d_H(t)$, defines per each time the distance from the observer above which points recede with $v > c$. From regions below the Hubble radius, light can reach the observer in $t < \tau_H = 1/H(t)$ (see e.g., [51]). By integrating eq. (2.21) over the past cosmic time, the **cosmological particle horizon** can be defined as well. It defines the distance below which points have ever been in causal contact with the observer and it accounts for its entire past history.

[9] The thermal story of the Universe is here summarized just to introduce notions that will be useful further on in the text. A full description and characterisation of these phases is beyond the scope of this thesis.

[10] GUT is a model in which the electromagnetic, weak and strong interactions are unified. When the energy scale decreased, they started to behave differently e.g., the electromagnetic and weak interactions separate one from another at $\simeq 100$ GeV, which corresponds to $t \simeq 10^{12}$ s after the Big Bang.

[11] Deuterium and Helium.

densities[12] evolved at different rates. In particular, for **non−relativistic matter**, $\rho_m \propto a^3$ follows from matter conservation, while for **relativistic species** $\rho_{\gamma,\nu} \propto a^4$ depends on the work that pressure exerts during the expansion [9]. Therefore, it can be shown that it exists an epoch in which the matter density (baryons and CDM) equals the radiation density (photons and neutrinos). This **matter−radiation equivalence** is defined through:

$$\frac{\rho_{m0}}{a_{eq}^3} = \frac{\rho_{r0}}{a_{eq}^4} = \frac{\rho_{\gamma 0}}{a_{eq}^4}\left[1 + \frac{7}{8}N_{eff}\left(\frac{4}{11}\right)^{4/3}\right] , \tag{2.23}$$

N_{eff} being the number of neutrino species and $\rho_{m0,\gamma0}$ the densities today, measured by *Planck* [13]. By solving eq. (2.23) and converting the scale factor to redshift, one finds:

$$1 + z_{eq} = 2.4 \cdot 10^4\ \Omega_{m0}h^2\ . \tag{2.24}$$

The value *Planck* estimated for the equivalence is $z_{eq} = 3387 \pm 21$ (TT, TE, EE+lowE+lensing+BAO, [13]), from which the Hubble radius $d_H(t_{eq})$ and the cosmological horizon at the equivalence can be found. By changing Ω_{m0} or h, and so z_{eq} in eq. (2.24), the size of the horizon changes as well. Before z_{eq}, the Universe was radiation dominated, while after that it became matter dominated and the different expansion rate in the two regimes has different effects on the **evolution of density perturbations** through gravitational instability (see section 2.2.1). For this reason, changing the minimum size that perturbations must have to enter the horizon before or after the matter−radiation equivalence can affect the perturbation evolution and consequently the large scale structure formation (see section 3.1).

In analogy to eq. (2.23), we can define the epoch at which DE density starts to dominate over matter density. In this case, the relation between the density and the scale factor is found by requiring that the pressure is negative, to guarantee the accelerated expansion. The **expansion rate across cosmic time**, depending on the dominant density component, can therefore be summarized (compare with eq. (2.7) and eq. (2.29)) as:

$$\rho_i \propto (1+z)^{3(1+\omega_i/c^2)} \longrightarrow \begin{cases} \rho_{\gamma,\nu} \propto (1+z)^4 & z < z_{eq} \simeq 3300 \\ \rho_m \propto (1+z)^3 & z_{eq} < z < z_{DE} \\ \rho_\Lambda \propto (1+z)^{3(1+w_0+w_a)\exp[-3w_a z/(1+z)]} & z > z_{DE} \simeq 0.29 \end{cases} . \tag{2.25}$$

In a non−flat Universe where $\rho_{\Bbbk} \neq 0$, the curvature density evolution would be $\rho_{\Bbbk} \propto (1+z)^2$. Figure 2.1 shows the redshift in which the transition from the radiation dominated era to the matter dominated and the DE dominated eras took place.

To conclude the thermal history of the Universe, one last chapter is needed: **recombination**. This represents the moment in which electrons and protons combined into hydrogen atoms: when this happened, Compton/Thompson scattering[13] were no longer effective and radiation decoupled from matter. From that moment, photons became free to stream across the Universe: today, we can observe them thanks to the CMB. By assuming that recombination took place instantaneously at $z \simeq 1090$ [13], the CMB can be thought to be emitted at the **last scattering surface**.

After recombination, the Universe was mainly filled with DM and neutral hydrogen, the number densities of which were so low that interactions no longer occurred and gravity became the main actor of evolution, as section 2.2.1 and section 3.1 describe. This condition was then broken at $z \simeq 7.5$ [13], when the light emitted by

[12] As pointed out in section 2.1, we always refer to energy densities, implicitly assuming $c^2\rho$.

[13] Thompson scattering and its relativistic version Compton scattering, are processes in which electrons and photons scatter one with respect to the other i.e., $e^- + \gamma \rightarrow e^- + \gamma$.

the formation of the first stars gave rise to the **reionisation** epoch, in which free electrons came back to fill the interstellar medium.

2.2 Cosmological Perturbations

The background evolution of the Universe is well described by the FLRW metric in eq. (2.1): this however only holds on average and on the largest scales. To understand the formation and evolution of structures such as dark matter halos or galaxies, instead, a tool is required to study the fluctuations of matter density with respect to the homogeneous background.

Independently from their astrophysical nature, structures can be considered as **matter inhomogeneities** over the space−averaged background density $\bar{\rho}$, being characterized by:

$$\delta(\boldsymbol{x}) = \frac{\rho(\boldsymbol{x}) - \bar{\rho}}{\bar{\rho}} \,, \tag{2.26}$$

where $\boldsymbol{x}$ in this case are the physical space coordinates. In an inflationary picture (see section 2.3) such fluctuations formed in the early Universe, arising from inflaton quantum fluctuations; the evolved mass distribution we see today still retains information about the initial state [53]. Perturbations started evolving via **gravitational instability**. This growth was slowed down, before recombination, by radiation pressure: after that, baryon drag perturbations could grow, eventually entering a non−linear regime.

When $\delta << 1$, the inhomogeneities behaviour can be analysed in the **(quasi−)linear regime** where the main carrier of their evolution is gravitational instability. When $\delta \gtrsim 1$, instead, **non−linear processes** take place and the analysis gets more complicated: in section 3.1 we describe e.g., how we can we deal with this when studying large scale structures through the use of Standard Perturbation Theory.

2.2.1 Evolution

Perturbations over the FLRW background are due to the primordial quantum fluctuations (see section 2.3) that were imprinted as classical perturbations on cosmological scales at the end of inflation [51]. Depending on their scales, perturbations entered the horizon in different epochs (larger scales entered later) and, as eq. (2.25) anticipated, started evolving with a rate that is linked with the dominant component at the time.

To study the evolution of inhomogeneities when their scale is smaller than the cosmological horizon, the Newtonian treatment can be used (see e.g., [53] for review). In this case, when the mean free path between two particles is small enough to treat the matter field $\rho(t, \boldsymbol{x})$ as a perfect fluid, the quantities:

$$\begin{aligned} \boldsymbol{x} = \frac{\boldsymbol{r}}{a(t)} &= \text{ comoving spatial coordinate ;} \\ \boldsymbol{v} = \dot{\boldsymbol{r}} - H\boldsymbol{r} = a\dot{\boldsymbol{x}} &= \text{ peculiar velocity field ;} \\ \phi(\boldsymbol{x}, t) &= \text{ peculiar Newtonian gravitational potential ,} \end{aligned} \tag{2.27}$$

can be defined. Peculiar velocities are the departure of matter motion from pure Hubble expansion, while peculiar gravitational potentials represent the fluctuations with respect to the homogeneous background caused by the density inhomogeneities. Within the Poisson gauge defined in section 3.1, in the flat Universe and weak field limit $\Phi = -\Psi = -\phi/c^2$.

The quantities in eq. (2.27) are related together by the **Euler equation**:

$$\frac{\partial(a\boldsymbol{v})}{\partial t} + (\boldsymbol{v} \cdot \nabla_x)\boldsymbol{v} = -\frac{1}{\rho}\nabla_x p - \nabla_x \phi \ , \tag{2.28}$$

the **continuity equation**:

$$\frac{\partial \rho}{\partial t} + 3H\rho + \frac{1}{a}\nabla_x(\rho \boldsymbol{v}) = 0 \ , \tag{2.29}$$

and the **Poisson equation**, which is the non−relativistic expression of the 00 term of the Einstein eq. (2.4):

$$\nabla_x^2 \phi = 4\pi G a^2(\rho - \bar{\rho}) = 4\pi G a^2 \bar{\rho}\delta \ . \tag{2.30}$$

By perturbing eq. (2.28), eq. (2.29) and eq. (2.30) at linear level, one can find:

$$\begin{cases} \dfrac{\partial \boldsymbol{v}}{\partial t} + \dfrac{\dot{a}}{a}\boldsymbol{v} = -\dfrac{1}{\rho a}\nabla_x p - \dfrac{1}{a}\nabla_x \phi \\ \dfrac{\partial \delta}{\partial t} = -\dfrac{1}{a}\nabla_x \cdot \boldsymbol{v} \\ \nabla_{\mathbf{x}}^2 \phi = 4\pi G a^2 \bar{\rho}\delta \end{cases} , \tag{2.31}$$

from which at linear order and by ignoring the pressure forces, the density evolution after recombination (see 2.1.3) is [54]:

$$\ddot{\delta} + 2H\dot{\delta} - \frac{3}{2}\Omega_{DM} H^2 \delta = 0 \ . \tag{2.32}$$

2.2.2 Statistics

Due to its origin, which is depicted in section 2.3, the fluctuation field $\delta(\boldsymbol{x}, a)$ is intrinsically random and it can therefore be studied through its statistical properties. For each value of a, the values of the random variable $\delta(\boldsymbol{x})$ are *extracted* from all the possible ones forming the ensamble $\mathscr{E}$ through a probability distribution $p(\bar{\delta})d\bar{\delta}$, where $\bar{\delta}$ is the value $\delta(\boldsymbol{x})$ assumes in $\bar{\boldsymbol{x}}$. The first momentum of the distribution i.e., its **expectation value**, can then be computed as:

$$\langle \bar{\delta} \rangle = \int_{\mathscr{E}} d\bar{\delta}\, p(\bar{\delta})\bar{\delta} \ . \tag{2.33}$$

If the probability distribution is the same in different points i.e., the probability of the realisation is translationally invariant, the random field is statistically homogeneous and eq. (2.33) becomes:

$$\langle \delta \rangle = \int_{\mathscr{E}} d\delta\, p(\delta)\delta \ . \tag{2.34}$$

If the probability of the realisation is also rotationally invariant, the field is statistically isotropic. In the case of cosmology, we we make an ergodic hypothesis and we compute the ensemble averages denoted by the angle brackets in eq. (2.33) and eq. (2.34) as the spatial average over different patches in the same Universe. The error made in exchanging the two can be estimated through the expectation value of $\left[\bar{\delta} - \langle\delta\rangle\right]^2$. This is 0 in the case in which the field is sampled over an infinite volume; in the case of cosmology, it is instead defined as the **cosmic variance**.

Matter 2-point correlation function and power spectrum

By considering two different points $\bar{\boldsymbol{x}}_1$ and $\bar{\boldsymbol{x}}_2$, the probability of the field assuming the values $\bar{\delta}_1$ and $\bar{\delta}_2$ is $p_{12}(\bar{\delta}_1, \bar{\delta}_2)d\bar{\delta}_1 d\bar{\delta}_2$. If $\bar{\delta}_1, \bar{\delta}_2$ are independent from one another, $p_{12}(\bar{\delta}_1, \bar{\delta}_2) = p_1(\bar{\delta}_1)p_2(\bar{\delta}_2)$ and the process is said to be Poissonian. The second moment of the distribution is $\sigma^2 = \langle\delta(\boldsymbol{x}_1)\delta(\boldsymbol{x}_2)\rangle - \langle\bar{\delta}_1\rangle\langle\bar{\delta}_2\rangle$, where the first element is the **2−point correlation function**:

$$\xi(\boldsymbol{x}_1, \boldsymbol{x}_2) = \langle\delta(\boldsymbol{x}_1)\delta(\boldsymbol{x}_2)\rangle = \int_{\mathscr{E}} d\bar{\delta}_1 d\bar{\delta}_2\, p_{12}(\bar{\delta}_1, \bar{\delta}_2)\bar{\delta}_1\bar{\delta}_2\,, \tag{2.35}$$

which for an homogeneous and isotropic field is $\xi(\boldsymbol{x}_1, \boldsymbol{x}_2) = \xi(|\boldsymbol{x}_1 - \boldsymbol{x}_2|) = \xi(r_{12})$ and from eq. (2.34): $\sigma^2 = \xi(r_{12}) - \langle\delta\rangle^2$. When considering a Poissonian process, this relation brings σ^2 to zero: this allows us to identify the 2−point correlation function as the excess joint probability with respect to a Poissonian probability of finding two overdensities δ at a certain distance r_{12}.

As described in section 2.2.1, it is useful to work in Fourier space.[14] The Fourier transform of the 2−point correlation function from eq. (2.35) is then the **power spectrum**:

$$P(\boldsymbol{k}_1, \boldsymbol{k}_2) = \int d^3x\, \xi(\boldsymbol{x}_1, \boldsymbol{x}_2)\exp\left[-i\boldsymbol{k}\cdot\boldsymbol{x}\right] = (2\pi)^3\langle\delta(\boldsymbol{k}_1)\delta^*(\boldsymbol{k}_2)\rangle\,, \tag{2.36}$$

where $\boldsymbol{x} = \boldsymbol{x}_1 - \boldsymbol{x}_2$. When translational and rotational invariances hold, this reduces to $P(k) = (2\pi)^3\delta^{D3}(\boldsymbol{k}_1 + \boldsymbol{k}_2)\, P(\boldsymbol{k})$.[15] If the k modes are uncorrelated, each $\delta(k)$ evolves independently and their superposition is Gaussian distributed:

$$p(\delta) = \frac{1}{\sqrt{2\pi}\sigma}\exp\left[-\frac{\delta^2}{2\sigma^2}\right]. \tag{2.37}$$

The covariance of $\delta(k)$ is in this case diagonal [55]. This is, at least at first approximation, the case for cosmological density perturbations, since they arise from primordial Gaussian quantum fluctuations in a scalar field [56, 57], as it is described in section 2.3. In this case, as the Wick's theorem states, the power spectrum provides a complete statistical description of the field since higher correlators are either 0 (the odd order) or combinations of $P(k)$ (the even order). Higher order statistics, such as the bispectrum[16] $B(k_1, k_2, k_3)$ are required instead to study non−Gaussianities, both of primordial origin or due to gravitational evolution.

By recalling eq. (2.57), the linear power spectrum evolution in a homogeneous and isotropic Universe can be written as $P(k, a) = T^2(k)D_1^2(a)\mathscr{P}(k)$, where $\mathscr{P}(k)$ is the primordial power spectrum described in eq. (2.61).

Matter angular power spectrum

To compute $P(\boldsymbol{k})$, it is necessary to know how the $\delta(\boldsymbol{x})$ fluctuations are distributed depending on the distance from the observer. This is not always true, neither it is easy, with the surveys currently available, to have the distance properly measured. To avoid this issue, a possible alternative is to project the density distribution on the

[14] The Fourier transform of a random field is a random field as well.

[15] δ^{D3} is the three dimensional Dirac delta

[16] The bispectrum is the Fourier transform of the 3−point correlation function $\zeta(r_1, r_2)$, defined as $\langle\delta(x)\delta(x + r_1)\delta(x + r_2)\rangle$.

observed sky i.e., on the sphere. In this way, the perturbation field can be studied through its expansion in spherical coordinates $\boldsymbol{x} = (r, \Omega) = (r, \theta, \phi)$, that is:

$$\delta(\boldsymbol{x}, \tau) = \sum_{\ell=1}^{\infty} \sum_{m=-\ell}^{\ell} \delta_{\ell m}(\boldsymbol{x}, \tau) Y_{\ell m}(\Omega) \,, \tag{2.38}$$

where $\delta_{\ell m}(\boldsymbol{x}, \tau)$ are the amplitudes coefficients, which vary in space and time:

$$\delta_{\ell m} = \int d\Omega \delta(\boldsymbol{x}, \tau) Y^*_{\ell m}(\Omega), \tag{2.39}$$

and $Y_{\ell m}(\theta, \phi)$ the spherical harmonics i.e., a complete set of eigenfunctions[17] on the sphere. Spherical harmonics are defined with respect to the angular coordinates as:

$$Y_{\ell m}(\theta, \phi) \;=\; \mathcal{N} e^{im\phi} \mathcal{P}_\ell^{|m|}(\cos\theta) \,, \tag{2.40}$$

being $\mathcal{N}$ the normalization and $\mathcal{P}_\ell^{|m|}(s)$ ($s = \cos\theta$) the associated Legendre polynomials (see e.g., [58]), which are defined as:

$$\begin{aligned} \mathcal{P}_\ell^m(s) =& (-1)^m (1-s^2)^{m/2} \frac{d^m}{ds^m} \mathcal{P}_\ell^0(s) \\ =& (-1)^m (1-s^2)^{m/2} \frac{d^m}{ds^m} \left[\frac{1}{2^\ell \ell!} \frac{d^{\ell+m}}{ds^{\ell+m}} (s^2-1)^\ell \right] \,, \end{aligned} \tag{2.41}$$

where $\ell = 0, 1 ... \propto 1/\theta$ and $m = -\ell, ... 0 ... + \ell$. The value of $\ell \sim \pi/\vartheta$ is related to the angular scale of the perturbations on the sphere; m to their orientation. Assuming the distribution to be isotropic, it is possible to average over m.

In this formulation, amplitudes are distributed with average $\langle a_{\ell m} \rangle = 0$ and variance:

$$\langle \delta_{\ell_1 m_1} \delta^*_{\ell_2 m_2} \rangle = \delta^D_{\ell_1 \ell_2} \delta^D_{m_1 m_2} C_\ell \,. \tag{2.42}$$

C_ℓ is called the **angular power spectrum**. The number of possible samplings for a given ℓ is $\sum_{m=-\ell}^{\ell} |m|$; this provides an uncertainty over C_ℓ that is analogous to the cosmic variance previously defined. Its value is computed [12] as:

$$\frac{\Delta C_\ell}{C_\ell} = \sqrt{\frac{2}{2\ell+1}} \,. \tag{2.43}$$

Lower multipoles ℓ i.e., larger angular scales θ, intrinsically have an higher uncertainty since only few patches on such sizes can be observed on the sky. The angular power spectrum C_ℓ can be reconducted to the power spectrum $P(k)$ described in the previous section since the Fourier space and the harmonic space can are related by:

$$\exp\left[-i\boldsymbol{k} \cdot \boldsymbol{x}\right] = 4\pi \sum_{\ell m} i^\ell j_\ell(k\chi) \, Y^*_{\ell m}(\Omega_k) Y_{\ell m}(\Omega) \,, \tag{2.44}$$

where Ω_k indicates the direction of $\boldsymbol{k}$ and Ω the direction of $\boldsymbol{x}$. $j_\ell(k\chi)$ are the spherical Bessel functions, computed with respect to the comoving distance χ (see section 2.1.2) as:

$$j_\ell(k\chi) = \sqrt{\frac{\pi}{2k\chi}} J_{\ell+\frac{1}{2}}(k\chi) \,, \tag{2.45}$$

where $J_{\ell+\frac{1}{2}}(k\chi)$ are the first type Bessel functions,[18] that can be written by using

[17] Taken a linear operator F defined over a function space, its eigenfunctions g satisfy the relation $Fg = \lambda g$ where λ is a scalar called the **eigenvalue**.

[18] First type Bessel functions have have finite value origin of the coordinate system if $\ell \geq 0$, while they diverge if $\ell < 0$.

$\Gamma(k\chi) = \int_0^{+\infty} dt\, t^{k\chi-1} \exp[-t]$ as:

$$J_\ell(k\chi) = \sum_{m=0}^{\infty} \frac{(-1)^m}{m!\,\Gamma(m+\ell+1)} \left(\frac{k\chi}{2}\right)^{2m+\ell} \tag{2.46}$$

By projecting eq. (2.36) in harmonic space through section 2.44, therefore, the angular power spectrum C_ℓ turns out to be expressed in terms of the power spectrum $P(k)$ as:

$$C_\ell = \frac{2}{\pi} \int dk\, k^2 P(k) \int d\chi_1\, j_\ell(k\chi_1) \int d\chi_2\, j_\ell(k\chi_2)\,. \tag{2.47}$$

2.2.3 Evolution in Fourier space

To study the solutions of this equation, it is convenient to work in Fourier space. In this framework, $\delta(\boldsymbol{x}, t)$ can be decomposed as the superposition of plane waves with different amplitudes:

$$\delta(\boldsymbol{k}) = \frac{1}{2\pi^3} \int d^3x\, \delta(\boldsymbol{x}) \exp(-i\boldsymbol{k}\cdot\boldsymbol{x})\,. \tag{2.48}$$

In the linear regime, each $\boldsymbol{k}$ mode evolves independently. By approximating the Universe with a cubic volume of side $L >> l_s$ where l_s is the maximum scale for the perturbations, the inverse of eq. (2.48) can be expressed as the Fourier series:

$$\delta(\boldsymbol{x}) = \sum_{\boldsymbol{k}} \delta_{\boldsymbol{k}} \exp(i\boldsymbol{k}\cdot\boldsymbol{x})\,, \tag{2.49}$$

where the wavevector $\boldsymbol{k}$ components are set by the assumption of periodic boundary conditions in all the directions e.g., $\delta^D(L, y, z) = \delta^D(0, y, z)$, as [59]:

$$k_{x,y,z} = \mathsf{n}_{x,y,z} \frac{2\pi}{L} \quad \text{with } \mathsf{n}_{x,y,z} \text{ scalars}\,, \tag{2.50}$$

and the Fourier coefficients $\delta_{\boldsymbol{k}}$ are:

$$\delta_{\boldsymbol{k}} = \frac{1}{L^3} \int_{L^3} d^3x\, \delta(\boldsymbol{x}) \exp(-i\boldsymbol{k}\cdot\boldsymbol{x}) \quad \text{with complex conjugate } \delta^*_{\boldsymbol{k}} = \delta_{-\boldsymbol{k}}\,. \tag{2.51}$$

The evolution of $\delta_{\boldsymbol{k}}$ across cosmic time (i.e., depending on $a(t)$) is related to the evolution of the Fourier transform of the gravitational potential $\phi(k, a)$ by means of the Poisson eq. (2.30). In standard general relativity, the dependence on a can be separated from the k dependence; the potential today is therefore obtained as:

$$\phi_0(\boldsymbol{k}, a_0) = \phi_p(\boldsymbol{k}) T(k) D_1(a)\,. \tag{2.52}$$

Here, $\phi_p(\boldsymbol{k})$ is the primordial value of the potential, $T(k)$ is the transfer function and D_1 the growth function. The **transfer function** describes the evolution of perturbations at the epoch of horizon crossing and during the radiation−matter transition (see section 2.1.3). It is conventionally defined [12] to get $T(k) = 1$ on Large Scales (LS) and:

$$T(k) = \frac{\phi(k, a_\mathrm{L})}{\phi^\mathrm{LS}(k, a_\mathrm{L})}\,, \tag{2.53}$$

where a_{L} is the scale factor at late time i.e., in the matter dominated era and well after the perturbation entered the horizon. In eq. (2.52), the **growth function** $D_1(a)$ describes instead the wavelength independent growth at late times; conventionally:

$$\frac{D_1(a)}{a} = \frac{\phi(a)}{\phi(a_{\mathrm{L}})} \, . \tag{2.54}$$

Both the transfer function and the growth function should be studied separately for different scales and different epochs; a full analysis can be found e.g., in [12]. In particular, perturbations freeze when their scale is larger than the horizon, defined in eq. (2.21), while evolve after entering it. While the evolution during the matter dominated era is fully due to gravity, the evolution in radiation dominated era also depends on the effect of radiation pressure that counterbalance the gravitational collapse, inducing acoustic oscillations. A full description of the processes which take place in the radiation dominated era is beyond the scope of this thesis; in section 3.1, instead, we will present the evolution in the matter dominated era in the Newtonian regime.

Here, we will just stress that the value of the factor in eq. (2.53) is $T(k) = 9/10$ within the matter dominated era, and to show the result for the growth function at late times ($z \lesssim 10$). In this case all the k modes experience the same $D_1(a)$ since they all have entered the horizon and the growth function can be computed analytically by integrating eq. (2.32) as:

$$D_1(a) = \frac{5\Omega_{DM}}{2}\frac{H(a)}{H_0}\int_0^a da' \left[a'\frac{H(a')}{H_0}\right]^{-3} , \tag{2.55}$$

which can also be expressed as:

$$D_1(z) = \frac{5\Omega_{DM}}{2}\frac{H(z)}{H_0}\int_z^\infty dz'(1+z')\frac{H_0^3}{H(z')^3} \, . \tag{2.56}$$

Figure 2.3 shows the growth function in the formulation by eq. (2.56) for a flat Universe with different values of Ω_{DM}: the more matter the Universe contains, the larger is the gravitational instability, determining a higher value of $D_1(z)$ in the local Universe.

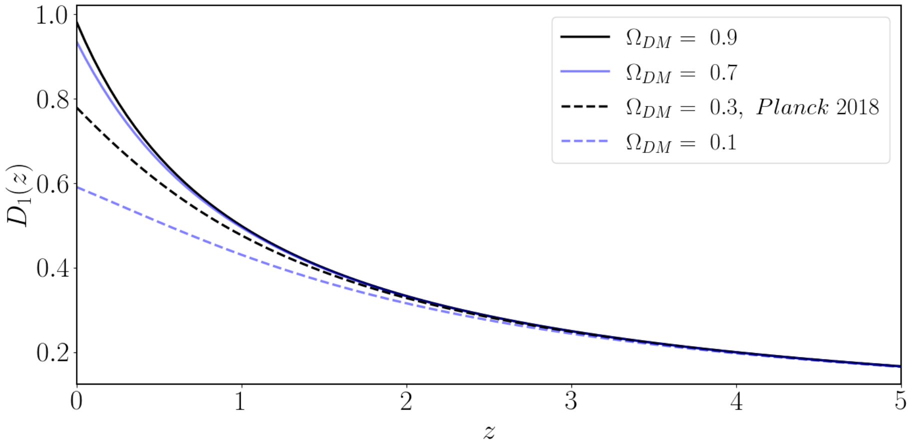

Figure 2.3: Growth function as described in eq. (2.56) for different values of Ω_{DM} in a flat Universe (i.e., $\Omega_\Lambda = 1 - \Omega_{DM}$). The case $\Omega_{DM} = 0.3$ represents the fiducial cosmology [13].

Finally, by the Poisson eq. (2.30) for $a > a_L$ and solving eq. (2.32), the density perturbation evolution can be described by two linear independent solutions $\delta(\boldsymbol{k}, t) \propto D_\pm(t)T(\boldsymbol{k})\phi(\boldsymbol{k})$: the growing mode $D_+(t) \propto a(t)$ [60] and the decaying mode $D_-(t)$, which can be neglect since it is energetically least favourably with respect to the other [9]. Therefore:

$$\delta(\boldsymbol{k},a) = \frac{2}{3}\frac{k^2 a}{\Omega_{DM}H_0^2}\phi_0(\boldsymbol{k},a) = \frac{3}{5}\frac{k^2}{\Omega_{DM}H_0^2}\,\phi(\boldsymbol{k})T(k)D_1(a)\,. \tag{2.57}$$

Eq. (2.57) describes the evolution of pressure−less CDM inhomogeneties: these form the potential wells that delineate the large scale structures, in which baryons fall after recombination. In section 3.1, we will show how this happens and we will describe the other ingredients that need to be taken into account.

2.3 The primordial Universe

To explain the origin of the perturbations from which large scale structures formed, the standard cosmological model described in section 2.1 has to be expanded. The solution that today is most widely accepted is the inflationary paradigm.

Inflation is a period of accelerated expansion that te Universe underwent at early times. It was firstly introduced by [61–64] to solve some fine−tuning problems emerged from the Hot Big Bang[19] theory: among those, the fact that the Universe is almost flat (*flatness problem*) and that it is almost homogeneous (*horizon problem*), as CMB observations highlight (see e.g., [6]). Both these conditions needs to be explained by a physical process, otherwise their realisation would seem an *ad hoc* prescription of the theory. This is done by requiring that, before the radiation dominated era described in section 2.1.3, an epoch exists in which the Hubble parameter H is constant i.e., the scale factor evolves as:

$$a \propto \exp(Ht)\,. \tag{2.58}$$

In this way, the curvature density parameter $\Omega_K = 1 - \sum_i \Omega_i$ from eq. (2.13) would evolve as $\Omega_K \propto 1/a^2$ through the Friedmann eq. (2.7), rapidly approaching the 0 value compatible with flatness.

The same condition solves the horizon problem: CMB homogeneity on scales larger than 1° would not be explainable since at recombination their angular diameter distance D_A (see eq. (2.19)) would be larger than the particle horizon[20] r_H that assures that the causality connection has occurred across cosmic time. Nevertheless, by including the inflation period $t \in [t^s_{infl}, t^e_{infl}]$ described by eq. (2.58), r_H at time t acquires the contribution:

$$r_H(t) \simeq \frac{a(t)}{a^e_{infl}H^e_{infl}}\exp(N_{ef})\,, \tag{2.59}$$

thus at recombination $D_A^{rec} > r_H^{rec}$ is satisfied if:

$$\frac{D_A^{rec}}{r_H^{rec}} \simeq \left[\frac{a^{rec}}{H_0}\right]\cdot\left[\frac{a^{rec}\exp(N_{ef})}{a^e_{infl}H^e_{infl}}\right]^{-1} > 1 \quad\Rightarrow\quad \frac{a^e_{infl}H^e_{infl}}{H_0} < \exp(N_{ef})\,, \tag{2.60}$$

where N_{ef} is called the **e−folds number** [50]. This mechanism is usually modelled through the use of one or more scalar fields ϕ, called the **inflaton(s)**, with potential term $V(\phi)$, through which the dynamical behaviour of the Universe can be characterized. The functional form and the origin of ϕ and $V(\phi)$ are still debated and a plethora of different models exist, the simplest of which consider a single

[19] Before the discovery of the accelerated expansion of the Universe in 1998 [41] and that brought to the rise of the ΛCDM paradigm, the standard model for cosmology was the Big Bang theory, based in turn on the FLRW description of the Universe.

[20] The particle horizon at a certain time $\bar{t}$ is obtained by integrating the cosmological horizon d_H in eq. (2.21) from $t = -\infty$ up to $\bar{t}$.

scalar field ϕ moving through a minimum of the $V(\phi)$ potential (see e.g., [65] for a review of the models in light of *Planck 2013* results [66]).

Independently on the particular model chosen to characterize it, on one hand, inflation explains the homogeneity of the background Universe by increasing the size of the cosmological horizon and bringing the thermal equilibrium condition (see section 2.1.3) to be satisfied onto the larger scales. On the other hand, the inflaton(s) display tiny quantum fluctuations which are stretched to super−horizon scales during the accelerated expansion inflation. Scalar quantum fluctuations[21] are in this sense the seeds of the density inhomogeneities we see today. Being produced by a stochastic process, they can be treated as independent random variables and described through their power spectrum (see section 2.2.2); their superposition is Gaussian as well, thanks to the independence and the stochasticity conditions. The general inflationary prediction is that the power spectrum is described by a power−law description:

$$\mathscr{P}(k) = A_s k^{n_s} \; , \tag{2.61}$$

where A_s is the amplitude, while the value of the **scalar spectral index**[22] n_s is defined through the dimensionless power spectrum $\Delta(k) = k^3\mathscr{P}(k)/2\pi^2$ as:

$$n_s(k) - 1 = \frac{d\ln\Delta(k)}{d\ln k} \; . \tag{2.62}$$

The easiest formulation for the primordial power spectrum is the Harrison−Zel'dovich scale invariant spectrum, in which $n_s = 1$ [67, 68]. When $n_s > 1$ the spectrum is described as **blue−tilted**, while when $n_s < 1$ it is referred to as **red−tilted**. A general prediction from inflation is a slight deviation from $n_s = 1$; this is now verified at $> 6\sigma$ evidence by *Planck 2018* measurements [13], that indicates that n_s is compatible with a slightly red−tilted power spectrum (see table 2.1). Even in the case in which the primordial fluctuations are well described by the Harrison−Zel'dovich scale−invariant spectrum, the transfer function introduced in eq. (2.53) would alter its shape during cosmic time.

2.3.1 Primordial black holes

Recently, a renewed attention has been given to the hypothesis of Primordial Black Holes[23] (PBH) existence [69–72]. PBH can be born in the early Universe, before the matter−radiation equivalence described in section 2.1.3: they are high density regions which collapsed under the effect of gravity, overcoming the pressure forces and the cosmic expansion acting at the time [70]. Because of their early formation, PBH are not considered as part of the baryonic matter produced during the primordial nucleosynthesis, but they enter as candidates DM candidates. Using Ω_{PBH} in analogy with section 2.1 to indicate the PBH density, it is customary to define:

$$f_{PBH} = \frac{\Omega_{PBH}}{\Omega_{DM}} \; , \tag{2.64}$$

as the DM fraction composed by PBH. The $f_{PBH} = 1$ would indicate that all the DM is made by PBH; values $f_{PBH} < 1$ would imply the existence of other DM kinds e.g., WIMPs or axions (see section 2.1.1).

To produce PBH, many mechanisms have been proposed, mostly related with the existence of large inhomogeneities at the smaller scales in the primordial power spectrum. This requires particular features in the scale−dependence of eq. (2.61), due for instance to a blue tilt (i.e., increasing spectrum with decreasing scales,

[21] Adiabatic fluctuations, which couple matter and radiation but in which entropy does not vary spatially, are usually considered.

[22] The same description can be realised for tensor perturbations (see section 2.2) i.e., the ones generating primordial gravitational waves (see section 4.1). In this case, the **tensor spectral index** is defined as: $n_t(k) = d\ln\Delta_t(k)/d\ln k$.

[23] For an object of mass M, the Schwarzshild radius is defined as:

$$R_s = \frac{2GM}{c^2} \; , \tag{2.63}$$

where c is the speed of light and G the gravitational constant. Objects having size $R < R_s$ are black holes; for a non−rotating black hole, R_s is as well the size of the event horizon i.e., the distance below which not even light can escape the black hole gravitational field.

see e.g., [73–75]) or to particular inflationary potentials that create peaks on the small scales (e.g., chaotic inflation in [76], where initial conditions are randomly distributed, or curvaton inflation in [77], where adiabatic density fluctuations are generated from isocurvature perturbations) or the presence of a running index[24] for n_s (e.g., [75, 78]). Other possible explanations for the existence of PBH exist, involving e.g., bubble collisions during phase transitions [79, 80] or cosmic strings [81, 82].

At first approximation, PBH formation can be studied through spherical collapse[25] of a positive curvature perturbation ψ over the FLRW background described in section 2.1 [72]. Initially, the comoving size of such perturbation would be larger than the cosmological horizon d_H from eq. (2.21); therefore, it can be described through the metric in eq. (2.1) in a locally closed Universe, where the curvature $ꝁ$ is described as:

$$ꝁ = -\frac{\psi'(r_p)}{r_p}\frac{2 + r_p\psi'(r_p)}{\exp(2\psi(r_p))}\,, \tag{2.65}$$

where r_p is related to the comoving coordinate through $r = r_p \exp(\psi(r_p))$ and ψ' is the derivative of the perturbation ψ with respect to r_p. This change in the metric with respect to the flat FLRW case described in section 2.1 propagates to the Friedmann eq. (2.7) and to the definition of the density contrast, which become [72]:

$$H^2(t) + \frac{ꝁ(r)}{a^2} = \frac{8\pi G}{3}\rho\,, \tag{2.66}$$

$$\delta = \frac{3ꝁ(r)}{8\pi G a^2\bar{\rho}} = \frac{ꝁ(r)}{H^2 a^2}\,. \tag{2.67}$$

The perturbation in the previous equation grows in time, reaching $\delta = 1$ at t_c: this can be considered as the moment of the PBH formation. The condition of the collapse at this moment is obtained by comparing the Jeans length $c_S H^{-1}$ to the perturbation size:

$$\frac{c_S^2 k^2}{a^2} = H^2 = \frac{ꝁ}{a^2}\,, \tag{2.68}$$

and by imposing that $\delta > \delta_c$, where the threshold value $\delta_c \simeq c_S^2$ is set by the Jeans theory [84]. c_S is the sound speed defined in eq. (3.8), the value of which is $1/3$ in the radiation−dominated era. Therefore, from eq. (2.68), it is possible to set $ꝁ = c_S^2 k^2$ and the condition for the PBH formation is found to be:

$$\frac{c_S^2 k^2}{H^2(t_c)a^2(t_c)} > \frac{1}{3}\,. \tag{2.69}$$

Since the Jeans length at t_c is roughly the size of the horizon [72], at first approximation the mass of the formed PBH can be estimated as the mass included in the horizon at the collapse, that is [71]:

$$M_{PBH} \simeq \frac{c^3 t_c}{G} \simeq 10^{15}\left(\frac{t_c}{10^{-23}\mathrm{s}}\right)\mathrm{g}\,. \tag{2.70}$$

Considering the Planck time $t_c = 10^{-43}$ s, eq. (2.70) states that PBH form with the Planck mass $M_{PBH} \simeq 10^{-5}$g. PBH that formed at $t_c \sim 10^{-4}$s after the Big Bang instead have mass $M_{PBH} \simeq 10\,M_\odot$, while for $t_c \sim 1$s the mass is $M_{PBH} \simeq 10^5\,M_\odot$. Different models of PBH formation assume different scales for the initial inhomogeneities, providing then different values for PBH masses: for simplicity,

[24] The running of the spectral index describes the scale−dependence of n_s and it is defined as $n' = dn_s/d\ln k$.

[25] Non−spherical effects can be non−negligible, leading to modifications of the threshold value δ_c that affect the PBH abundance, decreasing it [83].

usually a narrow, nearly monochromatic distribution is assumed to describe them. Such models are the simplest, but it is more accurate to use broad mass distributions [71]: they can be due both to a higher number of scales undergoing the primordial collapse (and therefore, collapsing in different moments and forming PBH with different masses) or to accretion of dark or baryonic matter on the PBH some time after the formation occurred.

Depending on the PBH mass, the value of f_{PBH} defined in eq. (2.64) is today constrained using different techniques and observations. In [71, 72] a summary of them can be found.[26] Briefly, depending on the PBH mass, the main constraints on f_{PBH} can be divided as follows.

Hawking radiation: black holes evaporate because of pair production and $\gamma-$ray emission near their event horizon and therefore have a finite lifetime $t_{BH} \simeq 10^{71}(M/M_{\odot})^3$s [89]. PBH having $M_{PBH} \lesssim 10^{15}$g, therefore evaporate in less than the Hubble time (i.e., the age of the Universe) and are no longer observable today. Their abundance in the early Universe, however, can be constrained from the extra−galactic $\gamma-$ray background and by modelling the effect they could have on the primordial nucleosynthesis [90, 91].

Non−Gaussianity: some of the models for PBH production implies the presence of primordial non−Gaussianities. These would be observed also on the CMB perturbation distribution [71], which is however well constrained by *Planck 2018* results [92].

Gravitational lensing: PBH can act as lenses that enhance the light of background sources or distort them. Depending on M_{PBH} and therefore on the size of the gravitational lens it produces, microlensing (for ∼ stellar mass PBH) or millilensing (for supermassive PBH) could occur. PBH constraints can be derived also from the lensing of supernovae IA (see section 3.3.2). As detailed e.g., in [93–95], lensing magnification induced by the presence of PBH (or other compact objects) can alter the estimate of the luminosity distance of the supernova and introduce particular features on the probability density function of the magnification itself.

Dynamical constraints: the PBH gravitational field would affect the astrophysical systems, altering them and eventually bringing to their disruption. The number of observations of such astrophysical systems, then, can be used to constrain the abundance of PBH with different masses. Small PBH can pass through white dwarfs increasing the kinetic energy of the atoms they are made of and so their temperature, eventually bringing to the ignition of nuclear fusion and the disruption of the stars [96]. Larger PBH can be constrained in relation with the existence of wide binaries in the DM halo around our Galaxy [97], of globular clusters [98] and dwarf−galaxies [99]. The Galactic center and the Galactic disk would be affected by the presence of PBH as well: on one side, dynamical friction would accumulate PBH in the center of the Galaxy, increasing the mass in this region and altering the dynamics of nearby stars [98]. On the other side, encounters with PBH would increase the speed of the stars in the disk [100], exceeding the observed limits [101].

Accretion constraints: PBH accrete material, both leaving imprints on the CMB and emitting electromagnetic waves. In the first case, the heating of the accreting gas and the consequent emission would distort the CMB temperature and polarization power spectra: limits on these can therefore constrain the PBH abundance [102]. In the second case, instead, constraints are related to

[26] In the years, other constraints on the PBH abundance have been proposed but then disputed or reduced. This is the case e.g., of constraints related with femtolensing due to light diffraction effects on tiny PBH ($M_{PBH} \lesssim 10^{-13} M_{\odot}$) having Schwarzshild radius comparable with the gamma-ray wavelength. These were discussed e.g., in [85], but then disregarded in [86] through arguments related with the size of gamma-ray bursts, which makes them inappropriate for femtolensing. Similarly happened to constraints related with the dynamical disruption of neutron stars due to the accretion of tiny PBH bounded inside thme [87]. These in fact carry lots of uncertainties, linked e.g., with the rotation of the neutron star that can inhibit the accretion [88].

the emission of the hot accreting gas, which should be detectable as a multi−wavelength radiation [103–105].

Large scale structures: the presence of PBH would enhance the matter inhomogeneities described in section 3.1 on the small scales [106], leading to observable features in the power spectrum of distant quasars and of their emission lines [107].

Gravitational waves: gravitational waves can be produced at the formation of PBH, since in the non−linear regime tensor modes can be sourced by scalar perturbations, as described in section 2.2. These gravitational waves would be part of the cosmological stochastic gravitational wave background [108] (see section 4.1) that future experiments will be able to detect; in particular, since their frequency is estimated as $f = 10^{-9}(M/30\,M_{\odot})^{-1/2}$Hz [72], for solar masses size PBH they should be detectable in the range of the PTA[27] experiments [111–113]. Moreover, across cosmic time PBH can bound in binaries, which eventually merge emitting gravitational waves. In the case of $M_{PBH} \simeq 10 - 100\,M_{\odot}$, such events could contribute to the black hole merger rate observed with current interferometers (see chapter 4) and in some cases overwhelm the signal produced by astrophysical black hole mergers alone. These are related with the so−called early binaries (see section 3.3.3), which however carries some uncertainties related with the disruption of such binaries during the formation of the first DM halos [114–116]. This scenario will be analysed in detail in chapter 6, where we will present the possibility of disentangling astrophysical and primordial black hole mergers though their clustering properties [117].

All the constraints we have today (in [118] the most recent version), assuming a monochromatic mass distribution, seem to exclude that $f_{PBH} = 1$ except in the small windows $M_{PBH} \in [10^{-16}, 10^{-10}]\,M_{\odot}$ (asteroid−sublunar size asteroids) and $M_{PBH} \in [10^{13}, 10^{19}]\,M_{\odot}$. Other two windows exist in which PBH density could be non−negligible i.e, $M_{PBH} \in [10^{-7}, 10^{-5}]\,M_{\odot}$ and $M_{PBH} \in [10, 100]\,M_{\odot}$. The latest are particularly important, as we will highlight in section 3.3 and chapter 6, since they can be part of the progenitors of the merger events observed by the LIGO-Virgo Collaboration [119]. Small abundances and lower values of f_{PBH} could still be allowed. At the same time, by considering a broad mass function, $f_{PBH} = 1$ could be recovered as well (see e.g., [120]). The answer to the question whether PBH are DM candidates or not, therefore, is still unknown.

[27] Pulsar Timing Array (PTA) refers to long−term observational campaigns that regularly measure the period of millisecond pulsars i.e., spinning neutron stars emitting radio wave beams from their magnetic poles. If the time of arrival of the signals of different sources varies coherently, this can hint to the presence of gravitational waves. See e.g., [109, 110] and references therein for review.

Tracers of the dark 3

3.1 Large scale structures 26
Dark matter halos 29
Clustering and bias 32
3.2 Number counts angular power spectrum 34
Redshift space distortions 37
3.3 Tracers 44
Galaxies 44
Supernovae IA 47
Binary mergers 49

To study the Large Scale Structure (LSS) of the Universe, we need tracers that map the DM distribution. DM evolves under the effect of gravity, enhancing the Gaussian distributed primordial peaks in the density field described in chapter 2. These are the backbone for the formation of virialized structures and the evolution of baryonic matter, which falls inside the potential wells, condense and cools, bringing to the formation of astrophysical structures.

Baryonic matter gives then birth to the luminous tracers, such as galaxies: since many decades from now, surveys in the different wavelengths of the electromagnetic spectrum have started mapping them, and cosmologists have built estimators to bridge their observed distribution with structure formation theoretical models and simulations. In this sense, optical surveys constitutes one of the main sources of information for cosmology: in their studies, galaxies are treated as discrete points tracing the underlying LSS.

Galaxies are not the only probe through which LSS are analysed: between the most known examples, there are the Cosmic Microwave Background and the Intensity Mapping technique (IM), developed for unresolved radio surveys.[1] Moreover, the discovery of gravitational waves (GW, see chapter 4), opened a new window in this kind of analysis: in the next few years, surveys including more and more GW events will become available, providing a new kind of tracer, alternative to the *traditional* electromagnetic ones. In particular, it will be possible to analyse GW produced by compact object binary mergers by applying the same statistical tools developed in the galaxy survey case: as chapter 5 will show, some subtleties will however be needed to make the GW analysis self−consistent.

In this chapter we revise the main features of structure formation and the strategies commonly adopted to link discrete tracers to the underlying DM distribution. In particular, in section 3.1 we describe large scale structures in the context of standard perturbation theory, with particular reference to DM halos. We summarize how their distribution and clustering can be modelled and we introduce the standard halo mass function and halo bias adopted in literature. In section 3.2 we specialize the use of the angular power spectrum to the analysis of discrete tracers. We define the shot noise contribution and the main observational effects the spectrum is affected by in redshift space. Finally, in section 3.3 we give an overview of the formation, distribution and bias of galaxies, SuperNovae IA (SN) and compact object binary mergers: galaxies are used as a benchmark for the analysis that will be developed in the next chapters, where binary mergers will be the tracer of interest. These can be used as standard sirens, using techniques that are analogous to the ones developed for standard candles in the case of supernovae IA.

3.1 Large scale structures

The primordial fluctuations in the dark matter field described in section 2.2 and section 2.3 evolved across cosmic time through gravitational collapse, leading to the

[1] For review see: for CMB [6, 121–123] and references therein; for IM [124–126] and references therein.

formation of the large scale structures we see today. During the radiation dominated era (see section 2.1.3), it is important to study how radiation pressure inhibits the growth of structures on small scales. During this time, acoustic waves set up in the cosmic fluid, but they are dissipated by the free streaming of relativistic particles or imperfect coupling between baryons and photons [127]. All these effects leave their imprints on the CMB (see e.g., [12]) and can be interpreted in light of the Jeans instability theory [84].

After matter−radiation equality, radiation pressure drops to zero and density fluctuations continue evolving under the effect of gravity. The evolution in this case is more complex and non−linear physics have to be taken into account. In order to study the evolution on large enough scales,[2] This is based on the n−th order expansion of the FLRW metric in eq. (2.1) and of the Einstein eq. (2.4) around their background values. As for the metric:

$$
\begin{aligned}
g_{00} &= -a^2(\tau)\left(1+2\sum_{n=1}^{\infty}\frac{1}{n!}\Psi^{(n)}\right), \\
g_{0i} = g_{i0} &= -a^2(\tau)\sum_{n=1}^{\infty}\frac{1}{n!}\omega_i^{(n)}, \\
g_{ij} &= a^2(\tau)\left[\left(1-2\sum_{n=1}^{\infty}\frac{1}{n!}\Phi^{(n)}\right)\delta^D_{ij}+\sum_{n=1}^{\infty}\gamma_{ij}^{(n)}\right].
\end{aligned}
\tag{3.1}
$$

This expansion relies on the **Scalar−Vector−Tensor decomposition** (SVT), under which any differentiable traceless symmetric 3−tensor field may be decomposed into a sum of scalar, vector and tensor fields [130]. Each type of component represents a different class of phenomena [131]: scalars can be brought back to Newtonian gravity, vectors are related with the kinetic effect of gravity (also known as gravitomagnetism) while tensors are produced by the gravitational radiation, which will described in the form of gravitational waves in chapter 4. In particular, in eq. (3.1) $\Psi^{(n)}$, $\Phi^{(n)}$, $\omega_i^{(n)}$ and $\gamma_{ij}^{(n)}$ are the expansions of the scalar potentials $\Psi(\mathbf{x},\tau)$, $\Phi(\mathbf{x},\tau)$, of the vector $\omega_i(\mathbf{x},\tau)$ and of the traceless tensor $\gamma_{ij}(\mathbf{x},\tau)$. The last two as well can be written as the sum of scalar contributions (indicated with $_{\parallel}$), vector contributions (indicated with $_{\perp}$) and, in the case of γ_{ij}, a tensor contribution γ_{ijT}. These are:

$$
\omega_i = \partial_i\omega_{\parallel} + \omega_{i\perp}\,, \tag{3.2}
$$

where $\partial_i\omega_{\parallel}$ is the gradient of the scalar potential and the vector has null divergence $\partial^i\omega_{i\perp} = 0$, and:

$$
\gamma_{ij} = D_{ij}\gamma_{\parallel} + \partial_i\gamma_{j\perp} + \partial_j\gamma_{i\perp} + \gamma_{ijT}\,, \tag{3.3}
$$

where $D_{ij} = (\partial_i\partial_j - 1/3\nabla^2\delta^D_{ij})$, the vector part is such that $\partial_i\gamma_{i\perp} = 0$ and the tensor part has $\gamma^i_{iT} = 0$, $\partial^i\gamma_{iT} = 0$. Here and in eq. (3.1), δ^D_{ij} is the Dirac delta in the spatial coordinates.

Eq. (3.1) depend on the **gauge** choice i.e., on the map through which perturbed points are linked to the background. Properly selecting it, it is possible to eliminate some non−physical degrees of freedom. Some of the most commonly used gauges are:

Poisson gauge: it is defined through $\nabla\cdot\boldsymbol{\omega} = 0$ and $\nabla\cdot\gamma = 0$ and it provides the relativistic cosmological generalisation of Newtonian gravity [51]. In this case, in which g_{0i} and g_{ij} are transverse and the SVT decomposition of the FLRW metric, it only involves the two scalar potentials Ψ, Φ (which are called **the Bardeen potentials** [128] and they are gauge invariant), one vector potential

[2] At $z = 0$, on scales $k \leq 0.1\,h\,\mathrm{Mpc}^{-1}$, perturbations are small enough to be analysed in the linear approximation. In chapter 7 we will deal in more detail with the analysis of large and small scales and we will describe the issues that the latter introduce. **Standard Perturbation Theory** (SPT) [128, 129] has been developed.

$\omega_{i\perp}$, and one transverse−traceless tensor γ_{ijT}. In this gauge, the perturbed FLRW metric from eq. (2.1) takes the form:

$$ds^2 = a^2(\tau)\Big[-(1+2\Psi)d\tau^2 + 2\omega_i dx^i d\tau + \big[(1-2\Phi)\delta^D_{ij} + 2\gamma_{ij}\big]dx^i dx^j\Big] \ . \quad (3.4)$$

Longitudinal gauge or **conformal Newtonian gauge:** it is the restricted version of the Poisson gauge which holds only for the scalar perturbations, in which $w_i = 0$, $\gamma_{ij} = 0$ and the metric $g_{\mu\nu}$ is diagonal [132]. The two scalar potentials in this gauge are $\Phi = -\Psi$; in the Newtonian limit, they can be reconducted to the gravitational potential [133]. eq. (2.1) takes the form:

$$ds^2 = a^2(\tau)\big[-(1+2\Psi)d\tau^2 + (1-2\Phi)\delta^D_{ij}dx^i dx^j\big] \ . \quad (3.5)$$

Synchronous gauge: by definition, in this gauge there are no time distortions i.e., the g_{00} and g_{0i} elements of the metric are unperturbed. The metric perturbation h_{ij} can instead be decomposed into a trace part h_{ii} and a traceless part, made by two vector components $w^{\parallel}_{ij}$, $w^{\perp}_{ij}$ and a tensor component γ_{ijT} [133]. In this gauge, the perturbed FLRW metric from eq. (2.1) takes the form:

$$d^2s = a^2(\tau)\big[-c^2 d\tau^2 + (\delta^D_{ij} + h_{ij})dx^i dx^j\big] \ . \quad (3.6)$$

Lorentz gauge: it is defined by $\partial_\mu g^{\mu\nu}\sqrt{-g} = 0$ and it can be seen as the linear order approximation of the De Donder harmonic gauge [134], in which the Einstein eq. (2.4) can be solved through the wave solutions. This gauge is commonly used when studying gravitational waves and it will be applied in chapter 4.

As the SVT theorem states, at first order the scalar, vector and tensor components of $\Psi(\mathbf{x},\tau)$, $\Phi(\mathbf{x},\tau)$, $\omega_i(\mathbf{x},\tau)$ and $\gamma_{ij}(\mathbf{x},\tau)$ are independent one from another i.e., they evolve separately and each type of perturbation can not originate from the others. At higher orders, instead, mode mixing takes place and e.g., scalar perturbations can generate tensor modes [135, 136] or vice−versa [137].

It is interesting to restrict to the linear order in the Poisson gauge from eq. (3.4). Usually, the vector component is neglected because its amplitude decreases rapidly in time; the scalar component generates density fluctuations, while the tensor component generates the cosmological stochastic gravitational wave background [138] section 4.1.2.

The perturbed metric elements can be related to their physical source through eq. (2.4). To expand them, first of all it is useful to express the density and the 4−velocity as:

$$\begin{aligned} \rho &= \bar{\rho} + \sum_{n=1}^{\infty}\frac{1}{n!}\delta^{(n)}\rho \ , \\ u^\mu &= \frac{1}{a}\left(\delta^\mu_0 + \sum_{n=1}^{\infty}\frac{1}{n!}v^{\mu(n)}\right) , \end{aligned} \quad (3.7)$$

where at linear order $u^\mu = \delta^\mu_0/a = \delta^\mu_0/\sqrt{-g_{00}}$ is the comoving fluid velocity[3] and $v = d\boldsymbol{x}/d\tau$ the proper 3−velocity; in the case of perturbed spacetime, this interpretation is not so straightforward [131]. Since the normalisation $g_{\mu\nu}u^\mu u^\nu = -1$ holds, at first order in the weak field, non−relativistic approximation $u_0 = -a(1+\Psi)$ and $u_i = a(v_i + \omega_i)$: Ψ represents the effect of redshift and ω_i the dragging of

[3] 3: The condition $u^i = 0$ over the spatial coordinates defines the frame comoving with the expansion.

inertial frames, which are due to the different clock rates in different position of the spacetime.

Using the EoS, the pressure perturbation is defined as:

$$\delta p = \left.\frac{\partial p}{\partial \rho}\right|_S + \left.\frac{\partial p}{\partial S}\right|_\rho = c_S^2 \delta\rho + \delta p_{na} \,, \tag{3.8}$$

where S is the entropy and the subscripts $_{S,\,\rho}$ indicate that the transformation assumes respectively constant entropy (adiabatic modes) and constant density (isocurvature modes). c_S^2 is the adiabatic speed of sound, while p_{na} the non−adiabatic pressure component. From eq. (3.7) and eq. (3.8), the perturbed form of the stress−energy−tensor $T^{\mu\nu}$ can be expressed and, once combined with eq. (3.4) into the linearized Einstein eq. (2.4), used to compute the perturbation evolution.

If we want to describe clustering on small scales e.g., $k > 0.1\, h\,\mathrm{Mpc}^{-1}$ at $z = 0$, then the linear approximation is not enough. In this case, the linear power spectrum does not capture the full statistical properties of the distribution. Non−linear terms therefore have to be included by expanding each of the $\delta(\boldsymbol{k}_1)$ and $\delta(\boldsymbol{k}_2)$ respectively to the n−th or m−th order, in analogy to eq. (3.7). Eq. (2.36) up e.g., to the fourth order, becomes:

$$\begin{aligned} P(k) =&(2\pi)^3\delta^{D3}\Big\langle\sum_{n=1}^{\infty}\delta^{(n)}(\boldsymbol{k}_1)\sum_{m=1}^{\infty}\delta^{(m)}(\boldsymbol{k}_2)\Big\rangle \\ =&(2\pi)^3\delta^{D3}\Big[\big\langle\delta^{(1)}(\boldsymbol{k}_1)\delta^{(1)}(\boldsymbol{k}_2)\big\rangle + 2\big\langle\delta^{(1)}(\boldsymbol{k}_1)\delta^{(2)}(\boldsymbol{k}_2)\big\rangle + \\ &+ 2\big\langle\delta^{(1)}(\boldsymbol{k}_1)\delta^{(3)}(\boldsymbol{k}_2)\big\rangle + \big\langle\delta^{(2)}(\boldsymbol{k}_1)\delta^{(2)}(\boldsymbol{k}_2)\big\rangle + \cdots\Big]\,. \end{aligned} \tag{3.9}$$

The leading order term $\big\langle\delta^{(1)}(\boldsymbol{k}_1)\delta^{(1)}(\boldsymbol{k}_2)\big\rangle$ is the linear power spectrum defined in eq. (2.36), while the next−to−leading order correction,[4] is given by [139]:

$$\begin{aligned} P^{NLO}(k) &= (2\pi)^3\delta^{D3}\big[2\big\langle\delta^{(1)}(\boldsymbol{k}_1)\delta^{(3)}(\boldsymbol{k}_2)\big\rangle + \big\langle\delta^{(2)}(\boldsymbol{k}_1)\delta^{(2)}(\boldsymbol{k}_2)\big\rangle\big] \\ &= 2P^{(13)}(k) + P^{(22)}(k)\,. \end{aligned} \tag{3.10}$$

The sum between the $P(k)$ defined in eq. (2.36) and $P^{NLO}(k)$ defined in eq. (3.10) is called the **1−loop power spectrum** [139]. Non−linear corrections are needed when studying the very small scales: we will use them in the analysis developed in section 7.4. In the remaining part of the thesis, instead, we will deal only with large scales and therefore we will strictly deal with linear order power spectra.

In this context, virialized structures[5] formed, namely DM halos and galaxies. The former can be studied under the spherical collapse model (see section 3.1.1), while the latter require to deal with astrophysical effects, such as gas cooling and fragmentation (see section 3.3.1).

3.1.1 Dark matter halos

Dark matter halos are virialized structures containing the large part of the matter of the Universe [141]. At first approximation, their formation can be described through the spherical collapse of a density perturbation having a top−hat [142] or more complicated profiles [143, 144]. Halo formation takes place if the initial overdensity

[4] 4: This holds in the case of Gaussian perturbation in which the even−order terms, such as $\big\langle\delta^{(1)}(\boldsymbol{k}_1)\delta^{(2)}(\boldsymbol{k}_2)\big\rangle$, vanish.

[5] 5: The virial theorem states that the kinetic energy averaged over time $\langle T\rangle$ of a stable system of n particles, bounded by the potential energy $\langle V_{TOT}\rangle$, is $2\langle T\rangle = n\langle V_{TOT}\rangle$. In cosmology, a virialized object is internally described by its own self−gravity; with respect to the cosmic expansion on the large scales, all its parts behave as a single point particle [140].

exceeds the mean background density $\bar{\rho}$ by [141]:

$$\delta_0 = \frac{\delta_c(z)}{1+z} = \frac{3}{5}\left(\frac{3\pi}{2}\right)^{2/3} . \tag{3.11}$$

Here, δ_0 is the overdensity at initial time, whose value is obtained by extrapolating through linear theory the critical density value δ_c up to the time of collapse. The value of δ_c can be described through a proper fitting function (see e.g., [145]) and it is independent from the mass initially included in the overdensity, that is:

$$M = \frac{4\pi}{3} R_0^3 \bar{\rho}\,(1+\delta_0) \simeq \frac{4\pi}{3} R_0^3 \bar{\rho} , \tag{3.12}$$

where R_0 is the comoving size of the is the initial δ_0 overdensity. Modifications to eq. (3.11) needs to be done if we want to account for non−spherical collapse (see e.g., [145]); these however are not considered in this work.

During the collapse, the overdensity size, R_0, shrinks as:[6]

$$\frac{R(z)}{R_0} = \frac{3(1+z)}{5|\delta_*|} \frac{1-\cos\theta}{2} , \tag{3.13}$$

where δ_* is δ_0 extrapolated to the present time through linear theory. The full collapse is said to happen when the parameter θ, whose initial value is $\theta = 0$, assumes the value $\theta = 2\pi$. This however would imply that the density, which evolves as $(1+\delta) = [R_0/R(z)]^3$, goes to infinity: this divergence is avoided assuming that the collapse is stopped by the virialization of the halo, which corresponds to $\delta = \delta_c$.

When studying the DM halos in the context of LSS, two are the properties that need to be modelled: the halo mass function and the halo number density. Some models for the spherical collapse e.g., [143] also suggest that DM halos develop an internal density profile $\rho(r|m)$, where the mass m is more concentrated at small r i.e., close to the center of the halo. This property, however, becomes important only when studying physical processes inside a single halo, while they can be neglected in the study of the large scale structures. Clearly, the real process is much more complicated and it can be described in detail only through simulations (see e.g., [146]). The main complications are the a−spherical asymmetry of the collapse and the **hierarchical clustering** i.e., the theory under which smaller structures form sooner and then merge to form larger structures. The spherical collapse, therefore, has to be combined with the statistics describing a hierarchical random field, which gives rise to substructures inside the halos themselves [146].

In the simple, spherical collapse scenario, the **halo mass function** $n_h(m) = dn_h/dm$ is defined as the number of DM halos per unit mass per comoving volume. It can be computed starting from the distribution of the peaks in the initial density field i.e., of the overdensities large enough to collapse and form the halos. This leads to the following equation, first developed in an expanding Universe by Press and Shechter [140]. In their work, they model:

$$\frac{m^2}{\bar{\rho}} \frac{dn_h}{dm} \frac{dm}{m} = \nu f(\nu) \frac{d\nu}{\nu} , \tag{3.14}$$

where $\nu = [\delta_c(z)/\sigma(m)]^2$ and $\sigma(m)^2$ is the variance of the initial density fluctuation field extrapolated at the present time through the linear theory. The functional form of $f(\nu)$ has been computed by different authors, both in semi−analytical ways

[6] 6: In this expression, the Universe expansion is neglected.

and through fitting formulas related with $N-$body simulations. In the standard Press−Schechter formalism [140], it leads to:

$$n_h(m) \propto m^{-1-\alpha} \exp\left[-const\left(\frac{m^{1-\alpha}}{a(t)}\right)^2\right] , \tag{3.15}$$

where the coefficient α depends on the mass variance. Other prescriptions, such as the ones from [147] and [148] are nowadays widely used as well.

In the case in which fluctuations are described by a top−hat profile having scale $R = (3m/4\pi\bar{\rho})^{1/3}$ and the initial power spectrum is $\Delta(k)$ defined in section 2.3, the variance is:

$$\sigma^2(m) = \int \frac{dk}{k} |W(kR)|^2 \Delta(k) , \tag{3.16}$$

where $|W(kR)| = |3[\sin(kR) - kR\cos(kR)]/(kR)^3|$ is the transform of the top−hat profile.

Figure 3.1 shows the halo mass function from [148] computed at different z by using the `python.hmf` library [149] and adopted in chapter 5.

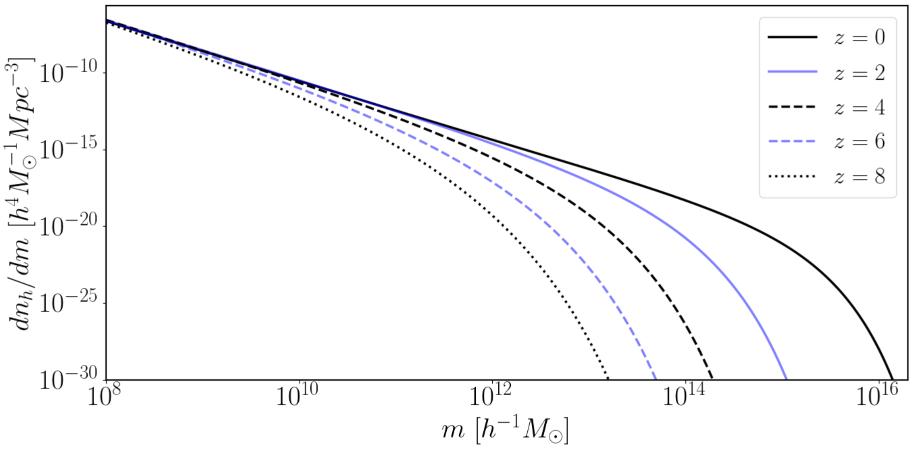

Figure 3.1: Halo mass function [148] at $z = [0, 2, 4, 6, 8]$ computed with the `python.hmf` library [149]. The minimum and maximum halo mass are set to $m^{min} = 10^8\, h^{-1}\, M_\odot$ and $m^{max} = 10^{19}\, h^{-1}\, M_\odot$ respectively.

As for the **halo number density**, this is modelled by dividing space into cells of comoving volume V, each of which contain a certain amount M of DM partitioned into halos [141]. Let $N(m, z_0|M, V, z)$ be the number of halos having mass m and formed at z_0 inside a certain cell observed at z. This is found by computing how many halos of a certain mass can form inside the cell at z_0 i.e., by applying the halo mass function prescription from eq. (3.14) to V_0, the comoving size of the cell before the collapse. Since initially, in the large cell limit, the density inside the cell is $\simeq \bar{\rho}$ and $|\delta_0| << 1$, one gets:

$$\begin{aligned} N(m, z_0|M, V, z) &= n(m, z_0|M, V, z)V_0 \simeq n(m, z_0|M, V, z)\frac{M}{\bar{\rho}} \\ &= n(m, z_0|M, V, z)V(1 + \delta_0) \, . \end{aligned} \tag{3.17}$$

The value of $n(m, z_0|M, V, z)$ can be expanded in terms of δ_c as a function of the average value of the initial halo mass function $n_h(m, z_0)$ as:

$$n(m, z_0|M, V, z) = n(m, z_0) + \frac{\delta_0}{1+z}\left(\frac{\partial n(m, z_0)}{\partial \delta_c}\right)\bigg|_{\delta_c(z_0)} + \ldots \tag{3.18}$$

Eq. (3.18) will be used in section 3.1.2 to define the clustering properties of the halos with respect to the underlying DM distribution.

Finally, following the formalism by [150, 151], the halo number density can be written as the discrete sum of the halos in each comoving position $\boldsymbol{x}_i$:

$$n(m) = \Big\langle \sum_i \delta^D(m - m_i)\delta^{D3}(\boldsymbol{x}' - \boldsymbol{x}_i) \Big\rangle \,. \tag{3.19}$$

3.1.2 Clustering and bias

Eq. (3.18) introduced the expression of the halo mass function inside a cell of a certain volume V containing the mass M of dark matter. The halo overdensity in a given cell with respect to the average [141] is described by:

$$\begin{aligned} \delta_h(m, z_f|M, V, z) &= \frac{N(m, z_f|M, V, z)}{n_h(m, z_f)V} - 1 = \delta - (1+\delta)\frac{\delta_0}{1+z}\left(\frac{\partial \ln n(m, z_0)}{\partial \delta_c}\right)\Bigg|_{\delta_c(z_0)} \\ &\simeq \left(1 + \frac{q\nu - 1}{\delta_c(z_0)} + \frac{2p/\delta_c(z_0)}{1+(q\nu)^p}\right)\delta \\ &= \big[1 + b_1(m, z_0)\big]\delta. \end{aligned} \tag{3.20}$$

where in the first line the expansion from eq. (3.18) was applied, while in the second we used the expression for $n_h(m, z_0)$ reported in [147] and only the linear terms in δ were kept. $\nu = [\delta_c(z)/\sigma(m)]^2$ was defined in section 3.1.1, while $p,\ q$ are fitting coefficients, whose values can be set to $q = 1,\ p = 0$ [141].

In eq. (3.20), the quantity $b_1(m, z_0)$ is the Lagrangian[7] **linear bias**. . This states that the halo overdensity is linearly proportional to the DM overdensity in the cells and it describes the difference between the clustering of the two: when $b_1(m, z_1) > 1$, halos are more clustered with respect to the average underlying DM field, while if $b_1(m, z_1) < 1$, their distribution is sparse. In the case in which $q = 1,\ p = 0$, the condition $b_1(m, z_1) > 1$ is satisfied for $\nu > 1$, that is for massive halos. These form in the densest cells i.e., in the densest regions of the DM Gaussian random field, which are found to be as well the most clustered [152].

The hierarchical merger model affects the linear bias redshift dependence. In fact, since smaller objects form before, the bias is expected to grow during cosmic time, since the massive halos are rarer in the past. At the same time, it was found in [153] that if the DM field contains some level of primordial non−Gaussianity, this induces a scale−dependent contribution to the halo bias. This is analytically parametrized as:

$$\Delta b(m, z_0, k) = b_1(m, z_0)\, f_{NL}\delta_c\, \frac{3\Omega_m(1+z)}{c^2k^2r_H^2D_1(z)} \,, \tag{3.21}$$

Linear bias $b_1(m, z_0)$ is only an approximated description of the halo clustering properties which applies to very large scales. On small scales, to have a proper description of the relation between DM overdensities and halos, a perturbative expansion (similar to the one described in section 2.2) [154] is needed:

$$\delta_t(\tau,\, \boldsymbol{x}) = \sum_O b_O(\tau)O(\tau,\, \boldsymbol{x}) + \sum_O \epsilon_O(\tau,\, \boldsymbol{x})O(\tau,\, \boldsymbol{x})\,. \tag{3.22}$$

In this case, $\delta_t(\tau,\, \boldsymbol{x})$ is the overdensity, depending on the conformal time τ and the comoving position $\boldsymbol{x}$, of the DM tracer t: this can represent the halos, but it

[7] In the Lagrangian frame, the observer follows the evolution of a single particle/cell/halo across time and space. This represents an alternative to the Eulerian frame, where the observer is kept in a fixed position.

can also be referred to galaxies or other tracers (see section 3.3). The key point of eq. (3.22) is the presence of the $O(\tau,\, \boldsymbol{x})$ operators and the $b_O(\tau)$ bias parameters, which describe the processes involved in the formation and clustering of tracers up to the a certain order, related to the smallest scale one wants to characterize. The second term in eq. (3.22) represents a **stochastic contribution** to the bias, due to the fact that the tracer formation depends also on the initial conditions on small scales [154], which have a random distribution, as seen in section 2.3. Each $\epsilon_O(\tau,\, \boldsymbol{x})$ is uncorrelated from the others on large scale.

As detailed in [154], $b_O(\tau)$ parameters are expressed in the Eulerian frame; the linear term is then related to its Lagrangian expression, which was used in eq. (3.20), by:

$$b_O^{(1)}(\tau) = 1 + b_1(m, z_0)\ . \tag{3.23}$$

The functional expression of all the Eulerian bias parameters is found by studying how the clustering evolves under the effect of gravity when the number of sources is conserved. In this case, δ_t must obey the continuity equation, which can be rewritten from its expression in eq. (2.29) as:

$$\frac{\partial \delta_t}{\partial \tau} + \partial_{x_i} v^i = -v^i \frac{\partial}{\partial x^i}\delta_t - \delta_t \partial_{x_i} v^i\ , \tag{3.24}$$

where v^i are the components of the tracer velocity, which is assumed to be equal to the matter velocity (i.e., no velocity bias). Solving the equation in the perturbative approach, the set of linearly independent operators $O(\tau,\, \boldsymbol{x})$ are found at each order in the expansion. Assuming DM as a pressure−less ideal fluid, one can find that, up to second order, two operators are necessary to describe the local, deterministic bias. These are related with the DM density contrast field δ and with the **tidal field** described by the traceless tensor [155]:

$$K_{ij} = \left(\frac{\partial_i \partial_j}{\nabla^2} - \frac{\delta_{ij}^D}{3}\right)\delta\ . \tag{3.25}$$

Stochastic and higher order operators[8] are needed when studying the smaller scales, where the deviation from the linear regime in not negligible [141]. These will be needed in chapter 7 when studying the bias of binary mergers on quasi−linear scales i.e., $k \in [0.1, 0.3]\, h\,\mathrm{Mpc}^{-1}$. In chapter 5, instead, the linear approximation will be assumed since only large scales are considered.

In the linear approximation, knowing the bias expansion for a generic tracer t, its auto−power spectrum is related to the DM power spectrum defined in section 2.2.2 simply through:

$$\begin{aligned} P^{tt}(k) =& (2\pi)^3 \delta^{D3} \left\langle \delta_t(\boldsymbol{k}_1)\delta_t(\boldsymbol{k}_2)\right\rangle \simeq (2\pi)^3 \delta^{D3} \left\langle b_O^1 \delta(\boldsymbol{k}_1) b_O^1 \delta(\boldsymbol{k}_2)\right\rangle \\ =& \left[b_O^{(1)}\right]^2 P(k) \end{aligned} \tag{3.26}$$

Depending on the tracer, the bias assumes a different functional form: in this section we referred to DM halos, but in practice these are unobservable.[9] To map the Large Scale Structures, luminous tracers are required: the most largely used are galaxies, which form inside the most massive DM halos: their formation is summarized in section 3.3. In the same section we will present also an alternative tracer, which is the focus of this thesis work, namely the gravitational wave events produced by binary compact object mergers.

[8] For a review of all the bias operators, see [154] and references therein.

[9] Different is the case of cosmological simulations, where both the DM power spectrum and the DM halo power spectrum can be estimated. We will analyse this possibility in chapter 7.

3.2 Number counts angular power spectrum

The starting point of a concrete survey analysis is the calculation of the power spectra of the point processes which sample the underlying DM density field through the discrete tracers. Since in the following chapters we will perform a tomographic analysis, in this section we illustrate in detail the derivation of the source angular power spectrum.

The observable to be taken into account is the source number density $n_t(\boldsymbol{x})$. Its value in the source rest frame can be related to the observed value per redshift bin dz per solid angle $d\Omega$ through:

$$n_t(\boldsymbol{x})dV = \frac{d^2N}{dzd\Omega}dzd\Omega\,. \tag{3.27}$$

The discrete nature of the sampling implies that $n_t(\boldsymbol{x})$ is:

$$n_t(\boldsymbol{x}) = \sum_{dV_i} \delta^D_t(\boldsymbol{x}-\boldsymbol{x}_i) = \sum_i \frac{1}{r^2\sin\theta}\left[\delta^K(r-r_i)\delta^K(\theta-\theta_i)\delta^K(\phi-\phi_i)\right]\,, \tag{3.28}$$

where the presence of the Dirac delta δ^D, discretized in the three spherical coordinates through the Kroenecker deltas δ^K, indicates that the counting of the tracers is performed in the infinitesimal volumes dV_i, each one containing either $N_i = 0$ or $N_i = 1$ tracer. The occupation number N_i is Poisson distributed. The source overdensity is then:

$$\hat{\delta}_t(\boldsymbol{x}) = \frac{1}{\bar{n}_t r^2\sin\theta}\sum_i N_i\left[\delta^K(r-r_i)\delta^K(\theta-\theta_i)\delta^K(\phi-\phi_i)\right]\,. \tag{3.29}$$

It is possible then to follow eq. (2.42) to project $\hat{\delta}_t(\boldsymbol{x})$ over the harmonic space, so to define the observed number counts angular power spectrum:

$$\hat{C}_\ell = \delta^D_{\ell_1\ell_2}\delta^D_{m_1m_2}\left\langle\hat{\delta}_{t,\ell_1m_1}\hat{\delta}^*_{t,\ell_2m_2}\right\rangle\,. \tag{3.30}$$

Neglecting the monopole term, and using eq. (3.29), $\hat{\delta}_{t,\ell m}$ can be expanded as:

$$\begin{aligned}\hat{\delta}_{t,\ell m} &= \sum_i \int d\Omega\,\frac{N_i}{\bar{n}_t r^2\sin\theta}\left[\delta^K(r-r_i)\delta^K(\theta-\theta_i)\delta^K(\phi-\phi_i)\right]Y^*_{\ell m,i}\\ &= \sum_i \frac{N_i}{\bar{n}_t r^2}\,\delta^K(r-r_i)\,Y^*_{\ell m,i}\,,\end{aligned} \tag{3.31}$$

where in the spherical harmonic $Y_{\ell m,i}$ (defined in eq. (2.40)) the Ω_i dependence has been omitted for clarity. Therefore:

$$\left\langle\hat{\delta}_{t,\ell_1m_1}\hat{\delta}^*_{t,\ell_2m_2}\right\rangle = \sum_{ij}\frac{\langle N_iN_j\rangle}{\bar{n}_t^2}\frac{1}{r^4}\left[\delta^K(r-r_i)\delta^K(r-r_j)\right]Y^*_{\ell_1m_1,i}\,Y_{\ell_2m_2,j}\,. \tag{3.32}$$

Using the properties of the Poisson distribution, eq. (3.32) can be split into two parts:

$$\begin{cases}\langle N_iN_j\rangle & = \bar{n}_t^2[1+\langle\delta_{t,i}\delta^*_{t,j}\rangle]\Delta V_i\Delta V_j \quad \text{if } i\neq j\\ \langle N_i^2\rangle & = \bar{n}_t\Delta V_i \quad \text{if } i=j\end{cases}\,. \tag{3.33}$$

where $\delta_{t,ij}$ represent the value of the intrinsic field from eq. (3.29) inside the volumes ΔV_{ij}.

By converting $\Delta V_{ij} = r^2 \Delta r \Delta\Omega$ and neglecting the monopole term again, eq. (3.32) becomes:

$$\begin{aligned}
\left\langle \hat{\delta}_{t,\ell_1 m_1} \hat{\delta}^*_{t,\ell_2 m_2} \right\rangle &= \Big\langle \sum_{i\neq j} \Delta r_i \Delta r_j \; \Delta\Omega_i \Delta\Omega_j \left\langle \delta_{t,i} \delta^*_{t,j} \right\rangle \cdot \\
&\quad \cdot \left[\delta^K(r-r_i)\; \delta^K(r-r_j) \right] Y^*_{\ell_1 m_1,i} Y_{\ell_2 m_2,j} + \\
&\quad + \sum_{i=j} \frac{1}{r^2 \bar{n}_t} \; \Delta r_i \Delta\Omega_i \delta^K(r-r_i)\; Y^*_{\ell_1 m_1,i} \; Y_{\ell_2 m_2,i} \Big\rangle \\
&\overset{\Delta r, \Delta\Omega \to 0}{=} \Big\langle \int dr \delta^K(r-r_i) \int dr \delta^K(r-r_j) \int d\Omega \int d\Omega Y^*_{\ell_1 m_1,i} Y_{\ell_2 m_2,j} \delta_{t,\ell_1 m_1} \delta^*_{t,\ell_2 m_2} \Big\rangle + \\
&\quad + \delta^K_{ij} \Big\langle \int dr \frac{1}{r^2 \bar{n}_t} \; \delta^K(r-r_i) \int d\Omega \; Y^*_{\ell_1 m_1,i} Y_{\ell_2 m_2,i} \Big\rangle \\
&= \quad \delta^D_{t,\ell_1\ell_2} \delta^D_{m_1 m_2} \left\langle \delta_{t,\ell_1 m_1} \delta^*_{t,\ell_2 m_2} \right\rangle + \delta^D_{t,\ell_1\ell_2} \delta^D_{m_1 m_2} \; \frac{\delta^K_{ij}}{r_i^2 \bar{n}_t} \; .
\end{aligned} \tag{3.34}$$

By moving to the observed redshift space (z, Ω), the observed angular power spectrum between the redshift bins $z_i = [z_i^{min}, z_i^{max}]$ and $z_j = [z_j^{min}, z_j^{max}]$ is:

$$\hat{C}_\ell(z_i, z_j) = C_\ell(z_i, z_j) + \frac{\delta^K_{ij}}{r_i^2 \bar{n}_t} = C_\ell(z_i, z_j) + \frac{\delta^K_{ij}}{\bar{N}_i} \; . \tag{3.35}$$

The second term in eq. (3.34) is the Poisson shot noise: $\bar{N}_i$ represents the average angular density of sources inside one bin, which is computed as:

$$\bar{N}_i = r_i^2 \bar{n}_t = \int_{z^i_{min}}^{z^i_{max}} dz \; \frac{d^2 N}{dz d\Omega} W(z_i, z) \, , \tag{3.36}$$

where the transformation from the source rest frame to the observed space is made by means of eq. (3.27) and through the change of coordinates $d^r = r^2 dr \longrightarrow dz d\Omega$, integrated over the radial distance. $W(z_i, z)$ describes how sources are distributed inside each redshift bin: usually, it is defined either as a top−hat or a Gaussian filter. If the survey does not observe the full sky, eq. (3.36) has to include either the detector angular selection function or a the observed sky fraction f_{sky}. The shot noise represents an extra−contribution to the observed angular power spectrum, arising from the variance of the Poisson point process, which is a direct consequence of the discrete and stochastic nature of the tracer.

As introduced in section 2.2.2, the number angular power spectrum can also be written as a function of the underlying DM power spectrum, in the following way:

$$\begin{aligned}
C_\ell(z_i, z_j) =& \frac{2}{\pi} \int dk \, k^2 P_t(k) \int d\chi_i \, j_\ell(k\chi_i) \int d\chi_j \, j_\ell(k\chi_j) \\
=& \frac{2}{\pi} \int dk \, k^2 P(k) \int dz_i \frac{d\chi_i}{dz_i} \, j_\ell[k\chi(z_i)] \mathcal{W}_\ell(z_i) \int dz_j \frac{d\chi_j}{dz_j} \, j_\ell[k\chi(z_j)] \mathcal{W}_\ell(z_j)
\end{aligned} \tag{3.37}$$

$$
\begin{aligned}
\simeq & \frac{2}{\pi}\int dk\, k^2 \mathscr{P}(k) T(k)\,\cdot \\
& \cdot \int dz_i \frac{d\chi_i}{dz_i}\, j_\ell(k\chi_i) W(z_i)\left[b_t(z_i)\frac{dN_t}{dz_i} D_1(z_i) + \Psi_\ell(k,z_i)\right]\cdot \\
& \cdot \int dz_j \frac{d\chi_j}{dz_j}\, j_\ell(k\chi_j) W(z_j)\left[b_t(z_j)\frac{dN_t}{dz_j} D_1(z_j) + \Psi_\ell(k,z_j)\right]\,.
\end{aligned}
$$

In the third line we introduced the linear approximation. We recall here that $\mathscr{P}(k)$ is the primordial power spectrum (see section 2.3), $T(k)$ and $D_1(z)$ respectively are the transfer function and the linear growth function introduced in section 2.2.1 and $\Psi_\ell(k,z)$ indicates the observational space distortions due to LSS described in section 3.2.1. Note that $D_1(z)$ depends on the dark energy or modified gravity model assumed. The **window functions**:

$$
\mathscr{W}_\ell(z_{i,j}) = W(z_{i,j})\left[b_t(z_{i,j})\frac{dN_t}{dz_{i,j}} D_1(z_{i,j}) + \Psi_\ell(k,z_{i,j})\right]\,, \tag{3.38}
$$

accounts for different aspects:

- The observed number distribution of the tracer dN/dz.
- The bias of the tracer with respect to the underlying DM distribution i.e., $b_t(z)$ defined through the relation $\delta_t(z) = b_t(z)\delta(z)$ introduced in section 3.1.2 and section 3.3, which in this case is assumed to be linear, local and scale−independent. This, combined with $D_1(z)$, can be rewritten as the term $\Psi^\delta(k,z)$.
- The survey selection effects, which are collected in the survey window function $W(z)$ introduced in eq. (3.36);
- The perturbations $\Psi_\ell(k,z)$, described in section 3.2.1.

Modelling eq. (3.37) is computationally expensive because of the presence of the spherical Bessel functions, which rapidly oscillate. To avoid this problem, at least on small scales, the flat sky approximation can be introduced. This is done through the Limber approximation [156], firstly applied to cosmological studies of the power spectrum in [157]. To apply it, let us rewrite the angular power spectrum in dependence of the first type Bessel functions $J_{\ell+\frac{1}{2}}(k\chi)$ the were already defined in section 2.2.2:

$$
C_\ell(z_i,z_j) = \int dkkP(k)\int d\chi_i f_i(\chi_i) J_{\ell+\frac{1}{2}}(k\chi_i)\int d\chi_j f_j(\chi_j) J_{\ell+\frac{1}{2}}(k\chi_j)\,, \tag{3.39}
$$

where we encapsulated in $f_{i,j}(\chi_{i,j}) = \left[\mathscr{W}_\ell(z_{i,j}) d\chi_{i,j}/dz_{i,j}\right]/\sqrt{\chi_{i,j}}$ all the radial dependencies. For $\ell + 1/2 = \nu > 0$, it is known that the Bessel functions grow monotonically if their argument $x = k\chi$ is comprises between 0 and ν, while they start rapidly oscillating for higher values. By following the procedure that it is revised e.g., in [158] and references therein, it is possible to express the Bessel functions as:

$$
\lim_{\epsilon\to 0}\int_0^{+\infty} dx\, \exp\left[-\epsilon(x-\nu)\right] f(x) J_\nu(x) = B_0 f(\nu) + B_1 f'(\nu) + B_2 f''(\nu) + \ldots \tag{3.40}
$$

where the B_n coefficients are computed through the Taylor expansion as:

$$
B_n = \frac{(-1)^n}{n!}\lim_{\epsilon\to 0}\frac{\partial}{\partial\epsilon^n}\int_0^{+\infty} dx\, \exp\left[-\epsilon(x-\nu)\right] J_\nu(x)\,. \tag{3.41}
$$

Since the integral of the Bessel is computed as:

$$\int_0^{+\infty} dx\, \exp\left[-\epsilon(x-\nu)\right] J_\nu(x) = 1 - \frac{\epsilon^2}{2} + \frac{\nu\epsilon^3}{6} + \ldots \tag{3.42}$$

the B_n coefficients from eq. (3.41) reduce to $B_0 = 1,\ B_1 = 0, B_2 = -1/2, \ldots$ and they can be used to simplify eq. (3.39). By keeping only the leading order (i.e., by approximating each Bessel function as the Dirac delta located at its first peak), in the limit $\epsilon \longrightarrow 0$ eq. (3.40) reduces to:

$$\int_0^{+\infty} d[k\chi]\, f(k\chi) J_{\ell+\frac{1}{2}}(k\chi) \simeq f\left(\ell + \frac{1}{2}\right), \tag{3.43}$$

and therefore, by setting $\ell + 1/2 = k\chi$ and by applying the change of variable $\chi \longrightarrow [k\chi]/k$, we can write:

$$C_\ell(z_i, z_j) \simeq \int dk\, kP(k) \frac{f_i(\chi_i)}{k} \frac{f_j(\chi_j)}{k}, \tag{3.44}$$

from which, by again changing the integration variable through $dk = d[k\chi]/\chi = kd\chi/\chi$, the angular power spectrum in the Limber approximation can finally recovered as:

$$C_\ell(z_i, z_j) \simeq \int \frac{d\chi}{\chi^2} P\left(\frac{\ell + 1/2}{\chi}\right) \left[\frac{d\chi_i}{dz_i} \mathcal{W}(z_i)\right] \left[\frac{d\chi_j}{dz_j} \mathcal{W}(z_j)\right]. \tag{3.45}$$

As e.g., [159–162] describe, this only works when the radial width of the selection function applied to 3.37 is $\Delta\chi >> 1/k$ i.e., it is larger than the scale of the perturbation. Moreover, ℓ has to be large and, when cross−spectra between different redshift bins are computed, their selection functions have to overlap.

Eq. (3.37) can be expanded to the case in which the cross−angular power spectrum is computed between two different tracers $t_1,\ t_2$. In this case, the expression simply has to be translated into:

$$C_\ell^{t_1 t_2}(z_i, z_j) = \frac{2}{\pi} \int dk\, k^2 P(k) \int dz_i \frac{d\chi_i}{dz_i} j_\ell(kz_i) \mathcal{W}_\ell^{t_1}(z_i) \int dz_j \frac{d\chi_j}{dz_j} j_\ell(kz_j) \mathcal{W}_\ell^{t_2}(z_j). \tag{3.46}$$

The window functions $\mathcal{W}_\ell^{t_1}(z_i)$ and $\mathcal{W}_\ell^{t_2}(z_j)$ in eq. (3.46) differ from one another, since each one separately characterizes the distribution and observed properties of the tracers t_1 and t_2. We will use such formulation in section 5.4.3 to derive forecasts of future survey combining gravitational waves and supernovae IA in a multi−tracer approach.

3.2.1 Redshift space distortions

The emitted signals (either EM or GW) have to travel through LSS. This leads to an apparent modification of the observed position of the tracers with respect to their intrinsic position [55, 163–167].

There are several physical contributions to the distortions that needs to be taken into account to build a fully consistent analysis:

Peculiar velocities and **Doppler effect:** the gravitational potential of matter overdensities induces a motion in the tracers, which is detached from the Universe expansion. If this provides a velocity component along the Line of Sight (LoS), the mis−estimation of the recession velocity can propagate to the Hubble law in eq. (2.3), leading to the wrong estimation for the tracer distance [163].[10] Peculiar velocities induce distortions both on the large and the small scales. In fact considering e.g., a set of sources circularly distributed around a DM overdensity, the observed distribution on large scales gets squeezed,[11] while the small scales, where velocities are bigger because of non−linearities, get stretched in the radial direction and form the so−called **Fingers−of−God** [176]. Figure 3.2 sketches these two configurations. In the following the distortions due to the mis−estimation of the Hubble law will be analysed in detail.

Weak lensing: this projection effect is due to the fact that lensing changes the luminosity of the tracers. It can happen then that some of them, which would be too dim to be observed, get magnified, entering the observational window. At the same time, the magnification brings to a mis−estimation of the observed distance of the source, making it look closer to the observer (see e.g., [161, 177–180]). This effect is analysed in detail in the following.

Gravitational potential effects: while travelling from the source to the observer, the photons and the gravitational waves enter the potential wells created by DM overdensities. In this way, on one side the time they need to travel a certain distance changes: according to GR, this determines the **Shapiro time delay**. Moreover, getting inside the potential well they gain energy, which is then lost when they leave it. Since the Universe expansion makes the overdensities *stretch* during the time the photons and GW travel inside them, the energy loss is lower than the energy gain; the opposite happens in the case of underdensities. These effects produce either a blue−shift (in the case of overdensities) or a redshift (in the case of underdensities) called **Sachs−Wolfe effect**, which can lead to the mis.estimation of the tracer position. Since this takes place anytime the photons and GW cross an overdensity, the effect is cumulative and has to be integrated along the LoS, giving rise to the **Integrated Sachs−Wolfe effect** [181].

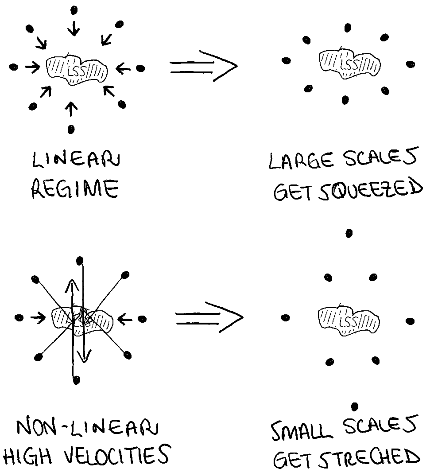

Figure 3.2: Sketch of the effect due to peculiar velocities in the linear (top row) and non−linear (bottom row) configurations. In the latter, the high value of the velocities largely alter the observed position of the sources.

At the most general level, when all of these effects are taken into account, cosmic translational invariance is broken, making it necessary to redefine eq. (2.42) and therefore changing the angular power spectrum definition. However, it is customary

[10] The effect of peculiar velocities in altering the observed position of nearby galaxies was already estimated in the previous years [168–171] and applied to the 2−point correlation function [172, 173].

[11] A similar effect can be related with the so called **Alcock−Paczyński effect**. This was firstly measured by the authors of [174] with respect to galaxy distribution in clusters and it was based on the comparison between their observed angular size and their radial dimension in redshift space. Since intrinsically the cluster should be spherical, the ratio between the two estimates provided a test for the cosmological models. The same reasoning can be generalized to the comparison between the estimate of the angular diameter distance D_A defined in eq. (2.19) and the radial distance related with $H(z)$ (see e.g., [175] and references therein).

to deal with different levels of approximation and in a practical analysis part of them are neglected. The appropriate approximation level to be used depends on the survey characteristics.

In this thesis, results are obtained by assuming the following prescriptions:

- The window function is sufficiently large, so the isotropy and homogeneity conditions are on average satisfied.
- All the tracers inside a certain redshift bin are found at the same distance from the observer, indicated either through the redshift z or the comoving distance.
- The observer is far enough from the tracers to assume that all the LoS are parallel one with respect to the others i.e., the **plane−parallel** approximation holds and the waveform of the incoming signal is well described by a plane wave. If this was not the case, **wide angle effects** would come into play (see [182–186] and figure 3.3 for an heuristic representation).

In these conditions, the leading order effects in the redshift space distortions are peculiar velocities and lensing magnification. These, together with the effect of lensing convergence, are the only ones taken into account in the analysis developed in chapter 5 and chapter 6.

Here we review the derivation of the redshift distortions due to peculiar velocities using the Newtonian formalism.[12] To do so, we will indicate with $\boldsymbol{s}$ the radial coordinate along the LoS in the observed redshift space, and with $\boldsymbol{r}$ the one in real space. Both can always be reconducted to the observed and real redshifts z^{obs}, z (or comoving distances χ^{obs}, χ); in the plane−parallel approximation, the identification between these coordinates is straightforward.

Peculiar velocities

As firstly described in [163], peculiar velocities induced by DM overdensities affect the estimation of the tracer distance with respect to the observer. In fact, the gravitational pull that DM exerts on the tracer makes it deviate from the Hubble flow. The observed velocity of the tracer along the LoS is then found by combining the contribution of the recession velocity $\boldsymbol{v}_H$ (due to the Universe expansion) and the peculiar velocity $\boldsymbol{v}_r$ (due to the DM gravitational potential). Using the projection along the LoS of this combined velocity $\boldsymbol{v}_{tot} = (\boldsymbol{v}_H + \boldsymbol{v}) \cdot \hat{\boldsymbol{x}}$ in the Hubble law from eq. (2.3), therefore, leads to a misestimation of the observed redshift with respect to the real one:

$$z^{obs} = z + \delta z = z + \boldsymbol{v} \cdot \hat{\boldsymbol{x}} \ . \tag{3.47}$$

By assuming the fiducial cosmology, the observed redshift is converted to the observed comoving distance, which again differs from the real one as:

$$\chi^{obs} = \chi + \frac{\partial \chi}{\partial z} \delta z = \chi + \frac{\boldsymbol{v} \cdot \hat{\boldsymbol{x}}}{H(z)} \ . \tag{3.48}$$

Let $s = \boldsymbol{s} \cdot \hat{\boldsymbol{x}} = \chi^{obs}$, $r = \boldsymbol{r} \cdot \hat{\boldsymbol{x}} = \chi$ and $v = \boldsymbol{v} \cdot \hat{\boldsymbol{x}}$ respectively be the radial coordinates in observed and real space and the velocity, all projected along the LoS. Since the peculiar velocities introduce a projection effect, the number of the tracers is conserved between the two spaces i.e., none of them is either destroyed or created. In this case, since the tracer number densities in the two spaces $n^{s,r}$ are both related to the mean number densities[13] $\bar{n}^{s,s}$ through $n^{s,r} = \bar{n}^{s,r}[1 + \delta^{s,r}]$, o:

[12] The derivation of space distortions in fully GR formalism (see e.g., [166, 167]) is beyond the scope of the thesis. The corrections this would introduce in the results of the analysis presented in chapter 5 and chapter 6 are anyway below the intrinsic level of accuracy of the forecast tools adopted.

[13] In the isotropic and homogeneous Universe, $\bar{n}^s = \bar{n}^r$. However, when considering the anisotropies due to LSS, the density distribution along two LoS can be different.

$$\begin{aligned} n^s d^3 s &= n^r d^3 r \\ \bar{n}^s [1+\delta^s] d^3 s &= \bar{n}^r [1+\delta^r] d^3 r \\ 1+\delta^s = [1+\delta^r] \frac{\bar{n}^r}{\bar{n}^s} \frac{r^2 dr}{s^2 ds} &= [1+\delta^r] \frac{n^r}{n^{r+v/H}} \frac{r^2 dr}{(r+v/H)^2 ds} \,, \end{aligned} \tag{3.49}$$

where the distance dependence of the Hubble factor H has been omitted for clarity. The quantity $d^3r/d^3s = r^2dr/[(r+v/H)^2ds]$ is the Jacobian J of the transformation between the observed and the real spaces. It can be rewritten as:

$$\begin{aligned} J &= \frac{r^2}{(r+v/H)^2}\left(\frac{ds}{dr}\right)^{-1} = \left[\frac{r}{r+v/H}\right]^2 \left[1+\frac{\partial}{\partial r}\left(\frac{v}{H}\right)\right]^{-1} \\ &\simeq \left[1+\frac{v}{rH}\right]^{-2}\left[1-\frac{\partial}{\partial r}\left(\frac{v}{H}\right)\right] \simeq 1-\frac{\partial}{\partial r}\left(\frac{v}{H}\right)-\frac{2}{r}\frac{v}{H} \,. \end{aligned} \tag{3.50}$$

In the last equation, non−linear terms have been neglected, therefore this expression only holds on the large scales. Combining eq. (3.49) and eq. (3.50) and expanding:

$$\frac{\bar{n}^r}{\bar{n}^{r+v/H}} = \left[\frac{\bar{n}(\boldsymbol{r}+\Delta\boldsymbol{r})}{\bar{n}(\boldsymbol{r})}\right]^{-1} \simeq 1-\frac{1}{\bar{n}^r}\Delta\boldsymbol{r}\frac{d\bar{n}^r}{dr} \simeq 1-\frac{1}{\bar{n}^r}\frac{v}{H}\frac{d\bar{n}^r}{dr} \,, \tag{3.51}$$

one gets:

$$\begin{aligned} 1+\delta^s &= [1+\delta^r]\left[1-\frac{1}{\bar{n}^r}\frac{v}{H}\frac{d\bar{n}^r}{dr}\right]\left[1-\left(\frac{\partial}{\partial r}+\frac{2}{r}\right)\frac{v}{H}\right] \\ \delta^s &= \delta^r - \left[\frac{\partial}{\partial r}+\frac{1}{r}\left(2+\frac{r}{\bar{n}^r}\frac{d\bar{n}^r}{dr}\right)\right]\frac{v}{H} = \delta^r - \left(\frac{\partial}{\partial r}+\frac{\alpha}{r}\right)\frac{v}{H} \,, \end{aligned} \tag{3.52}$$

where:

$$\alpha = 2 + \frac{d\ln\bar{n}^r}{d\ln r} = \frac{d\ln r^2\bar{n}^r}{d\ln r} \,. \tag{3.53}$$

The α/r term, which is usually called the **Doppler effect** [185–187], is commonly neglected in the plane−parallel approximation, being subdominant with respect to the other one, when the observer is far from the tracer. It is relevant, however, when considering wide angle surveys, since its contribution depends on the different distribution DM can have along different LoS. Figure 3.3 sketches the behaviour of the peculiar velocity space distortions in the parallel approximation and of the Doppler term.

The peculiar velocity and Doppler terms depend on how LSS are distributed in the Universe, therefore on their evolution history and on the particular model assumed to describe the dark energy or modified gravity contributions that dominate the energy density of the Universe (see section 2.1.1 and section 2.2.1 for detail). For this reason, it is useful to rewrite them in terms of the growth rate:

$$f = \frac{d\ln D_1}{d\ln a} \,. \tag{3.54}$$

Through the continuity eq. (2.31), in fact, $\partial v/\partial r = \nabla_{\boldsymbol{x}}\cdot\boldsymbol{v} = -Hf\delta^r$ is found, since:

$$\begin{aligned} &\frac{d\delta^r}{dt} + \nabla_{\boldsymbol{x}}\cdot\boldsymbol{v} = 0 \\ &\frac{1}{a}\frac{da}{dt}\frac{a}{\delta^r}\frac{d\delta^r}{da}\delta^r + \nabla_{\boldsymbol{x}}\cdot\boldsymbol{v} = \left[H\frac{d\ln\delta^r}{d\ln a}\delta^r\right] + \nabla_{\boldsymbol{x}}\cdot\boldsymbol{v} = 0 \,, \end{aligned} \tag{3.55}$$

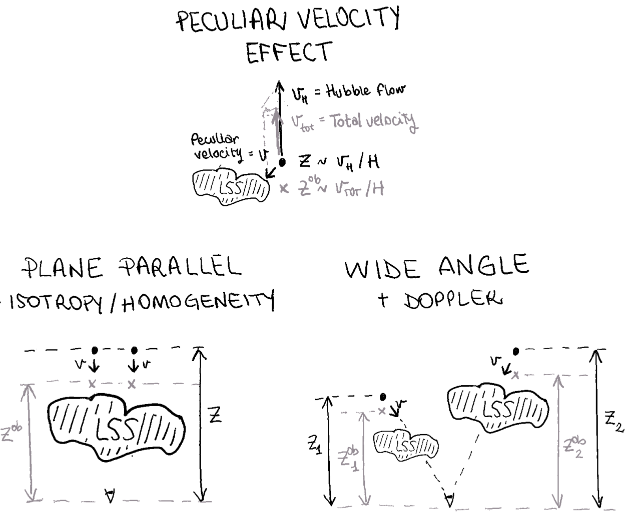

Figure 3.3: Sketch of the induced perturbations of the observed source position due to peculiar velocities. The black dot represents the source position in real space with its intrinsic redshift z, while the grey crosses represents its estimated position and redshift z^{ob} in redshift space. The upper plot shows how the peculiar velocity $\boldsymbol{v}$ due to the presence of a DM overdensity (indicated as LSS) deviates the measured $\boldsymbol{v}_{tot}$ with respect to the recession velocity linked to the Hubble law. The lower plots, instead, shows the difference between the induced effect in plane−parallel approximation and in wide angle configuration, where also different DM distributions along the different LoS are considered.

and $d \ln \delta^r / d \ln a \simeq d \ln D_1 / d \ln a$. It is useful now to move the analysis in Fourier space. The Fourier transform of the peculiar velocity contribution is:

$$v_k = \left(\frac{k_r}{k}\right)^2 (\nabla_x \cdot v) = -\mu^2 f H \delta^r = -\left(\frac{i}{k}\frac{\partial^2}{\partial r^2}\right) f H \delta^r \,, \tag{3.56}$$

where k_r is the Fourier transform of the LoS component, while k is the full wavevector. The factor $\mu = \boldsymbol{r} \cdot \boldsymbol{k}$ is expressed in terms of the derivative along the LoS transformed to the Fourier space. Then, in the plane−parallel approximation:

$$\delta^s_k = \delta^r_k + \mu^2 f \delta^r_k = \delta^r_k \left[1 + \frac{f}{k^2}\left(\frac{\partial^2}{\partial r^2}\right)\right] . \tag{3.57}$$

The relation in eq. (3.56) is used to compute the Ψ contribution in eq. (3.37) in the plane−parallel approximation, where the radial coordinate is identified with the redshift $\boldsymbol{r} \sim z$:

$$\Psi \simeq \Psi^\delta + \Psi^{\partial v} = b_t(z) D_1(z) + \frac{f}{k^2}\frac{\partial^2}{\partial \chi^2} \,, \tag{3.58}$$

therefore the angular power spectrum assumes the expression:

$$\begin{aligned} C_\ell = \frac{2}{\pi} \int & dk k^2 \mathcal{P}(k) T(k) \cdot \\ \cdot \int & dz_i \left[b_t(z_i) \frac{dN_t}{dz_i} D_1(z_i) j_\ell(k\chi(z_i)) - j''_\ell(k\chi_i) \frac{f_i}{k^2} \right] \cdot \\ \cdot \int & dz_j \left[b_t(z_j) \frac{dN_t}{dz_j} D_1(z_j) j_\ell(k\chi_j) - j''_\ell(k\chi_j) \frac{f_j}{k^2} \right] . \end{aligned} \tag{3.59}$$

where $j''_\ell(k\chi)$ is the second derivative of the spherical Bessel function. Note that the use of the plane−parallel approximation that lead to expression eq. (3.59) neglects the α/r term related with the Doppler effect.

Lensing

A direct consequence of the equations of general relativity is that light gets bent in the presence of a gravitational potential. When applied to the study of the Universe, this implies that at each redshift the distribution of LSS affects the propagation of the light coming from further sources; in the context of GR, a similar effect exist for gravitational waves.

LSS, in fact, behaves as extended lenses and, depending on the relative position between them, the observer and the background tracers, their effects can be divided into two classes: strong lensing and weak lensing. **Strong lensing** takes place when the angular separation between the lens and source, as seen by the observer, is small. In this case, the image of the source gets highly distorted or even multiple images can show up. When, instead, the angular separation is large, the **weak lensing** regime has to be considered. In this case, the image of a single source gets barely modified, but its distortion is coherent with the ones of all the other sources in the projected field around the lens. Therefore, performing statistical analysis over an ensamble of tracers makes it possible to detect the effect of the lens and to put constraints on the LSS: first analyses in this directions can be found in [161, 177–180].

In the study of cosmological survey, only weak lensing effects are taken into account. To model them, the FLRW metric from eq. (2.1) needs to be written in the case of small fluctuations in the longitudinal gauge as in eq. (3.5):

$$ds^2 = a^2(\tau)\left[-(1+2\Phi)d\tau^2 + (1-2\Phi)d\chi^2 + \chi^2(1-2\Phi)(d\theta^2 + \sin^2\theta d\phi^2)\right] . \quad (3.60)$$

The weak gravitational potential Φ can be modelled as a thin, plan lens [188] which affects the travel path of a photon through the deflection angle:

$$\alpha = -\frac{2}{c^2}\int_0^{\chi} \nabla_{\perp}\Phi \, d\chi \, , \quad (3.61)$$

where the gradient $\nabla_{\perp}$ is computed in the orthogonal direction with respect to the LoS. This deviation leads to a change in the observed position and luminosity of the source, depending on the lens mass distribution and on the relative position between the source, the lens and the observer.

As described in [189], in a flat Universe, assuming the comoving rest frame and the linear approximation, the **lensing potential** is defined as:

$$\phi = \frac{2}{c^2}\int_0^{\chi} d\chi' \, \frac{\chi-\chi'}{\chi\chi'}\Phi, \quad (3.62)$$

In this case, eq. (3.61) can be related to the change from the *unlensed* to the *lensed* coordinates by:

$$\begin{aligned}
\mathcal{M}_{ij} &= \delta^D_{ij} - \frac{\partial\alpha}{\partial\theta_i} = \mathcal{M}\delta^D_{ij} - \frac{\partial}{\partial\theta_i}\frac{\partial}{\partial\theta_j}\phi \\
\mathcal{M} &= = \begin{pmatrix} 1 - \frac{\phi_{11}+\phi_{22}}{2} - \frac{\phi_{11}-\phi_{22}}{2} & -\phi_{12}+\omega \\ -\phi_{12}+\omega & 1 - \frac{\phi_{11}+\phi_{22}}{2} + \frac{\phi_{11}-\phi_{22}}{2} \end{pmatrix} \\
&= \begin{pmatrix} 1-\kappa-\gamma_1 & -\gamma_2+\omega \\ -\gamma_2+\omega & 1-\kappa+\gamma_1 \end{pmatrix} .
\end{aligned} \quad (3.63)$$

This relation holds also in the case of more than one thick and non−planar lens [189]. $\mathcal{M}$ is called the **magnification matrix** and its elements depends on the **scalar convergence** $\kappa = \nabla^2\phi/2$, the **shear** $\gamma = \gamma_1 + i\gamma_2$ and the anti−symmetric rotation ω, which is negligible. The shear quantifies an anisotropic stretching, while the convergence represents an isotropic change of the observed size of the source, computed integrating eq. (3.62) along the LoS [165]:

$$\kappa = \int_0^{\chi} d\chi' \frac{(\chi - \chi')}{\chi\chi'} \nabla^2_{\hat{x}}\, \phi[\chi', \hat{n}\chi'] \, , \tag{3.64}$$

where $\nabla^2_{\hat{n}}\, \phi[\chi', \hat{x}\chi']$ are the angular components of the covariant derivative of the lensing potential on a sphere having radius χ'.

The inverse of the magnification matrix describes how the tracer brightness gets magnified by the presence of the lens [190, 191]:

$$\mu = \left(\det|\mathcal{M}|\right)^{-1} = \frac{1}{|(1-\kappa)^2 - \gamma^2|} \simeq 1 + 2\kappa \, . \tag{3.65}$$

μ is called the **magnification**. Its presence can determine a variation in the observed power spectra of DM tracers. Let us consider a tomographic survey in which sources are assigned to different redshift bins through the observed window function $W(z)$ from eq. (3.36). It can happen that a magnified source, due to the increase of its apparent brightness and to the mis−estimation of its redshift, is assigned to the *wrong* bin. This effect changes the observed number of sources in each bin with respect to the intrinsic one through:

$$n_{obs} = n_{true}[1 + (5s_* - 2)]\kappa \, . \tag{3.66}$$

This equation introduces the so called **magnification bias** s_*, which depends on the slope of the logarithm of the source distribution in redshift and it can be described through:

$$s_*(z) = -\left.\frac{\left[d\log N/dz\right]\left(\mathcal{B}(z) > \mathcal{O}(z)_{lim}\right)}{d\mathcal{O}(z)}\right|_{\mathcal{O}(z)} \tag{3.67}$$

where $\mathcal{O}(z)$ defines the boundary above which a source having observed brightness $\mathcal{B}$ is associated with a certain bin. In the case of EM surveys, usually $\mathcal{O}(z)$ is identified with the apparent magnitude.[14] For gravitational wave survey instead the Signal−to−Noise Ratio (SNR) eq. (4.46) is used.

Combining the effects of the convergence field and of the magnification, the window function Ψ^{lens} required by eq. (3.37) can be defined. Following [165], it can be written as:

$$\Psi^{lens} \simeq (2 - 5s_*)\kappa \, , \tag{3.68}$$

then, by using the Fourier transform and the harmonic projection, the term:

$$\begin{aligned} C_\ell^{lens} = \frac{2}{\pi} \int dk k^2 \mathcal{P}(k) T(k) \cdot \\ \cdot \int dz_i \, (2 - 5s_*^i) \frac{\ell(\ell+1)}{2} \int_0^{\chi_i} d\chi' \left[\frac{\chi_i - \chi'}{\chi_i \chi'} \left[\Phi(\chi') + \Psi(\chi')\right] j_\ell(k\chi') \right] \cdot \\ \cdot \int dz_j \, (2 - 5s_*^j) \frac{\ell(\ell+1)}{2} \int_0^{\chi_j} d\chi' \left[\frac{\chi_j - \chi'}{\chi_j \chi'} \left[\Phi(\chi') + \Psi(\chi')\right] j_\ell(k\chi') \right] , \end{aligned} \tag{3.69}$$

has to be added to eq. (3.59). Here, the lensing potential has been split as $\phi = \Phi + \Psi$

[14] Note that in the case of magnitude $\mathcal{B}(z)$ has to be below $\mathcal{O}(z)$ for the source to be associated with the bin, since magnitude has a reverse scale.

by using the scalar potentials from the longitudinal gauge metric perturbation in eq. (3.5) [165].

3.3 Tracers

The LSS can be mapped using different tracers; these are distributed differently across cosmic time and in space. The plethora of instruments that nowadays observe the sky in all the EM bands, together with the recently−born observational campaigns of gravitational waves (which will be described in detail in chapter 4), neutrinos and cosmic rays, provide an enormous set of data, that can be analysed through the statistical tools presented in section 3.2. As long as we are concerned with the estimation of cosmological parameters through clustering, regardless of the kind of observation performed or of the instrument needed, all the tracers are treated analogously, since they are located and mapped as point Poisson processes.

However, their different formation processes are fundamental to characterize the relation they have with the distribution of DM halos and therefore with the smooth DM field i.e., their bias. Such processes are usually highly non−linear: semi−analytical prescriptions can be given to model them, but simulations are needed to deal with the variety of parameters included.

In the following, we will introduce the formation processes and the characteristics of the distribution and clustering of galaxies (section 3.3.1), supernovae (section 3.3.2) and compact object binary mergers (3.3.3) of both astrophysical and primordial origin. The firsts are the most widely used tracers in current cosmology, while the others will be used in the analysis developed in chapter 5, chapter 6 and chapter 7.

3.3.1 Galaxies

In the approach firstly outlined in [192], galaxies and stars form from the cooling of the baryonic gas that fell in the potential wells created by the virialized DM halos described in section 3.1.1. The efficiency of galaxy formation and the properties a galaxy inherits depend first of all on the mass of the host halo. This determines the quantity of cold gas available: e.g., small halos are unable to form bright, and hence massive, galaxies. The situation however is complicated by many physical effects: for example, the gas cooling time increases with m,[15] making the galaxy formation slower in massive halos [141, 193]. The star formation rate, the feedback due to stellar evolution (e.g., energy injection due to supernovae explosion, see section 3.3.2) and the angular momentum of the DM halo influence the evolution history as well [141]. Mergers of galaxies can also take place, decreasing the number of dim galaxies but increasing the number of the luminous ones.

Usually, to describe galaxy formation a broken power−law is adopted [193]. This defines the average number $\bar{N}_g^k$ of galaxies of a certain type k that can be found inside an halo as:

$$\bar{N}_g^k = \begin{cases} 0 & \text{if } m < m^{min} \\ (m/m_1)^{\alpha} & \text{if } m^{min} \leq m \leq m^{crit} \\ (m/m_2)^{\beta} & \text{if } m > m^{crit} \end{cases} . \tag{3.70}$$

[15] 15: Higher m implies an higher velocity dispersion inside the halo, therefore the cooling is less efficient and it takes more time.

The parameters m^{min}, m^{crit}, m_1, α, β fully characterize the galaxy formation: m^{min} is the minimum mass an halo can have, to be able to form such galaxies, m^{crit} is where the power−law breaks and m_1 represents the mass of the halos that, on average, contain only one galaxy of this kind. For continuity $m_2 = (m_1)^{\alpha/\beta} \cdot (m^{crit})^{1-\alpha/\beta}$.

The prescription that is commonly adopted [194–197] states that, when a single galaxy is present, it forms in the central region of the halo. If the halo is massive enough to form other galaxies, these are distributed around it and they are called **satellite galaxies**. The central−satellite galaxies configuration is a first level approximation, which is altered e.g., when galaxy mergers take place.

Observationally, instead, galaxies are characterized by the luminosity function and the stellar mass function. The **luminosity function** $\Phi(L_*)$ describes the number of galaxies per unit volume with luminosity in the range $[L_*, L_* + dL_*]$. This is related to the absolute magnitude[16] $\mathcal{M}_*$ through:

$$L_* = L_*^0 \cdot 10^{-0.4\mathcal{M}_*} \,, \tag{3.72}$$

where L_0 is the zero point of the scale through which the luminosity is calibrated. The luminosity function is usually described through the double-Schechter function [198–200]:

$$\Phi(L_*)dL_* = \left[\phi_1^*\left(\frac{L_*}{\bar{L}_*}\right)^{\alpha_1} + \phi_2^*\left(\frac{L_*}{\bar{L}_*}\right)^{\alpha_2}\right] \exp\left[-\frac{L_*}{\bar{L}_*}\right] \frac{dL_*}{\bar{L}_*} \,, \tag{3.73}$$

where $\bar{L}_*$ is the characteristic luminosity, $\phi_{1,2}^*$ are normalization factors and $\alpha_1 < 0$ is the parameter describing the slope of the function, which makes the number of galaxies increasing when the luminosity is lower. This can lead to divergences: to avoid them, the turn−over parameter α_2 is adopted to change the slope in the luminosity function at the lower L_*.

The **stellar mass function** $\Phi(z, M_*, SFR)$ measures the number of galaxies per unit volume depending on their stellar mass M_* i.e., the mass of the galaxy made by stars, and **star formation rate** SFR. This measures how much of the baryonic gas mass is converted into stars in a certain time interval e.g., $M_\odot\,\text{yr}^{-1}$, and it is generally estimated from observations (see [201] for a review) or simulations. The stellar mass function is in turn described by a Schechter function, with a similar functional form as to the one in eq. (3.73). The stellar mass function is directly related with the luminosity function through the mass−to−light ratio, which depends on the initial mass function[17] and the evolution of the star formation rate. It is usually described as:

$$\frac{M_*}{L_*} \simeq const \,. \tag{3.75}$$

In [203], the value of the ratio is computed considering different IMF and assumptions; in the case of the Kroupa IMF from eq. (3.74), $M_*/L_* \in [0.6, 1.4]$.

The analytic description of both the luminosity function in eq. (3.73) and the stellar mass function for a certain galaxy class, together with the parameters that characterize it, are usually calibrated on simulations. For example, the stellar mass function of the EAGLE simulation suite[18] [206, 207] (integrated over the SFR and interpolated) is shown in figure 3.4. Note that $\Phi(z, M_*)$ decreases with M_* and that larger halos are formed only at low z.

[16] The absolute magnitude is defined as the observed magnitude an object would have if it was located at 10 pc from the observer. It can be computed from the observed apparent magnitude m_* through the distance modulus:

$$m_* - \mathcal{M}_* = 5\log_{10}\left[\frac{D_L}{10\,\text{pc}}\right] \,, \tag{3.71}$$

where D_L is the luminosity distance (compare with eq. (2.16)). Here we refer to bolometric magnitudes i.e., the measurement of the total energy emitted by the object.

[17] The initial mass function (IMF) describes how stellar masses that form in one star−formation event distribute. One of the most widely used is the Kroupa IMF [202]:

$$\mathcal{K}(M_*)dM_* = AM_*^{-\alpha} \,, \tag{3.74}$$

where $\alpha = 0.3$ if $0.01\,M_\odot \leq M_* < 0.08\,M_\odot$, $\alpha = 1.3$ if $0.08\,M_\odot \leq M_* < 0.5\,M_\odot$ and $\alpha = 2.3$ if $M_* \geq 0.5\,M_\odot$.

[18] The EAGLE suite is described in 7.1.2; this is the simulation used by [204, 205] to produce the catalogues I used to develop the analysis in chapter 5, chapter 6 and chapter 7.

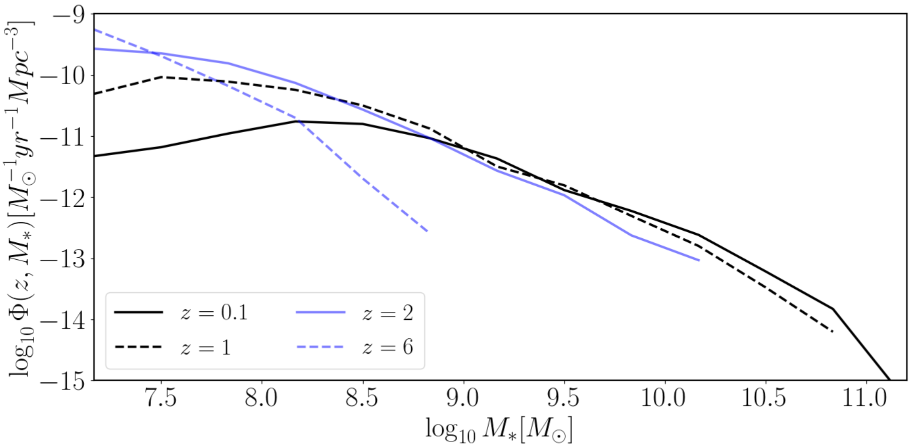

Figure 3.4: Stellar mass function modelled from the EAGLE simulation. The SFR dependence has been marginalized. The different curves refer to different snapshots: $z \simeq 0.1$ (black continuous line), $z \simeq 1$ (black dashed line), $z \simeq 2$ (blue continuous line), $z \simeq 6$ (blue dashed line). The lines are interrupted where $\Phi(z, M_*) = 0$. See chapter 5 for detail.

HOD bias

To analytically model the clustering of galaxies with respect to the underlying DM field, the Halo Occupation Distribution (HOD) framework can be used.

This is based on the conceptual separation between the description of halo formation and distribution from section 3.1.1 and the galaxy formation introduced in the previous section. While the first one is completely determined (at least at linear level) once that the cosmological model is chosen, the second relies on many physical processes that take place within the halos and turn out to populate them with galaxies having different properties [193]. The HOD framework relies on the assumption that galaxy formation inside a certain halo is statistically independent from the environment the halo is found in i.e., processes that happens on scales larger than the halo size are not taken into account.

By applying the HOD formalism, it is possible to characterize the galaxy clustering dependence on the halo and galaxy properties one is interested in (e.g., mass, color or luminosity) and to relate it with the different formation models and with simulations,[19] in order to test them (see e.g., [196, 197, 208–210]).

The key element of the HOD framework is the probability distribution $P(N_g^k|m)$ that a DM halo of virial mass m forms N_g^k galaxies. This can be defined separately for each galaxy class k and it is based on the efficiency of galaxy formation in dependence of the halo mass, as described in section 3.3.1. Additional elements in the HOD framework are the relations between the galaxy and DM position and velocity distributions within halos [193]. All of them can be modelled either from simulations or through semi−analytical approaches.

Starting from the conditional probability $P(N_g^k|m)$, the expected number of galaxies within an halo is computed as:[20]

$$\langle N_g^k|m\rangle = \int_{m^{min}}^{+\infty} dm\, P(N_g^k|m) N_g^k \,. \tag{3.76}$$

From this quantity, the galaxy bias can be estimated. Many works exist in this direction (see e.g., [141, 195, 209, 211, 212]), in which it is customary to distinguish between the 1−halo and the 2−halo contributions: the former term refers to galaxies forming inside the same halo, while the latter is related with the presence of galaxy

[19] See chapter 7 for a summary of the different simulation types.

[20] In chapter 5, when speaking about the HOD we will always refer to $\langle N_g^k|m\rangle$, implicitly assuming that all the properties and conditions described in this section are satisfied.

pairs from spatially correlated halos. The 1−halo term gives the galaxy number density and dominates on small scales [193]. It reads:

$$n^k_{g,1h}(z) = \int_{m^{min}}^{+\infty} dm\; n(z,m)\, \frac{\langle N^k_g(N^k_g - 1)|m\rangle}{2}\;. \tag{3.77}$$

The quantity $n(z,m)$ is the halo mass function defined in section 3.1.1, while $\langle N^k_g(N^k_g - 1)|m\rangle$ is computed applying eq. (3.76) to $N^k_g(N^k_g - 1)$.

On the large scales, instead, the galaxy number density mainly depends on the 2−halo contribution and it is:

$$n^k_{g,2h}(z) = \int_{m^{min}}^{+\infty} dm\; n(z,m)\, \langle N^k_g|m\rangle\;. \tag{3.78}$$

The large scale contribution is the most relevant in the study of cosmological surveys: as described in section 3.1.1 and section 3.1.2, on large scales the cosmological perturbations are well described by the linear approximation. The clustering of the DM halos with respect to the underlying DM distribution is then described by the linear bias in eq. (7.29). From this, the bias of the tracer (galaxies in this case) is estimated in the HOD framework as the weighted average of the halo bias $b(z,m)$ [141, 193, 194], therefore:

$$b^k_g(z) = \int_{m^{min}}^{+\infty} dm\; n(z,m)\, b(z,m) \frac{\langle N^k_g|m\rangle}{n^k_g(z)}\;. \tag{3.79}$$

The galaxy bias $b^k_g(z)$ in eq. (3.79) depends on how the galaxy class k is defined: this implies that different galaxy populations are differently clustered with respect to the underlying DM field. For example, the bias behaves differently in dependence of:

- The galaxy stellar mass and star formation rate. This is analysed in detail in chapter 5; in particular figure 5.9 shows that galaxies with higher star formation rate are more clustered. The same happens for more massive galaxies: this is due to the fact that such galaxies form in more massive DM halos, which are born from the densest, and therefore the most clustered [152], peaks of the DM distribution.
- The galaxy luminosity. Following the mass−to−light ratio prescription from eq. (3.75), the more a galaxy is luminous, the more it is massive. Therefore, analogously to the previous point, more luminous galaxies are more clustered since they form in the most massive halos.
- The galaxy color and morphological type. [213] e.g., shows that early−type galaxies (i.e., the ones where star formation is no longer active) are found in bigger halos, since on average they are more massive than late−type ones (i.e., star forming, mainly spiral galaxies), therefore they are more clustered. This is confirmed observationally by the fact that galaxy clusters are mainly made by early−type galaxies, while late−type ones are mainly found in the field [214].

3.3.2 Supernovae IA

Supernovae are transient events in which a star suddenly increases its brightness and then fades away. Two main classes of supernovae exist, which have different progenitors and are caused by different explosion mechanisms: type IA, related with white dwarfs in binary systems, and type II, which corresponds to the final fate of a massive star (see section 3.3.3).

From the cosmological point of view, **supernovae IA** constitute the most interesting group.[21] Their origin resides in the evolution of stellar binaries in which a white dwarf (see section 3.3.3) accretes material from a companion star. When the white dwarf mass reaches the Chandrasekhar limit M_{Ch} [215], violent thermal reactions are ignited and the white dwarf is completely destroyed by the supernova event [216–219]. Supernovae Ia can be found in all kinds of galaxies, both the star forming and the quiescent ones [220].

Whenever a supernova IA is observed, the explosion mechanism and the decay processes which the stellar material undergoes are similar. For this reason, as firstly noted by [221, 222], the shape of the observed light curves is at first approximation homogeneous, with the brightness peak reached within 15 days and followed by a slow decline. Once that corrections of the systematic effects, such as dust absorption, have been performed, empirical relations exist to describe the light curve shapes in the different observational bands (see [220] for a general review).

Standard candles

As well as the shape of the light curve, also the supernova intrinsic luminosity near the peak can be estimated from physical motivated models [220]. This turns out to be related with the mass at which the white dwarf explodes: since it is always $\simeq M_{Ch}$, the intrinsic luminosity is to first approximation the same for all the supernovae [223]: for this reason they are called **standard candles**.

The intrinsic luminosity is related to the absolute magnitude as depicted in section 3.3.1. This can be compared with the observed apparent magnitude by the means of the distance modulus in eq. (3.71): in this way, the supernova luminosity distance D_L can be estimated.[22] At the same time, the redshift z of the supernova can be estimated from the spectrum either of its host galaxy or the supernova itself (see e.g., [225] for a comparison between the two methods).

Luminosity distance and redshift are related through the Hubble parameter defined in eq. (2.10). Locally, the relation is simply $D_L = cz/H_0$, while at higher redshift it gets expanded into [15]:

$$D_L \simeq \frac{cz}{H_0}\left[1 + \frac{1}{2}[1 - q_0]z - \frac{1}{6}[1 - q_0 - 3q_0^2 + j_0]z^2\right], \tag{3.80}$$

where $q_0 = q(t = 0) = -(\ddot{a}/a)(\dot{a}/a)^{-2}|_0$ and $j_0 = j(t = 0) = \dddot{a}a(\dot{a}/a)^{-3}$. Therefore having a SN dataset, the parameter H_0 can be estimated. In the Hubble diagram that compares either D_L or the apparent magnitude with z or, analogously, the recession velocity, the value of H_0 depends on the inclination of the (quasi−)linear dependence between the two. As introduced in chapter 2, the quantity obtained through this technique [15–17] is in tension with respect to the value estimated from CMB data analysis [13].

[21] For this reason, from now on we will only deal with supernovae IA; when speaking about supernovae or SN, we will always refer to this class.

[22] To develop the full analysis, calibrations of the absolute magnitude are needed to deal with systematic effects (see e.g., [224]).

3.3.3 Binary mergers

A brand new tracer for cosmological surveys lies in compact object binaries. As chapter 4 explores in detail, the orbital motion of these systems evolves solely through the emission of gravitational radiation [134, 226]. The signal they emit in the form of gravitational waves changes in frequency and amplitude according to parameters as the compact object masses and relative inclination, their distance, the orbital velocity.

Regardless on the specific characteristics of the GW signal, which are presented in section 4.3, compact binaries can be considered as point sources that map the LSS, in complete analogy to galaxies in section 3.3.1 and supernovae in section 3.3.2. For this purpose, we will always refer to the merger phase of tenths of solar mass−size binaries:[23] current and future ground GW detectors, in fact, are designed to observe mainly their typical frequencies and amplitudes (see section 4.2 for detail).

In this class of sources, the progenitor origin can be of two types: astrophysical or primordial. To the first type belong black holes and neutron stars that are remnants of the stellar evolution, while in the second case primordial black holes introduced in section 2.3 are considered. All these objects get bound either at their birth or through dynamical processes: in this way, they create the binary systems that then evolve and eventually merge, producing GW.

Binaries of interest are the ones that merge within the Hubble time:

$$\tau_{H_0} = \frac{1}{H_0} \, , \tag{3.81}$$

i.e., whose GW emission is observable today. Since the orbital separation evolves according to eq. (4.50), the binary coalescence time i.e., the time that elapses between its formation and the merger, can be estimated through [227]:

$$t_{coal} = \frac{5}{256} \frac{c^5}{G^3} \frac{a_0^4}{m_1 m_2 (m_1 + m_2)} \frac{1}{F(e)} \, , \tag{3.82}$$

where m_1, m_2 are the masses of the compact objects in the binary, the factor $F(e)$ depends on the binary eccentricity and a_0 is the progenitor separation when the binary evolution starts to be governed only GW emission. Requiring that $t_{coal} < \tau_{H_0}$ provides an estimate for a_0: figure 3.5 shows some examples depending on the progenitor masses. It is evident that only when the progenitors are very close one to the other, the binary can be driven by GW to merge in a time that allows its observation. Therefore, either the progenitors are really close since the binary formation, or other processes must shrink their orbits.

Depending on the channel that brought to the binary formation, GW events have a different distribution in the spacetime of the Universe. The clustering they have with respect to the underlying DM field, and therefore their bias, changes as well. With the goal in mind of using binary mergers as tracers of LSS, it is then important to well understood and characterize the binary formation processes. This is done in the following.

Astrophysical binaries

The stellar evolution can produced three kind of compact objects: white dwarfs (WD), neutron stars (NS) and Astrophysical Black Holes (ABH).

[23] The GW signal produced by the inspiral phase of binary evolution has lower frequency and amplitude with respect to the merger ones, therefore it is more difficult to be observed from the ground. The ring−down phase, on the other hand, is more difficult to be modelled and analysed. Things would change if one considers different GW detectors e.g., the space ones, or different **progenitors** i.e., compact objects in different classes of mass. However, as long as the GW sources are resolved and they can be interpreted in light of a point−like Poisson distribution, the analysis here described can be self−consistently extended to include them. Things, obviously, change when the study focuses on the GW stochastic background section 4.1.

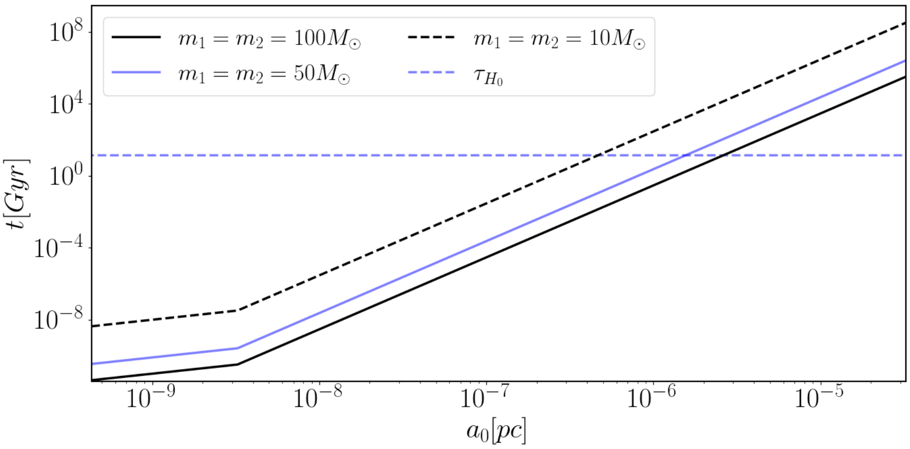

Figure 3.5: Coalescence time t_{coal} in Gyr computed as in eq. (3.82) as a function of the initial separation a_0 expressed in pc and of the progenitor masses. These are assumed to have equal mass in each system i.e., $m_1 = m_2 = 100\,M_\odot$ (black continuous line), $50\,M_\odot$ (blue continuous line), $10\,M_\odot$ (black dashed line). t_{coal} is compared with the Hubble time τ_{H_0} (blue dashed line) from eq. (3.81): note that, to merge within the Hubble time, the initial separation should be $a_0 \simeq 10^{-6}$ pc $\simeq$ 0.2AU (AU is the distance between the Earth and the Sun).

White dwarfs are core remnants produced by the evolution of small stars. They are composed by electron−degenerate matter and emit light only through thermal radiation [228]. The gravitational collapse of such compact objects is prevented by the pressure of the degenerate gas; however, an upper limit $M_{Ch} \simeq 1.4\,M_\odot$ exists for their mass, above which self−gravity can no longer be sustained: this is called the **Chandrasekhar limit** [215]. Because of their small mass, the GW they produce are not observable with ground detectors section 4.2; for this reason, we will ignore them in the following.

Massive stars i.e., with masses $m_* \geq 8\,M_\odot$, instead, produces **neutron stars** and **black holes**. Single massive stars evolve[24] through nuclear reactions until iron is produced in the core: since subsequent atom fusions do not release energy, the pressure drops and the stellar core contracts up to nuclear density $\simeq 10^{17}$kg m^3 [229]. The core collapse prompts the type II supernova event, which expels the outer layers of the star while converting the core into a very compact object: depending on its mass, the degenerate neutron pressure can either stop the collapse, forming a neutron star, or be beaten by self−gravity, in which case a black hole is left as a remnant [230–232]. The possibility for these compact objects to form a binary that merge within the Hubble time is related to the density of the environment in which they are found: while stars in the field are too spread for this to happen, crowded places such as star clusters[25] are ideal. Here, three−body encounters produce energy exchange between the different bodies, bringing some of them to bound in binaries close enough to merge and produce observable GW [233].

Sometimes, from the same gas cloud two gravitationally bound stars might form [234]. It happens that one of them evolves into a compact object and the other transfers mass onto it: by doing so, its core and the compact object can be incorporated into a **common envelope**. The drag produced by the presence of the envelope shrinks the orbit of the two objects: after this phase, either they merge or the energy they release during the inspiral removes the envelope (see [233, 235] for a review). The close binary formed in the second scenario, after that the second star evolves into a compact object as well, gives rise to the binaries of interest for GW observations [236].

[24] Clearly, a very streamlined and wrapped up description is given here.

[25] Three different types of star clusters exist: globular clusters, young clusters and nuclear clusters. **Globular clusters** are very old ($\simeq$ 12 Gyr), quiescent systems. They are strongly bounded by the gravitational interactions between the $\simeq 10^4 - 10^6$ stars of which they are formed, which distribute in a spherical shape of $\simeq$ 3 pc radius. **Young clusters** ($\simeq$ 0.1 − 1 Gyr) are star forming regions which contain less than 10^3 massive stars. **Nuclear clusters** are found near the center of the galaxies. They are old ($\simeq$ 12 Gyr), very dense systems, which contain $\simeq 10^6 - 10^8$ stars inside a region of $\simeq 2 - 5$ pc side.

Primordial black hole binaries

As described in section 2.3, current constraints on the abundance on primordial black holes [118] leave open the possibility that such objects exist in the mass window $m_{PBH} \in [10, 100]\, M_\odot$. It is then worth to investigate if PBH form binaries that merge within a Hubble time. There are two possible formation channels to account for, from which so−called **early PBH binaries** and **late PBH binaries** form.

Early PBH binaries were firstly theorized by [237, 238] as systems that bound together and decoupled from the Universe expansion in the radiation dominated era section 2.1.3. To estimate their abundance and merger rate, the first ingredient required is the mean comoving separation between two points at the time t_{eq} of the matter−radiation equivalence:

$$\bar{\chi} = \frac{1}{a(t_{eq})}\left(\frac{m_{PBH}}{\rho_{eq}}\right)^{1/3} , \tag{3.83}$$

where ρ_{eq} is the average background density at t_{eq} and $a(t_{eq})$ the scale factor at that time. Assuming that PBH with a monochromatic mass distribution (see section 2.3) form at $\bar{t}$ and that their comoving distances are uniformly distributed in $[0, \bar{\chi}]$, the condition for the binary formation at time t [237] is set by:

$$\rho_{PBH}(t) > \rho_r(t) \;\rightarrow\; \rho_{eq}\left(\frac{\bar{\chi}}{\chi(t)}\right)^3 > \frac{\rho_{eq}}{a(t)^4} \tag{3.84}$$

where $\chi(t)$ is the comoving distance between two PBH, which defines the radius of a sphere enclosing the density $\rho_{PBH}(t)$. When this density becomes larger than the average background density $\rho_r(t)$, whose value is computed from ρ_{eq} by assuming the density time evolution described in eq. (2.25), the binary bounds and decouples from the cosmic expansion. This happens when $a^4(t) = \left[\chi(t)/\bar{\chi}\right]^3$, which using physical distances implies $a(t) = \left(x(t)/\bar{x}\right)^3\big]$. Since binaries randomly bounds wherever PBH are located, they follows closely the DM distribution both at the formation and throughout the cosmic time evolution [114]. For this reason, their bias can be modelled as a constant, whose value is:

$$b^E = 1\,. \tag{3.85}$$

The second ingredient to take into account at this point is that the binary is not isolated, but surrounded by the rest of the DM field, being this made of other PBH or not. The presence of other bodies exerts tidal forces on the binary, which enhance the angular momentum of the PBH it is made of, preventing their heads−on collision [238] and increasing the time required for the binary to inspiral, retarding the merger and making it observable today [237]. Moreover, when other PBH are present, they can disrupt the binary through three−body interactions [115], reducing the number of mergers observable today. For this reason, the early PBH binary merger rate $\mathcal{R}^E$ has to be defined in dependence on the PBH abundance and therefore to the f_{PBH} factor defined in eq. (2.64). In section 6.2, a model for $\mathcal{R}^E(f_{PBH})$ based on [114] is introduced.

Late PBH binaries represent another possible formation channel, which is related with dynamical encounters. Such systems are formed when two PBH approach each other and, after losing energy through GW emission due to the variation of

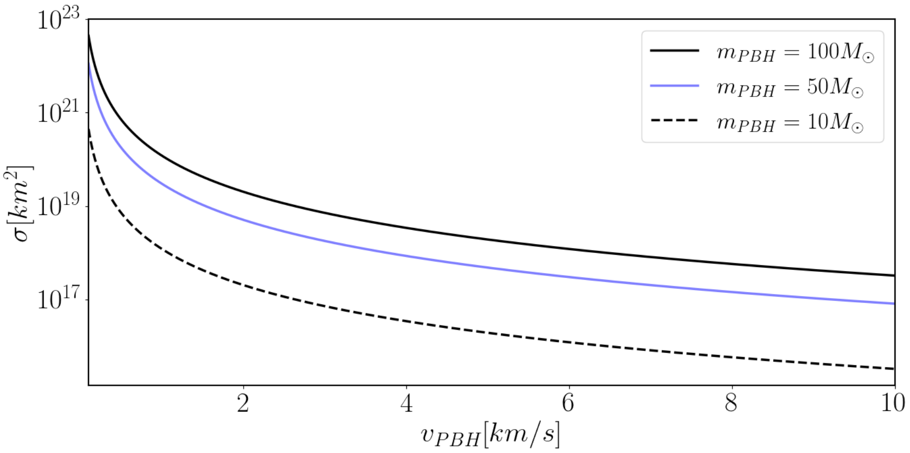

Figure 3.6: Cross−section σ of the PBH−PBH encounter described in eq. (3.86). The masses as chosen to describe the window of interest of the analysis i.e., $m_{PBH} = 100\,M_\odot$ (black continuous line), $m_{PBH} = 50\,M_\odot$ (blue continuous line), $m_{PBH} = 10\,M_\odot$ (black dashed line). The relative velocities instead takes the values $v_{PBH} \in [0.1, 10]\,\mathrm{km/s}$, which are the most relevant for two−body formation [119] (the lower bound relates with the virial velocities of the oldest halos, while the upper is chosen to have a negligible number of heads−on collisions).

their quadrupole moment (see section 4.1), get bound [119]. If the relative velocity of the PBH is v_{PBH}, the cross−section of this process can be computed as [239, 240]:

$$\sigma = 2\pi\left(\frac{85\pi}{6\sqrt{2}}\right)^{2/7}\frac{G^2(m_1+m_2)^{10/7}m_1^{2/7}m_2^{2/7}}{c^{10/7}v_{PBH}^{18/7}} = \pi\left(\frac{85\pi}{3}\right)^{2/7}R_s^2\left(\frac{v_{PBH}}{c}\right)^{-18/7}, \quad (3.86)$$

where the second equality assumes that the distribution of the PBH masses is monochromatic i.e., $m_1 = m_2 = m_{PBH}$. The Schwarzschild radius is defined in eq. (2.63); figure 3.6 shows the cross−section for monochromatic PBH in different class of masses.

Also in this case, PBH bounds in binaries closely following the DM distribution. However, since dynamical captures take place later on in the Universe history, they have to be analyse considering that DM halos already formed. Therefore, the values v_{PBH} assumes are distributed depending on the velocity dispersion inside them, which in turns depends on the halo mass m. As [117, 119] firstly highlighted, this implies that massive halos are disfavoured as PBH binaries hosts, since the high v_{PBH} their mass distribution determines lowers the value of the cross−section in eq. (3.86).

Typical halos where late PBH binaries can be found have $m < 10^6\,M_\odot$ [117]. The clustering of their mergers, therefore, is in first approximation the same as this kind of halos; their bias can be then approximated with the halo bias from eq. (5.35): in [117], its value is constant with redshift and it is set to be:

$$b^L = 0.5\,. \quad (3.87)$$

Mixed scenarios can be considered in which PBH form both early and late binaries. In this case, the overall abundance of PBH with respect to the overall DM abundance depends on both the formation mechanisms. Generally, in this case, the merger rate is found to be higher in the case of early PBH binaries [241]; different combinations of the two will be described in chapter 6.

Astro + primordial scenario

Nothing *a priori* prevents the formation of binaries in which one progenitor has primordial origin while the other comes from stellar evolution. In this case as well more than one possible channel exist: either the PBH takes part in the stellar evolution *since the beginning*, or it gets bound to an astrophysical black hole through a dynamical encounter.

The first case is similar to the common envelope scenario described for astrophysical black holes: estimates on its efficiency and rate are currently under development [242].

The second, instead, can be modelled analogously to the formation of late PBH binaries. The key point of its analysis is the cross−section of the process σ, defined in eq. (3.86) where, in this case, m_1, m_2 are the masses respectively of the astrophysical compact object and of the PBH, and $v_{PBH} = v_{rel}$ is the relative velocity between the two. Some interesting considerations can be made by looking at the functional form of σ: first of all, its value decreases for small masses; the existence of NS−PBH systems therefore is largely disfavoured with respect to ABH−PBH. Moreover, as already discussed in the case of late PBH binaries, an high relative velocity, such as the one PBH acquires in massive halos, would prevent the bounding between the two objects. Since, however, ABH form inside galaxies and therefore, as discussed in section 3.3.1, in massive halos, the probability of existence of ABH−PBH binaries seems to be at first look highly suppressed.

The only places in which the formation of such systems should be relevant are limited regions, inside the massive halos, in which the density is high and the velocities are low. This can happen e.g., inside star clusters. Some recent works [243, 244] study the probability of ABH−PBH dynamical encounters inside globular clusters, but young and nuclear clusters should be interesting candidates as well. Since, however, deeper analysis still needs to be performed in this direction, ABH−PBH systems are neglected in the analysis developed in chapter 5 and chapter 6.

The era of gravitational wave science 4

4.1 GW theory 54
GW propagation 55
GW sources 57
4.2 GW detectors ... 61
Present: second generation detectors 64
Future from the ground: ET 65
Future from the space: LISA, BBO 65
4.3 GW and cosmology 66
Binary mergers 66

Since their first observation in 2015 [245], gravitational waves (GW) established themselves as a new, powerful tool to study the Universe.

GW are described by general relativity as spacetime perturbations produced by accelerated masses. Their observation is carried on through instruments called **gravitational wave interferometers**: in the first observational campaign (from 09/2015 to 01/2016 [246]) the LIGO interferometers (Hanford and Livingston, USA [247]) were used, while in the second (11/2016 − 08/2017 [246, 248, 249]) and third (04/2019 − 03/2020 [250, 251]) campaigns also the Virgo interferometer (Pisa, Italy [252]) was included. A bit less than 100 GW events have been observed during the three campaigns, all produced by the inspiral and collapse of two astrophysical compact objects one on the other, mainly black hole pairs. These are commonly called **merger binaries**. In the years to come, the number of GW observations will increase, thanks to the upgraded versions of the LIGO and Virgo instruments and to new interferometers entering their network (e.g., KAGRA in Japan [253, 254]). The building of the so called **third generation interferometers**, such as the Einstein Telescope [255–257], will finally lead in the mid 2030 to GW maps of the full sky, accounting for $10^5 - 10^6$ merger events probed up to very high distances.

Such GW maps will provide an invaluable tool to study cosmology and to understand the structure and content of the Universe as a whole. Having a larger GW dataset will deepen this kind of analysis, allowing to study GW surveys in analogy to the already existing galaxy surveys, as chapter 3 described.

In this chapter we revise the main features that has to be considered when dealing with GW, from both the theoretical side and with regard to observations. The review presented in this chapter does not pretend to be exhaustive: we limit ourselves to introduce the most important concepts, to give a taste of the great potentialities that this new−born kind of measurement reserves. In particular, section 4.1 we show how general relativity implies the existence of gravitational waves and their propagation. Moreover, we revise how GW can be generated and the different kind of sources today we are aware of. In section 4.2 we summarize the main features of gravitational wave interferometers and we describe the current and future detectors and the sources they will be sensitive of. Finally in section 4.3 we describe two applications of GW to cosmological studies, namely using them as standard sirens and to map large scale structures.

4.1 GW theory

Gravitational waves are defined by the analytical solution of the Einstein eq. (2.4) in the weak field limit and in the linear approximation (see e.g., [11, 134]). In this:[1]

$$g_{\mu\nu} = \eta_{\mu\nu} + h_{\mu\nu} \; , \tag{4.1}$$

[1] $G = c = 1$ is assumed in the derivation. Using the standard units would show that the solutions of eq. (4.6) travel at the speed of light.

$|h_{\mu\nu}| << 1$ being a little perturbation over the flat Minkowski background described by the metric $\eta_{\mu\nu} = (-1, 1, 1, 1)$. Eq. (4.1) is used to perturb the Riemann tensor:

$$R^{\sigma}_{\mu\rho\nu} = \partial_\rho \Gamma^{\sigma}_{\mu\nu} - \partial_\nu \Gamma^{\sigma}_{\mu\rho} + \Gamma^{\sigma}_{\alpha\rho}\Gamma^{\alpha}_{\mu\nu} - \Gamma^{\sigma}_{\alpha\nu}\Gamma^{\alpha}_{\mu\rho} \ , \tag{4.2}$$

as $R^{\mu}_{\nu\rho\sigma} = [\partial_\rho h^{\mu\beta}(\partial_\nu h_{\beta\sigma} + \partial_\sigma h_{\beta\nu} - \partial_\beta h_{\nu\sigma}) - \partial_\sigma h^{\mu\beta}(\partial_\nu h_{\beta\rho} + \partial_\rho h_{\beta\nu} - \partial_\beta h_{\nu\rho})]/2$, where $\Gamma^{\sigma}_{\mu\nu}$ is the Christoffel symbol related to the covariant derivatives in a curved spacetime:

$$\Gamma^{\sigma}_{\mu\nu} = \frac{1}{2} g^{\sigma\rho}(\partial_\mu g_{\rho\nu} + \partial_\nu g_{\rho\mu} - \partial_\rho g_{\mu\nu}) \ . \tag{4.3}$$

At the first order in $h_{\mu\nu}$, by contracting the β index and setting $\partial_\beta h^{\mu\beta} = 0$ if $\beta \neq \mu$, the previous equation can be written as:

$$R_{\mu\nu\rho\sigma} = \frac{1}{2}(\partial_\nu\partial_\rho h_{\mu\sigma} + \partial_\mu\partial_\sigma h_{\nu\rho} - \partial_\mu\partial_\rho h_{\nu\sigma} - \partial_\nu\partial_\sigma h_{\mu\rho}) \ . \tag{4.4}$$

Eq. (4.4) is used to linearize the Einstein eq. (2.4) through the definition of $h = \eta^{\mu\nu} h_{\mu\nu}$ and $\bar{h}_{\mu\nu} = h_{\mu\nu} - \eta_{\mu\nu} h/2$:

$$\Box \bar{h}_{\mu\nu} + \eta_{\mu\nu}\partial^\rho\partial^\sigma \bar{h}_{\rho\sigma} - \partial^\rho\partial_\nu \bar{h}_{\mu\rho} - \partial^\rho\partial_\mu \bar{h}_{\nu\rho} = -16\pi T_{\mu\nu} \ . \tag{4.5}$$

where $\Box = \eta_{\mu\nu}\partial^\mu\partial^\nu = \partial^\mu\partial_\mu$ is the d'Alembert operator. In the Lorentz gauge defined in section 3.1, $\partial^\nu \bar{h}_{\mu\nu} = 0$ and eq. (4.5) reduces to:

$$\Box \bar{h}_{\mu\nu} = \left(-\partial_0^2 + \nabla^2\right)\bar{h}_{\mu\nu} = -16\pi T_{\mu\nu} \ . \tag{4.6}$$

The study of eq. (4.6) in the case $T_{\mu\nu} \neq 0$ describes the production of the metric perturbations $h_{\mu\nu}$ because of the matter−energy distribution defined by $T_{\mu\nu}$. The condition $T_{\mu\nu} = 0$ characterizes instead the perturbation propagation outside the matter distribution i.e., in the vacuum. Since eq. (4.6) in this case can be solved as a wave equation, the perturbations are identified as gravitational waves.

4.1.1 GW propagation

Eq. (4.6) with $T_{\mu\nu} = 0$ is solved in each of its components $\mathsf{h}(x_\mu)$ by the plane wave $\mathsf{h}(x_\mu) = A \exp\left[ik^\mu x_\mu\right]$ (see e.g., [11, 134]), A being the amplitude and $k^\mu = (\omega, \boldsymbol{k})$. ω is defined with respect to the wave frequency f as $\omega = 2\pi f$, and $\boldsymbol{k} = k^j$ is a vector along the propagation direction. k^μ is a null 4−vector, for which $k^\mu k_\mu = -(k^0)^2 + (k^j)^2 = 0$.[2] The plane wave solution can be extended to $\bar{h}_{\mu\nu}$: the propagation of these perturbations is then described as $\bar{h}_{\mu\nu} = \mathcal{A}_{\mu\nu} \exp\left[ik^\mu x_\mu\right]$, $\mathcal{A}_{\mu\nu}$ being a 4×4 symmetric matrix containing the amplitudes of all the $\mathsf{h}(x_\mu)$ components [11].

As shown e.g., in [134], the $\bar{h}_{\mu\nu}$ can be transformed into a transverse−traceless tensor by the means of the Lorentz gauge condition $\partial_\mu g^{\mu\nu}\sqrt{-g} = 0 = \partial_\mu \bar{h}_{\mu\nu}$ and through the coordinate transformation $x_\mu \longrightarrow x_\mu + \xi_\mu$. This is done by choosing ξ_0 in order to set the traceless condition $Tr(\bar{h}_{\mu\nu}) = \eta^{\mu\nu}\bar{h}_{\mu\nu} = 0$. In this case it is possible to define:

$$\begin{aligned} \bar{h} = \eta^{\mu\nu}\bar{h}_{\mu\nu} &= \eta^{\mu\nu}\left(h_{\mu\nu} - \frac{1}{2}\eta_{\mu\nu} h\right) \\ &= h - \frac{1}{2}4h = -h = 0 \ . \end{aligned} \tag{4.8}$$

[2] This condition is derived by inserting the wave expression in eq. (4.6):

$$\begin{aligned} 0 &= \left(-\frac{\partial^2}{\partial x_0^2} + \frac{\partial^2}{\partial x_j^2}\right)\cdot \\ &\cdot A \exp\left[ik^\mu x_\mu\right] \\ &= -\frac{\partial}{\partial x_0}\left(-Aik^0 \cdot\right. \\ &\cdot \left.\exp\left[-ik^0 x_0 + ik^j x_j\right]\right) + \\ &+ \frac{\partial}{\partial x_j}\left(Aik^j \cdot\right. \\ &\cdot \left.\exp\left[-ik^0 x_0 + ik^j x_j\right]\right) \\ &= -A^2(k^0)^2 + A^2(k^j)^2 \cdot \\ &\cdot \exp\left[-ik^0 x_0 + ik^j x_j\right] \ . \end{aligned} \tag{4.7}$$

The remaining 3 functions ξ_j are used to set $h_{0j} = 0$; in this way, the 0 component of the Lorentz gauge conditions becomes $-\partial^0 h_{00} + \partial^j h_{0j} = 0$ and therefore h_{00} is constant in time. This represents the static part of the gravitational potential, due to the GW sources, while it implies that $h_{00} = 0$ for GW. Consequently, the Lorentz gauge condition requires that also the spatial components are $\partial^j h_{ij} = 0$, making the tensor transverse.

When these conditions are fulfilled, the **Transverse−Traceless (TT) gauge** is defined. Here, the tensor $h_{\mu\nu} = h^{TT}_{\mu\nu}$ is symmetric and it has only 2 degrees of freedom, which indicate that GW have two different polarizations.

The solutions of eq. (4.6) in the TT gauge are the plane waves defined by:

$$h_{ij} = e^A_{ij}(\boldsymbol{k}) \exp\left[i k_\mu x^\mu \right] . \tag{4.9}$$

e^A_{ij} are the two polarization tensors:

$$\begin{cases} e^+_{ij} = u_i u_j - v_i v_j \\ e^\times_{ij} = u_i v_j + v_i u_j \ , \end{cases} \tag{4.10}$$

where $u_{i,j}$ and $v_{i,j}$ are the components of the basis vectors $\boldsymbol{u} \perp \boldsymbol{v} \perp \boldsymbol{k}$. For a plane wave propagating in the $\boldsymbol{k}$ direction, the components lay on the $\boldsymbol{k}$ transverse plane [134], since:

$$\partial^j h_{ij} \ = \frac{\partial}{\partial x^j} (e^A_{ij} \exp\left[-ik^0 x_0 + k^j x_j \right]) = ik^j (e^A_{ij} \exp\left[ik^\mu x_\mu \right]) = 0 \ , \tag{4.11}$$

which implies $ik^j h_{ij} = 0$ and $k^j h_{ij} = 0$. Thanks to this property, by defining a Cartesian coordinate system in which $\boldsymbol{k}$ is along the $z = (0,0,1)$ axis while $\boldsymbol{u} = (1,0,0) = x$ and $\boldsymbol{v} = (0,1,0) = y$,[3] h^{TT}_{ij} can be written as:

$$h^{TT}_{ij} = \begin{pmatrix} h_+ & h_\times & 0 \\ h_\times & -h_+ & 0 \\ 0 & 0 & 0 \end{pmatrix}_{ij} \cos(\omega(t - z)) \ . \tag{4.12}$$

The values h_+ and $h_\times$ are the amplitudes of the two polarizations and t describes the time evolution. Their effect on a circular distribution of masses is sketched in figure 4.1.

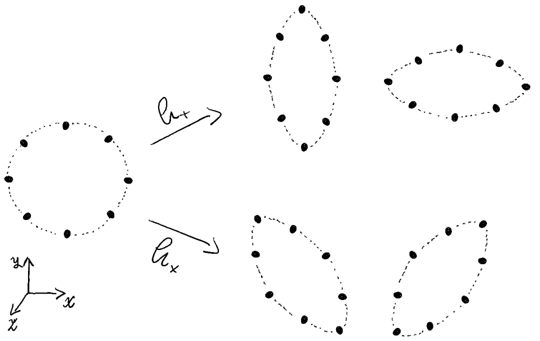

Figure 4.1: Sketch of the h_+ (top) and $h_\times$ (bottom) polarization effects on a circular distribution of masses. The GW in this case propagates in the z direction, orthogonal with respect to the plane (x, y) in which the mass distribution is found.

[3] In this case the cartisian coordinates therefore are $\boldsymbol{x} = (x, y, z)$.

Under these conditions, GW affect the 4–interval ds^2 as (see e.g., [134]):

$$\begin{aligned} ds^2 = &- dt^2 + d\mathscr{z}^2 + [1 + h_+ \cos(\omega(t - \mathscr{z}))]d\mathscr{x}^2 + \\ &+ [1 - h_+ \cos(\omega(t - \mathscr{z}))]d\mathscr{y}^2 + 2h_\times \cos(\omega(t - \mathscr{z}))d\mathscr{x}d\mathscr{y} \ . \end{aligned} \tag{4.13}$$

Moreover, the GW tensor can be expanded in the frequency space[4] as:

$$h_{ij}^{TT}(t, \boldsymbol{x}) = \int_{-\infty}^{+\infty} \tilde{h}_{ij}(f, \boldsymbol{x}) \exp\left[-2\pi i f t\right] df \ , \tag{4.15}$$

where $\tilde{h}_{ij}(f, \boldsymbol{x})$ is the Fourier transform of the components in the plane transverse to $\mathscr{z}$.

4.1.2 GW sources

To study how GW are produced when $T_{\mu\nu} \neq 0$, let us consider the generic equation:

$$-\frac{\partial^2}{\partial t^2} F(\boldsymbol{x}) + \nabla^2 F(\boldsymbol{x}) = j(\boldsymbol{x}) \ , \tag{4.16}$$

where $j(x_\mu) = \delta^D(t)\delta^{(D3)}(\boldsymbol{x})$ is a scalar field. The solution of its homogeneous part[5] is $G(\boldsymbol{x}) = [O(t - r) + I(t + r)]/r$ (where $r = \sqrt{\mathscr{x} + \mathscr{y} + \mathscr{z}}$) i.e., the superposition of the waves $O(t - r)$ and $I(t + r)$. The first one is the causal solution, propagating from the source to infinity with $v = c$, while the second propagates from infinity to the source: this is usually neglected since it has no physical meaning. For non–homogeneous equations, solutions are reached for the limit $r \longrightarrow 0$ in a small volume V through:

$$\lim_{r \to 0} \int_V d^3x \left[-\frac{\partial^2}{\partial t^2} G(\boldsymbol{x}) + \nabla^2 G(\boldsymbol{x}) \right] = \lim_{r \to 0} \int_V d^3x \ j(x_\mu) = \delta^D(t) \ . \tag{4.18}$$

In this limit, $O(t - r)$ does not diverge, $G(\boldsymbol{x}) \simeq 1/r$ and $\partial^2 G(\boldsymbol{x})/\partial t^2 \simeq 1/r$. Moreover, $d^3x \simeq r^2 dr$, therefore $d^3x \cdot \partial^2 G(x)/\partial t^2 \longrightarrow 0$. By using the divergence theorem:

$$\lim_{r \to 0} \int_V d^3x \nabla^2 G(\boldsymbol{x}) = \lim_{r \to 0} \int_{\partial V} ds \ \boldsymbol{k} \cdot \nabla G \ , \tag{4.19}$$

eq. (4.18) becomes:

$$\lim_{r \to 0} \int_{\partial V} ds \ \boldsymbol{k} \cdot \nabla G \simeq \lim_{r \to 0} 4\pi r^2 \left[\frac{1}{r^2} O(t - r) + \frac{1}{r} \frac{dO(t - r)}{dr} \right] = -4\pi O(t) = \delta^D(t) \ . \tag{4.20}$$

Therefore, considering $r = |\boldsymbol{x} - \boldsymbol{x}_e|$ where $\boldsymbol{x}_e = \boldsymbol{x}(t_e)$, t_e being an arbitrary origin, the **Green functions** are defined as:

$$G(\boldsymbol{x}) \ = \ \frac{1}{r} O(t - r) \ = \ -\frac{\delta^D(t - t_e - |\boldsymbol{x} - \boldsymbol{x}_e|)}{4\pi |\boldsymbol{x} - \boldsymbol{x}_e|} \ . \tag{4.21}$$

These solve the eq. (4.16) through the convolution:

$$F(t, \boldsymbol{x}) = \int dt_e d\boldsymbol{x}_e \ j(t_e, \boldsymbol{x}_e) \ G(t - t_e, \boldsymbol{x} - \boldsymbol{x}_e) \ . \tag{4.22}$$

[4] This is equivalent to the Fourier space since:

$$\begin{aligned} d^3k &= |k|^2 dk d\Omega \\ &= (2\pi)^3 f^2 df d\Omega \ . \end{aligned} \tag{4.14}$$

[5] The homogeneous part of eq. (4.16) is:

$$-\partial^2 G(\boldsymbol{x})/\partial t^2 + \nabla^2 G(\boldsymbol{x}) = 0 \ . \tag{4.17}$$

In the specific case of GW production (see e.g., [134]), the Green functions can be used to solve eq. (4.6). In fact, in this case, $G(t-t_e,\boldsymbol{x}-\boldsymbol{x}_e)$ is a solution of $\Box G(t-t_e,\boldsymbol{x}-\boldsymbol{x}_e)=\delta^{(D4)}(t-t_e,\boldsymbol{x}-\boldsymbol{x}_e)$, where $(t_e,\boldsymbol{x}_e)$ are the time at which the GW is emitted and the source position, respectively. The GW expression therefore is found analogously to eq. (4.22) through the convolution:

$$\begin{aligned}\bar{h}_{\mu\nu}(x) &= -16\pi\int dt_e\int d^3x_e\; G(t-t_e,\boldsymbol{x}-\boldsymbol{x}_e)T_{\mu\nu}(t_e,\boldsymbol{x}_e)\\ &= 4\int d^3\boldsymbol{x}_e\,\frac{1}{|\boldsymbol{x}-\boldsymbol{x}_e|}T_{\mu\nu}(t-|\boldsymbol{x}-\boldsymbol{x}_e|,\boldsymbol{x}_e)\,.\end{aligned} \tag{4.23}$$

Using the local conservation of $T_{\mu\nu}$, one can demonstrate (see e.g., [11, 134] for the full derivation) that the mass and the linear momentum are conserved,[6] therefore no monopole and dipole radiations are produced. However:

$$\bar{h}^{ij}(t,\boldsymbol{x})\underset{r\to\infty}{\longrightarrow}\frac{2}{r}\ddot{\mathcal{I}}(t-r)\,, \tag{4.24}$$

where:

$$\mathcal{I}^{ij}(t)=\int d^3x\; T^{00}(t,\boldsymbol{x})x^ix^j\simeq\int d^3x\;\rho(t,\boldsymbol{x}_e)\;x^ix^j\;, \tag{4.25}$$

is the mass tensor, which describes how the mass is distributed depending on the second time derivative.[7] Eq. (4.24), therefore, indicates that to produce the GW **strain** $\bar{h}^{ij}(t,\boldsymbol{x})$, the mass quadrupole is needed i.e., the second time derivative of the mass distribution has to vary: this can either happen on a short time scale or continuously, as the following sections describe.

Transient sources

Transient sources whose emission can be singularly detected are also indicated as **resolved sources** (see e.g., [258, 259] for a review). Two main categories are identified in this case: bursts and binary emissions.

GW **bursts** are produced by very energetic and asymmetric events, such as supernovae explosions (see e.g., [260]), magnetars i.e., neutron stars with very high magnetic fields see (e.g., [261]), or more exotic sources, such as cosmic string i.e., primordial topological defects[8] (see e.g., [262]). The GW signal of all these bursts is still not well modeled: signatures of their presence is searched in the datasets by looking at relevant peaks through a coherent analysis between different interferometers (see e.g., [126, 258]).

The case is very different for **binary mergers**. Once they form (and eventually shrink) as described in section 3.3.3, the orbital evolution is completely due to GW: these are produced by the quadrupole moment (see eq. (4.24) produced by the motion of the two compact objects orbiting each other. In the Newtonian approximation, if the objects have masses m_1, m_2 and orbit in the (x, y) plane:

$$x = R\cos\left(\omega t+\frac{\pi}{2}\right)y = R\sin\left(\omega t+\frac{\pi}{2}\right)z = 0\,, \tag{4.26}$$

where R is the orbital radius and ω their angular velocity. In this case, the

[6] 6: The mass and momentum conservation are valid only on first approximation: since the GW emission makes the source lose energy and momentum, a back−reaction should be introduced. This is considered when solving the Einstein eq. (2.4) in the non−linear regime.

[7] 7: T^{00} in eq. (4.25) indicates that the total energy density should be considered; for non−relativistic sources, this can be approximated through the matter density ρ.

[8] 8: A topological defect can be visualized as a discontinuity between two manifolds e.g., due to a phase transition that behaves differently between them.

quadrupole components are:

$$
\begin{aligned}
\ddot{\mathcal{I}}_{xx} &= 2\mu R^2\omega^2 \cos(2\omega t) \\
\ddot{\mathcal{I}}_{yy} &= -\ddot{\mathcal{I}}_{xx} \\
\ddot{\mathcal{I}}_{xy} &= 2\mu R^2\omega^2 \sin(2\omega t)\ .
\end{aligned}
\tag{4.27}
$$

In the previous expression, $\mu = m_1m_2/(m_1+m_2)$ is the reduced mass and $f = 2\omega/2\pi$ is the frequency of the emitted GW [134], which increases while the objects move faster, approaching one another. The evolution of f depends on the **chirp mass**:

$$
M_{chirp} = \frac{(m_1m_2)^{3/5}}{(m_1+m_2)^{1/5}} = \mu^{3/5}M^{2/5}\ , \tag{4.28}
$$

where $M = m_1 + m_2$ is the total mass. In fact, by computing the energy emitted through GW through the derivative of the quadrupole momentum:

$$
\frac{dE}{dt} \propto -\left\langle \dddot{I}_{xy}\dddot{I}_{xy} - \frac{1}{3}(\dddot{I}_{xx})^2 \right\rangle \propto -(\omega M_{chirp})^{10/3}\ , \tag{4.29}
$$

the GW frequency evolution turns out to be:

$$
\dot{f} \propto f^{11/3} M_{chirp}^{5/3}\ . \tag{4.30}
$$

The amplitudes of the two polarizations h_+, $h_\times$ defined in eq. (4.12) varies depending on the direction in which the GW is observed. Perpendicularly to the orbital plane (i.e., in z direction), h_{ij}^{TT} is circular polarized and the two components are:[9]

$$
h_+ = -8m\omega^2\frac{R^2}{r}\cos(2\omega t)\ , \quad h_\times = 8m\omega^2\frac{R^2}{r}\sin(2\omega t)\ . \tag{4.31}
$$

Along any direction in the orbital plane, instead, the radiation is completely + polarized and its amplitude is $h_+ = 4m\omega^2R^2/r$, weaker than the previous case. Intermediate cases present an elliptical polarization due to the relative amplitude of h_+ and $h_\times$. As it is evident from eq. (4.31), the amplitude of the signal depends as well from the masses of the two bodies in the binaries: the larger the mass, the louder the signal will be [134].

Depending on how the GW is modelled, the evolution of the motion of coalescing binaries can be divided into three phases:

- The inspiral, a long−lasting, small periodic emission, in which the signal is analytically modelled as emitted by a quasi−circular motion in Newtonian or post−Newtonian[10] approximation.
- The merger between the objects, where numerical, post−Newtonian techniques are used.
- The ring down, a very fast process during which the object formed in the merger stabilizes, whose modelization is the most difficult.

For each phase, templates of the GW waveform are available [263]. These depend on many parameters (see e.g., [264]): the masses and spins of the progenitors, the binary position in the sky and its distance and orientation with respect to the observer. Waveform templates are used to performed the **matched−filtering** analysis of the datasets: they are built spanning the full parameter space, including information on the detector noise described in section 4.2, and they are convoluted

[9] 9: The expression can be straightforward generalized for a GW propagating in a generic direction.

[10] 10: In the **post−Newtonian approximation**, spin angular momenta are considered for the bodies that make up the binary. The GW waveform then includes higher order multipoles of the energy−momentum tensor and corrections for the amplitude of each multipole component.

with the detector output, so to find slices of it that correlate with the modelled signal shape [263].

Continuous sources

Continuous GW emitters exist as well and they should be detectable in the background of the resolved ones. Examples of astrophysical sources are spinning non−axisymmetric neutron stars, accretion disks and early−stage binary inspirals [258].

Numerous and weak sources e.g., mergers from very distant or low mass sources, can as well overlap incoherently and build up the continuous emission of the so called **astrophysical background** (see e.g [265–267] for reviews on the topic). Because of their stochastic nature, GW emissions that produce the backgrounds can be treated as random variables:

$$h_{ij}(t,\boldsymbol{x}) = \int df \int d^2\Omega\, h_{ij}(f,\boldsymbol{n}) \exp\left[i2\pi f(t+\boldsymbol{n}\cdot\boldsymbol{x})\right] , \tag{4.32}$$

i.e., as a superposition of sinusoidal plane waves, having frequency is f and propagating along all the $\boldsymbol{n}$ directions in the sky. In analogy to section 2.2.2 and section 3.2, the GW statistical description can be given through their power spectra (see e.g., [267, 268]):

$$\begin{aligned}\left\langle h_A(f,\Omega)h^*_{A'}(f',\Omega')\right\rangle &= \frac{3H_0^2}{32\pi^3}\delta^{(D2)}(\Omega,\Omega')\delta^K(A,A')\delta^D(f-f')\frac{\Omega_{GW}|f|}{f^3} ,\\ &= \frac{1}{16\pi}S_h(f)\delta^{(D2)}(\Omega,\Omega')\delta^K(A,A')\delta^D(f-f') ,\end{aligned} \tag{4.33}$$

where in the first line we defined:

$$\Omega_{GW} = \frac{f_{obs}}{\rho_c}\int \frac{dz}{(1+z)H(z)}\frac{dE(f,z)}{df} . \tag{4.34}$$

as the fractional **energy density spectrum**, whose functional form depends on the source of the background. The equivalence takes into account the fact that the frequency observed f_{obs} is redshifted with respected to the emitted one f; ρ_c is the critical density defined in section 2.1. In particular, when the source of the GW energy are the unresolved binaries,[11] eq. (4.34) becomes [266]:

$$\Omega_{GW} = \frac{f_{obs}}{\rho_c}\int dz \frac{N(z)}{(1+z)H(z)}\frac{dE(f,z)}{df} \propto M_{chirp}^{5/3} f_{obs}^{2/3} N_0 \left\langle (1+z)^{-1/3}\right\rangle , \tag{4.35}$$

where $N(z)$ is the comoving number density of sources, N_0 its value integrated over all the redshifts and:

$$\left\langle (1+z)^{-1/3}\right\rangle = \frac{1}{N_0}\int_{z_{min}}^{z_{max}} \frac{N(z)}{(1+z)^3}dz . \tag{4.36}$$

The fractional energy density spectrum is related to the strain power spectral density function $S_h(f)$ defined in eq. (4.47) and introduced in the second line of eq. (4.33), simply through:

$$S_h(f) = \frac{3H_0^2}{2\pi^2}\frac{\Omega_{GW}(f)}{f^3} . \tag{4.37}$$

[11] For ground−based detectors, unresolved binary black holes and binary neutron stars coalescences build up the strongest astrophysical background [257].

The existence of a **cosmological background** has been hypothesised as well (see e.g [138, 269–271] for reviews on the topic). GW in this case can be produced by many different processes. Some of them are related with the inflationary era: primordial quantum oscillations give rise to tensor metric fluctuations (compare with chapter 2) that represents a tiny but irreducible contribution to the stochastic gravitational wave background [271]. The presence of extra−fields with respect to the standard slow−roll inflation or of particular symmetries can enhance the amount of GW expected (details can be found e.g., in [270, 271]). Other contributions to the cosmological GW background can come from PBH formation and merger, topological defects, phase transitions or physical processes that take place between the end of inflation and the primordial nucleosynthesis (see section 2.1.3. Depending on the process which is taken into account, the energy density spectrum Ω_{GW} and the power spectral density $S_h(f)$ can be modelled. In general, the cosmological GW background is expected to be isotropic (i.e., $\delta^{(D2)}(\Omega, \Omega')$ over different sky directions), stationary (i.e., $\delta^D(f - f')$), Gaussian and unpolarized[12] (i.e., $\delta^K(A, A')$).

No direct detection either of the astrophysical nor the cosmological stochastic background have been measured yet [272]. To separate the background contribution from the detector noise it is crucial to cross−correlate data from pairs of detectors, located in different places. Even if challenging, the detection of the astrophysical background is taken for granted in the near future with the new observational runs of LIGO−Virgo−Kagra Collaboration [273]. The goal of observing the cosmological background is even more tough: first of all, it is necessary to remove the astrophysical contribution through an accurate data processing. Even if this point would be achieved, the amplitude of the cosmological GW background could be too tiny to be observed. From some of the theoretical models for the inflationary mechanism, however, a high enough signal is expected to be observed in the LISA band [270, 271] and also through the Einstein Telescope [257]. The sensitivity curves of these detectors are showed in figure 4.3 and their characteristics are presented in the following section.

4.2 GW detectors

Despite other ideas have been proposed for the direct or indirect detection of GW, the detectors that up to now played the central role for GW science are the interferometers. These are based on two main concepts:

- GW deform spacetime differently in the various directions.
- Light beams that travel different paths and accumulate relative phases interfere constructively or destructively.

The easiest configuration that can be thought for a GW interferometer is the Michelson−Morley sketched in figure 4.2 (see e.g., [274] for a review). Here, the light beam produced by a laser passes though a beam split that divides it into two path. These defines the interferometer arm, at the end of which two mirrors reflects the light back to the start. The reflected light beams recombine inside the beam splitter when crossing it the second time: in this way, in the final signal an interference figure can be found, due to the different optical path lengths the two arms defined.

[12] In some theories e.g., involving parity symmetry breaking, the unpolarized condition is broken.

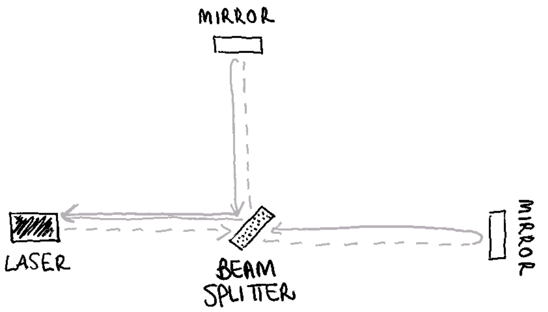

Figure 4.2: Sketch of the Michelson−Morley interferometer. The laser enters the system from the left (dashed grey line), impacts on the beam splitter and gets separated in two beams. These are reflected by the mirrors (continuous grey line) and recombines in the beam splitter. The output light (double−continuous grey line), when measures, contains the interference due to the phase difference accumulated by the two beams along the interferometer arms.

In particular, after the beams recombine, the light energy is:

$$E = E_x + E_y = \frac{E_0}{2}\left(\exp\left[i(k_l x - \omega_l t + \phi_x)\right] + \exp\left[i(k_l y - \omega_l t + \phi_y)\right]\right) \tag{4.38}$$

where $x,\ y$ are the two arms, E_0 the energy[13] the laser enters the system with, and ω_l $k_l = \omega_l$ its angular frequency and wavevector.[14] $\phi_{x,y}$ are the phases due to the mirror reflections and to the different arm lengths. Therefore, the intensity the detector measures *at rest* is:

$$\begin{aligned} I &= E \cdot E^* \\ &= \frac{E_0^2}{4}\left(2 + \exp\left[i(k_l x + \phi_x - k_l y - \phi_y)\right] + \exp\left[-i(k_l x + \phi_x - k_l y - \phi_y)\right]\right) \\ &= \frac{E_0^2}{2}\left[1 + \cos\left(k_l(x - y) + \phi_x - \phi_y\right)\right] . \end{aligned} \tag{4.39}$$

When a GW passes by, the spacetime is stretched. As [134] describes, working in the TT gauge defined in section 4.1, the interferometer mirrors can be thought as free falling particles, while the metric in which the laser photons travel is the one in eq. (4.13). The different contributions the GW provides in the two arm directions determine a change in the time the laser beams require to travel them. Let us consider a GW orthogonal to the detector plane i.e., $x,\ y$ coincides with the detector arms. The TT gauge metric is then reduced to:

$$ds^2 = -dt^2 + (1 + h_+(t))dx^2 + (1 - h_+)dy^2 + dz^2 = 0 , \tag{4.40}$$

and the travelled distance in each arm is:[15]

$$\begin{aligned} 2L_x &= \left|\int_0^{Lx} dx\right| + \left|\int_{Lx}^0 dx\right| = \int_{t_0}^{t_1} dt\left(1 - \frac{1}{2}h_+(t)\right) + \int_{t_1}^{t_2} dt\left(1 - \frac{1}{2}h_+(t)\right) \\ &= t_2 - t_0 + \frac{1}{2}\int_{t_0}^{t_2} dt\ h_0(t)\cos\left(\omega_{GW} t\right) , \end{aligned} \tag{4.41}$$

where in the last equation we applied eq. (4.12). After some algebraic manipulations [134] eq. (4.41) can be rewritten to express the laser travel time inside the x arm as:[16]

$$t_2 - t_0 = 2L_x + L_x h_+\left(t_0 + L_x\right)\frac{\sin\left(\omega_{GW} L_x\right)}{\omega_{GW} L_x} . \tag{4.42}$$

[13] We are assuming that energy is conserved inside the interferometer.

[14] Remember that $G = c = 1$ in this chapter.

[15] Here we refer to the arm along the x axis but the same holds for the one along y. The beam splitter is located in $(0, 0)$ in the detector plane, while the mirror is in Lx, being L the length of the detector arm *at rest*. t_0, t_1 and $t_2 \simeq t_0 + 2L_x$ are respectively the times when the laser photons leaves from the beam splitter position, reach the mirror and gets back to the beam splitter, where they interfere.

[16] For the y arm the sign of the second term is inverted.

For $L_x >> 2\pi/\omega_{GW}$, the GW oscillations average out while travelling along the interferometer arm: this sets to $f \simeq 2/L$ the minimum GW frequency the detector can observe depending on the length of its arms. Finally, considering the light beams travelling both the x and y arms that rejoin the beam splitter at the same t_2 i.e., with different $t_0^{x,y}$, the phase shift between them is:

$$\begin{aligned}\Delta\phi &= \omega_l(t_0^x - t_0^y) \\ &\simeq \left[2(L_x - L_y) + 4Lh_0\cos\big(\omega_l(t-L)\big)\frac{\sin\big(\omega_l L\big)}{\omega_l L}\right]\omega_l = \Delta\phi_0 + \Delta\phi_{GW}\ .\end{aligned} \tag{4.43}$$

While the first term can be reconducted to the *at rest* phase shift, the second is the phase shift induced by the GW. Depending on the GW frequency, $\Delta\phi_{GW}$ determines the optimal length the detector should have to measure it; this is reached when:

$$\Delta\phi_{GW} \simeq \sin(\omega L) = 1 \quad \longrightarrow \quad L \simeq \frac{\pi}{2\omega_{GW}} \simeq \frac{1}{2f}\ . \tag{4.44}$$

The previous equation indicates that for e.g., $f \simeq 100$Hz the optimal length of the detector arms would be $L \simeq 750$km. Clearly, this is not achievable: to increase the photon travelled paths, therefore, optical cavities are inserted in the interferometer arms (see e.g., [275]). These are mirrors configurations that increase the number of reflections the laser goes into: in this way, the effective travelling−time before the recombination in the beam splitter is longer and the phase shift between the two beams gets increased.

Real interferometers are more complicated than the standard Michelson−Morley one sketched in figure 4.2. On top of the presence of optical cavities, other technical supplies have been introduced to lower as much as possible the instrumental noise and to increase the detector sensitivity (see e.g., [275–277] for a summary). This is usually defined through the **noise power spectral density**: this is the Fourier transform of the auto−correlation function of the noise (see e.g., [264, 278]):

$$\big\langle n(f)n(f')^*\big\rangle = \frac{1}{2}\delta^D(f-f')\,S_n(f) = \frac{h_n^2(f)}{f} \tag{4.45}$$

where in the second equation the noise characteristic strain has been defined.[17] Figure 4.3 shows the value of $\sqrt{S_n(f)}$ for some of the current and future planned GW detectors (these will be described later on in this section), compared with the power spectral density that would be observed for GW emitted by binaries in different mass ranges.

Generally, the main noise contribution that shapes the noise power spectral density are (see e.g., [276, 277]):

Quantum noise: it dominates at high frequencies and it is due to the quantum nature of light. On one side, it provides a shot noise contribution in the counting of the laser photons, while on the other it determines a radiation pressure on the mirrors, introducing spurious contributions to the variations of their positions.

Thermal noise: it is present at all frequencies and it is due to the internal dissipation of the instruments e.g., mechanical variations in the mirror suspensions due to temperature variations or Brownian thermal noise in the mirror coatings.

Seismic noise: for ground−based detectors, it dominates at low frequencies and it is due to the movements in the mirror positions due to human activities and tides.

[17] The noise characteristic strain can be compared with the strain of the observed GW $\tilde{h}(f)$. In this way, the signal−to−noise ratio is defined as:

$$\begin{aligned}SNR^2 &= \int_0^{+\infty} df\,\frac{4|\tilde{h}(f)|^2}{S_n(f)} \\ &= \int_{-\infty}^{+\infty} d\log f\left[\frac{h_s(f)}{h_n(f)}\right]^2,\end{aligned} \tag{4.46}$$

where $h_s(f) = 2f|\tilde{h}(f)|$ is the source characteristic strain, defined in order to compute the signal power spectral density in analogy to eq. (4.45) as:

$$S_h(f) = \frac{h_s^2(f)}{f}\ . \tag{4.47}$$

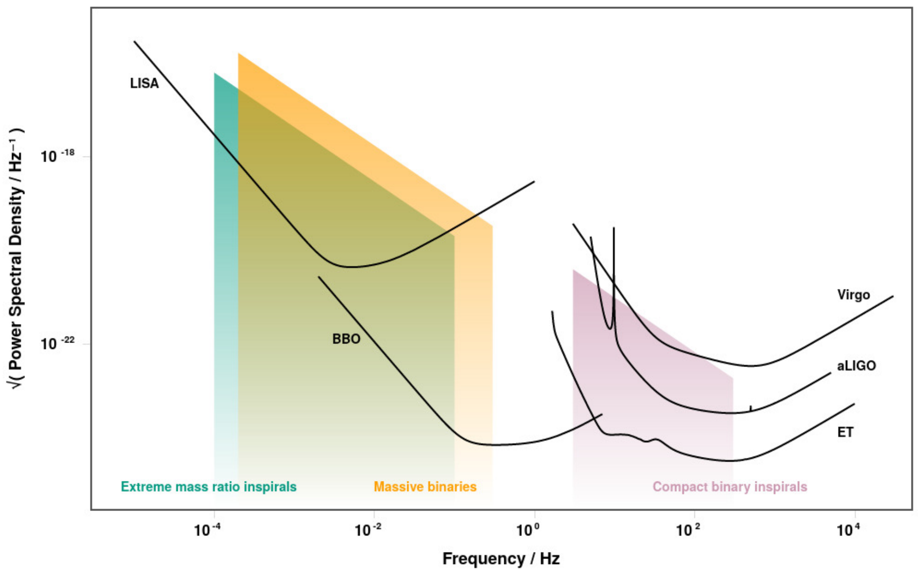

Figure 4.3: Noise power spectral density from eq. (4.45) computed for the detectors discussed in the text (aLIGO is one of the notations used in literature to indicate the updated configurations of this detector; in the text we will refer it simply as LIGO). This is compared with the GW power spectral density computed through eq. (4.47) of binaries in different mass ranges: $[1, 100]\,M_\odot$ size black holes (purple, on the right), massive $[10^4, 10^7]\,M_\odot$ black holes (orange, in the central region) and extreme mass ratio inspirals (blue, on the left) i.e., stellar mass size black holes falling onto a supermassive black hole. The plot is obtained through the publicly available code `gwplotter` [278].

Newtonian noise: for ground−based detectors, it dominates the lowest frequencies; it is related to the stochastic fluctuations of the local gravitational field e.g., due to variations in the atmospheric pressure or to seismic waves.

The relative relevance of each noise contribution and the possible solutions that have been studied to deal with it differs depending on the interferometer configurations. In the following, we will present a small overview of the GW detectors today available and of the ones coming online in the next future.

4.2.1 Present: second generation detectors

The GW detectors that operated until now are the two advanced LIGO [247] and the Virgo [252] interferometers, respectively located in the USA and in Italy. Their configuration is the one described in the previous section: two orthogonal arms, 4km long for LIGO and 3km long for VIRGO, forming an L−shape inside which the laser light travels in vacuum condition. The directions of the arms of the two LIGO interferometers are aligned: in this way, when a GW is detected, its waveform is the same in both the LIGO instruments, providing a cross−check of the reliability of the detection above the local noise. However, since in this way the two have a very similar antenna pattern (see section 4.3), this choice reduces the possibility of disentangling the two polarizations. LIGO and VIRGO are currently being upgraded so to improve their sensitivity; observational activities will restart at the end of 2022. A further improvement is then planned in order to reach the target sensitivity during the fifth observational campaign (O5, planned ∼ 2025).

L−shape detectors with sensitivities comparable with the advanced LIGO and Virgo are commonly called **second generation interferometers**. Another detector of this kind already exist: Kagra [253, 254], in Japan, who became operational at the beginning of 2020 and that will join the O4 campaign. Kagra has 3km long arms and mirrors in cryogenic conditions to reduce the thermal noise. The plan exists [273] to build another detector, analogous to the LIGO ones, in India: this would join the network during O5. In this way, having four second generation interferometer, we will improve the SNR of detected GW between 10 and 1000 Hz coming from almost all directions in the sky.

The detector horizons of LIGO and Virgo during the third observational run (O3, [250, 251]), together with the planned horizon for next campaigns are indicated in table 4.1.

	BBH		BNS	
	Distance	Redshift	Distance	Redshift
LIGO O3	$2-3\,\mathrm{Gpc}$	$0.3-0.5$	$110-130\,\mathrm{Mpc}$	$\simeq 0.02$
Virgo O3	$1\,\mathrm{Gpc}$	0.2	$50\,\mathrm{Mpc}$	$\simeq 0.1$
LIGO O5	$8\,\mathrm{Gpc}$	1.1	$330\,\mathrm{Mpc}$	0.07
Virgo O5	$3-6\,\mathrm{Gpc}$	$0.5-0.9$	$150-260\,\mathrm{Mpc}$	$0.03-0.05$
Kagra	$200-600\,\mathrm{Mpc}$	$0.04-0.1$	$8-25\,\mathrm{Mpc}$	< 0.01
Kagra O5	$3\,\mathrm{Gpc}$	0.5	$130\,\mathrm{Mpc}$	0.03
LIGO India O5	$8\,\mathrm{Gpc}$	1.1	$330\,\mathrm{Mpc}$	0.07

Table 4.1: Estimated observed horizon for the current and future second generation interferometers up to the target sensitivity forecasted for O5. The horizon distances for binary neutron stars (BNS) are taken from [273]; the ones for binary black holes (BBH) are estimated as $d_{BBH} \simeq d_{BNS}(M^{BBH}_{chip}/M^{BNS}_{chirp})^{5/6} \simeq d_{BNS} \cdot 25^{5/6}$. Redshifts are computed form distances by inverting 2.15 in the fiducial cosmology table 2.1.

4.2.2 Future from the ground: ET

In about 10 years, the so called **third generation interferometers** will be realized. They will be able to measure GW with smaller amplitudes and they will increase the sensitivity frequency band, both on the low[18] an high frequency region.

One possible configurations to do so is the one proposed for the Einstein Telescope (ET, [255–257]): it will suffer less by seismic noise since it will be placed underground and it will have cryogenically cooled mirrors to reduce the thermal vibrations. ET is proposed to be built having 10km arms placed in a triangular−shape, so to be equally sensitive to both the h_+, $h_\times$ polarizations. Each arm will contain two interferometers, one specialized to measure the lower frequencies and the other for the higher frequencies. ET horizon, especially for BBH, will be incredibly larger with respect to the second generation detectors: as described in table 4.2, it will observe the Universe up to the time when the first stars were born [255–257]. For this reason, ET will be crucial for cosmological studies: this is the detector we will adopt in chapter 5 and chapter 6 to perform forecasts on future GW surveys.

4.2.3 Future from the space: LISA, BBO

The only solution we have to remove the Newtonian noise so to measure the lower frequencies is to observe GW from space. Isolated from every ambient noise and from the terrestrial gravity gradient, thanks to $\simeq 10^6$km long arms, they will measure GW in the frequency range $f \in [10^{-5}, 10^{-1}]$Hz (see [279, 280] and references therein). The sources of GW in this range are different with respect to the ones probed with ground−detectors: in fact, such low frequencies are produced either during the merger phase of very massive black holes with $M \in [10^4, 10^7]\, M_\odot$ or in the inspiralling of stellar mass size BNS and BBH. This open a very interesting perspective for multi−band GW analysis: inspiralling binaries observed at the higher edge of the frequency band of space interferometers can reach the merger

---

[18] ET will reach $f \simeq 1$Hz: lower frequencies are inaccessible from the ground, because of Newtonian noise, which can not be removed neither shielded.

phase in a few year, becoming then observable with ground−based detectors (see e.g., [257, 281]). Another important GW source for space−based detectors will be the GW stochastic background (both of astrophysical and cosmological origin) described in section 4.1.2.

The building of a space interferometer has some peculiarities with respect to the ground based ones. First of all, they have to be constructed by placing spacecrafts in orbit along the ecliptic:[19] the length of the baseline, therefore, is enormous and it allows the measurement of very low f. Each of the spacecrafts is a free falling mass, from which a laser is sent in the direction of the others: the received laser is not reflected but its phase is registered, while a similar laser is sent back to the origin. The interference between the two lasers, therefore, does not take place directly but it is realized in post−processing through the so called **time−delay interferometry** (see e.g., [282]). Moreover, the motion of the spacecrafts along the orbit make them change their relative inclination with respect to the observed sky: the sensitivity to the two polarizations, as well as the antenna patterns defined in section 4.3, are in this case time dependent. Noise sources of space interferometers are different as well e.g., the effect of quantum noise is dominant and the positions of the spacecraft can be affected by the solar radiation pressure.

LISA (Laser Interferometer Space Antenna, [279, 280]) will be the first space detector we will build. It will be made of three spacecrafts, each equipped with two lasers so to create six interferometers. They will lay in a plane inclined of $\simeq 60^\circ$ with respect to the ecliptic, in near−equilateral triangular formation. The arms will be $\simeq 2.5 \cdot 10^6$ km long. LISA operations are planned to start in the end of the 2030.

Another proposed future space−based detectors is BBO (Big Bang Observer, see e.g., [283]). In its pre−-conceptual design, a constellation of 4 clusters of 3 spacecrafts is created, each of which forming a LISA−like detector. Two of these clusters, being located at the same position, will enhance the sensitivity of the detector; the others, widely separated around the orbit, will increase the angular resolution. BBO will be the most sensitive to GW in the $0.1 - 1$Hz band [284].

4.3 GW and cosmology

Astrophysical, being them transient or continuous, and cosmological GW sources described in section 4.1.2 can both be used to set constraints on the cosmological models that describe the structure and the evolution of the Universe.

Particularly relevant are binary mergers, since they are by far the most numerous sources that will be detected by current and future interferometers. Their study provides different applications for cosmology; here we summarize two of them that will be relevant for the analyses developed in chapter 5 and chapter 6.

4.3.1 Binary mergers

Let us summarize how the observed GW signal produced by binary orbital evolution looks like.

As described e.g., in [264, 285], the GW strain measured by a detector is:

$$h(t) = \mathcal{F}^{ij} h_{ij}(t) \propto \frac{Q(\theta, \phi, \psi, \iota)\mu M}{R(t)D} \cos\left(\int 2\pi f \, dt \right) , \tag{4.48}$$

[19] 19: The ecliptic is the apparent path over which the Sun moves when seen from the Earth reference system. It is given by the intersection between the terrestrial orbital plane and the celestial sphere.

where $\mathscr{F}^{ij}$ is the **antenna pattern** i.e., the operator that transforms the GW tensor into the scalar output measured by the detector, which defines the functional form of the Q function. The antenna pattern mixes the contribution of the two GW polarizations: to disentangle them, more than one detection of the same wave is needed. D is the distance to the source, (θ, ϕ) describe the sky position, ψ is the polarization angle and ι the inclination of the binary orbit with respect to the LoS $= (\sin\theta\cos\phi, \sin\theta\sin\phi, \cos\theta)$. It holds:

$$\cos\iota = \hat{\boldsymbol{L}} \cdot \boldsymbol{n} \ , \tag{4.49}$$

being $\hat{\boldsymbol{L}}$ the orbital angular momentum unit vector. The function $R(t)$ is obtained by integrating:

$$\frac{dR}{dt} = \frac{dR}{dE}\frac{dE}{dt} = -\frac{R}{E}\frac{dE}{dt} = -\frac{64}{5}\frac{\mu M^2}{R^3} \ , \tag{4.50}$$

where dR/dE is the orbit size, which decreases due to the GW energy loss (see e.g., as [264] and reference therein).

The strain tensor h_{ij} can be divided into the two components $h_A = h_+,\ h_\times$, which can be Fourier transformed into:

$$\tilde{h}_A(f) = \Xi_A(\cos\iota)\tilde{h}_0(f) \tag{4.51}$$

where $\Xi_+ = (1 + \cos 2\iota)/2$, $\Xi_\times = -i\cos\iota$ and [264]:

$$\tilde{h}_0(f) = \sqrt{\frac{5}{24}}\pi^{-2/3}D^{-1}M_{chirp}^{5/6}f^{-7/6}\exp[i\Psi(f)] \quad \text{for } f \geqslant 0 \ . \tag{4.52}$$

In the previous equation, the function $\Psi(f)$ depends on the chirp mass M_{chirp} defined in eq. (4.28), the reduced mass function μ, the spin parameter β and the time t_C and waveform phase ϕ_C at the coalescence. The signal amplitude and frequency both increases as $t \longrightarrow t_C$. The measured strain (see [264] for the full calculation) is then:

$$\begin{aligned}\tilde{h}(f) &= Q(\theta, \phi, \psi, \iota)\Xi_A(\cos\iota)\exp\left[-2\pi i(\boldsymbol{n}\cdot\boldsymbol{x})f\right]\tilde{h}_0(f) \\ &= \frac{Q}{D}M_{chirp}^{5/6}\ f^{-7/6}\exp[i\Psi(f)] \ .\end{aligned} \tag{4.53}$$

This expression is valid until the model transits to the ring down phase.

Finally, the antenna pattern determines also the sensitivity of the detector with respect to the different parts of the sky. Except for the regions aligned with the arms bisector, interferometers are sensitive to GW coming from all directions. The localization of their source through a single measurement, therefore, is very difficult. Having a network of detectors, instead, solves the issue since triangulation can be performed [273, 286, 287]. This is based on the comparison between the arrival times of the wave at the different detectors. When two of them are considered, the observed region is a ring concentric with their baseline; with three detector, the sky localization reduces to two patches on the sky, symmetric with respect to the plane in which the three detectors lay. One of the patches can usually be excluded through the analysis of the GW amplitudes and phases measured by the different detectors [288], or through the presence of a fourth detector. The size of the uncertain sky localization region depends on the accuracy in the measurement of the delay−time between the detectors on top on other parameters that determines the SNR of the waveform e.g., the mass of the progenitors.

Standard sirens

When observing GW sources at cosmological distances, the measured frequency differs from the intrinsic one as $f_{obs} = f/(1+z)$, because of the Universe expansion. The no−shifted measured waveform from eq. (4.53) can not be reconstructed, since $h(t)$ is invariant under the transformation:

$$\left[f, M_{chirp}, \mu, R, D, t\right] \to \left[\frac{f}{1+z}, M_{chirp}(1+z), \mu(1+z), R(1+z), D(1+z), t(1+z)\right] . \tag{4.54}$$

On one hand, this represents an issue since the redshifted parameters:

$$M_z = (1+z)M_{chirp} , \quad \mu_z = (1+z)\mu , \tag{4.55}$$

are degenerate with the redshift z, therefore the value of the latter can no be estimated. However, from the redshifted waveform it is possible to get a direct estimate of the luminosity distance $D_L = D(1+z)$ defined in eq. (2.18).

This opens an incredible opportunity: binary mergers turns out to be **self−calibrated**[20] **standard sirens** [25, 153, 290, 291].

Let us consider a binary neutron star merger.[21] Its GW emission can be accompanied by an electromagnetic multi−band counterpart, powered by the energetic processes that disrupt the neutron stars and produce shock waves and nuclear reactions [292]. A short γ−ray burst can be observed right after the GW, followed by a bright UV, optical and infrared kilonova transient. In the end, X−ray and radio emissions are produced as well.

In the case of the binary neutron star merger GW170817 [293], the EM counterpart was observed in all the wavelengths, starting from the γ−emission (GRB 170817A, [294]), up to the kilonova, whose observations lasted from hours to days depending on the wavelength, and to the X−ray (9 days after the merger) and radio (16 days) emissions [292]. Such an incredible dataset brought to a huge amount of scientific results, including the H_0 estimate [26]. The GW waveform of GW170817 was used to infer the luminosity distance to the source, while the redshift was estimated through the electromagnetic counterpart.

The value of H_0 estimated with this approach is right in the middle between the CMB and the local estimates described in section 3.3.2 and it is independent from both of them. Since GW170817 is up to now the only event that allowed us to perform this analysis, however, the H_0 confidence regions have large uncertainties. The situation will certainly improve in the next years: [27] estimates that with the observation of $\simeq 50$ binary neutron star events ($\simeq 5$ yr observations with O5, see section 4.2) it will be possible to constrain H_0 with a $\simeq 2\%$ precision. Whether this will confirm the validity of one of the existing estimates or push for the search for new physics to solve the H_0 tension, is still to be seen.

LSS tracers

As anticipated in chapter 3, binary mergers can be used as tracers of the large scale structures. Their distribution and clustering properties depend on the origin of their progenitors and on the formation channel assumed: section 3.3.3 already showed some examples, that will be operationally adopted and analysed in chapter 5 and chapter 6.

[20] The only assumption required to estimate D_L from the GW waveform is that it is well described by GR. Following e.g., [134] or [289], it is possible to show that combining the GW strain in eq. (4.53) with the GW frequency evolution from eq. (4.30), at first approximation it holds:

$$D_L = \frac{5}{96\pi^2}\frac{c}{h}\frac{\dot{f}}{f} . \tag{4.56}$$

[21] The use of binary black holes in this sense is more challenging. This will be exploited in section 5.1.

It is worth mentioning here which are the peculiarities of GW surveys that make them an interesting alternative to the already well−known and largely used galaxy surveys. Clearly, since with current detectors only a small number of events in the local Universe can be observed (see e.g., catalogues from [248, 250, 251]), such considerations has to be made with respect to future surveys. Since binary mergers are the main interest for this thesis, the best choice is to deal with third generation ground−based detectors, such as the Einstein Telescope [255–257], and to compare it with a near future galaxy survey such as *Euclid* [295].

Table 4.2 compares a 1 yr ET−like survey with a *Euclid*−like survey. ET GW catalogues will contain a smaller number of events with respect to the *Euclid* galaxy maps. However, ET horizon will spread up to very high redshifts, well above the observational limit of *Euclid*. Considering also that, as described at the beginning of this section, ET can observe GW coming from almost all directions, this implies that the cosmic volume it will probe will be bigger than a future *Euclid*−like survey. It is then the perfect instrument to study large scale effects: the linear bias is one of them, but also primordial non−Gaussianity and wide angle space distortions (which were described in section 3.2.1) will be perfect targets for such an instrument. On the contrary, small scales will be inaccessible to ET because of its poor sky localization, unless detector networks are take into account.

Table 4.2: Comparison between the specs of a 1 yr ET−like survey for binary black holes (BBH) and binary neutron stars (BNS) as described in [257] and a photometric *Euclid*−like survey as from [295].

	ET−like BBH $m \in [20, 100]\, M_\odot$	BNS	*Euclid*−like
Observed number of sources	$10^5 - 10^6$	$7 \cdot 10^4$	$3 \cdot 10^6$
Maximum redshift observed	$\simeq 20$	$\simeq 2 - 3$	$\simeq 2$
Sky fraction observed	Full sky (put in sqdeg)	Full sky	$15000 \mathrm{deg}^2 \simeq 40\%$
Sky localization uncertainty	$> 100 \mathrm{deg}^2$	$\geq 100 \mathrm{deg}^2$	negligible

GW surveys are therefore complementary to galaxy surveys under many different points of view. This is not all: more than using the two as independent probes, each of which finalized to the study of particular topics, the cross−correlation between GW and galaxy surveys will as well be a tool for the cosmological studies First of all, as section 5.1 will describe in more detail, cross−correlations will allow us to associate redshift to gravitational wave events through statistical techniques (see e.g., [296, 297]). Moreover, they provide a way to compare luminosity distance and redshift space distortions. Some studies exist (see e.g., [298, 299]) that show how this will be suitable to perform tests on modified gravity models. Cross−correlations will also be useful to study the GW progenitor formation channels. As we will describe in detail in chapter 6, in fact, astrophysical and primordial black hole binaries have different distributions relatively to galaxies. While we will exploit the implication of this information for GW−only surveys, previous works that proposed this technique adopted it in the context of cross−correlations [117, 300, 301].

The following chapters will present the analyses we carried on in this direction.

RESEARCH WORK

Forecasts for future GW surveys

5

5.1 The dark sirens problem 72
5.2 Modelling observational effects 73
Peculiar velocities 74
Lensing 77
Numerical implementation 78
5.3 Modelling source distribution and bias 80
Merger distribution 80
Merger clustering 82
Supernovae distribution and bias 86
5.4 Forecast analysis 88
Survey specifications . . 88
Fisher matrix formalism 90
Multi-tracer technique . 93
Analysis set-up 94
5.5 Results: First analysis 95
Cosmological parameter constraints 96
Bias parameter constraints 96
5.6 Results: Follow-up analysis 98
Single-tracer analysis . . 99
Multi-tracer analysis . . 100
Effects of using a prior on bias parameters 103

The observation of Gravitational Waves described in chapter 4 opened a new window to study the Universe. As described in chapter 2 and chapter 3, cosmology has so far mainly relied on ElectroMagnetic signals (EM): the possibility we have now to exploit a new kind of measurement represents an unprecedented occasion for researchers in all fields, pledging to provide an incredible amount of data in the years to come. Interesting prospects arise from the idea of analysing GW surveys in the same fashion as galaxy surveys: by studying the statistics of GW as independent but correlated tracers of the large scale structure, would then boost our understanding of the cosmological and astrophysical models describing the formation of GW progenitors.

Despite the fact that LIGO and Virgo interferometers already registered tens of GW events from binary black hole mergers [246, 248, 250, 251, 302], this kind of analysis is still not possible: because of the limited detector horizon, all the events were observed in the very local Universe. With the building of third generation (see section 4.2) ground−based detectors such as the Einstein Telescope [255–257], instead, statistical analysis of GW survey will become reality: not only the sensitivity of these instruments will be higher by an order of magnitude and their horizon will be pushed up to very high distances, but also lower frequency bands will become observable. Despite this, however, the total number of events will still be small with respect to galaxy surveys. It is clear then that a huge effort is required from the scientific community to prepare the ground to analyse these data in the most optimal way.

The study of the clustering of the mergers, in particular, can be used as a tool to study both cosmology and astrophysics. As described in section 3.1.1, dark matter in the Universe was initially smoothly distributed. The fluctuations that arose in its field evolved under their gravitational potentials, and formed the randomly distributed DM halos. As [192] firstly showed, within DM halos galaxies were born: as it was seen in section 3.3 their statistical properties are then derived from the halo distribution itself. Through a slight expansion of this procedure, the distribution of GW events from binary mergers can be used to trace DM as well. Since mergers either happen inside galaxies (if they are of astrophysical origin) or sparse along the LSS (when their progenitors are primordial), they can be used as LSS tracers as well.

In this chapter we focus on GW produced by astrophysical binary mergers, either involving black holes or neutron stars. We present the work we realised to produce some forecast for ET. All the results reported here were published in [2, 3], while the analysis is here presented in more detail. In the next chapter we will instead deal with the possible existence of primordial black hole mergers.

In particular, in section 5.1 we present the problem of dark sirens i.e., binary mergers without electromagnetic counterpart, for which the redshift can not be measured. We describe some possible solutions, among which we decided to focus on the use of luminosity distance space: here, the computation of space distortions and lensing requires some modifications with respect to the standard redshift space.

In section 5.2 we compute a first approximated expression for both of them. In section 5.3 we describe how we modelled the source number distribution and bias we adopted in our analysis. The technique through which we computed the forecasts is described in section 5.4, while our results are presented in section 5.5 and section 5.6. In the former section we perform a first analysis to understand the capability of ET and other, more advanced, detector configurations in constraining cosmological and bias parameters. In the latter, we improve the analysis over several points, the most important of which is the implementation of a multi−tracer technique involving supernovae IA.

5.1 The dark sirens problem

As discussed in chapter 4, binary mergers of compact objects will become a powerful tool to study cosmology thanks to their property of being **standard sirens** [284, 290]. This means that the distance from the source to the observer can be estimated relying only on the model of the GW waveform, without the need of calibrations. When working in the framework of general relativity, the distance measured from the GW source is analogous to the luminosity distance defined in eq. (2.18). In this case, even if it is measured differently, luminosity distance represents the same coordinate for both GW events and electromagnetic tracers, such as galaxies or supernovae. In some scenarios involving dark energy or modified gravity, this is no longer true: the luminosity distance estimated from the gravitational wave signal D_L^{GW} turns out to be different from the electromagnetic one D_L^{EM}, both in the background (see e.g., [303, 304]) and when considering fluctuations (compare with [305, 306]). The radial coordinates D_L^{GW} and D_L^{EM} in these frameworks therefore differ one from the other and the combination of the two should constrain dark energy or modified gravity models (see e.g., [307]). In the following, I will always assume GR as the framework where both GW and EM surveys are analysed.

Despite the great potential, particularly to measure H_0 (see e.g., the pioneering work of [25] and the recent measurements by [26, 308]), the use of standard sirens presents a huge drawback: while luminosity distance can be directly estimated from the GW, this is not the case for the redshift. Redshift, as described in chapter 2 and chapter 3, is the standard coordinate used to map cosmological surveys: when studying low z EM surveys, it can be simply derived from the galaxy emission spectrum and it is easily related to cosmology through the Hubble law in eq. (2.3). When considering mergers that produce GWs, instead, redshift is not a direct observable.

As described in chapter 4, in the case of neutron star mergers, if an EM counterpart is identified, the redshift can be estimated from its emission. This, however, happened only once so far. Other two binary neutron star mergers were confirmed [302] but no EM counterpart was identified.

This technique can not be used for black hole mergers, since it is difficult that an EM signal would be emitted[1] : for this reason, binary black hole mergers are also called **dark sirens**. Other techniques then need to be developed if one wants to associate a redshift to the GW event. The first is to identify the **host galaxy** where the merger took place. The direct match between the GW emission and the galaxy is not straightforward: as described in chapter 4, sky localization for GW interferometers is very poor if less than three detectors are considered. Even in that cases, the uncertainty can difficultly be lower than $\simeq 5-10\mathrm{deg}^2$: in such large

[1] 1: EM signals in this case require the presence of gas. Currently, there are no confirmed detections for binary black hole counterparts; some possible candidates related with accretion disks of active galactic nuclei (AGN) are reported in [309].

patches, many galaxies can be found. Each of them resides at different redshift: understanding which is the one that hosts the merger usually requires to apply statistical techniques related with the probability distribution of the merger (see e.g., [310]). When performing statistical analyses of GW events, however, the knowledge of the redshift of each merger is not crucial. Cross−correlations between GW surveys and galaxy survey, in this case, can *solve* the problem of dark sirens through statistical techniques as e.g., the authors of [296, 297] show. This however introduce uncertainties related to the formation process and degeneracies with cosmological parameters.

Another interesting application of cross−correlation techniques in this field is the so called **clustering−based redshift method**. This was first developed in [311–313] for photometric and continuum radio surveys, in which the redshift of the sources is unknown. It is based on the computation of the angular cross−spectrum (defined in eq. (3.46)) between this sample with unknown redshift and a survey where the redshift distribution is well measured (e.g., a spectroscopic galaxy survey). Let us assume that the *known−redshift* sample is unbiased with respect to the *unknown−redshift* one and that all the sources of the latter are located at the same redshift $\bar{z}$. In this case, it is possible to split into redshift bins $[z_i, z_i + dz]$ the *known−redshift* sample; the *unknown−redshift* source distribution dN/dz will therefore be directly related with the amplitude of the cross−signal in the different z bins [311]. In fact, the correlation will be higher in the bin in which $\bar{z} \in [z_i^*, z_i^* + dz]$: the *unknown−redshift* sample will therefore be associated to this redshift. This method can be generalized to surveys with wider redshift distribution [311–313]; however, if the two samples are not completely unbiased one from another, the redshift estimate becomes degenerate with the bias, limiting therefore the possibility of constraining the cosmological parameters through the analysis of the *unknown−redshift* survey.

The solution to the dark siren problem can be found also by following an alternative approach, independent from both external datasets or statistical techniques. Instead of matching the GW events with some redshift, in fact, it is possible to map them using luminosity distances only [2, 3, 298, 314, 315]. A fully consistent analysis can then be realized in Luminosity Distance Space (LDS).

LDS can be used also for EM sources that are standard candles, such as supernovae IA (see section 3.3). Therefore, in LDS[2] both GW and supernovae survey can be mapped: the two can be studied independently or cross−correlated in a multi−tracer fashion. This, as it will be described in section 5.4.3, improves the capability of this kind of studies in constraining both cosmological and bias parameters.

If we want to perform a tomographic study using angular power spectra, the transition from redshift space to LDS requires however to recompute how observed positions are affected by the matter content of the Universe i.e., the redshift space distortions we defined in section 3.2.1. Calculations of perturbation effects on GW are shown in e.g., [316], and a fully detailed investigation of GW clustering in LDS is still under study [317]. In our works we relied on the first analysis for peculiar velocities and lensing available in [298, 315]: these are presented in section 5.2.1.

5.2 Modelling observational effects

When using LDS instead of redshift space, the mapping between the intrinsic density field and the observed one introduced in eq. (3.47) gets modified. Large

[2] In the GR framework, $D_L^{EM} = D_L^{GW}$ i.e., the luminosity distance coordinate is analogous for the two types of signals. In modify gravity frameworks it is possible to break this equality: in that case, the radial coordinate in LDS defined in the case of EM or GW signals differ. However, by knowing the gravity model, it is possible to re−map one survey with respect to the other so to make the analysis self−consistent.

scale structures induce a perturbation ϵ on the luminosity distance, defined at leading order as follows (compare with [318, 319]):

$$\frac{\bar{D}_L + \delta D_L}{\bar{D}_L} = 1 + \epsilon = 1 + 2v + \dots \,, \tag{5.1}$$

where $\bar{D}_L$ is the background, unperturbed luminosity distance, δD_L is the induced perturbation, v is the radial velocity of the source along the line of sight. [315] adds to eq. (5.1) a term to describe the lensing effect: this enters as $-\kappa$, the convergence defined in eq. (3.64). In the perturbed FLRW Universe described through GR, [316] shows that other terms should be take into account. These are the Sachs−Wolfe (SW), the Integrated Sachs−Wolfe (ISW) and the Shapiro time delay effect, already described in section 3.2.1. Moreover, since future GW survey will observe large portions of the sky, wide angle effects [185–187] should be taken into account as well. However, we decided to neglect these contribution and to only rely on the peculiar velocity and lensing effect as modelled respectively in [298] and in [315] and to implement them into the publicly−available code `CAMB` [165]. In particular, in [2] we only included the effect of peculiar velocities in the computation of the angular power spectra: this was motivated by the fact that (as discussed for example in [298]) peculiar velocities were expected to be the dominant source of distortion. After our analysis was completed, the lensing contribution was explicitly computed in [315], showing that, while indeed subdominant, such contribution is not negligible on large scales: for this reason, we included it in the follow−up paper [3].

The peculiar velocity and lensing effects are summarized in section 5.2.1 and section 5.2.2.

5.2.1 Peculiar velocities

The way peculiar velocities affect the observed position in LDS is slightly different with respect to redshift space. In the general relativity framework, however, the positions of a GW source and of an EM source should be altered analogously: for this reason, in the following we refer to light to derive the peculiar velocity contribution to luminosity distance space distortions.

The term $+2v$ in eq. (5.1) is found by considering that the D_L perturbation suffers both of the change in the observed position and of the relativistic light aberration (see e.g., [320]). To get the full expression, D_L shall be related with the angular distance D_A through eq. (2.18) and eq. (2.19):

$$D_L = (1+z)^2 D_A \,. \tag{5.2}$$

Here both z and D_A are affected by peculiar velocities. The first is found by perturbing the redshift measurement as:

$$(1 + z_{obs}) = (1 + \bar{z})(1 + z_{pec}) \,, \tag{5.3}$$

where z_{obs} is the observed redshift (i.e., the perturbed one), $\bar{z}$ the background redshift in real space and:

$$z_{pec} = (\boldsymbol{v}_e - \boldsymbol{v}_o) \cdot \hat{\boldsymbol{n}} \,, \tag{5.4}$$

being $\boldsymbol{v}_e$ the source peculiar velocity, $\boldsymbol{v}_o$ the observer velocity and $\hat{\boldsymbol{n}}$ the LoS direction. The second effect instead, is calculated by considering that the source has emitting surface δA_e and it is observed under a solid angle $\delta\Omega$. The relative D_A turns out to be:

$$D_A = \sqrt{\frac{\delta A_e}{\delta\Omega}}\ . \tag{5.5}$$

Thus, the peculiar velocity of the observer induces an aberration in the emitted light, modifying the measured D_A as:

$$D_A^{obs} = \bar{D}_A(1 - 2\boldsymbol{v}_o \cdot \hat{\boldsymbol{n}})^{-1/2} \simeq \bar{D}_A(1 + \boldsymbol{v}_o \cdot \hat{\boldsymbol{n}}), \tag{5.6}$$

where $\bar{D}_A$ is the background angular distance. Eq. (5.3), eq. (5.4) and eq. (5.6) can be substituted into eq. (5.2), resulting in:

$$D_L^{obs} = (1 + \bar{z})^2[1 + (\boldsymbol{v}_e - \boldsymbol{v}_o) \cdot \hat{\boldsymbol{n}}]^2 \bar{D}_A(1 + \boldsymbol{v}_o \cdot \hat{\boldsymbol{n}})\ . \tag{5.7}$$

At first order, this leads to

$$\begin{aligned} D_L^{obs} &\simeq (1 + \bar{z})^2 \bar{D}_A(1 + 2\boldsymbol{v}_e \cdot \hat{\boldsymbol{n}} - \boldsymbol{v}_o \cdot \hat{\boldsymbol{n}}) \\ &\simeq (1 + \bar{z})^2 \bar{D}_A(1 + 2\boldsymbol{v}_e \cdot \hat{\boldsymbol{n}})\ , \end{aligned} \tag{5.8}$$

where in the last equality $\boldsymbol{v}_o$ is neglected. Therefore, it holds:

$$D_L^{obs} = \bar{D}_L(1 + 2\boldsymbol{v}_e \cdot \hat{\boldsymbol{n}})\ , \tag{5.9}$$

and eq. (5.1) is recovered if only peculiar velocities are considered.

Eq. (5.9) is used by [298] to describe the LDS distortions. They can be calculated following the standard procedure used to get the redshift space distortions in [163]. In the plane−parallel approximation defined in eq. (3.2.1), we define:

$$\boldsymbol{v}_e \cdot \hat{\boldsymbol{n}} = \mu v_e. \tag{5.10}$$

The association between background coordinates in real space and perturbed, observed coordinates in LDS can be finally made using the comoving distance space from eq. (2.15), through which it holds $\chi(D_L^{obs}) = aD_L^{obs} = a\bar{D}_L + a\delta D_L$. Considering eq. (5.9) and substituting the approximation from eq. (5.10), it holds:

$$\chi^{obs} = a\bar{D}_L(1 + 2\mu v) = \chi + \delta\chi\ , \tag{5.11}$$

where $[\chi,\ \chi^{obs}] = [\chi(\bar{D}_L),\ \chi(D_L^{obs})]$ are computed by inverting eq. (2.18). Therefore, eq. (5.11) can be rewritten as:

$$\begin{aligned} \chi^{obs} &= \chi(\bar{D}_L + \delta D_L) = \chi + \left.\frac{\partial\chi^{obs}}{\partial D_L^{obs}}\right|_{\bar{D}_L} \delta D_L \\ &= \chi + \frac{\partial\chi^{obs}}{\partial z}\left.\left(\frac{\partial D_L^{obs}}{\partial z}\right)^{-1}\right|_{\bar{D}_L} \delta D_L. \end{aligned} \tag{5.12}$$

Writing δD_L explicitly and considering that in a flat Universe $\delta\chi^{obs}/\delta z \simeq \delta\chi/\delta z = 1/H(z)$, eq. (5.12) becomes:

$$\begin{aligned} \chi^{obs} &= \chi + \frac{1}{H(z)}\left.\left(\frac{\partial D_L^{obs}}{\partial z}\right)^{-1}\right|_{\bar{D}_L} 2\mu v\bar{D}_L \\ &= \chi + \left[2\bar{D}_L\left(\frac{\partial\bar{D}_L}{\partial z}\right)^{-1}\right]\frac{\boldsymbol{v}_e \cdot \hat{\boldsymbol{n}}}{H(z)}. \end{aligned} \tag{5.13}$$

When the low redshift limit $H(z) \simeq H_0$ is considered, eq. (5.13) is identical in the structure to the redshift version of the peculiar velocity effect introduced in eq. (3.48); the only difference between the two is the pre−factor between square brackets. In the limit of the approximations used in this section, the Jacobian[3] of the transformation from $\chi(D_L^{obs})$ to $\chi = a\bar{D}_L$ depends on the same pre−factor multiplied by a. Therefore:

[3] The Jacobian is defined as the vector containing the derivatives with respect to all the directions.

$$\begin{aligned} J &= \left[\frac{z}{z + f_{D_L}(\boldsymbol{v_e}\cdot\hat{\boldsymbol{n}})/H(z)}\right]^2 \left[1 + f_{D_L}\frac{\partial}{\partial z}\left(\frac{\boldsymbol{v}\cdot\hat{\boldsymbol{n}}}{H(z)}\right)\right]^{-1} \\ &\simeq \left[1 + f_{D_L}\frac{\boldsymbol{v_e}\cdot\hat{\boldsymbol{n}}}{zH(z)}\right]^{-2}\left[1 - \frac{f_{D_L}}{H(z)}\frac{\partial(\boldsymbol{v}\cdot\hat{\boldsymbol{n}})}{\partial z} - f_{D_L}(\boldsymbol{v}\cdot\hat{\boldsymbol{n}})\frac{\partial H(z)^{-1}}{\partial z}\right] \\ &\simeq \left[1 + f_{D_L}\frac{\boldsymbol{v_e}\cdot\hat{\boldsymbol{n}}}{zH(z)}\right]^{-2}\left[1 - \frac{f_{D_L}}{H(z)}\frac{\partial(\boldsymbol{v_e}\cdot\hat{\boldsymbol{n}})}{\partial z} - \frac{f_{D_L}(\boldsymbol{v_e}\cdot\hat{\boldsymbol{n}})}{H(z)^2}\right] \\ J &\simeq 1 - f_{D_L}\frac{\partial}{\partial z}\left(\frac{\boldsymbol{v_e}\cdot\hat{\boldsymbol{n}}}{H(z)}\right) \end{aligned} \tag{5.14}$$

In the previous equation, we defined:

$$f_{D_L} = \frac{2\bar{D}_L}{1+z}\left(\frac{\partial\bar{D}_L}{\partial z}\right)^{-1}, \tag{5.15}$$

which is analogous to the one described by [298], where it is indicated as leading order term of the LDS distortions. The factor f_{D_L} is showed in figure 5.1 and it depends on the distance from the observer: through f_{D_L}, LDS distortions are enhanced with respect to redshift space distortions at $z \gtrsim 1.7$, while they become smaller than redshift space distortions at $z \lesssim 1.7$; due to this pre−factor, LDS distortions are also vanishing as $z \longrightarrow 0$.

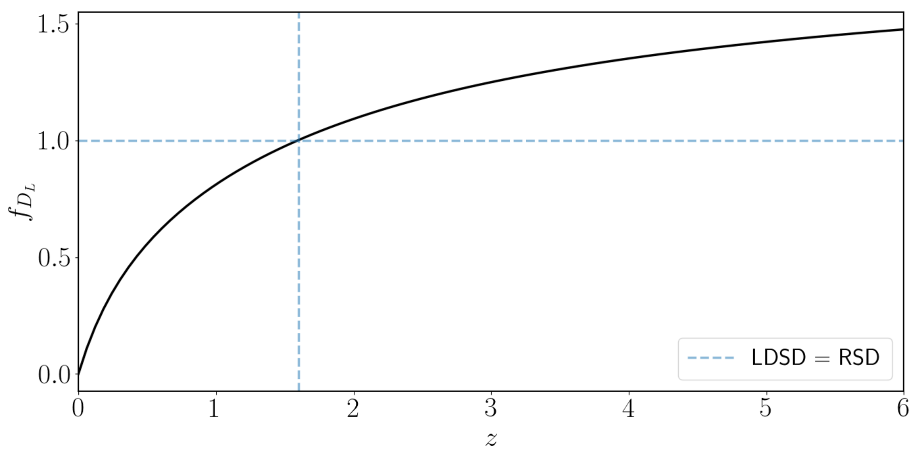

Figure 5.1: f_{D_L} factor computed in eq. (5.15) assuming the fiducial cosmology from [13] and summarized in table 2.1. The dotted lines indicate the point in which LDS distortions are equivalent to redshift space distortions.

Eq. (5.13) can be used to recompute in LDS the density perturbation as it was done in the case of redshift space in section 3.2.1. The conversion from redshift space to LDS only change the value of the factor f defined in eq. (3.54) it turns out to be converted into $f_1 = f \cdot f_{D_L}$, with f_{D_L} from eq. (5.15) [298].

5.2.2 Lensing

The lensing term in LDS is relevant even at low z [316, 321]. As a first implementation, I modelled it following [315] and rewriting the transformation of the comoving distance as:

$$\chi^{obs} = \chi + \frac{\partial \chi}{\partial D_L} \delta D_L = \chi + \frac{\partial \chi}{\partial D_L} D_L \epsilon \ , \tag{5.16}$$

where ϵ is the D_L perturbation defined in eq. (5.1), to which the lensing contribution $-\kappa$ was added to follow the same procedure as in [315]. The comoving distance χ^{obs} can be as well expressed as the perturbed quantity $\chi^{obs} = \chi(1+\epsilon^{\chi})$, where from eq. (5.16):

$$\begin{aligned} \epsilon^{\chi} &= \frac{\partial \chi}{\partial D_L} \frac{D_L}{\chi} \epsilon = \left[\left(\chi + (1+z) \frac{\partial \chi}{\partial z} \right) \left(\frac{\partial \chi}{\partial z} \right)^{-1} \right]^{-1} \frac{\epsilon}{a} \\ &= \left(\chi + \frac{1}{aH} \right)^{-1} \frac{1}{H} \frac{\epsilon}{a} = \frac{\epsilon}{1+r_H} \ , \end{aligned} \tag{5.17}$$

and $r_H = Ha\chi$. Therefore, $\chi^{obs} = \chi[1 + 1/(1+r_H)]$. By applying the number conservation to the source mean number density $n(\chi)$ in analogy to the standard approach described in section 3.2.1 [163], one gets:

$$\begin{aligned} (1+\delta^{obs}) &= (1+\delta) \frac{n(\chi)}{n(\chi + \epsilon^{\chi}\chi)} \left(\frac{d^3 \chi^{obs}}{d^3 \chi} \right)^{-1} \\ &= (1+\delta) \frac{n(\chi)}{n(\chi) + \epsilon^{\chi} \chi \, \partial n / \partial \chi} \left(\frac{\chi^{obs}}{\chi} \right)^{-2} \left(\frac{\partial}{\partial \chi} (\chi + \chi \epsilon^{\chi}) \right)^{-1} \\ &\simeq (1+\delta) \left(1 - \epsilon^{\chi} \frac{d \ln n}{d \ln \chi} - 3\epsilon^{\chi} - \chi \frac{d\epsilon^{\chi}}{d\chi} \right) \end{aligned} \tag{5.18}$$

Therefore:

$$\begin{aligned} \delta^{obs} &= \delta - \epsilon^{\chi} \left(\frac{d \ln n}{d \ln \chi} + 3 \right) - \chi \frac{d\epsilon^{\chi}}{d\chi} \\ &= \delta - \frac{\epsilon}{1+r_H} \left(\frac{d \ln n}{d \ln \chi} + 3 - \frac{f_{DL}}{2} + \frac{\chi^2 (Ha)^2}{1+r_H} \frac{(Ha)_{,\tau}}{(Ha)^2} \right) - \frac{\chi Ha}{1 + r_H Ha} \frac{d\epsilon}{d\chi} \ , \end{aligned} \tag{5.19}$$

and, by substituting the relation $\epsilon = 1 + 2\boldsymbol{v} \cdot \hat{\boldsymbol{n}} - \kappa$ (where we modified eq. (5.1) with the convergence term as in [315]), then:

$$\begin{aligned} \delta^{obs} &= \delta - \left(\alpha + \frac{f_{D_L}}{2Ha} \right) (1 + 2\boldsymbol{v} \cdot \hat{\boldsymbol{n}} - \kappa) \\ &= \delta - 2\alpha v - \frac{f_{D_L}}{Ha} \frac{dv}{d\chi} + \left(\alpha + \frac{f_{D_L}}{2Ha} \frac{d}{d\chi} \right) \kappa \ . \end{aligned} \tag{5.20}$$

In the previous equation, f_{D_L} is the same as in eq. (5.15), while:

$$\alpha = \frac{1}{1+r_H} \left(\frac{d \ln n}{d \ln \chi} + 3 - \frac{f_{D_L}}{2} + \frac{f_{D_L}}{2(Ha)^2} (Ha)_{,\tau} \right) , \tag{5.21}$$

which depends to the choice made for the source mean number density $n(\chi)$ and its evolution $d \ln n / d \ln \chi$.

Figure 5.2 shows the values of α computed for the source distributions described in section 5.3, which slightly differ from those in [315], because of the different comoving number densities used.

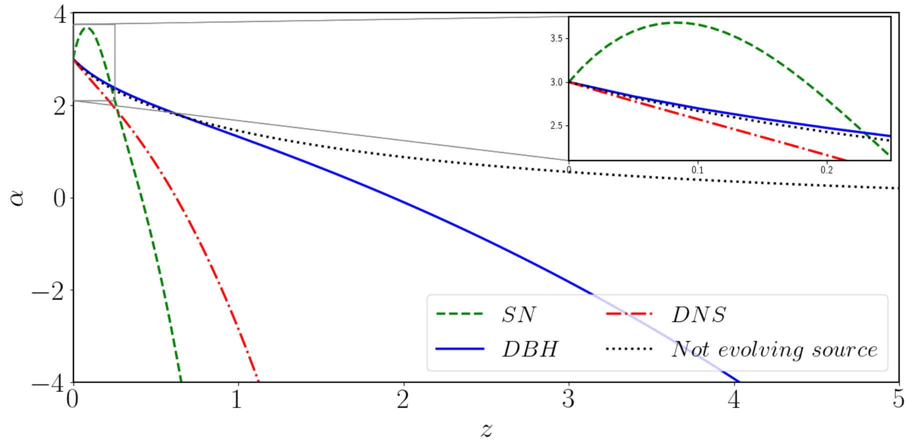

Figure 5.2: α computed using eq. (5.21). Each curve assumes a different evolution of $n(\chi)$. By referring to section 5.3, the green dashed line is related to the distribution of supernovae, the red dot−dashed to binary neutron stars and the continuous blue line to binary black holes. The black dotted line instead is associated to non−evolving sources, for which $d \ln n_i / d \ln \chi = 0$. In the case $z = 0$, all the distributions consider $\alpha = 3$: this directly follows from the number conservation of sources between LDS and real space.

In [315], the lensing contribution to LDS distortions is computed by including in the integration kernel both the term in eq. (5.21) and the standard term -2κ, due to the lensing distortion of the angular position. Both these terms, together with the peculiar velocity contribution described in section 5.2.1, alter the observed density fluctuations δ_{LDS} with respect to the intrinsic ones δ. Naming δ^{v}_{LDS} and δ^{κ}_{LDS} the peculiar velocity and lensing distortions on δ, the observed density fluctuations can be described as:

$$\begin{aligned}\delta_{LDS} &= \delta + \delta^{v}_{LDS} + \delta^{\kappa}_{LDS} \\ &= \delta - 2\alpha v - \frac{f_{D_L}}{aH}\frac{dv}{d\chi} + \left(-2 + \alpha + \frac{f_{D_L}}{2aH}\frac{d}{d\chi}\right)\kappa \,.\end{aligned} \tag{5.22}$$

Eq. (5.22) is the same as the one originally derived in [315], where $\gamma = f_{D_L}/2$ is used. The lensing contribution of [315] to the overdensity can then be written as:

$$\delta^{\kappa}_{LDS} = \int_0^{\infty} d\chi' w(\chi, \chi') \nabla^2_{\hat{\boldsymbol{n}}}\, \psi[\tau', \hat{\boldsymbol{n}}\chi'] \,, \tag{5.23}$$

where the lensing kernel $w(\chi, \chi')$ is computed using eq. (3.64), its derivative and eq. (5.22):

$$w(\chi, \chi') = \frac{\chi'}{\chi}\left[(-2 + \alpha)(\chi - \chi') + \frac{f_{D_L}}{2aH}\frac{\chi'}{\chi}\right] . \tag{5.24}$$

This expression differs from that of the redshift space kernel defined in eq. (3.64), which is $w(\chi, \chi') = (-2 + 5s_*)(\chi - \chi')\chi'/\chi$ (compare with [165]). In particular, the f_{DL} and α terms in eq. (5.15) and eq. (5.21) introduce the dependence on the distance from the observer, on the lensing convergence derivative along the LoS and on the source mean number density $n(\chi)$. Moreover, the magnification bias, s_*, is not included: this term is neglected in [315], and I decided to keep its formulation at this level.

5.2.3 Numerical implementation

LDS distortions can be formally treated as redshift space distortions, once the corrections described in sections 5.2.1 and 5.2.2 are properly taken into account.

These modify the transfer function defined in section 2.2.2: in particular, in the case of peculiar velocity effects, each term including v_k in $\Delta_l(z,k)$ inherits the factor f_{D_L} from eq. (5.15). In the case of lensing, as described in [315], the correction comes from the lensing kernel from eq. (5.24).

These corrections have been implemented in the public code `CAMB` [165]. When calculating the spectra in redshift space, the original code relies on the integrated version of the expressions in eq. (3.59) and eq. (3.69), which all depend on the spherical Bessel function $j_l(k\chi)$ and not on its derivatives. The conversion to LDS is made by considering a sufficiently fine distance binning of the data: in this case, without loss of accuracy, inside each bin it is possible to neglect the χ dependence of f_{D_L}. By doing so, `CAMB` built−in expressions are simply multiplied by f_{D_L}, which is computed through eq. (5.15) in the centre of the bin. Analogously, the lensing kernel in LDS is implemented in place of the original one.

Figure 5.3 shows the resulting contribution of peculiar velocity and lensing to LDS distortions, with respect to the intrinsic overdensity, in the case of low and high distances. The shift in the lensing term when moving from redshift to LDS is bigger than the shift in the peculiar velocity case, as figure 5.4 shows; however, the lensing term still remains subdominant in LDS.

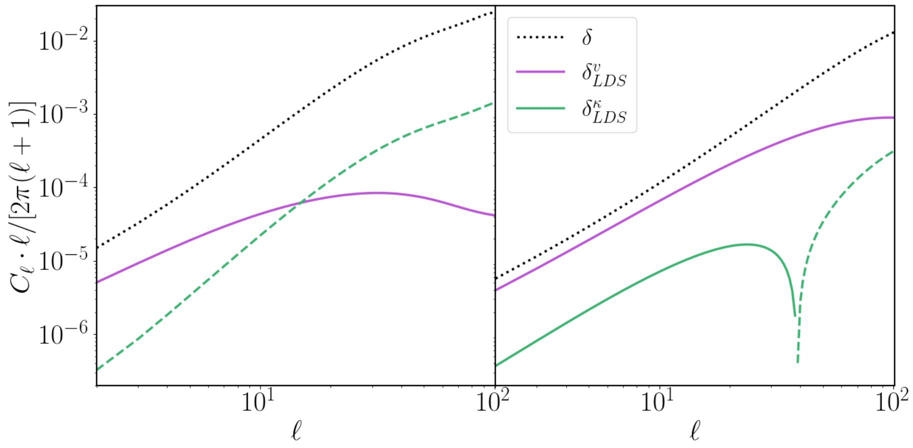

Figure 5.3: Overdensity (black dotted), LDS distortions due to peculiar velocities (purple) and lensing (green) contribution to the C_l when Limber is not considered. Dashed lines are used for negative contributions. The left plot refers to low redshift $z \in [0.6, 0.8]$, while the right one to high redshift $z \in [2.6, 2.8]$. All the curves refer to the binary black hole distribution described in section 5.3.

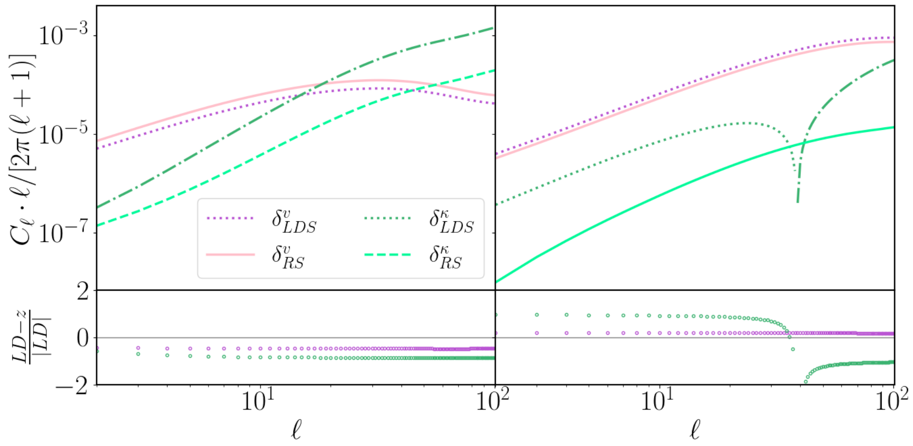

Figure 5.4: Comparison between peculiar velocities distortions in LDS (purple dotted) and redshift space (pink) and between lensing in LDS (green dotted) and redshift space (light green); dashed or dot−dashed lines are used for negative contributions. On the left, the binary black hole distribution from section 5.3 at low redshift $z \in [0.6, 0.8]$ is considered, while on the right the same at $z \in [2.6, 2.8]$ is used. The lower plots show the residuals relative to the absolute values of quantities in LDS.

5.3 Modelling source distribution and bias

The analysis performed in [2, 3] is based on the study of the clustering in LDS. To perform it, both the number distribution depending on the distance[4] and the bias with respect to the underlying smooth DM distribution need to be modelled. The following sections describe how these were found for gravitational waves from binary mergers and supernovae.

5.3.1 Merger distribution

To study the clustering of GW merger events, both their number distribution in redshift[5] and their bias with respect to the underlying smooth DM distribution need to be modelled. To do so, simulations of binary compact object mergers[6] from [204, 205, 322] are considered: these are run inside a box having comoving side $L = 25\,\mathrm{Mpc}$, which is evolved across cosmic time.

Here, galaxies from the EAGLE cosmological simulation [206, 207] are seeded with binary compact objects from population−synthesis simulations obtained with MOBSE [323, 324]. Further detail about the simulations are given in chapter 7. We adopted the number distribution extracted from the simulations for mergers of Binary Neutron Stars (BNS), Binary Black Holes (BBH) and Black Hole Neutron Star systems (BHNS; these have been analysed, but since their results are intermediate between BNS and BBH for the clarity of the text we decided to not report them). depending on the redshift z, the stellar mass M_* and the Star Formation Rate SFR of the host galaxy. The metallicity[7] dependence is present in the simulation, but it is marginalised over at the beginning of the analysis.

Table 5.1, and table 5.2 respectively describe the 22 redshift snapshot in which the simulations has been run and the $[M_*, SFR]$ bins in which the host galaxies of the mergers are divided. The number of events in each snapshot does not take place at a very fixed redshift, but within $[z - \delta z, z + \delta z] = T^{SIM}$. Each snapshot is associated with a different interval; all of them are reported in table 5.1 in units of time. From the simulations, two distributions have been extracted: the intrinsic one and the one reduced by including observational effects from the Einstein Telescope.

Table 5.1: Redshift and time duration T^{SIM} $[Gyr]$ of the snapshots from which simulated data are extracted. The snapshots $z = 2.22 \cdot 10^{-16}$ and $z = 0.1$ are considered together in the analysis.

z	T^{SIM} [Gyr]	z	T^{SIM} [Gyr]	z	T^{SIM} [Gyr]	z	T^{SIM} [Gyr]
$2.22 \cdot 10^{-16}$	0.676	0.61	0.737	1.74	0.525	3.98	0.223
0.10	1.161	0.73	0.685	2.00	0.409	4.49	0.194
0.18	0.947	0.86	0.634	2.24	0.312	5.04	0.150
0.27	0.902	1.00	0.757	2.48	0.402	5.49	0.113
0.37	0.987	1.26	0.770	3.02	0.429	6.00	0.145
0.50	0.930	1.49	0.596	3.53	0.294		

Figure 5.5 and figure 5.6 report some examples of the ET−selected distributions extracted from the simulation. In particular, figure 5.5 shows that at lower z host galaxies with smaller M_* can host an higher number of binary black hole mergers. Figure figure 5.6 shows instead that galaxies with higher SFR hosts more mergers.

[4] Even if the analysis is preformed in luminosity distance space, we will often refer to redshift, since it is the quantity commonly used in cosmological studies. If not explicitly specified, the conversion between z and D_L is done through eq. (2.18) in the fiducial cosmology table 2.1.

[5] Even if the analysis is preformed in luminosity distance space, we will usually refer to redshift, since it is the quantity commonly used in cosmological studies. If not explicitly specified, the conversion between z and D_L is done through eq. (2.18) in the fiducial cosmology table 2.1.

[6] When talking about distributions, we will refer to binary compact object merger or GW event interchangeably, since the former trigger the latter.

[7] The metallicity describes how abundant metal elements are with respect to the Hydrogen content of the galaxy.

Table 5.2: Stellar mass M_* $[M_\odot]$ and star formation rate (SFR $[M_\odot\ yr^{-1}]$) bins in which the galaxies hosting the mergers are divided.

$\log M_*$ bins	$\log M_*$ bins	$\log M_*$ bins	$\log SFR$ bins	$\log SFR$ bins	$\log SFR$ bins
$7.00, 7.33$	$7.33, 7.67$	$7.67, 8.00$	$-5.50, -4.97$	$-4.97, -4, 43$	$-4.43, -3.90$
$8.00, 8.33$	$8.33, 8.67$	$8.67, 9.00$	$-3.90, -3.37$	$-3.37, -2.83$	$-2.83, -2.30$
$9.00, 9.33$	$9.33, 9.67$	$9.67, 10.0$	$-2.30, -1.77$	$-1.77, -1.23$	$-1.23, -0.70$
$10.0, 10.3$	$10.3, 10.7$	$10.7, 11.0$	$-0.70, -0.17$	$-0.17, 0.37$	$0.37, 0.90$
$11.0, 11.3$	$11.3, 11.7$	$11.7, 12.0$	$0.90, 1.43$	$1.43, 1.97$	$1.97, 2.50$

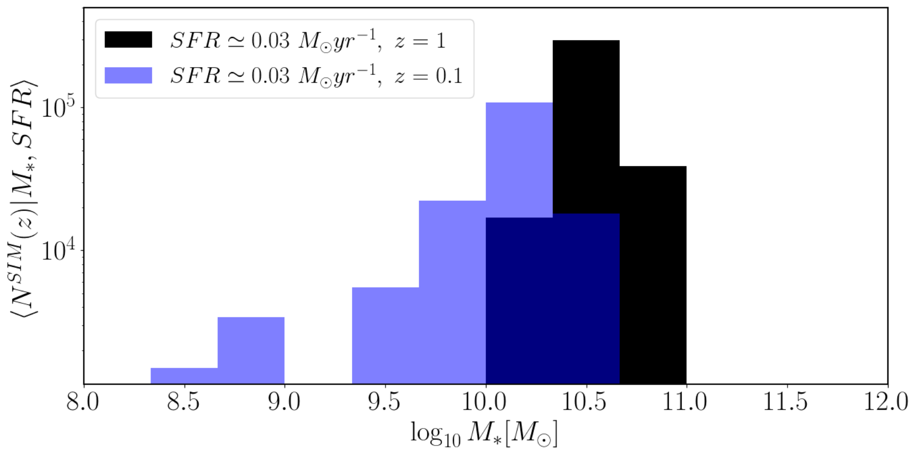

Figure 5.5: Number of ET−selected binary black hole mergers extracted from the simulations in function of M_*. The bin in SFR is fixed (the value in the legend indicates the mean in the bin), while z is varied. The transparency in the blue distribution allows to see where the distributions overlap.

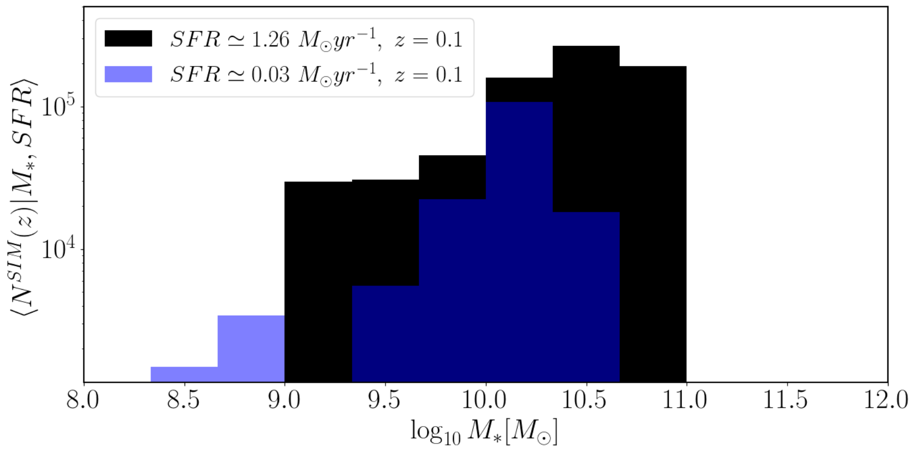

Figure 5.6: Number of ET−selected binary black hole mergers extracted from the simulations in function of M_*. The bin in z is fixed, while SFR (the value in the legend indicates the mean in the bin) is varied. The transparency in the blue distribution allows to see where the distributions overlap.

For each merger type m = BNS, BBH, BHNS, the distribution extracted from the simulation is indicated as $\langle N_m^{SIM}(z)|M_*^{bin}, SFR\rangle$ since it represents the expected value of the probability distribution of having N_m^{SIM} mergers inside an host galaxy described by M_*, SFR at a certain z. All the distributions are marginalized over M_* and SFR: thanks to the bin discretization, this can be simply done setting:

$$N_m^{SIM}(z) = \sum_{M_*} \sum_{SFR} \langle N^{SIM}(z)|M_*^{bin}, SFR\rangle \,. \tag{5.25}$$

$N^{SIM}(z)$ indicates the number of binaries that merge inside the box comoving volume $V^{SIM} = L^3$ in certain time interval $T^{SIM}(z)$ (see table 5.1). Therefore, the merger rate of these events can be found as $N^{SIM}(z)/T^{SIM}(z)$. This can then be transformed into detection rate by converting the clock in the source rest frame into the clock in the observer one. The conversion in made through:

$$\frac{dt^{SIM}}{dt^{OBS}} = \frac{1}{1+z}. \tag{5.26}$$

Therefore it holds:

$$N_m(z) = T^{OBS}\,\frac{N_m^{SIM}(z)}{T^{SIM}(z)}\,\frac{dt^{SIM}}{dt^{OBS}} = T^{OBS}\,\frac{N_m^{SIM}(z)}{T^{SIM}(z)}\,\frac{1}{1+z}\,, \tag{5.27}$$

where T^{OBS} is the survey duration expressed in years. The same conversion can be done before the marginalization is performed i.e., over $\langle N_m^{SIM}(z)|M_*^{bin}, SFR\rangle$:

$$\langle N_m(z)|M_*^{bin}, SFR\rangle = \frac{T^{OBS}}{T^{SIM}(z)}\,\frac{\langle N_m^{SIM}(z)|M_*^{bin}, SFR\rangle}{1+z}\,. \tag{5.28}$$

The merger number distribution from eq. (5.27) is converted into number density observed per redshift bin per solid angle $d^2N_m/dzd\Omega$. To do so, the side of the simulated box L has to be projected at each redshift both on the LoS and on its perpendicular direction. This is done by setting:

$$\Delta z = L\frac{H(z)}{c}\,, \qquad \Delta\Omega_{box} = \left(\frac{L}{D_A(z)}\right)^2 = \left(\frac{L}{D_L(z)/(1+z)^2}\right)^2 \tag{5.29}$$

where $D_A(z)$ is the angular distance from eq. (2.19) and c the speed of light. Thus, the merger number density is:

$$\frac{d^2N_m}{dzd\Omega} = N_m(z)\frac{c}{LH(z)}\left(\frac{D_L(z)}{L(1+z)^2}\right)^2. \tag{5.30}$$

The values of $d^2N_m/dzd\Omega$ are computed in the 22 snapshots of the simulation and then interpolated through the skewed Gaussian:

$$\frac{d^2N_m}{dzd\Omega} = 2\left[A\exp\left(-\frac{(z-\bar{z})^2}{2\,\sigma^2}\right)\right]\left[\frac{1}{2}\left(1+\mathrm{erf}\left(\frac{\alpha(z-\bar{z})}{\sigma^2\sqrt{2}}\right)\right)\right], \tag{5.31}$$

finding $A = 10^{3.22}, \bar{z} = 0.37, \sigma^2 = 1.42, \alpha = 5.48$ if m = BBH, while $A = 10^{3.07}, \bar{z} = 0.19, \sigma^2 = 0.15, \alpha = 0.8$ if m = BNS. The distributions founds are in agreement with results from [325], keeping into account that the observational ET selection function produces a stronger decrease, in our case, in the number of BNS compared to BBH.

The observed number density is reported in figure 5.7; a 3 yr observation run is assumed.

5.3.2 Merger clustering

Section 3.1.1 and section 3.3 introduced the idea that GW surveys observing astrophysical binary mergers can be statistically described in relation to the host galaxy distribution and, consequently, they can be related to the underlying DM halos and to the DM field. For this reason, the bias of the binary merger distribution can be computed analogously to the galaxy bias, by relying on the HOD based approach defined in section 3.3.

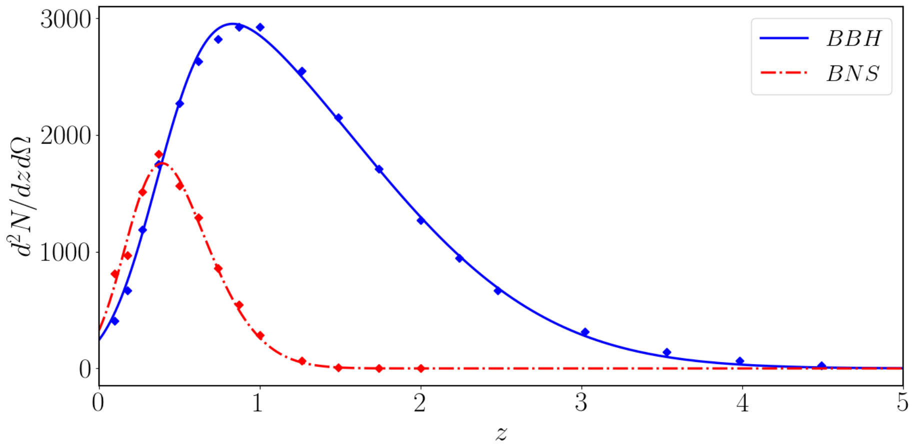

Figure 5.7: Merger number distribution $dN^2/dzd\Omega$; the dots are data computed in the simulated snapshots, while the line is interpolated through eq. (5.31). A 3 yr observation run with ET is assumed. The total number of sources integrated in dz and $d\Omega$ is $10^{4.14}$ for BNS (red, dot dashed line), $10^{4.79}$ for BBH (blue, continuous line).

We express therefore the merger bias as:

$$b_m(z) = \int_{M_*^{min}}^{M_*^{max}} dM_* \int_{SFR^{min}}^{SFR^{max}} dSFR\, n_g(z, M_*, SFR)\, b_g(z, M_*, SFR) \frac{\langle N_m(z)|M_*, SFR\rangle}{n_m(z)} . \tag{5.32}$$

where M_*, SFR are the host galaxy stellar mass and star formation rate and $\langle N_m(z)|M_*, SFR\rangle$, already introduced in eq. (5.28), is the the expected value of the probability distribution[8] of having N_m mergers inside an host galaxy of a certain class at a certain z. The merger number density $n_m(z)$, which is expressed in h^3 Mpc^{-3}, is computed as:

$$n_m(z) = \int_{M_*^{min}}^{M_*^{max}} dM_* \int_{SFR^{min}}^{SFR^{max}} dSFR\, n_g(z, M_*, SFR)\, \langle N_m(z)|M_*, SFR\rangle . \tag{5.33}$$

As for the galaxy number density $n_g(z, M_*, SFR)$ and bias $b_g(z, M_*, SFR)$ in eq. (5.32), they are computed following the standard HOD approach applied in each of the M_*, SFR bins. In particular, referring to eq. (3.78) and eq. (3.79):

$$\begin{aligned} n_g(z, M_*, SFR) &= \int_{m^{min}}^{+\infty} dm\; n_h(z, m)\, \langle N_g(M_*, SFR)|m\rangle \\ b_g(z, M_*, SFR) &= \int_{m^{min,(*,SFR)}}^{+\infty} dm\; n_h(z, m)\, b_h(z, m) \frac{\langle N_g(M_*, SFR)|m\rangle}{n_g(z, M_*, SFR)} , \end{aligned} \tag{5.34}$$

where the galaxy type introduced in the HOD expression from eq. (3.76) has been identified with the $[M_*,\ SFR]$ bins. $n_h(z, m)$ is the halo mass function defined in section 3.1.1 and eq. (3.14): the minimum mass $m^{min,(*,SFR)}$ required from a halo to form a certain galaxy depends on its stellar mass and star formation rate.

In the following, we summarize the expressions assumed or obtained per each of the distributions entering, in the order, eq. (5.34), eq. (5.33) and eq. (5.32).

Halo properties

The statistical properties required for the halo distribution are extracted from the `python.hmf` library [149]; the critical density for the spherical collapse $\delta_c(z)$ and the mass variance $\sigma(z, m)$ are obtained from `python.hmf` as well. The halo mass

---

[8] We will refer to this quantity as the merger Galaxy Occupation Distribution (HOD/GOD), in analogy to the galaxy halo occupation distribution defined in eq. (3.76).

function $n_h(z,m)$ (see section 3.1.1) defined in [148] is used; as for the halo linear bias, this is computed as [326] suggests, through:

$$b_h(z,m) = 1 + \frac{1}{\sqrt{a}\delta_c}\left[\sqrt{a}\, a\nu + \sqrt{a} b (a\nu)^{1-c} - \frac{(a\nu)^c}{(a\nu)^c + b(1-c)(1-c/2)}\right], \quad (5.35)$$

where $\nu = \nu(z,m) = \delta_c^2(z)/\sigma(z,m)^2,\ a = 0.707,\ b = 0.5,\ c = 0.6$; the expression is fitted on cosmological simulations. As minimum and maximum mass for the halos, the values $m^{min} = 10^8\, h^{-1}\, M_\odot$ and $m^{max} = 10^{19}\, h^{-1}\, M_\odot$ are arbitrarily set. Figure 3.1 and figure 5.8 show respectively the halo mass function and the linear halo bias adopted. As it was motivated in section 3.1.2, the bias is larger for more massive halos: these, in fact, are related with the denser peaks in the DM matter distribution, which turn out to be more clustered. The same reason explains why the bias is larger for higher z, since the denser peaks collapse sooner.

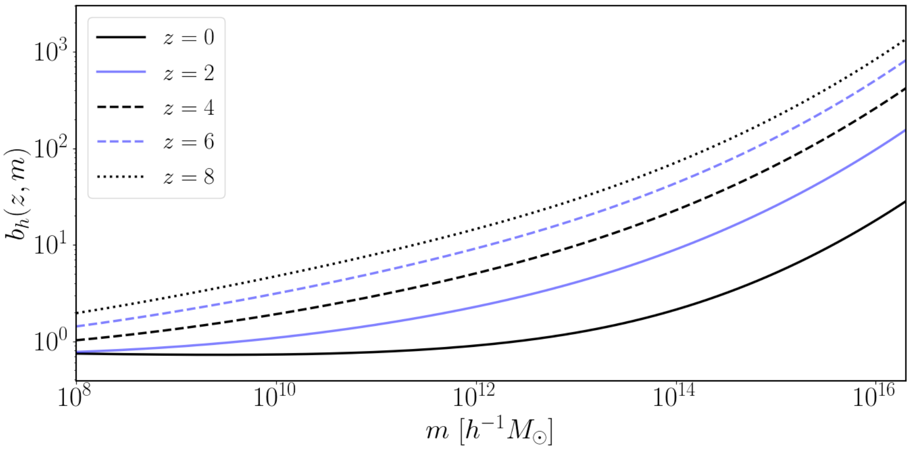

Figure 5.8: Linear halo bias at $z = [0,2,4,6,8]$ as a function of the halo mass. The bias is computed as in eq. (5.35) [326]. The values required to get $\nu(z,m)$ are computed with the `python.hmf` library [149]. The minimum and maximum halo mass are set respectively to $m^{min} = 10^8\, h^{-1}\, M_\odot$, $m^{max} = h^{-1} 10^{19}\, M_\odot$.

Galaxy properties

To obtain information on the galaxy distribution, it is possible to match the Stellar Mass Function (SMF) $\Phi(z, M_*, SFR) = d^3N/dV dM_* dSFR$ i.e., the number of galaxies per unit comoving volume, unit stellar mass and unit star formation rate, with the HOD model $\langle N_g | m\rangle$ of the simulated data.

The SMF of the simulation dataset is obtained by interpolating the data extracted from the EAGLE simulation (e.g., see [204]) in the snapshots reported in table 5.1. Through the distribution obtained, the galaxy number density in units of h^3 Mpc^{-3} is computed in each redshift snapshot per each stellar mass bin and star formation rate bin (see table 5.2). This is done through:

$$n_g(z) = h^3 \int_{M_*^{min}}^{M_*^{max}} \Phi(z, M_*)\, dM_*\ , \quad (5.36)$$

which is then combined with the HOD of the EAGLE simulation. Such model is

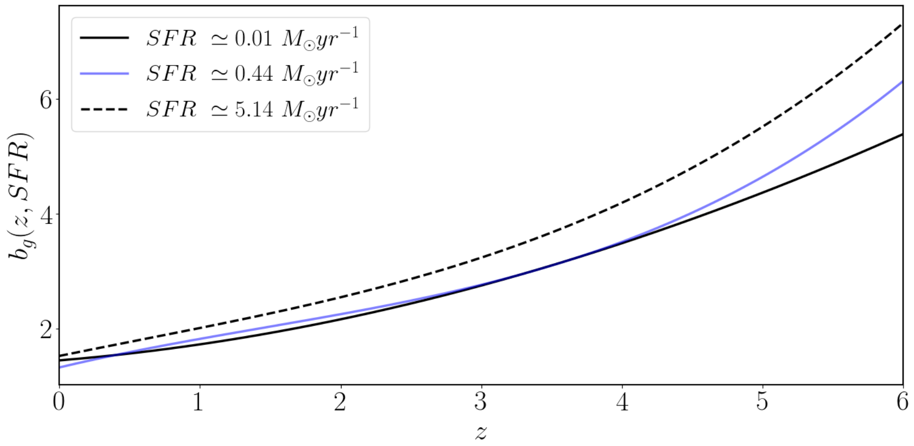

Figure 5.9: Galaxy bias depending on z in 3 different SFR bin. The M_* dependence has been marginalized out. All the bias models are computed by interpolating $b_g(z)=a_0+a_1z+a_2z^2+a_3z^3$ as described in eq. (5.39).

defined in [204] as:

$$\langle N_g|m\rangle = \langle N_g^{central}\rangle+\langle N_g^{satellites}\rangle = \frac{\left[1+\mathrm{erf}\left(\frac{\log(m)-\log(m^{min})}{\sigma_{\log m}}\right)\right]}{2} + \begin{cases}\left[\frac{m-m^{cut}}{m_1}\right]^{\alpha} & \text{if} \quad \frac{m-m^{cut}}{m_1}\geqslant 0 \\ 0 & \text{otherwise}\end{cases} . \tag{5.37}$$

The parameters $\sigma_{\log(m)}=0.318$, $m^{cut}=10^{11.90}\,h^{-1}\,M_{\odot}$, $\alpha=1.17$ are fixed, while m_1 is calculated as $m_1=14.25\cdot 10^{13.32}-m^{cut}$. The parameter m^{min}, is free instead: its value $m^{min,(*,SFR)}$ has to be related with the $[M_*,\ SFR]$ bins of the simulation. This is done per each redshift snapshot through the minimization [327] of:

$$\Delta n_g = h^3\int_{M_*^{min}}^{M_*^{max}} dM_* \int_{SFR^{min}}^{SFR^{max}} dSFR\Phi(M_*,SFR) - \int_{m^{min,(*,SFR)}}^{m^{max}} dm\,\langle N_g|m\rangle\, n_h(z,m)\,. \tag{5.38}$$

The galaxy HOD and number density obtained through this procedure are combined to compute the bias $b_g(z,M_*,SFR)$ as in eq. (5.34). Figure 5.9 shows some example of galaxy bias depending on z computed in different SFR bins. The M_* dependence, in this case, has been marginalized out. Each curve is described by the polynomial interpolation:

$$b_g(z)=a_0+a_1z+a_2z^2+a_3z^3\,, \tag{5.39}$$

where $a_0,\ a_1,\ a_2,\ a_3$ depend on the SFR bin considered. In the cases showed in the plot,[9] they are find to be:

$$\begin{aligned} &a_0=1.45,\ a_1=0.2,\ a_2=0.08,\ a_3=0.0 \text{ if } SFR\simeq 0.01\,M_{\odot}\,yr^{-1} \\ &a_0=1.32,\ a_1=0.58,\ a_2=-0.11,\ a_3=0.03 \text{ if } SFR\simeq 0.44\,M_{\odot}\,yr^{-1} \\ &a_0=1.52,\ a_1=0.5,\ a_2=-0.03,\ a_3=0.02 \text{ if } SFR\simeq 5.14\,M_{\odot}\,yr^{-1}\,. \end{aligned} \tag{5.40}$$

Figure 5.9 highlights that galaxies where the SFR is higher have a larger bias: this implies that they are found in the more massive halos.

[9] The SFR indicated is the mean value in the bin which the galaxies belong to.

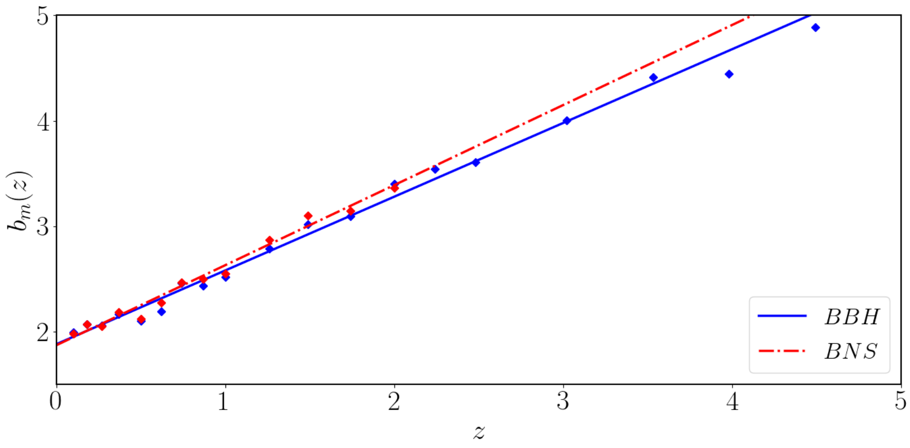

Figure 5.10: Bias of BNS (red) and BBH (blue) ET−selected distributions. The dots indicate the values obtained in each simulation snapshot from table 5.1, while the line shows the linear interpolation obtained through eq. (5.41). BNS dots stops at $z \sim 2$ in agreement with the distribution shown in figure 5.7.

Merger bias

The bias associated with the mergers i.e., the weighted bias of the galaxies that host them, is finally computed using eq. (5.32). As figure 5.10 shows, for both BBH and BNS the bias is modelled by fitting a linear function:

$$b_m(z) = A_m z + q_m = A_m(z + B_m)^{P_m} \ , \tag{5.41}$$

where $P_{BBH} = P_{BNS} = 1$, while $A_{BBH} = 0.7, \ B_{BBH} = A_{BBH}/q_{BBH} = 2.68$ for BBH and $A_{BNS} = 0.76, B_{BNS} = 2.46$ for BNS. Fiducial values are fitted on the simulated data.

A linear merger bias is often assumed in the few studies on the subject currently available in literature (see e.g., [328]). By using the HOD/GOD based approach, however, we have not made any initial assumption: the linear bias is obtained starting from merger distributions based on simulations that take into account stellar population synthesis models, so that the relation between binary mergers and the properties of their host galaxies is motivated by astrophysical models (more detail about the simulations are given in chapter 7 and in [204, 205, 322]). The linear trend of the BBH bias curve in figure 5.10 is in full agreement with e.g., the results from [325] at redshift $z < 4$. At higher redshift, the results in [325] display a flattening of the bias curve: this is likely due to the fact that [325] includes only mergers from star−forming galaxies, which are a subset of the total amount of galaxies that is instead consider in the EAGLE simulation used here. The impact of the mergers at such high redshift, anyway, does not significantly affect the forecast analysis carried on in section 5.5 and section 5.6, since the low abundance of mergers at $z > 4$ makes their contribution to the final constraints negligible.

5.3.3 Supernovae distribution and bias

In the analysis developed in [3], supernovae IA has been included so to develop the multi−tracer technique described in section 5.4. To model the number distribution, the SN rate provided in [329] has been combined with the *Status Quo* completeness that the work by [330] describes for the Vera Rubin Observatory. The rate in the source rest frame is modelled as:

$$r_{IA} = 2.6 \cdot 10^{-5}(1+z)^{2.5} \, h_{70}^3 \, \mathrm{Mpc}^{-3}\mathrm{yr}^{-1} \ , \tag{5.42}$$

where h_{70} is the rescaling of $H_0 = 70$ km s^{-1} Mpc^{-3} determined by the fiducial cosmology. The conversion to the observer rest frame is performed using the same factor as in eq. (5.27). The completeness of the survey i.e., the fraction of events that are detected, is modelled as:

$$\mathscr{C} = \gamma_{SN} \left(\frac{z}{\alpha_{SN}} \right)^{\beta_{SN}-1} e^{(-z/\alpha_{SN})^{\beta_{SN}}} , \tag{5.43}$$

where α_{SN}, β_{SN}, γ_{SN} are chosen to reproduce the completeness trend in [330]. A box having comoving size $L = 1$ Mpc and a $T^{OBS}_{SN} = 5$ yr observational run are considered to compute the observed number of SN events as:

$$N_{SN}(z) = T^{OBS}_{SN} \mathscr{C} L^3 r_{IA} . \tag{5.44}$$

The distribution obtained is shown in figure 5.11; the total number of events is $\sim 10^{4.86}$, which is slightly more pessimistic than what both [330, 331] report.

To model the SN bias, a constant value is assumed in the full redshift range observed by LSST i.e., $z \in [0, 1]$. This follows the conservative prescription made in [332], where SN are assumed to follow galaxy bias. The value we choose is $b_{SN} = 1.9$, which is the $b_g(z)$ value obtained by integrating the galaxy bias from eq. (5.39) over M_* and SFR and averaging it between $z = 0$ and $z = 1$. In order to use the same model as in eq. (5.41), the parameters $A_{SN} = 1.9$, $B_{SN} = 0$ and $P_{SN} = 0$ are defined. Figure 5.12 shows the bias obtained.

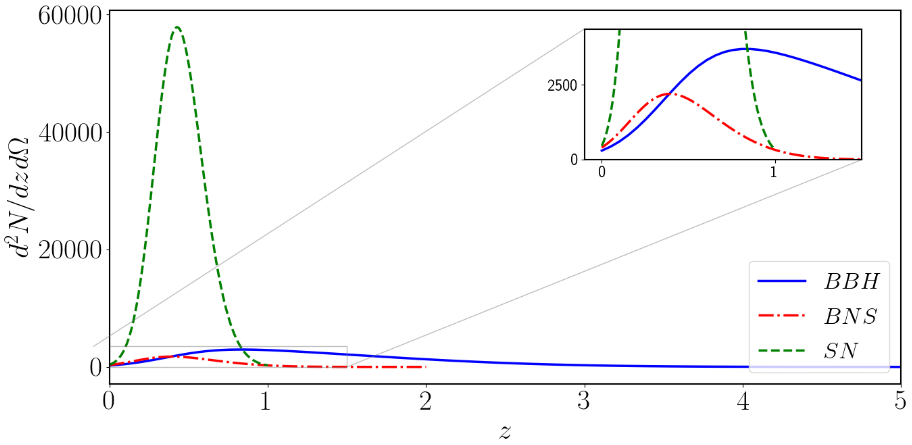

Figure 5.11: $d^2N/dzd\Omega$ for the sources considered in the analysis: SN observed by the Vera Rubin Observatory in the *Status Quo* configuration (green dashed, see section 5.3.3), BNS (red dot–dashed, see section 5.3.1) and BBH observed by ET (blue, see section 5.3.2). Merger distributions are the same as figure 5.7 z_{max} per each source depends on the detector horizon described in table 5.3.

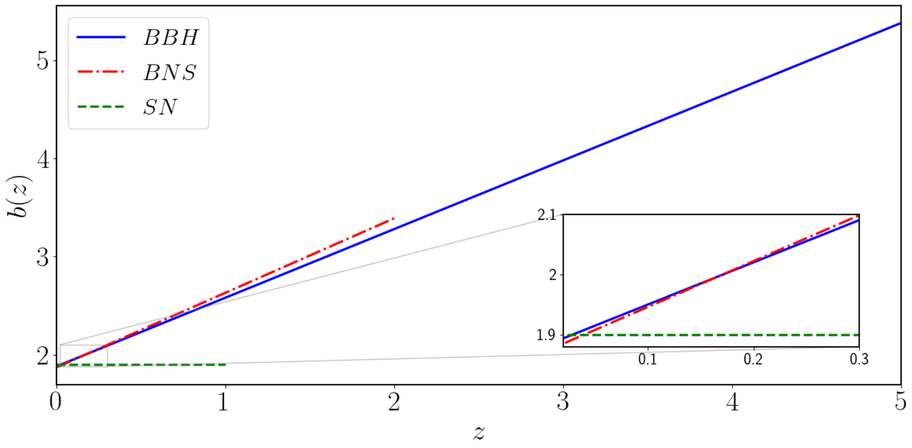

Figure 5.12: Fiducial bias models considered in the analysis. The color legend is the same as in figure 5.11; the bias lines for the mergers are the same as in 5.10.

5.4 Forecast analysis

In [2, 3], we developed a forecast analysis of future surveys in luminosity distance space to understand their constraining power on cosmological and bias parameters. Section 5.4.1 characterizes the properties of the surveys we considered. Section 5.4.2 and section 5.4.3, instead, present the statistical tools adopted. Results are then reported in section 5.5 and section 5.6.

5.4.1 Survey specifications

In this work, we refer to third gravitational wave detector from the ground. As described in chapter 4, the ground choice is made according to the kind of sources we assume to observe: mergers of compact binaries of ~ tenths solar masses, in fact, produce GW which rely in the sensitivity band of ground detectors. Currently existing interferometers, however, are characterised by a local horizon, inside which only sources at $z << 1$ can be observed: for this reason, third generation interferometers are required.

The baseline case for the analysis, therefore, is the Einstein Telescope [257]; other, more futuristic scenarios are analysed as well. Each detector is characterized through the horizon, the detected number of sources, the luminosity distance uncertainty and the sky localization uncertain: all the specifications are summarized in table 5.3. The table includes also the characteristics of the Vera Rubin Observatory (VRO) which is assumed in section 5.4.3 to include the supernovae survey in the analysis

Table 5.3: Survey specifications (specs): observed sky area, luminosity distance and sky localization uncertainties ($\Delta D_L/D_L$, $\Delta\Omega$, respectively; where the sky localization is ≤ few arcmin^2 we assumed $\Delta\Omega \sim 0$), detector horizon z_{max}. VRO specs are in accordance with [331]. ET specs are compatible with [333] (full description depending on frequency and distance for BNS) and [334] (full analysis for BBH). N^{TOT} is computed as described in section 5.3.1 and section 5.3.3 assuming T^{OBS}.

Survey	Source	Area [deg^2]	$\Delta D_L/D_L$	$\Delta\Omega$ [deg^2]	z_{max}	T^{OBS}	N^{TOT}
ET	BNS BBH	Full sky	0.3 0.1	100	2 5	3 yr	$10^{4.14}$ $10^{4.79}$
ET×3	BNS BBH	Full sky	0.3 0.1	10 3	2 5	3 yr	$10^{4.14}$ $10^{4.79}$
ET×3 High localization	BNS BBH	Full sky	0.3 0.1	0.5	2 5	3 yr	$10^{4.14}$ $10^{4.79}$
High precision	BNS BBH	Full sky	0.1 $z \leq 2$ 0.03 $z > 2$	~ 0	2 5	3 yr	$10^{4.14}$ $10^{4.79}$
High precision Numerous sources	BNS BBH	Full sky	0.1 $z \leq 2$ 0.03 $z > 2$	~ 0	2 5	3 yr	$10^{6.14}$ $10^{6.79}$
VRO	SN	18000	0.15	~ 0	1	5 yr	$10^{4.86}$

The **horizon** is defined as the maximum distance at which sources can be observed. For all the detectors, we set it to be $z = 5$ for BBH, $z = 2$ for BNS, according with the source distributions modelled in section 5.3.1. In luminosity distance space, these correspond respectively to $D_L^{max} \simeq 4.8 \cdot 10^4$ Mpc for BBH and $D_L^{max} \simeq 1.6 \cdot 10^4$ Mpc for BNS.

As for the **detected number of sources**, we distinguish between ET−like surveys and surveys which can observe an higher number of events. In the first case, the total number of sources is simply obtained by integrating the distribution in eq. (5.31) over all the sky and up to the horizon. In the second case, instead, a scale factor $\mathcal{S} = 100$ is applied to the same distribution, so to increase it. This toy−model is used to characterize detectors which will be able to see more sources than ET e.g., thanks to a better sensitivity that would allow to detect lower signals or to a different antenna pattern that would improve the detectability of the sources on the sky (see section 4.3 for detail).

The **luminosity distance uncertainty** is used to define the amplitude of the D_L bins inside which the angular power spectra in section 5.4.2 and section 5.4.3 are computed. We assumed different configurations for BBH and BNS in the baseline ET−like case that, in agreement with [333] and sticking to rather conservative assignments,[10] are:

$$\frac{\Delta D_L}{D_L} = 10\% \text{ for BBH}, \quad \frac{\Delta D_L}{D_L} = 30\% \text{ for BNS}. \tag{5.45}$$

We also analysed a more optimistic configuration, beyond the accuracy allowed by ET, in which:

$$\frac{\Delta D_L}{D_L} = \begin{cases} 10\% & \text{if } z < 2 \\ 3\% & \text{if } z \geq 2 \end{cases} \quad \text{for both BBH and BNS.} \tag{5.46}$$

While being still conservative at low distances,[11] this configuration significantly increases the accuracy of the D_L measurement at high distances.

The amplitudes of the luminosity distance bins defined through eq. (5.45) are such that the factor f_{D_L} introduced in section 5.2.1 has little variation inside each them. In particular:

$$\Delta f_{D_L}\Big|_{D^{min}_{L,i}}^{D^{max}_{L,i}} \leq 0.1 f_{D_L}(D^{min}_{L,i}) \,, \tag{5.47}$$

therefore the approximation $f_{D_L} \simeq cost$ in a given bin is completely reasonable. For D_L approaching 0, the variation of f_{D_L} becomes more and more rapid and the number of bins at low redshift rapidly increase. Therefore, to avoid computational issues and stabilize the number of bins at low redshift, a lower distance bound is set at $D_L^{min} \simeq 476$ Mpc which corresponds to $z^{min} = 0.1$ in the fiducial cosmology reported in table 2.1. This lower limit does not introduce any loss of cosmological information.

A more refined definition of the error should be distance dependent and linked to the detector antenna pattern defined in section 4.3 through the sky position and inclination of each merger. This however goes beyond the accuracy level required for the Fisher matrix forecast performed in this work.

Last but not least, the **sky localization** affects the capability of observing the smaller scales by smoothing the higher values of ℓ in the computation of the angular power spectra in section 5.4.2 and section 5.4.3. First of all, at each redshift we consider only modes in the linear regime, by implementing the cut-off scale:

$$\ell_{max}(z_i, z_j) = k^0_{nl} \min\left[(1 + z_{i,j})^{2/(2+n_s)} \chi(z_{i,j})\right] \,, \tag{5.48}$$

where $\chi(z_{i,j})$ is the comoving distance computed in the central points of the bins between which the angular power spectrum in computed and n_s the primordial scalar power spectral index from eq. (2.62). The quantity k^0_{nl} is the non−linear cut−off scale at $z = 0$ i.e., the scale at which non−linear effects are considered too large to be properly taken into accounted. In section 5.5 [2] We considered two

[10] For example, the 10% relative error in D_L for BBH is larger than the one forecasted by [316], in the entire redshift range taken into account in this work.

[11] This choice is due to the fact that further reducing the D_L bin size at such redshifts would introduce numerical instabilities, without improving the overall result.

prescriptions for this value: in the more optimistic case, we relied on the accuracy of the halofit model, which is used in `CAMB` to compute the non−linear power spectrum, by including scales up to $k^0_{nl} = 0.4\,h$, Mpc^{-1} (see [335]). In the more conservative case, instead we limited the analysis to the linear scales by choosing $k^0_{nl} = 0.1\,h\,\mathrm{Mpc}^{-1}$; in section 5.6 [3], only this second approach is considered.

The cut−off scale in eq. (5.48) is only an upper bound, which does not take into account the effect of the sky localization uncertainty. At first approximation, in fact, this smooths out the fluctuations above a given scale ℓ_{eff}, defined as:

$$\ell_{eff}(z_i, z_j) = \chi(z_{i,j})k_{eff} = \frac{\chi(z_{i,j})\sqrt{8\ln 2}}{\chi(z_{i,j})\Delta\Omega^{1/2}} \,. \tag{5.49}$$

In the high precision cases described in table 5.3, where $\Delta\Omega$ few arcmin^2, at all redshifts $\ell_{eff} < \ell_{max}$; in the other cases, the cut−off scale is lower than the one set by the linear condition, therefore in section 5.5 [2] we cut the angular power spectra above ℓ_{eff}. In section 5.6 [3] we refine this approximation by considering a Gaussian beam profile[12] with $\sigma = \sqrt{\Delta\Omega}/8\ln 2$, that is:

$$B_\ell = \exp\left[-\ell(\ell+1)\sigma^2\right] \,. \tag{5.50}$$

The Gaussian beams adopted for each kind of sources in the ET and ET×3 cases at the horizon are visualized in figure 5.13.

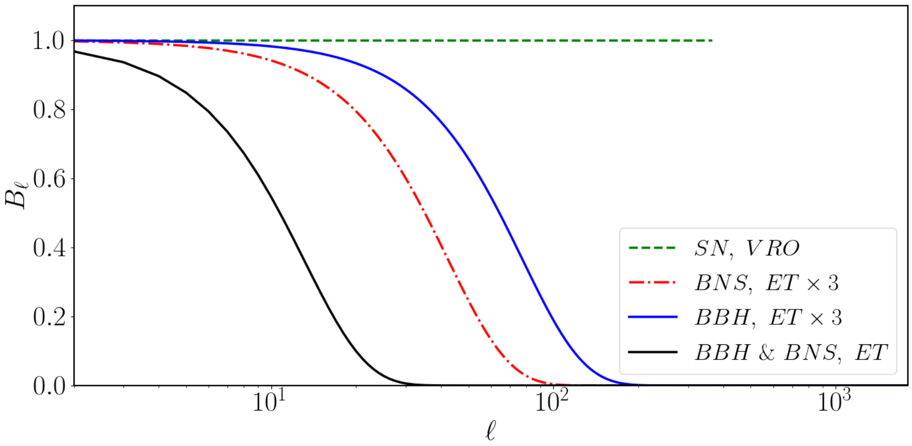

Figure 5.13: Beam window defined through eq. (5.50) for SN (green dashed) and sources observed through ET (black continuous for both BNS and BBH) or ET×3 (blue continuous for BBH, red dot−dashed for BNS). Each line is computed considering ℓ_{max} as the one associated through eq. (5.48) to the z_{max} reached for the source (see table 5.3).

5.4.2 Fisher matrix formalism

To forecast how well a future detector will constrain cosmological and bias parameters, the Fisher matrix formalism can be used. This allows to predict the minimum error the detector will commit simply by knowing the model that links the parameters with the data, even if this are still not gathered.

Let $\boldsymbol{\theta} = (\theta_1 ... \theta_N)$ be the parameter set and $(\mathbb{O}_1 ... \mathbb{O}_M)$ the set of observable estimators, such that each of them is a function of the parameter themselves:

$$\mathbb{O}_m = \mathbb{O}_m(\theta_1, ..., \theta_N) \,. \tag{5.51}$$

[12] 12: The expression here reported refers to auto−spectra of a single source; the full expression in the multi−tracer case is presented in section 5.4.3.

Per each parameter, a fiducial model exists to provide an *a priori* estimate of its value. Each entry of the **Fisher matrix** is computed as:

$$F_{\alpha\beta} = \sum_{m=1}^{M} \frac{1}{\sigma_m^2} \frac{\partial \mathscr{O}_m}{\partial \theta_\alpha} \frac{\partial \mathscr{O}_m}{\partial \theta_\beta} \,, \tag{5.52}$$

where σ_m^2 is the uncertainty of the estimate of $\mathscr{O}_m$. The Fisher matrix is defined as the Hessian of the logarithm of the maximum likelihood of the data $\mathscr{L}$ defined in section 6.1 (see e.g., [336]:

$$F_{\alpha\beta} = \left\langle - \frac{\partial^2 \mathscr{L}}{\partial \theta_\alpha \partial \theta_\beta} \right\rangle \Bigg|_{\boldsymbol{\theta} = \boldsymbol{\theta}_{max(\mathscr{L})}} \,. \tag{5.53}$$

When $\mathscr{L}$ is described by a multivariate Gaussian distribution[13] , the Fisher matrix in eq. (5.53) is related to the likelihood covariance **covariance** $\mathscr{C}$ by [337]:

$$F_{\alpha\beta} = \frac{1}{2} Tr\left[\mathscr{C}^{-1}\mathscr{C}_{,\alpha}\mathscr{C}^{-1}\mathscr{C}_{,\beta} + \mathscr{C}^{-1}(\boldsymbol{\mu}^T_{,\alpha}\boldsymbol{\mu}_{,\beta} + \boldsymbol{\mu}^T_{,\beta}\boldsymbol{\mu}_{,\alpha}\right] \,. \tag{5.54}$$

In eq. (5.54), the inverse of the covariance matrix $\mathscr{C}^{-1}$ is combined with the covariance derivative with respect to the parameters of interest $\mathscr{C}_{,\alpha/\beta}$; $\boldsymbol{\mu}$ is the average of the data.

Let us summarize some of the properties of the Fisher matrix formalism in the multivariate Gaussian framework.

When a **prior** knowledge[14] of some parameter θ_α exist e.g., from previous observations its value is estimated with uncertainty $\pm\sigma_\alpha^2$, this can be included in the Fisher through [337]:

$$F^{with\ prior} = F + \begin{pmatrix} 1 & 0 & \dots & 0 \\ 0 & \sigma_\alpha^2 & \dots & 0 \\ 0 & 0 & \dots & 1 \end{pmatrix}^{-1} \,. \tag{5.55}$$

If the Fisher matrix contains some nuisance parameters, it is possible either to condition them i.e., to fix their values at the fiducial, or to marginalize them i.e., to integrate over the space where they can exist. The **conditioning** procedure can be done by removing the line and column related to the nuisance parameter from F^{-1}; the **marginalization** instead consists in removing them directly from F.

When the estimator of the parameters are unbiased[15] , the Cramér–Rao inequality assures [336] that:

$$\sigma_\alpha^{marg} \geqslant \sqrt{(F^{-1})_{\alpha\alpha}} \,. \tag{5.56}$$

Asymptotically, the Cramér–Rao bound is saturated by the maximum likelihood, which then represent the best unbiased estimator [337]. The value $\sigma_\alpha = \sqrt{(F^{-1})_{\alpha\alpha}}$ can be used as an estimate for the uncertainty in the measurement of the parameter: it is called the **marginal error**.

The Fisher diagonal elements, therefore, represent the minimum errors the parameters estimation will have, while the elements out of the diagonal give the correlation between the different estimates. The correlation can be due both to physical relations between the parameters and to the way they affect data: independent parameters can have similar effects and their estimates can therefore correlate [336].

[13] This is called the **Laplace approximation**.

[14] The prior represents the probability distribution that the parameter θ_α acquires a certain value conditioned by the fact that a set of hypothesis for the model M (or a set of previous observations which the observer trusts) is already known. In this work, if not differently specified, we always assume the prior to be uniform and uninformative inside a certain range i.e., $p(\theta_\alpha|M) = 1/\Delta\theta_\alpha = 1/(\theta_{alpha}^{max} - \theta_\alpha^{min})$ (this notation will be clarified in section 6.1). When, instead, a prior σ_α is provided, this is assumed to be Gaussian i.e., the probability distribution of θ_α follows a Gaussian distribution peaked in the fiducial value and having variance σ_α^2.

[15] An estimator is unbiased when its expectation value provides the true value of the parameter i.e., $\langle\hat{\boldsymbol{\theta}}\rangle = \boldsymbol{\theta}$.

Fisher matrix for cosmological survey

In the context of cosmological survey e.g., the future GW survey we are studying, the Fisher matrix formalism can be applied considering that the observables are the angular power spectra $C_\ell(z_i, z_j)$ defined in eq. (3.37), which are treated as estimators of the underlying density field. These are computed with respect to the density fluctuations of the tracer, which on large scales are well approximated by a Gaussian field (as we described in section 2.2.2). The $\boldsymbol{\mu}$ average is therefore zero, while the covariance matrix is defined as:

$$\mathscr{C}_{\ell,ij} = \delta^D_{ij}\left[C_\ell(z_i, z_j) + \frac{1}{\bar{n}_{ij}}\right], \tag{5.57}$$

being $1/\bar{n}_{ij}$ the shot noise from eq. (3.36). In the luminosity distance space in which we are working (see section 5.2.1), the expression remains the same once that the bins $[z_i, z_j]$ are converted to $[D^i_L, D^j_L]$ by assuming a certain set of cosmological parameters.

As [12, 337] shows, eq. (5.54) in this case can be reduced to:

$$F_{\alpha\beta} = \sum_{\ell_{min}}^{\ell_{max}} \frac{2\ell+1}{2} f_{sky} \mathrm{Tr}[(\partial_\alpha \boldsymbol{C}_\ell)\, \boldsymbol{\mathscr{C}}_\ell^{-1} (\partial_\beta \boldsymbol{C}_\ell)\, \boldsymbol{\mathscr{C}}_\ell^{-1}]\,, \tag{5.58}$$

where the matrices $\boldsymbol{C}_\ell$ and $\boldsymbol{\mathscr{C}}_\ell$ respectively contain the $C^{ij}_\ell = C_\ell(D^i_L, D^j_L)$ and $\delta^D_{ij}/[C^{ij}_\ell + 1/\bar{n}_{ij}]$ elements. The trace Tr in this case sums the ij contributions: this implies that all the information obtained through the tomographic analysis of the C^{ij}_ℓ are combined as each spectra was computed through an independent experiment. Note that in eq. (5.58) both the auto− ($i = j$) and cross− ($i \neq j$) angular power spectra enter the computation.

In eq. (5.58), f_{sky} is the observed fraction of the sky (i.e., 1 for ET), while ℓ_{min} and ℓ_{max} are the multipoles defining the interval in which the angular power spectra is calculated. In particular $\ell_{min} = 2\pi/\vartheta = 2$, being $\vartheta = \pi$ the maximum angular scale observed, and ℓ_{max} is set by considering non−linearities and sky localization uncertainties, as section 5.4.1 describes.

With the formalism here depicted, in section 5.5 and section 5.6 marginalised errors are computed on cosmological and bias parameters by the means of the Fisher matrix. That is, the eq. (5.58) is computed by estimating the C^{ij}_ℓ and their derivatives, so to get for each parameter the marginalized error:

$$\sigma^{marg}_\alpha = \sqrt{(F^{-1})_{\alpha\alpha}}. \tag{5.59}$$

Confidence ellipses

Once that the Fisher matrix is estimated, confidence regions can be computed to represent the reliability of the estimates in the parameter space. These represent the fact that, by repeating the same analysis, the estimated value of θ_α would fall within a certain interval a certain amount of times.

For each couple of parameters $[\theta_\alpha, \theta_\beta]$, if the Laplace approximation holds and the other parameters have been marginalized, the confidence region is an ellipses defined by the elements $(F_\alpha)^{-1}$, $(F_\beta)^{-1}$, $(F_{\alpha\beta})^{-1}$ of the inverse of the Fisher matrix (i.e., the covariance matrix). In particular, the semi−axes a, b and inclination ι of the ellipse are [338]:

$$a^2 = \zeta\left[\frac{\sigma_\alpha^2 + \sigma_\beta^2}{2} + \sqrt{\frac{(\sigma_\alpha^2 + \sigma_\beta^2)^2}{4} + \sigma_{\alpha\beta}^2}\right] \quad , \quad b^2 = \zeta\left[\frac{\sigma_\alpha^2 + \sigma_\beta^2}{2} - \sqrt{\frac{(\sigma_\alpha^2 + \sigma_\beta^2)^2}{4} + \sigma_{\alpha\beta}^2}\right]$$
$$\mathrm{tg}(2\iota) = \frac{2\sigma_{\alpha\beta}}{\sigma_\alpha^2 - \sigma_\beta^2} \, . \tag{5.60}$$

The value of the parameter ζ sets the confidence level of interest e.g., $zeta = 1.52$ for the $1-\sigma$ level where the parameter estimate falls 68.3% of the times, $zeta = 3.44$ for the $3-\sigma$ level with 99.3% probability. The confidence ellipse is tilted when the two parameters correlate.

5.4.3 Multi-tracer technique

When more than one tracer is involved in the analysis, the multi−tracer technique can be used to enhance the constraining power of clustering measurements. This technique was firstly developed in [339] (see also [340–342]) to overcome the cosmic variance problem defined in section 2.2.2, which is relevant at large scales, where only a few realizations of the stochastic distribution of DM overdensities exist. Since, however, different tracers map the same underlying distribution, by comparing them it is possible to improve the results of the analysis.

On one side, having different tracers allows us to compute the ratio of their biases without modelling the DM field itself (compare with [343]); in fact having two tracers $s_1,\ s_2$:

$$\begin{cases} \langle \delta_{s_1}\delta_{s_1} \rangle & \simeq\ b_{s_1}^2 \langle \delta\delta \rangle \\ \langle \delta_{s_2}\delta_{s_2} \rangle & \simeq\ b_{s_2}^2 \langle \delta\delta \rangle \end{cases} \rightarrow \frac{b_{s_1}}{b_{s_2}} = \sqrt{\frac{\langle \delta_{s_1}\delta_{s_1} \rangle}{\langle \delta_{s_2}\delta_{s_2} \rangle}} \, . \tag{5.61}$$

The same relation holds for the observed 3D and angular power spectra. The enhancement of the constraints on bias sensitive parameters are therefore a straightforward consequence of the multi−tracer Fisher matrix. Although cosmology and bias are not degenerate, they are correlated [344, 345]: improving the constraints of the bias parameters, therefore, increases indirectly the cosmological constraints through parameter correlations.

On the other side, having the cosmic variance shared among different tracers mixes their signal [342, 346] and it improves total signal−to−noise ratio.

In the case of multi−tracer analysis, what is discussed in section 5.4.2 and 5.4.1 still holds, but it has to be extended to the existence of more than one tracer. For example, in the case of 2 tracers $[s_1,\ s_2]$ and 2 bins $i = 0 = [D_L^{0,min}, D_L^{0,max}]$ and $j = 1 = [D_L^{1,min}, D_L^{1,max}]$,[16] the matrix containing all the angular power spectra $\boldsymbol{C}_\ell$ is defined as the block matrix:

$$\boldsymbol{C}_\ell = \left(\begin{array}{cc|cc} C^{00}_{s_1,s_1} & C^{00}_{s_1,s_2} & C^{01}_{s_1,s_1} & C^{01}_{s_1,s_2} \\ C^{00}_{s_2,s_1} & C^{00}_{s_2,s_2} & C^{01}_{s_2,s_1} & C^{01}_{s_2,s_2} \\ \hline C^{10}_{s_1,s_1} & C^{10}_{s_1,s_2} & C^{11}_{s_1,s_1} & C^{11}_{s_1,s_2} \\ C^{10}_{s_2,s_1} & C^{10}_{s_2,s_2} & C^{11}_{s_2,s_1} & C^{11}_{s_2,s_2} \end{array}\right)_\ell \, . \tag{5.62}$$

[16] In this notation, for the same source auto−power spectra are indicated as $C_\ell^{ii} = C_\ell(D_L^i, D_L^i)$ and cross−spectra as $C_\ell^{ij} = C_\ell(D_L^i, D_L^j)$. Considering two sources instead, if they are observed in the same bin the angular power spectrum is $C^{ii}_{s_1s_22,\ell} = C_\ell(s_1 \in D_L^i, s_2 \in D_L^i)$, while in different bins $C^{ij}_{s_1s_22,\ell} = C_\ell(s_1 \in D_L^i, s_2 \in D_L^j)$.

All the angular power spectra are computed by considering the ℓ smoothing factor due to the sky localization uncertainty $\Delta\Omega$ that is defined in section 5.4.1. If the two surveys have different $\Delta\Omega$, the smoothing factor from eq. (5.50) is recomputed as:

$$B_\ell^{s_1 s_2} = \exp\left[-\frac{\ell(\ell+1)}{2}\sigma_{s_1}^2\right]\exp\left[-\frac{\ell(\ell+1)}{2}\sigma_{s_2}^2\right] . \tag{5.63}$$

Analogously to eq. (5.62), the covariance matrix $\mathscr{C}$ can be obtained; the Fisher matrix from eq. (5.58) is then computed straightforwardly once that f_{sky} is set to be the sky fraction covered by both the surveys. The multi−tracer analysis developed in section 5.6 [3] brings together the GW survey performed by ET/ET×3 (see section 5.3.1, section 5.3.2, section 5.4.1) and VRO observations of supernovae IA (see section 5.3.3, section 5.4.1). As a further case, I check the results for the combination of different merger events: despite being performed with the same detector (i.e., ET/ET×3), GW from different types of astrophysical mergers can be considered as independent surveys since their signal can be easily distinguished. This will no longer be true in the analysis performed in chapter 6, where a *blind* survey involving astrophysical and primordial black hole is considered.

5.4.4 Analysis set-up

This section summarizes the forecasts obtained for future GW surveys of dark sirens; a set including both cosmological and bias parameters is analysed. All the angular power spectra required by the Fisher matrix from eq. (5.58) are computed with a modified version of the publicly available code `CAMB` [165],[17] where the functions that we customized are:

- The contribution of peculiar velocity effects and lensing to the luminosity distance space distortions, as described respectively in section 5.2.1 and section 5.2.2.
- The observed source distribution $d^2N/dzd\Omega$, modelled as is eq. (5.31) separately for binary black holes, binary neutron stars and supernovae IA.
- The bias of the sources, modelled as 5.41 with fiducial values for the parameters extracted from the simulations, as described in section 5.3.2 and section 5.3.3.

In particular, section 5.5 follow the procedure depicted in [2] to analyse separately BBH and BNS as observed by ET, ET×3 and more futuristic configurations, described in table 5.3. Only peculiar velocities, as described in section 5.2.1, are included to model the LDS distortions. An analysis is performed on the effect of including priors on cosmological parameters.

Section 5.6, instead, is based on [3], where three main improvements are considered. Firstly, a multi−tracer analysis in LDS is developed as described in section 5.4.3, by considering BBH, BNS and SN, which play a significant role in breaking degeneracies arising in a GW−only analysis. In this case, only the ET and ET×3 configuration are considered. Secondly, the lensing contribution from [315] is included in the computation of the LDS distortions. Finally, the parameter set used in the analysis is slightly different, both for the number of cosmological parameters used and for the way bias parameters are defined and the sky localization uncertainty is used to model a smoothing of the multipoles instead of a sharp cut−off section 5.4.1. An insightful analysis on the effect of prior inclusion is considered as well.

---

[17] In the current version of the code, the original `CAMB` [347] is integrated with `CAMBsources` [165].

5.5 Results: First analysis

Forecasts in [2] are derived separately for BBH and BNS in the different scenarios described by table 5.3 for the parameter set:

$$\boldsymbol{\theta} = \left[H_0, \Omega_c h^2, w_0, w_a, b(D_L^0), ..., b(D_L^{N_{bin}})\right] , \tag{5.64}$$

where H_0 is the local value of the Hubble parameter and h its dimensionless value, Ω_c is the dimensionless dark matter density parameter and w_0, w_a describe the dark energy equation of state in the CPL parametrization of eq. (2.12) (see chapter 2 for detail). The bias parameters are defined as the values $b(D_L^0), ...b(D_L^{N_{bin}})$ the bias from eq. (5.41) assumes in each of the D_L bins where the angular power spectra are computed. Therefore, since the D_L bins are defined through the luminosity distance uncertainty $\Delta D_L/D_L$ in table 5.3, a different number of bias parameters N_{bin} is considered for BBH and BNS in the different detector configurations.

The analysis considers four different runs:

run A: the merger bias parameters are fixed to their fiducial values and constraints are derived for the remaining cosmological parameters i.e., $\boldsymbol{\theta} = [H_0, \Omega_c h^2, w_0, w_a]$. Uniform priors are set on all the parameters, except H_0 for which the Gaussian prior from *Planck 2018* [13] is considered;

run B: the full set of parameters, including biases, is considered i.e., $\boldsymbol{\theta}$ from eq. (5.64). Uniform priors are set on all the parameters, except H_0 for which the *Planck 2018* prior [13] is considered;

run C: the full set of parameters, including biases, is considered i.e., $\boldsymbol{\theta}$ from eq. (5.64). *Planck 2018* priors [13] are considered for all the cosmological parameters;

run D: the full set of parameters, including biases, is considered i.e., $\boldsymbol{\theta}$ from eq. (5.64). Uniform priors are assumed over all the parameters. This run is cosidered only when studying bias parameters.

In computing eq. (5.58), the derivatives $\partial_{\alpha,\beta} \boldsymbol{C}_\ell^{ij} = \partial C_\ell(D_L^i, D_L^j)/\partial\theta_{\alpha,\beta}$ are calculated numerically with respect to the parameters of interest. To do so, `CAMB` has to be run with different inputs for $\theta_\alpha \pm \delta\theta_\alpha$. Since the code asks for redshift bins as an input, $z_{i,j}$ are computed from $D_L^{i,j}$ assuming the same variations $\pm\delta\theta_\alpha$ in the cosmological parameters. This implicitly takes into account the fact that not only $C_\ell(z_i, z_j)$ changes with the parameters variations, but also the bins boundaries $z_{i,j}(D_L^{i,j})$ are modified. This numerical effect is due to the chain rule in the derivative process, where:

$$\frac{\partial C_\ell[z(D_L)]}{\partial\theta_\alpha} = \frac{\partial C_\ell[z(D_L)]}{\partial\theta_\alpha}\frac{\partial z(D_L)}{\partial\theta_\alpha} , \tag{5.65}$$

where the effect of $\partial z(D_L)/\partial\theta_\alpha$ is directly accounted for by the change in the z bin boundaries. This instead does not happen in the case of bias parameters, which only affects the C_ℓ and not the $D_L - z$ conversion.

Results are computed with respect to the different detector configurations described in table 5.3. In particular, the ET−like results are considered only for bias parameters, while for cosmological parameters the impossibility of accessing the smaller scales prevent having a good result. In the ET×3 scenario, forecasts are computed with either the conservative or the optimistic $k_{nl}^0 = 0.1 - 0.4\, h\,\mathrm{Mpc}^{-1}$ cut−off (see section 5.4.1) while all the other, more futuristic, scenarios are computed with the conservative $k^0_{nl} = 0.1\,h\,\mathrm{Mpc}^{-1}$ choice. The effect of the sky localization uncertainty is taken into account by introducing a sharp cut−off at ℓ_{eff} defined as in eq. (5.49).

5.5.1 Cosmological parameter constraints

The parameter H_0 can not be well constrained with this procedure, since it appears as an overall normalization after differentiating the $D_L - z$ conversion, leading to degeneracies in the computation. Marginalized $1-\sigma$ errors are computed for each of the cosmological parameters $[\Omega_c h^2, w_0, w_a]$ separately for a BBH and a BNS survey: these are reported in table 5.4. The different lines of the table refer to the different detector configurations described in table 5.3.

Table 5.4: Forecasted $1-\sigma$ marginalized errors for the cosmological parameters in the different scenarios for both BBH and BNS.

D_L error	Parameter	BBH			BNS		
		run A	run B	run C	run A	run B	run C
ET×3 $k^0_{nl} = 0.1\,h\,\mathrm{Mpc}^{-1}$	$\Omega_c h^2$	0.0037	0.0095	0.0082	0.0192	0.0230	0.0191
	w_0	0.1460	0.2185	0.1911	0.4697	0.5058	0.4951
	w_a	0.5030	1.0941	0.8487	1.3186	11.378	1.3390
ET×3 $k^0_{nl} = 0.4\,h\,\mathrm{Mpc}^{-1}$	$\Omega_c h^2$	0.0025	0.0075	0.0068	0.0165	0.0206	0.0168
	w_0	0.0797	0.1296	0.1205	0.3239	0.3554	0.3525
	w_a	0.2993	0.7946	0.6843	0.9026	11.019	1.3384
ET×3 High localization	$\Omega_c h^2$	0.0037	0.0095	0.0083	0.0191	0.0229	0.0191
	w_0	0.1453	0.2177	0.1906	0.4615	0.5063	0.4953
	w_a	0.5009	1.0951	0.8491	1.3191	11.377	1.3390
High precision	$\Omega_c h^2$	0.0033	0.0084	0.0076	0.0050	0.0090	0.0083
	w_0	0.1250	0.1675	0.1536	0.1423	0.2001	0.1848
	w_a	0.4319	0.9710	0.7875	0.4587	1.4172	0.9765
High precision Numerous sources	$\Omega_c h^2$	0.0024	0.0075	0.0070	0.0050	0.0088	0.0082
	w_0	0.0746	0.1249	0.1184	0.1417	0.1986	0.1841
	w_a	0.2682	0.8565	0.7228	0.4553	1.3933	0.9686

For the ET×3 forecasts in the strictly linear regime ($k^0_{nl} = 0.1\,h\,\mathrm{Mpc}^{-1}$), the results for both the merger kinds show that we can achieve error bars on $\Omega_c h^2$ and w_0 which are worse, but not far from those expected via galaxy clustering analysis in the near future (using for example the *Euclid*−like catalogue). For w_a instead the error bars are about 5 times worse in the BBH case. The difference between BBH and BNS is due to the different redshift range covered by the two distributions i.e., to the fact that BNS tracers can be used only up to $z^{max} \sim 2$. Of course, pushing the analysis into more non−linear scales or considering a higher precision in the sky position or distance determination, or a higher number of sources, significantly improves these figures.

The run B results are used to compute the confidence ellipses in figure 5.14, which refer to the ET−like configuration.

5.5.2 Bias parameter constraints

When focusing on merger properties, rather than on cosmology, it is appropriate and useful to include cosmological priors from e.g., CMB surveys such as *Planck 2018* [13]; therefore, the run C configuration in considered. Results are obtained

Figure 5.14: Confidence 1σ ellipses obtained for BNS (red) and BBH (blue) in the ET×3 survey run B, obtained as described in eq. (5.60). The plots for $(\theta_\alpha, \theta_\alpha)$ show the posterior distributions (see section 6.1). The dashed line shows results obtained setting $k^0_{nl} = 0.4\,h\,\mathrm{Mpc}^{-1}$, while the continuous line refers to $k^0_{nl} = 0.1\,h\,\mathrm{Mpc}^{-1}$.

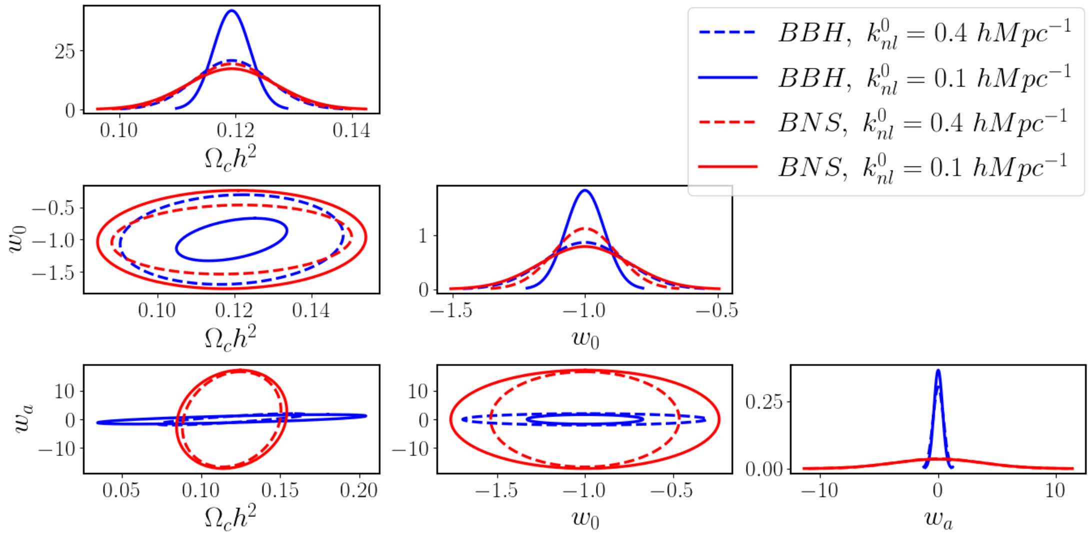

considering both the ET and the ET×3 detectors with $k^0_{nl} = 0.1\,h\,\mathrm{Mpc}^{-1}$; we verified that $k^0_{nl} = 0.4\,h\,\mathrm{Mpc}^{-1}$ does not provide significant improvements in the bias forecasts.

Figure 5.15 and figure 5.16 show both the fiducial values and error bars, $b_m(z^i) \pm \sigma_{b_m}(z^i)$.[18] The modulation that can be seen in the error bars for the BBH bias (i.e., $\sigma_{b_{BBH}}(z_i = 1.5) < \sigma_{b_{BBH}}(z_i = 0.7)$) is due to the combination of two effects: the presence of a peak in the number of sources around $z \sim 1$ (compare with figure 5.7) on one side, and the increasing luminosity distance error $\Delta D_L / D_L$ on the other; this leads to a minimum in the error bar at $z \sim 1.2$. The same effect is not seen in the BNS case since the larger amplitude of the D_L intervals covers the modulation.

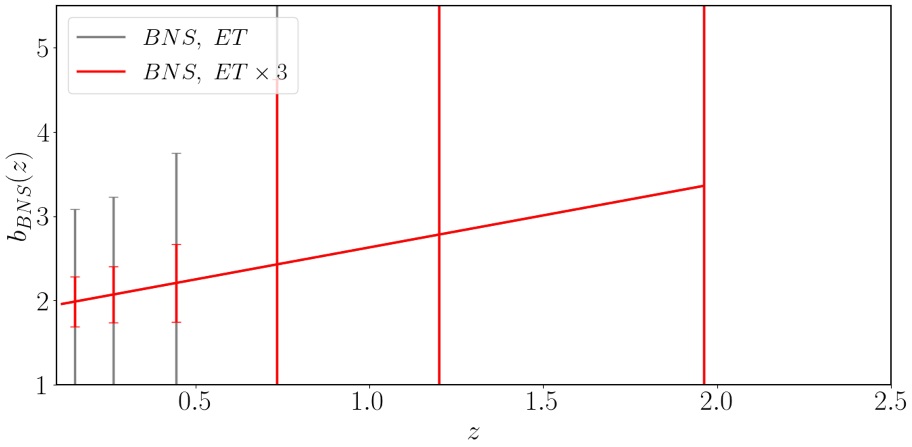

Figure 5.15: Fiducial bias with marginalized forecasted errors in run C for BBH. Grey lines refer to the ET−like survey, while blue lines refer to ET×3. Each point highlights the central z_i of the bins; for sake of clarity in showing the results, only the i = even bins for which $[\sigma_{b_{BBH}}/b_{BBH}](z_i) < 0.7$ are showed, that is $z < 2.88$.

To verify whether this method allows to constrain merger bias without any cosmological assumption, the run D configuration is studied as well, in which uniform priors are assumed on all the cosmological parameters. Results from run C and run D are compared in figure 5.17, for both BBH and BNS in the case of an ET×3: their results differ slightly at low z, particularly for the BNS case, while at high

[18] 18: The conversion between LDS and redshift space is done here by assuming the fiducial cosmology [13].

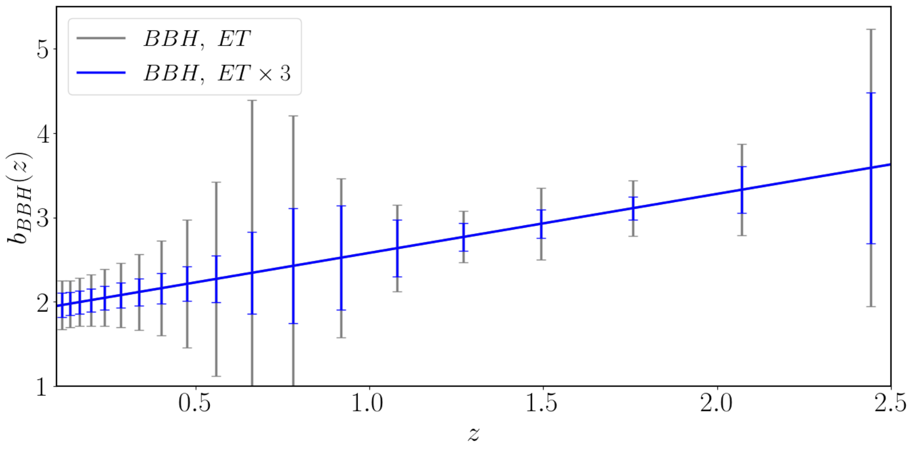

Figure 5.16: Fiducial bias with marginalized forecasted errors in run C for BNS. Grey lines refer to the ET−like survey, while red lines refer to ET×3. Each point highlights the central z_i of the bins; all the bins have been plotted.

z the difference between the two becomes negligible. Therefore, in this setting, the constraining power on bias almost does not depend on the prior assumed for cosmology, particularly in the BBH case.

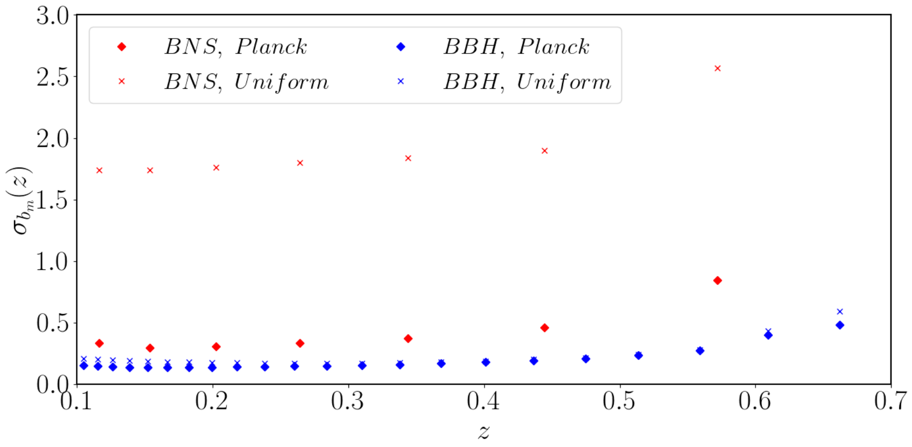

Figure 5.17: Bias forecasted errors obtained through run C with *Planck 2018* [13] priors on cosmology (red dots for BNS, blue dots for BBH) compared to the ones get from run D with uniform prior (red crosses for BNS, blue crosses for BBH). The plots shows that, in this case, the prior on cosmology is relevant only at low z for the BNS case.

It is possible to conclude that, using this technique, merger bias should be detected by both ET and ET×3 at high significance, all the way up to $z \sim 2$ for BBH, up to $z \sim 0.5$ for BNS.

5.6 Results: Follow-up analysis

The analysis developed in section 5.5 [2] has been widened and deepened in [3]. Both single and multi−tracer Fisher matrices have been computed, assuming to observe BBH and BNS either with ET or ET×3 and to map them in LDS. Here, SN from the VRO are mapped as well (see section 5.4.1). As showed in section 5.3.3, the SN distribution and clustering are very different with respect to the GW ones, being relevant only for $z \lesssim 1$. This encourages the use of the multi−tracer technique: as described in section 5.4.3, in fact, the more the tracers differentiate, the more their combination allows us to break important degeneracies between the parameters.

Parameters adopted in this case for the Fisher analysis are:

$$\boldsymbol{\theta} = \left[H_0, \Omega_c h^2, w_0, w_a, \Omega_b h^2, n_s, A_s, A_i, P_i\right] . \tag{5.66}$$

With respect to eq. (5.64), eq. (5.66) introduces three new cosmological parameters: the dimensionless baryon density Ω_b, the primordial scalar index n_s and the amplitude of the primordial power spectrum A_s (see chapter 2 for detail). The choice of the bias parameters, instead, depends on the surveys that are taken into account. Each tracer i, in fact, has its own bias, which can be described through the bias model $b_i(z) = A_i(z + B_i)^{P_i}$ obtained in eq. (5.41). A_i and P_i represent respectively the amplitude and the slope of b_i, while B_i describes the bias local value. In the analysis, its value is conditioned since it is fully degenerate with A_i. Fiducial values for A_i and B_i are described in section 5.3.2 and section 5.3.3: in particular, $A_{BBH} = 0.7$, $A_{BNS} = 0.7$, $A_{SN} = 0.7$. P_i is set to 1 for BBH and BNS (linear bias, found from the HOD/GOD model), 0 for SN (analytical prescription). Note that, differently from section 5.5, per each tracer the bias parameters are the same over all the distance interval observed: their constraints, therefore, will be found by integrating the information over all the D_L bins. In this case, the derivatives required by eq. (5.58) are computed numerically for the cosmological parameters, analytically for the bias ones. In particular, since $C^{ij}_{\ell,s_1s_2} = b_1b_2\, C^{ij}_{\ell,DM}$, one gets per each angular power spectrum:

$$\begin{aligned}
\frac{\partial C_{\ell,s_1s_2}}{\partial A_1} &= (z_i + B_1)^{P_1} b_2\, C_{\ell,DM} \\
\frac{\partial C_{\ell,s_1s_2}}{\partial A_2} &= b_1 (z_j + B_2)^{P_2}\, C_{\ell,DM} \\
\frac{\partial C_{\ell,s_1s_2}}{\partial P_1} &= A_1 \ln[z_i + B_1](z_i + B_1)^{P_1} b_2\, C_{\ell,DM} \\
\frac{\partial C_{\ell,s_1s_2}}{\partial P_2} &= b_1 A_2 \ln[z_j + B_2](z_j + B_2)^{P_2}\, C_{\ell,DM}\ .
\end{aligned} \tag{5.67}$$

Uniform priors are initially assumed for all the parameters. Subsequently, the effects of the presence of a prior on the bias slope are analysed. Including *Planck 2018* [13] priors on cosmological parameters in the single−tracer analysis, would dominate over the signal in the case of GW, whereas analogously to section 5.5, in the case of ET×3 does not produce a significant improvement in the final constraints.

5.6.1 Single-tracer analysis

The single-tracer analysis is performed separately for SN, BBH and BNS mergers; in the case of GW surveys, both ET and ET×3 are considered.

In the case of cosmological parameters, as table 5.5 shows, forecasts for SN are very good since VRO probes small scales. On the contrary, the low−precision sky localization of ET prevents us from having good constraints for both BNS and BBH; for this reason, ET forecasts are not reported in the table. Considering ET×3 leads to significant improvements, even though the overall constraining power remains relatively small, compared to other cosmological probes.

As for the bias parameters (A_i, P_i), their marginalized errors are described in table 5.6.

These are used to compute the uncertainties σ_{b_i} on the estimates of the bias

	H_0	$\Omega_c h^2$	w_0	w_a
SN	7.864	$1.168 \cdot 10^{-2}$	$1.070 \cdot 10^{-1}$	$9.828 \cdot 10^{-1}$
BNS ET×3	76.67	$1.470 \cdot 10^{-2}$	1.798	12.23
BBH ET×x3	16.28	$2.446 \cdot 10^{-2}$	$2.552 \cdot 10^{-1}$	1.622

	$\Omega_b h^2$	n_s	A_s
SN	$1.468 \cdot 10^{-3}$	$8.924 \cdot 10^{-2}$	$3.315 \cdot 10^{-10}$
BNS ET×3	$2.651 \cdot 10^{-2}$	$3.613 \cdot 10^{-1}$	$2.947 \cdot 10^{-9}$
BBH ET×3	$5.134 \cdot 10^{-3}$	$1.783 \cdot 10^{-1}$	$5.976 \cdot 10^{-10}$

Table 5.5: Marginalized $1-\sigma$ errors for cosmological parameters, single-tracer analysis.

	A_{BBH}	P_{BBH}	A_{BNS}	P_{BNS}	A_{SN}	P_{SN}
SN	–	–	–	–	0.156	0.020
BNS	–	–	12.80	14.65	–	–
BNS ET×3	–	–	4.572	5.014	–	–
BBH	1.446	1.607	–	–	–	–
BBH ET×3	0.382	0.404	–	–	–	–

Table 5.6: Marginalized $1-\sigma$ errors for bias parameters, single-tracer analysis. Fiducial values for the parameters are $A_{BBH} = 0.7$, $P_{BBH} = 1$, $A_{BNS} = 0.76$, $P_{BNS} = 1$, $A_{SN} = 1.9$, $P_{SN} = 0$.

coefficients, $b_i(z)$ through error propagation:

$$\sigma^2_{b_i} = \begin{bmatrix} \frac{\partial b_i}{\partial A_i} & \frac{\partial b_i}{\partial P_i} \end{bmatrix} \begin{bmatrix} \sigma^2_{A_i} & \mathrm{cov}(A_i, P_i) \\ \mathrm{cov}(A_i, P_i) & \sigma^2_{P_i} \end{bmatrix} \begin{bmatrix} \frac{\partial b_i}{\partial A_i} \\ \frac{\partial b_i}{\partial P_i} \end{bmatrix} . \tag{5.68}$$

As figure 5.18 shows, this kind of technique provides very good constraints for SN bias: its relative error is $\sigma_{b_{SN}}/b_{SN}(z)|_z \lesssim 10\%$ over all the redshifts considered. As for GW events instead, our results for BBH bias can be compared with e.g., with results from [297]. The technique implemented there is based on cross−correlations between GW and galaxy surveys, aimed at estimating the redshift for the observed mergers. Their analysis reaches values of $\sigma_{b_{BBH}}/b_{BBH}|_{z=0} \simeq 20-30\%$ for a dataset of $\simeq 200$ BBH events observed with 10deg^2 sky localization uncertainty; the set of cosmological parameters there adopted only includes either $[H_0, \Omega_c]$ with $[w_0, w_a]$ fixed or $[\Omega_\Lambda, \Omega_c]$ with $[H_0, w_0, w_a]$ fixed. With our technique, a similar level of accuracy can be reached with ET×3 configuration, which has similar sky localization (3deg^2) but comprises a larger number of sources ($\simeq 10^4 - 10^5$), or through the use of the multi−tracer technique described in the following section. This is due to the degeneracies that exist both between cosmological (e.g., H_0) and bias parameters in LDS and between the bias amplitude and slope parameters (see figure 5.22), which propagate inside the σ_{b_i} computation. Due to the same reason, both ET and ET×3 forecasts in this section are a bit worse with respect to the ones found using the method described in section 5.5 [2].

5.6.2 Multi-tracer analysis

The multi−tracer analysis considers different combinations of tracers and detectors, to test their impact on the final forecasts. It is based on the use of cross−power spectra of sources having different clustering properties: as described in section 5.4.3, the use of two LSS tracers with different bias improves the bias−related constraints on large scales because it allows us to overcome the need of modelling the underlying DM distribution [339–342]. In the case we are analysing i.e., the combination of GW events and SN, the presence of the former makes it possible to cover a larger redshift

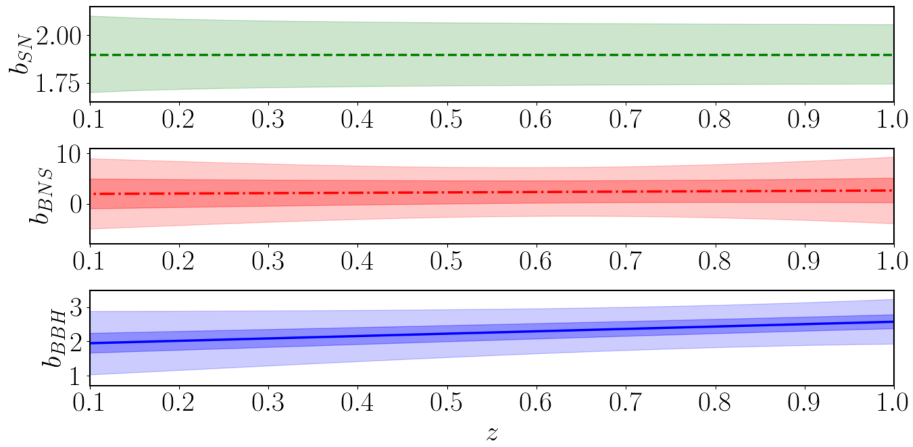

Figure 5.18: Marginalized $1-\sigma$ errors for the bias at low z for SN (green dashed line, upper panel), BNS (red dot–dashed line, central panel) and BBH (blue continuous line, lower panel) single–tracer analysis. The bold line represent the fiducial models from eq. (5.41), while the shaded areas are included between $b_i \pm \sigma_{b_i}$, with σ_{b_i} from eq. (5.68). For BNS and BBH both the ET (lighter) and ET×3 (darker) constraints are showed.

range than single–tracer analysis that only includes the latter. Moreover, improving constraints on bias–related parameters allows us also to break degeneracies and to enhance the constraints on correlated parameters e.g., on cosmology [344, 345]. Finally, using more than one tracer we can enlarge the sampling of the larger scales and therefore we can improve the total signal–to–noise ratio by lowering the cosmic variance effect [342, 346].

In the case of cosmological parameters, table 5.7 shows the forecasted $1-\sigma$ marginalized errors, while figure 5.19 shows their confidence ellipses.

On one hand, the BNS+BBH(ET×3) scenario only slightly improves the forecasts with respect to the single–tracer case, since the ratio of BNS and BBH biases is small. Therefore, even when combining them, the tracing of the underlying DM field is not improved. On the other hand, when including SN, forecasts largely improve with respect to the only–GW cases. In the ET configuration, forecasts for BBH(ET)+SN are very close to those obtained in the SN single–tracer analysis, since their contribution is dominant with respect to the BBH. In the ET×3 configuration, instead, BBH and SN constraints in the single–tracer analysis are comparable. Therefore, when they are combined by mean of the multi–tracer analysis, they both contributes to the improvements of the final constraints. In this case, in fact, the multi–tracer results reach a very good constraining power: this is clear by looking at figure 5.19, where confidence ellipses related with the BBH(ET×3)+SN multi–tracer technique (black, continuous line) are way smaller than both BBH(ET×3) (blue, continuous line) and SN (green, dotted line) in the single–tracer configuration.

Table 5.7: Marginalized $1-\sigma$ errors for cosmological parameters, multi–tracer analysis.

	H_0	$\Omega_c h^2$	w_0	w_a
BNS + BBH (ET×3)	7.472	$1.987 \cdot 10^{-2}$	$1.938 \cdot 10^{-1}$	1.035
BBH (ET) + SN	6.386	$8.378 \cdot 10^{-3}$	$9.135 \cdot 10^{-2}$	$1.158 \cdot 10^{-1}$
BBH (ET×3) + SN	3.012	$6.983 \cdot 10^{-3}$	$6.701 \cdot 10^{-2}$	$2.532 \cdot 10^{-1}$

	$\Omega_b h^2$	n_s	A_s
BNS + BBH (ET×3)	$3.772 \cdot 10^{-3}$	$1.603 \cdot 10^{-1}$	$3.405 \cdot 10^{-10}$
BBH (ET) + SN	$2.108 \cdot 10^{-3}$	$6.716 \cdot 10^{-2}$	$1.023 \cdot 10^{-10}$
BBH (ET×3) + SN	$5.675 \cdot 10^{-4}$	$5.554 \cdot 10^{-2}$	$5.842 \cdot 10^{-11}$

As a benchmark, these results can be compared with those for galaxy clustering in a future *Euclid*–like survey [295]. The multi–tracer forecasts are comparable with the *Euclid*–like ones for most of the parameters, the main exceptions being

Figure 5.19: Confidence 1− and 2 − σ ellipses for cosmological parameters computed for BBH (ET×3, blue), SN (green dashed) and BBH(ET×3)+SN (black).

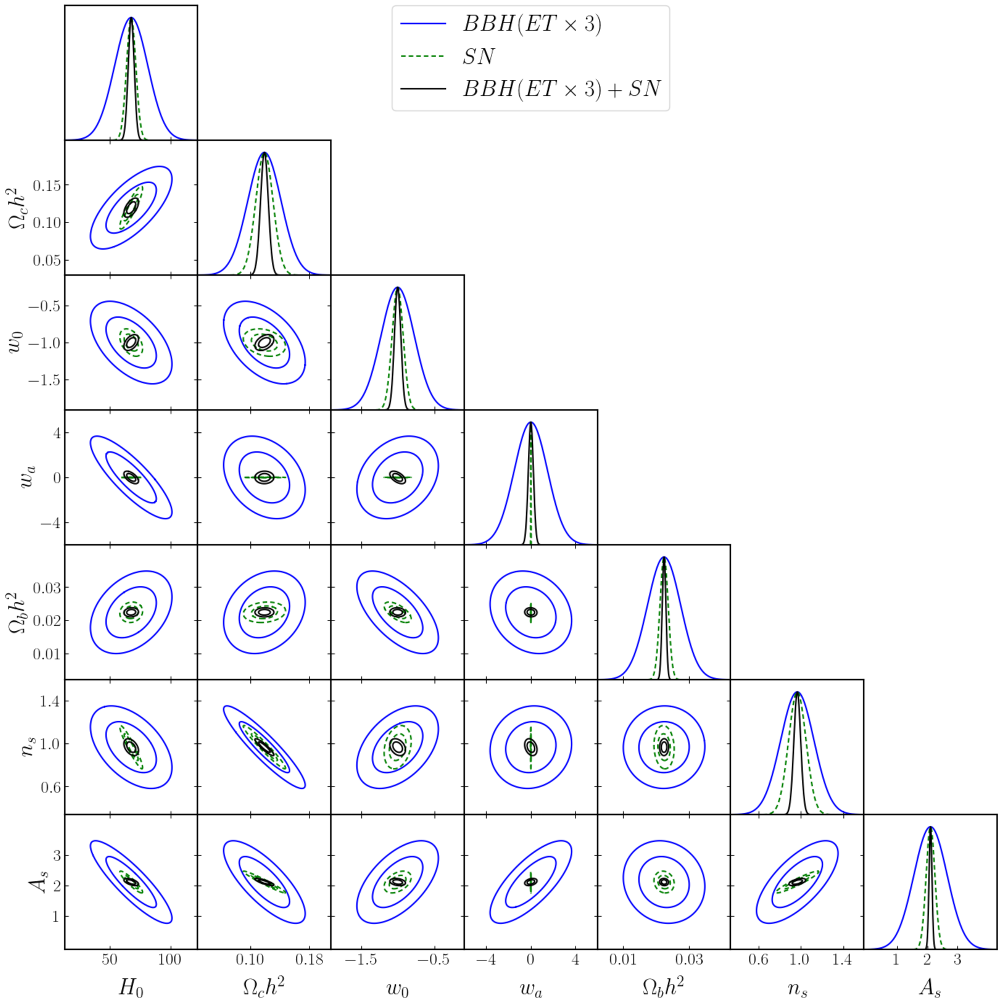

the dark energy parameters w_0, w_a and the Hubble parameter H_0. In the case of DE parameters, the results are improved by the combination of the small scales reached by SN with the large volumes probed by BBH. In the case of Hubble parameter, instead, GW+SN have a small constraining power due to the degeneracy this parameter has with respect to the bias parameters A_i, P_i. This is visualized by the elongated ellipse in figure 5.20, where it is shown that the multi−tracer technique improves the situation but can not break completely the degeneracy.

For the bias parameters as well, the improvements in the multi−tracer approach are significant considering both ET and ET×3. Table 5.8 shows that the constraining power on A_i and P_i improves considerably especially when the GW+SN analysis is considered.

	A_{BBH}	P_{BBH}	A_{BNS}	P_{BNS}	A_{SN}	P_{SN}
BNS + BBH (ET×3)	0.303	0.322	0.379	0.456	–	–
BBH (ET) + SN	0.308	0.384	–	–	0.085	0.018
BBH (ET×3) + SN	0.126	0.145	–	–	0.058	0.013

Table 5.8: Marginalized 1 − σ errors for bias parameters, multi−tracer analysis.

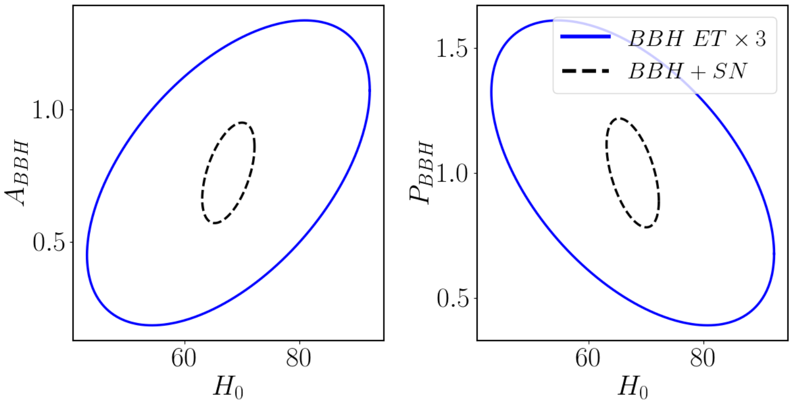

Figure 5.20: Confidence $1-\sigma$ ellipse for the H_0 and A_{BBH} (left) and P_{BBH} (right) parameters. The ET×3 single−tracer analysis is shown through the continuous blue line, while the dashed black line refers to the BBH+SN case.

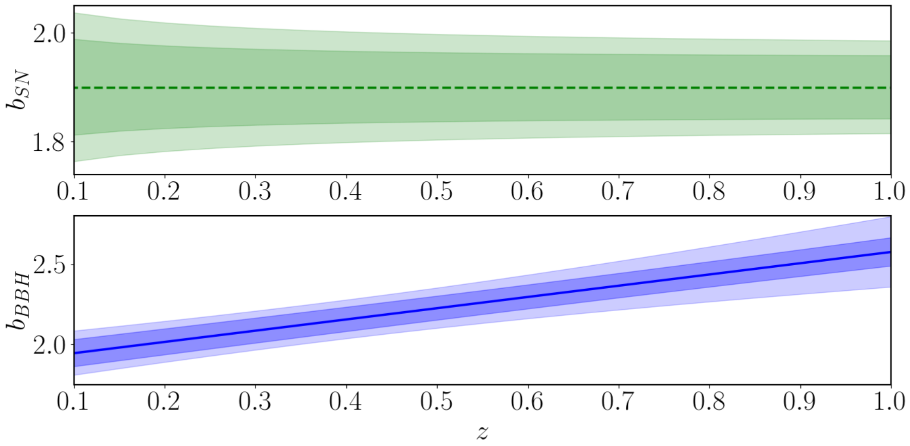

Figure 5.21: Bias error forecasts for SN and BBH in the BBH(ET)+SN and BBH(ET×3)+SN cases; the legend is the same as figure 5.18.

5.6.3 Effects of using a prior on bias parameters

Since the ET catalogues will be dominated by BBH observations, it is particularly interesting to understand the detectability of their bias. The bias error $\sigma_{b_{BBH}}$ depends on both the uncertainties on the amplitude A_{BBH} and on the slope P_{BBH} parameters, but the two are degenerate one with respect to the other, as the elongated ellipse in figure 5.22 shows. The multi−tracer technique slightly improves the situation.

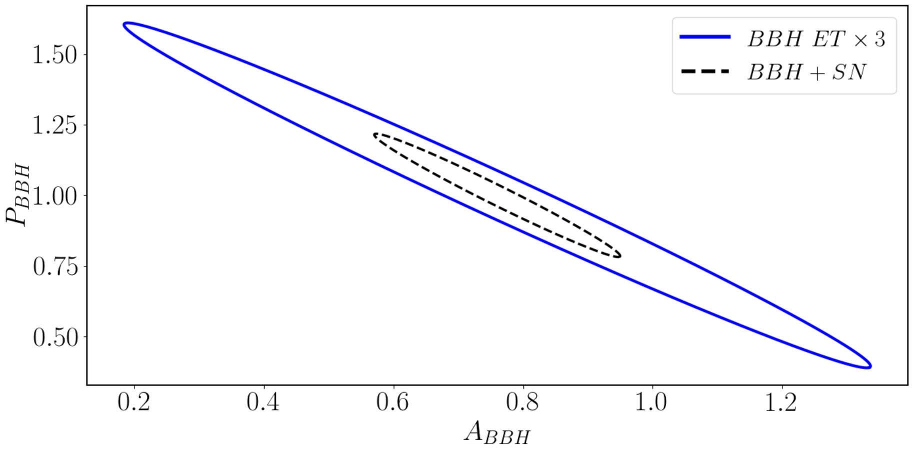

Figure 5.22: Confidence $1-\sigma$ ellipse for the A_{BBH} and P_{BBH} parameters. The ET×3 single−tracer analysis is shown through the continuous blue line, while the dashed black line refers to the BBH+SN case.

A good alternative to solve this issue is to change the priors assumed on the bias parameters. Up to now, they were considered as uniform; however, the linear trend obtained for the slope parameter P_{BBH} from the analysis in section 5.3.1 not only is based on the HOD/GOD analysis of hydrodynamical simulations [204, 205, 322], but also it is find in agreement with other works in the literature (see e.g., [297, 301]). For this reason, it seems reasonable to increase the level of reliability of the fiducial value $P_{BBH} = 1$ by associating a Gaussian prior to it.

Table 5.9 shows the effect of including different P_{BBH} priors in the single− and full multi−tracer cases; all the measurements refer to the ET or ET×3 scenarios. As expected, the more information the survey provides, the less impact the prior inclusion has in the analysis. The error propagation through eq. (5.68) changes as well depending on the P_{BBH} prior. This is showed by figure 5.23 in the case of ET; the constraints obviously further improve considering ET×3.

$\sigma^{prior}_{P_{BBH}}/P_{BBH}$	tracer	ET		ET×3	
		A_{BBH}	P_{BBH}	A_{BBH}	P_{BBH}
80%	BBH	0.663	0.716	0.341	0.361
	BBH + SN	0.278	0.346	0.124	0.142
50%	BBH	0.461	0.477	0.299	0.314
	BBH + SN	0.245	0.305	0.121	0.139
20%	BBH	0.249	0.198	0.176	0.179
	BBH + SN	0.146	0.177	0.103	0.117

Table 5.9: Effects of different P_{BBH} Gaussian priors on the marginalized errors of bias parameters.

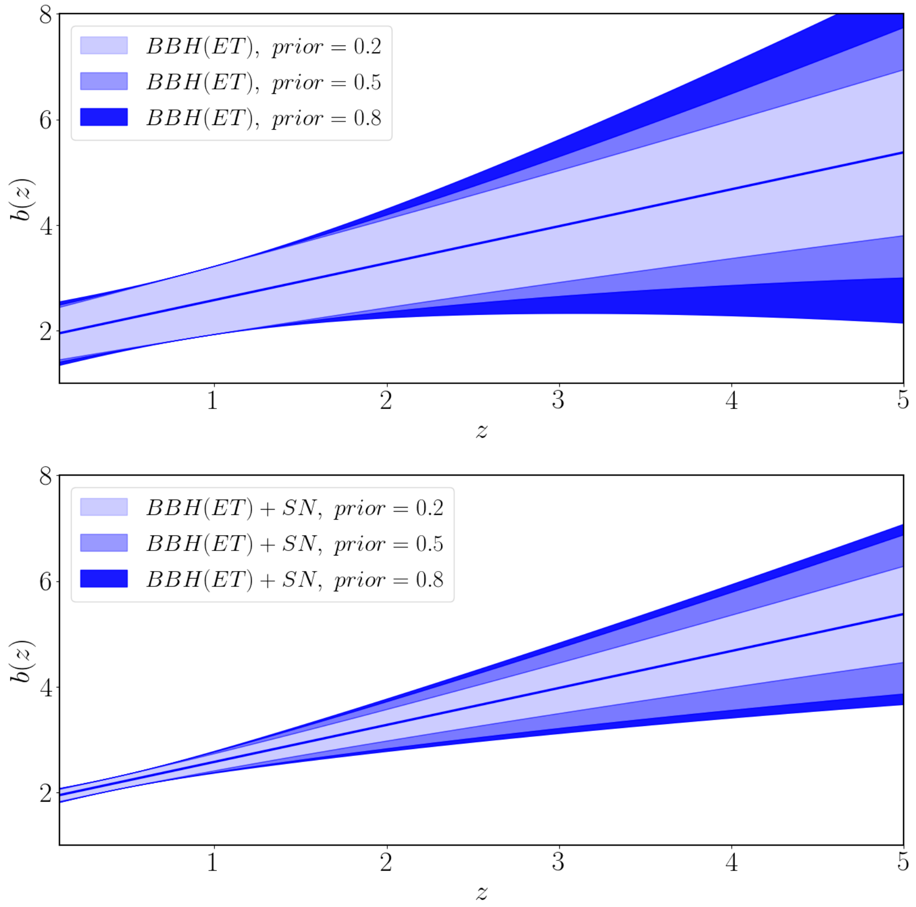

Figure 5.23: BBH bias error obtained in the single ET case (top panel) and in the BBH(ET)+SN case (bottom panel) assuming the different priors on P_{BBH} described in table 5.9. The darker area is related to the larger prior.

This analysis confirms what section 5.5 anticipated: future GW surveys will be able to detect and constrain the bias of astrophysical BBH. Einstein Telescope itself will be able to provide a first measurement for this: properly choosing the analysis technique and eventually relying on the possibility of assuming some prior or combining ET with other tracers, the bias will possibly be detect with a high accuracy.

This result opens the road for a new kind of analysis, which chapter 6 develops: using the bias to disentangle mergers produced by astrophysical black hole binaries from mergers due to black holes of primordial origin.

Model selection for PBH scenarios 6

6.1 Bayesian statistics 108
Model selection and Bayes factor 108
Laplace approximation and Gaussian prior . . . 109
6.2 Merger distribution and clustering . 112
ABH 112
PBH 113
Blind survey 115
6.3 Results 116

Section 3.3.3 introduced the idea that different formation channels for the progenitors of binary mergers can lead to different clustering properties. In particular, the difference is significant when comparing astrophysical black hole mergers with primordial black hole mergers (note that in this chapter, when indicating ABH or PBH we will always refer to binaries, not to single compact objects). While ABH are mainly located in the massive halos where galaxies originate (see section 3.3.1), PBH are either distributed consistently with dark matter (early binaries, E) or they belong to small halos, where the velocities are smaller and dynamical captures are efficient (late binaries, L).

Section 5.5 and section 5.6, then, showed that future gravitational wave surveys will be able to constrain the bias of astrophysical black hole mergers with a good level of accuracy through the use of tomographic angular power spectra in luminosity distance space. Other works e.g., [297, 300, 301], showed similar results also for redshift space when using cross−correlations with galaxy surveys. Therefore, the bias of the black hole mergers i.e., of their hosts, will be a well−constrained observable for next−future gravitational wave surveys. As soon as the Einstein Telescope [255–257] will be online, the number of observed GW events will enormously increase (see references in section 4.2): in a few years, merger catalogues will contain hundreds of thousands of events, observed over the full sky and up to very high distances.

Assuming that PBH in the $[10, 100]\,M_\odot$ window exist and that they make up a fraction f_{PBH} of the DM in the Universe (see eq. (2.64)), the GW signal produced by the merger of their binaries would be completely indistinguishable from that of ABH mergers, since they will both be characterized by the same waveform i.e., the one described in section 4.3. ET observations, therefore, will provide a **blind survey** for these two kinds of events, being unable to disentangle their progenitor origin by looking at the signal alone.

Measurements of their clustering will then be crucial to break this degeneracy: as first proposed by [117] and then further explored in [300, 301, 348], an ABH−dominated or a early PBH−dominated survey should show a different behaviour due to the different bias describing their binary distributions. All these works relied on cross−correlation between GW and galaxy surveys to forecast the possible outcomes of this kind of analysis. In fact, the more ABH dominate the distribution over early PBH, the higher the correlation is; as long as the number of early PBH mergers is increased, the correlation between the blind survey and galaxy reduces.

In a work currently in its final stages, we propose an alternative method to understand whether a future GW blind survey will be able to test the existence of PBH or not. The different bias behaviours of ABH and PBH, in fact, combine in an overall *blind* bias, the functional form of which depends on the relative abundance of the two. This is parametrized by the parameter:

$$\Gamma(z) = \frac{\mathcal{N}^P(z)}{\mathcal{N}^{tot}(z)} = \frac{\mathcal{N}^E(z) + \mathcal{N}^L(z)}{\mathcal{N}^A(z) + \mathcal{N}^E(z) + \mathcal{N}^L(z)}\ , \tag{6.1}$$

where $\mathcal{N}^A(z)$, $\mathcal{N}^E(z)$, $\mathcal{N}^L(z)$ are respectively the number of ABH, early PBH and late PBH. $\mathcal{N}^E(z)$ and $\mathcal{N}^L(z)$ then combines into the number of PBH $\mathcal{N}^P(z)$, observed in a redshift bin centered in z. Figure 6.1 shows how the term from eq. (6.1) behaves when ABH and PBH are described as in section 6.2.1 and section 6.2.2. The differences in the bias related to $\Gamma(z)$ propagate to differences in the observed angular power spectra and, as described in chapter 5, they will be well constrained even by a single ET detector. The estimate of the bias of the blind survey therefore will be suitable to perform model selection analysis and to disentangle between the scenario which results are consistent with ABH mergers alone, and the one in which PBH are required to explain the data.

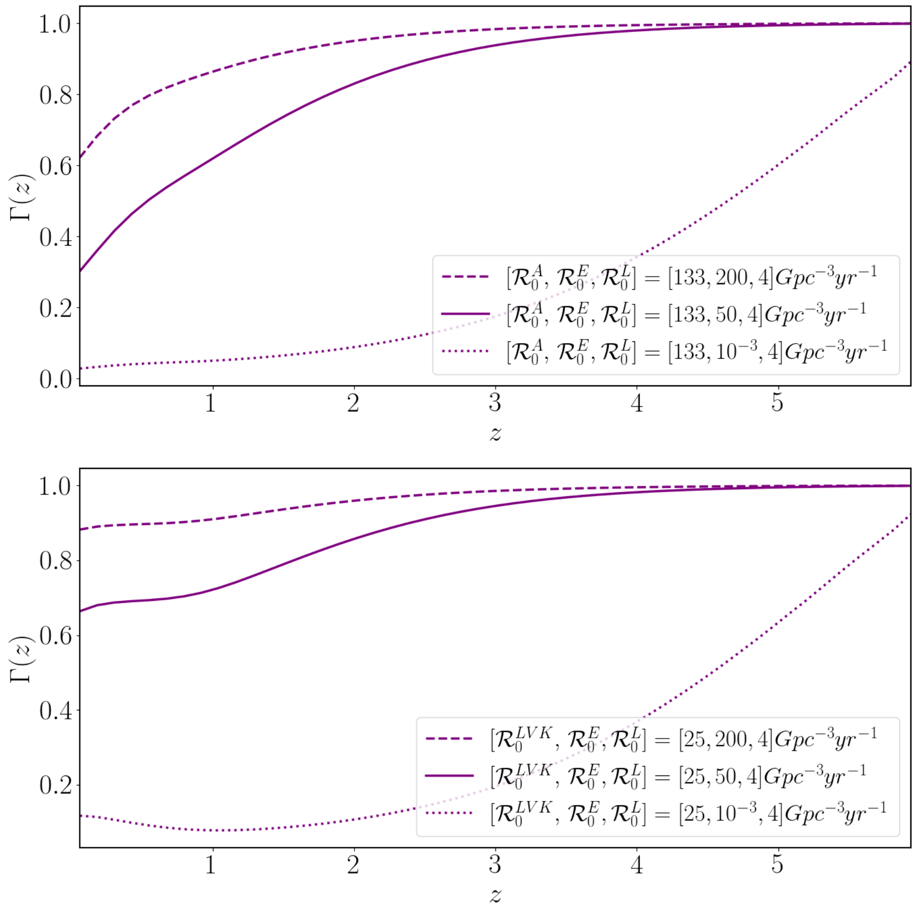

Figure 6.1: $\Gamma(z)$ computed for the ABH and PBH configurations described in section 6.2.1 and section 6.2.2. These are $\mathcal{R}_0^A = 133\,\mathrm{Gpc}^{-3}\mathrm{yr}^{-1}$ (top panel), $\mathcal{R}_0^{LVK} = 25\,\mathrm{Gpc}^{-3}\mathrm{yr}^{-1}$ (bottom panel), $\mathcal{R}_0^L = 4\,\mathrm{Gpc}^{-3}\mathrm{yr}^{-1}$, $\mathcal{R}_0^E = [10^{-1},\ 50,\ 200]\,\mathrm{Gpc}^{-3}\mathrm{yr}^{-1}$ (respectively the dotted, continuous and dashed lines).

In this chapter we present model selection forecasts to verify whether this technique has the potential to discriminate between these two possibilities. The analysis is performed in luminosity distance space, in analogy to chapter 5; however, we always use the redshift notation since it is more familiar in LSS studies. As in chapter 5, z is computed from D_L assuming the fiducial cosmology from [13] described in table 2.1.

In particular, in section 6.1 we revise the main features of the Bayesian statistics required in the analysis and we introduce the Bayes factor through which model selection is performed. In section 6.2 we characterize the ABH and PBH number distribution and bias adopted in the analysis, together with the *blind* configurations they produce. Finally, in section 6.3, we discuss the analysis set–up and we present the results obtained. A paper describing the work discussed in this chapter will soon be published [4]: here, the analysis will be expanded with respect to the one presented in this thesis. In particular, we will consider different configurations for both the detector setup and the observed source number distribution and we will provide an insightful analysis of the case in which correlations and degeneracies exist between the parameters of the models under study.

6.1 Bayesian statistics

Bayesian statistics interprets probability as the degree of belief in some hypothesis $\boldsymbol{\theta}$ given that $\mathscr{O}$ is measured [336, 337, 349]. With $\mathscr{O}$ we generally indicate either the data itself or some quantity estimated from the data e.g., the power spectrum. The two are related via the **Bayes theorem**:

$$p(\boldsymbol{\theta}|\mathscr{O}) = \frac{p(\mathscr{O}|\,\boldsymbol{\theta})p(\boldsymbol{\theta})}{p(\mathscr{O})} \,. \tag{6.2}$$

In eq. (6.2), $p(\mathscr{O})$ and $p(\boldsymbol{\theta})$ are respectively the probabilities that the data and the hypothesis sets occur, while $p(\mathscr{O}|\boldsymbol{\theta})$ and $p(\boldsymbol{\theta}|\mathscr{O})$ are the conditional probabilities of data on hypothesis or vice versa i.e., the probability that the first of them occurs given that the second has occurred. In Bayesian statistics, these quantities are identifies [336, 337, 349] as:

$p(\boldsymbol{\theta}|\mathscr{O})$: the **posterior**, which represents the degree of belief in the hypothesis provided that the data are measured;

$p(\boldsymbol{\theta})$: the **prior**, which encloses the initial degree of belief based on some starting knowledge;

$p(\mathscr{O}|\,\boldsymbol{\theta})$: the **likelihood**, which describes the probability that the data−set is measured given that the hypothesis are correct;

$p(\mathscr{O})$: the **evidence** of the data. This is an irrelevant normalization in parameter estimation (such as in the analysis carried on in section 7.3 and section 7.4), but it is crucial for model selection.

Usually in cosmological studies $\boldsymbol{\theta} = (\theta_1 ... \theta)$ represent the parameters that a certain model $\mathscr{M}$ uses to describe an observable quantity. In this sense, the posterior measures how good the values $(\bar{\theta}_1 ... \bar{\theta}_H)$ are in describing the estimates $\mathscr{O}$ of the observable. When data are actually measured, the true likelihood can be built from them and used to model the posterior (see e.g., chapter 7); instead, in forecast analysis, it is customary to assume the **Laplace approximation** [336, 350], in which the expected likelihoods are described by a multivariate Gaussian:

$$\mathscr{L} = \left\langle p(\mathscr{O}|\,\boldsymbol{\theta}) \right\rangle = \mathscr{L}_0 \exp\left[-\frac{1}{2} (\boldsymbol{\theta} - \boldsymbol{\theta}_0)_\alpha F_{\alpha\beta} (\boldsymbol{\theta} - \boldsymbol{\theta}_0)_\beta \right] , \tag{6.3}$$

where the $F_{\alpha\beta}$ is the Fisher matrix defined in eq. (5.53) for a Gaussian distribution, $\boldsymbol{\theta}_0$ are the parameters value at the likelihood peak and $\mathscr{L}_0$ is the normalization.

6.1.1 Model selection and Bayes factor

In the Bayesian framework, model selection techniques are used to understand whether a theoretical model $\mathscr{M}_1$ is preferred above another $\mathscr{M}_2$ in describing a certain data−set $\mathscr{O}$. To do so, if the two models have the same *a priori* probability, the Bayesian evidence ratio between them is used to estimate the probability of one with respect to the other. Particularly, in section 6.3 we will compare the two models:

- $\mathscr{M}_1$ = only ABH contributes to the GW merger emission.
- $\mathscr{M}_2$ = both ABH and PBH contribute to GW merger emissions that ET will observe.

Let $\boldsymbol{\theta}_1,\ \boldsymbol{\theta}_2$ be the parameters describing the two models, with parameter vectors having dimension $n_1,\ n_2$, with $n_1 < n_2$. The evidence ratio of the models, named the **Bayes factor**, is defined as [336, 337, 349–351]:

$$B_{12} = \frac{\int d\boldsymbol{\theta}_1\ p(\mathbb{O}|\boldsymbol{\theta}_1, \mathscr{M}_1)p(\boldsymbol{\theta}_1|\mathscr{M}_1)}{\int d\boldsymbol{\theta}_2\ p(\mathbb{O}|\boldsymbol{\theta}_2, \mathscr{M}_2)p(\boldsymbol{\theta}_2|\mathscr{M}_2)}\ . \tag{6.4}$$

Eq. (6.4) can be used also in a forecast analysis (see e.g., [350, 351]). This is particularly interesting to study cases in which the $\mathscr{M}_1$ is nested in $\mathscr{M}_2$, that is $\boldsymbol{\theta}_1 \in \boldsymbol{\theta}_2$ and $n_e = n_2 - n_1$ is the number of extra−parameters. As shown in [350], assuming the Laplace approximation from eq. (6.3), the Bayes factor becomes:

$$\langle B_{12}\rangle = (2\pi)^{-n_e/2}\frac{\sqrt{\det F_2}}{\sqrt{\det F_1}}\exp\left[-\frac{1}{2}\delta\theta_2^{\alpha}F_2^{\alpha\beta}\delta\theta_2^{\beta}\right]\prod_{q=1}^{n_e}\Delta\theta_2^{n_1+q}\ . \tag{6.5}$$

$F_{1,2}$ are the Fisher matrices evaluated for the two models, $\Delta\theta_2^{n_1+1,\dots\, n_2}$ the prior ranges of the extra−parameters and $\delta\theta_2^{\alpha,\beta}$ the shifts in the fiducial values $\bar{\boldsymbol{\theta}}_{1,2}$ of all the n_1, n_2 parameters between the two models. These are defined as:

$$\delta\theta^{\alpha} = \begin{cases} |\bar{\theta}_1^{\alpha} - \bar{\theta}_2^{\alpha}| & \text{if } \alpha > n_1 \text{ (i.e., extra-parameters)} \\ -(F_{1(2)}^{-1})^{\alpha\gamma}G^{\gamma\zeta}\delta\theta_2^{\zeta} & \text{if } \alpha < n_1 \text{ (i.e., common parameters)} \end{cases} \tag{6.6}$$

$G^{\gamma\zeta}$ is a $n_1{\times}n_e$ subset of F_2, considering the $\gamma = 1, \dots n_1$ rows related to the common parameters and the $\zeta = n_1 + \ \dots\ n_e$ columns related with the extra ones. $F_{1(2)}$ is the $n_1 \times n_1$ submatrix in F_2 which only includes the common parameters. Note that, while $F_{1(2)}$ is computed with respect to the fiducial values of the parameters in M_2, F_1 in eq. (6.5) is computed at the fiducial values in M_1 i.e., after that the shifts defined in eq. (6.6) are applied.

In the case $n_e = 1$, the Bayes factor can be estimated also through the **Savage−Dickey ratio**. This is defined as:

$$\langle B\rangle = \frac{p(\theta_2^{\alpha}|\mathbb{O})|_{\tilde{\theta}_2^{\alpha}(\mathscr{M}_1)}}{p(\theta_2^{\alpha})}\ . \tag{6.7}$$

This formula applies for any likelihood, not necessarily a Gaussian one. In eq. (6.7), θ_2^{α} is the extra−parameter and $p(\theta_2^{\alpha})$ its prior. The $\mathscr{M}_2$ posterior $p(\theta_2^{\alpha}|\mathbb{O})$ is computed at $\tilde{\theta}_2^{\alpha}(\mathscr{M}_1)$, which is the value at which the extra−parameter must be fixed to recover $\mathscr{M}_1$. In the case in which $\mathscr{M}_1$ does not properly describe the data, conditioning the extra−parameter at $\tilde{\theta}_2^{\alpha}(\mathscr{M}_1)$ shifts the likelihood values of the $\boldsymbol{\theta}_1^{\gamma}$ common parameters to values that are different with respect to their fiducials $\bar{\boldsymbol{\theta}}_1^{\gamma}$. Figure 6.2 sketches the meaning of such shifts with respect to the two likelihoods.

6.1.2 Laplace approximation and Gaussian prior

The setup described in the previous section and the Bayes factor defined in eq. (6.5) imply the use of the Laplace approximation, in which:

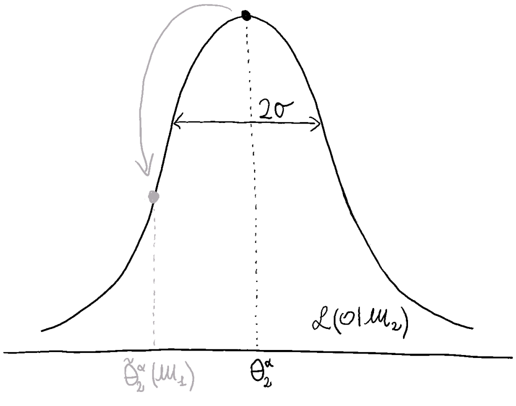

Figure 6.2: Descriptive representation: if $\mathcal{M}_2$ is the correct model, the fiducial value of the extra−parameter θ_2^α maximizes the likelihood of the data $\mathcal{L}(\mathfrak{D}|\mathcal{M}_2)$. In $\mathcal{M}_1$, the value of this parameter is conditioned to a different value $\tilde{\theta}_2^\alpha(\mathcal{M}_2)$. If this is outside the confidence interval 2σ, the likelihood is no longer able to describe the data: therefore, to compensate this issue, also the values of the other parameters $\boldsymbol{\theta}_1^\gamma$ gets shifted according to eq. (6.6).

- the likelihoods $p(\mathfrak{D}|\boldsymbol{\theta}_{1,2})$ in the analysis are well described by multivariate Gaussian distributions;
- the covariance of the likelihoods can be estimated through their averages in the peak i.e., by the means of the inverse of their Fisher matrices;
- the parameter priors are uniform and their boundaries are found in the tails of the likelihoods i.e., where their values are negligible.

However, if some of the parameters correlate, degeneracies can be found in the Fisher matrix and the second condition is not satisfied. To break the degeneracies, a Gaussian prior can be defined for the parameters of interest; in this way, however, the last condition as well is neglected. Therefore, the Laplace approximation can not be adopted and eq. (6.5) can not be recovered.

It is possible to find a new formulation for the forecasted Bayes factor, that does not require the previous assumptions. To do so, we assume that:

- the likelihoods $p(\mathfrak{D}|\boldsymbol{\theta}_{1,2},)$ in the analysis are well described by *unnormalized* multivariate Gaussian distributions;
- the priors $p(\boldsymbol{\theta}_{1,2})$ are as well described by *normalized* multivariate Gaussian distributions, centred in the fiducial values and having covariance σ^2_{prior} for each parameter.

Therefore, we can use eq. (6.4):

$$\begin{aligned}\langle B\rangle &= \left\langle \frac{\int d\boldsymbol{\theta}_1\, p(\mathfrak{D}|\boldsymbol{\theta}_1)\, p(\boldsymbol{\theta}_1)}{\int d\boldsymbol{\theta}_2\, p(\mathfrak{D}|\boldsymbol{\theta}_2)\, p(\boldsymbol{\theta}_2)} \right\rangle \\ &\simeq \frac{\langle \int d\boldsymbol{\theta}_1\, p(\mathfrak{D}|\boldsymbol{\theta}_1)\, p(\boldsymbol{\theta}_1)\rangle}{\langle \int d\boldsymbol{\theta}_2\, p(\mathfrak{D}|\boldsymbol{\theta}_2)\, p(\boldsymbol{\theta}_2)\rangle} \simeq \frac{p(\boldsymbol{\theta}_1|\mathfrak{D})}{p(\boldsymbol{\theta}_2|\mathfrak{D})}\,.\end{aligned} \tag{6.8}$$

To write explicitly the Bayes factor in this configuration, we need to compute the product between the likelihood and the prior. Let us consider two d−dimensional multivariate Gaussian distributions:

$$\mathcal{N}^{un}(a,A) = \exp\left[-\frac{1}{2}(x-a)^T A^{-1}(x-a)\right] = (2\pi)^{d/2}\sqrt{\det A}\,\mathcal{N}(a,A)\,, \tag{6.9}$$

$$\mathcal{N}(b,B) = \frac{1}{(2\pi)^{d/2}\sqrt{\det B}}\exp\left[-\frac{1}{2}(x-b)^T B^{-1}(x-b)\right]. \tag{6.10}$$

We assume that $\mathcal{N}^{un}(a, A)$ is unnormalized, while $\mathcal{N}(a, A)$, $\mathcal{N}(b, B)$ are normalized. The product between the two distributions is the normalized multivariate Gaussian:

$$\mathcal{N}(c, C) = \mathcal{N}^{un}(a, A)\,\mathcal{N}(b, B) = (2\pi)^{d/2}\sqrt{\det A}\,\mathcal{N}(a, A)\,\mathcal{N}(b, B)\,, \tag{6.11}$$

having covariance and mean respectively equal to:

$$C = (A^{-1} + B^{-1})^{-1}\,, \quad c = CA^{-1}a + CB^{-1}b\,. \tag{6.12}$$

The amplitude of $\mathcal{N}(c, C)$ is rescaled through the Gaussian factor:

$$z_c = (2\pi)^{-d/2}\sqrt{\frac{\det C}{\det A \det B}}\exp\left[-\frac{1}{2}\left(a^T A^{-1}a + b^T B^{-1}b - c^T C^{-1}c\right)\right]. \tag{6.13}$$

Therefore, the distribution resulting from the product is:

$$\begin{aligned}
\mathcal{N}(c, C) = {} & (2\pi)^{-d/2}\sqrt{\frac{\det C}{\det A \det B}}\exp\left[-\frac{1}{2}\left(a^T A^{-1}a + b^T B^{-1}b - c^T C^{-1}c\right)\right]\cdot \\
& \cdot\frac{(2\pi)^{d/2}\sqrt{\det A}}{(2\pi)^{d/2}\sqrt{\det C}}\exp\left[-\frac{1}{2}(x - c)^T C^{-1}(x - c)\right] \\
= {} & \frac{(2\pi)^{-d/2}}{\sqrt{\det B}}\exp\left[-\frac{1}{2}\left(a^T A^{-1}a + b^T B^{-1}b - c^T C^{-1}c\right)\right]\cdot \\
& \cdot\exp\left[-\frac{1}{2}(x - c)^T C^{-1}(x - c)\right]
\end{aligned} \tag{6.14}$$

In the analysis performed in the following sections, we need to compute eq. (6.14) for both $\mathcal{M}_1$ and $\mathcal{M}_2$. In each case:

- $A^{-1} = F_{1,2}$ is the Fisher matrix;
- $B = P_{1,2}$ is the prior diagonal covariance matrix, whose elements are σ^2_{prior};
- $C = (F_{1,2} + P^{-1}_{1,2})^{-1} = (F^*_{1,2})^{-1}$ represents the inverse of the Fisher matrix once that the Gaussian priors are taken into account;
- $a = b = \bar{\boldsymbol{\theta}}_{1,2}$ are the fiducial values of the parameters; consequently, $c = \bar{\boldsymbol{\theta}}_{1,2}$ as well;
- $d = n_{1,2}$ is the number of parameters in the model $M_{1,2}$.

Separately for the two models, eq. (6.14) becomes:

$$\begin{aligned}
\mathcal{N}(c, C) = {} & \frac{(2\pi)^{-n_{1,2}/2}}{\sqrt{\det P_{1,2}}}\exp\left[-\frac{1}{2}\left(\bar{\boldsymbol{\theta}}_2^T\left[F_{1,2} + P^{-1}_{1,2} - F^*_{1,2}\right]\boldsymbol{\theta}\right)\right]\cdot \\
& \cdot\exp\left[-\frac{1}{2}(\boldsymbol{x} - \bar{\boldsymbol{\theta}}_{1,2})^T F^*_{1,2}(\boldsymbol{x} - \bar{\boldsymbol{\theta}}_{1,2})\right] \\
= {} & (2\pi)^{-n_{1,2}/2}\sqrt{\frac{1}{\det P_{1,2}}}\exp\left[-\frac{1}{2}(\boldsymbol{x} - \bar{\boldsymbol{\theta}}_{1,2})^T F^*_{1,2}(\boldsymbol{x} - \bar{\boldsymbol{\theta}}_{1,2})\right]
\end{aligned} \tag{6.15}$$

The expression in eq. (6.15) enters the Bayes factor at the numerator for $\mathcal{M}_1$, at the denominator for $\mathcal{M}_2$ and it is integrated over the full parameter range. It can be seen that:

$$\int d\boldsymbol{\theta}_1\, p(\mathbb{O}|\boldsymbol{\theta}_1)\, p(\boldsymbol{\theta}_1) = \int d\boldsymbol{\theta}_1\, \mathcal{N}(c, C) = \sqrt{\frac{1}{\det P_1}}\, \mathcal{L}_1 \tag{6.16}$$

$$\int d\boldsymbol{\theta}_2\, p(\mathbb{O}|\boldsymbol{\theta}_2)\, p(\boldsymbol{\theta}_2) = \int d\boldsymbol{\theta}_2\, \mathcal{N}(c, C) = \sqrt{\frac{1}{\det P_2}}\, \mathcal{L}_2 \tag{6.17}$$

$$\tag{6.18}$$

Note that, in the previous equations, P_1 is the $n_1 \times n_1$ subset of P_2 related with the common parameters, while F_1 is the Fisher matrix of the nested model computed in the shifted set of parameters $\boldsymbol{\theta}_2^*$, which are obtained by using $F_{1,2}^*$ in eq. (6.6). The fiducial shifts propagates to the likelihood shift analogously to the standard case in Laplace approximation i.e., as:

$$\mathcal{L}_1 = \mathcal{L}_2 \exp\left[-\frac{1}{2}\delta\boldsymbol{\theta}_2^T\, F_2^*\, \delta\boldsymbol{\theta}_2\right] .$$

Finally, the Bayes factor with Gaussian priors turns out to be:

$$\begin{aligned} \langle B_{12} \rangle &= \sqrt{\frac{\det F_2^* \det P_2}{\det F_1^* \det P_1}} \exp\left[-\frac{1}{2}\delta\boldsymbol{\theta}_2^T F_2^*\, \delta\boldsymbol{\theta}_2\right] \\ &= \sqrt{\frac{\det F_2^*}{\det F_1^*}} \exp\left[-\frac{1}{2}\delta\boldsymbol{\theta}_2^T F_2^*\, \delta\boldsymbol{\theta}_2\right] \prod_{q=1}^{n_e} \sigma_{prior}^{n_1+q} , \end{aligned} \tag{6.19}$$

where in the second equality we used the fact that the inverse of the prior matrix determinants is computed as $\prod \sigma_{prior}^2$. Note that when the prior is very strict, $F_{1,2}^* \longrightarrow F_{1,2}$ and $\sigma_{prior} \longrightarrow (2\pi)^{(n_2-n_1)/2}\Delta\theta$, so that eq. (6.19) converges to eq. (6.5).

6.2 Merger distribution and clustering

To forecast the Bayes factor in eq. (6.2), it is necessary to compute the angular power spectra that enters the Fisher matrix. This is done by using a modified version of `CAMB` [165]: in this, we implemented the luminosity distance space distortion terms described in 5.2.3 and we specified the observed number of tracers per redshift bin per solid angle $d^2N/dzd\Omega$ and bias $b(z)$ of the blind survey. These are modelled combining the information on the distribution and clustering of ABH (section 6.2.1) and PBH (section 6.2.2). Different choices for their local merger rates are made in order to test how the blind survey (section 6.2.3) and the Bayes factor depend on the relative abundances of the two kinds of progenitors. These are described in this section and then analysed in section 6.3.

6.2.1 ABH

The ABH number distribution is modelled from the same numerical hydrodynamical simulations used in chapter 5 [204, 205, 322]. In this case, however, the number distribution is not interpolated as in 5.31, but in order to estimate the ABH merger rate as:

$$\mathcal{R}^A(z) = \left[\mathcal{R}_0^A + \alpha_1^A z + \alpha_2^A z^2 + \alpha_3^A z^3\right] e^{-\alpha_4 z} , \tag{6.20}$$

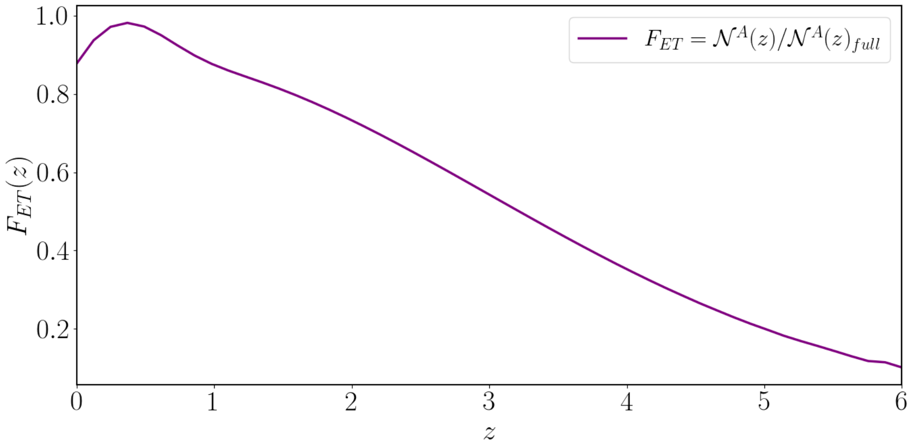

Figure 6.3: ET selection effect applied to PBH, computed as in eq. (6.21).

where $\alpha_1^A = 4.68 \cdot 10^{-8}$, $\alpha_2^A = 1.34 \cdot 10^{-7}$, $\alpha_3^A = -2.29 \cdot 10^{-8}$, $\alpha_4^A = 1.47$. The local rate is $\mathcal{R}_0^A = 133\,\mathrm{Gpc}^{-3}\mathrm{yr}^{-1}$: this value is a bit higher than the constraints provided by the last release of O3 observations from the LIGO−Virgo−Kagra Collaboration [251]. Therefore, we study also the case in which the local rate in eq. (6.20) lies in between the confidence intervals provided by the different algorithms described in [251] i.e., instead of $\mathcal{R}_0^A$ we adopted $\mathcal{R}_0^{LVK} = 25\,\mathrm{Gpc}^{-3}\mathrm{yr}^{-1}$. ABH rate and observed distribution are compared with the PBH ones respectively in figure 6.7 and figure 6.8.

As for the ABH bias, we model it analogously to 5.41 in chapter 5 i.e., $b(z) = A(z+B)^P$, where the fiducial values for the parameters are estimated from the simulations: $A = 0.7,\ B = 2.68,\ P = 1$. This is compared with PBH bias in figure 6.5.

6.2.2 PBH

The merger rate of PBH is derived from theoretical assumptions; as a generic prescription, its redshift dependence can be modelled as a power−law [352]. To account for detector selection effects, we assume that the fraction of observed mergers with respect to their totality is the same for PBH as for ABH. Therefore, using the simulated catalogues from [204, 205, 322] we define:

$$F_{ET}(z) = \frac{\mathcal{N}^A(z)}{\mathcal{N}^A(z)_{full}} \tag{6.21}$$

as the ratio between the number of ABH obtained from the simulation that accounts for ET selection effects (which are used both in chapter 5 and in section 6.2.1) and their number in the *full* simulation (which are used in chapter 7). The computed factor $F_{ET}(z)$ is showed in figure 6.3. This is then applied to PBH rate separately for late and early binaries (see section 3.3.3).

As for late type PBH, we model their merger rate as:

$$\mathcal{R}^L(z) = F_{ET}(z)\mathcal{R}_0^L(1+z)^{\alpha^L}\ , \tag{6.22}$$

where $\mathcal{R}_0^L = 4\,\mathrm{Gpc}^{-3}\mathrm{yr}^{-1}$ [300] and $\alpha^L = 0$ [119]. As for early binaries instead, we model their rate as:

$$\mathcal{R}^E(z) = F_{ET}(z)\mathcal{R}_0^E(1+z)^{\alpha^E}\ , \tag{6.23}$$

where $\alpha^E = 1.25$ is obtained by interpolating the distributions described in [115]. The value of the local rate of early binaries $\mathcal{R}_0^E$, as described in section 3.3.3, depends on the assumed PBH fraction among DM components i.e., f_{PBH} from eq. (2.64). In [114], this is computed as:

$$\mathcal{R}_0^E \sim 0.042\, X_* \, \frac{f_{PBH}}{m_{PBH}} \frac{\rho_M^0}{t_0} \,, \tag{6.24}$$

where $t_0 \simeq 14\,\mathrm{Gyr}$ is the present time, $m_{PBH} = 10\,M_\odot$ and:

$$\rho_M^0 = 3H_0^2(\Omega_{DM} + \Omega_b)/(8\pi G)\,, \tag{6.25}$$

$$X_* = 0.032\, f_{PBH}\, m_{PBH}^{5/37} (f_{PBH}^2 + \sigma_E^2)^{-21/74}\,, \tag{6.26}$$

$$\sigma_E \sim 0.005 \text{ is the variance of fluctuations of DM that are not PBH.} \tag{6.27}$$

The values that $\mathcal{R}_0^E$ can assume are showed in figure 6.4. The change in the slope at $f_{PBH} \simeq 10^{-2}$, as described in [114], is due to the tidal torque that is exerted on the PBH binary, which is dominated by large scale density perturbations when $f_{PBH} < \sigma_E$ and by the near−by presence of other primordial black holes when $f_{PBH} > \sigma_E$.[1] In the analysis presented in section 6.3, we focus on three different choices: $\mathcal{R}_0^E = [10^{-1},\ 50,\ 200]\,\mathrm{Gpc}^{-3}\mathrm{yr}^{-1}$, which correspond respectively to $f_{PBH} \simeq [0.01\%,\ 0.2\%,\ 0.5\%]$: this values are compatible with the updated constraints of [118].

Early and late PBH rates and observed number distributions are compared with the ABH ones in figure 6.7 and figure 6.8. It is noticeable that, with the assumptions made in eq. (6.23) and eq. (6.22), late PBH binaries only slightly contributes to the overall GW budget. The detectability of PBH is instead mostly related with early PBH binaries: when their rate is not negligible, in the intermediate and high redshift regions where $z > 1$, it turns out that PBH dominate above ABH.

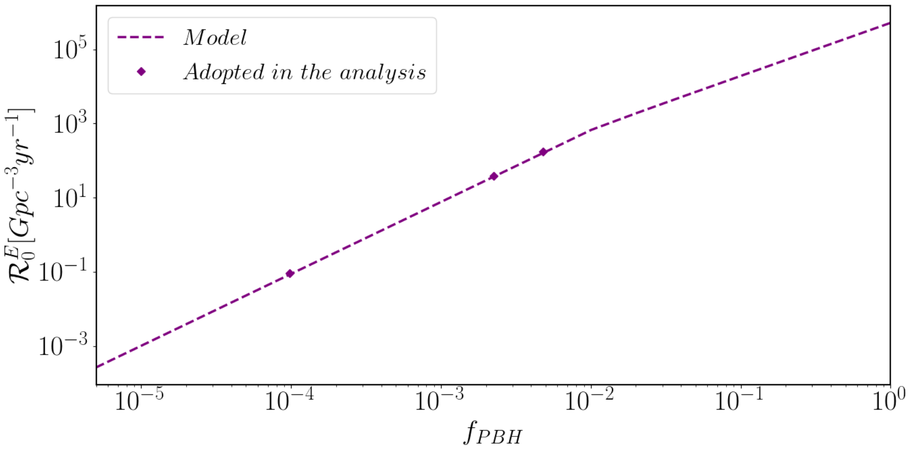

Figure 6.4: Early binary local merger rate computed as in eq. (6.24). The dots represents the values used as $\mathcal{R}_0^E$ fiducials in section 6.3. These are: $\mathcal{R}_0^E = 10^{-1}\,\mathrm{Gpc}^{-3}\mathrm{yr}^{-1}$ i.e., $f_{PBH} \simeq 10^{-4}$, $\mathcal{R}_0^E = 50\,\mathrm{Gpc}^{-3}\mathrm{yr}^{-1}$ i.e, $f_{PBH} \simeq 0.002$, $\mathcal{R}_0^E = 200\,\mathrm{Gpc}^{-3}\mathrm{yr}^{-1}$ i.e., $f_{PBH} \simeq 0.005$.

As for the PBH bias, as described in section 3.3.3 and according to [119, 300], we assume a constant value for both late and early binaries (compare with eq. (3.87) and eq. (3.85)): in particular, $b^L = 0.5$ and $b^E = 1$. The PBH bias models are compared with the ABH bias in figure 6.5.

[1] Note that in [114] the full computation of the early binary merger rate is performed, while here we directly implemented the functional result obtained in [114].

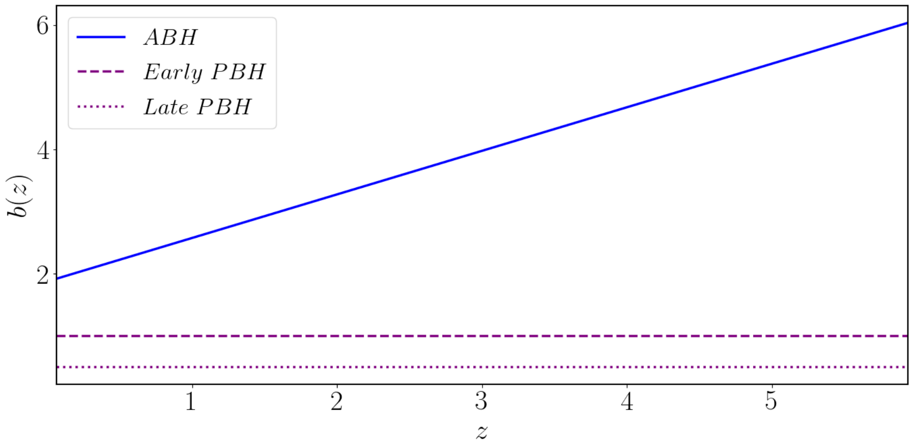

Figure 6.5: Bias $b^A(z)$ (blue), $b^E(z)$ (purple dashed), $b^L(z)$ (purple dotted).

6.2.3 Blind survey

Let us remind that, in this context, we indicate as *blind* a survey in which both astrophysical and primordial black hole mergers are observed. Since the two have completely indistinguishable signals, the survey can not *see* the different origin of the mergers and it is not possible to separate events that are generated by the two different sources. To describe the blind survey, the observed number distribution and bias of ABH and PBH are combined through a weighted average that takes into account their relative abundance.

The total number of black hole binary mergers observed is then:

$$\mathcal{N}^{tot}(z) = \mathcal{N}^A(z) + \mathcal{N}^P(z) = \mathcal{N}^A(z) + \left[\mathcal{N}^E(z) + \mathcal{N}^L(z)\right] , \tag{6.28}$$

while the observed number distribution per redshift bin z and solid angle Ω $d^2N/dzd\Omega$ and the bias $b(z)$ are:

$$\begin{aligned} \frac{d^2N}{dzd\Omega} &= \frac{d^2N^A}{dzd\Omega} + \frac{d^2N^P}{dzd\Omega} = \frac{d^2N^A}{dzd\Omega} + \left[\frac{d^2N^E}{dzd\Omega} + \frac{d^2N^L}{dzd\Omega}\right] \\ &= cT_{obs}\frac{\chi^2(z)}{(1+z)H(z)}\left[\mathcal{R}^A(z) + \mathcal{R}^E(z) + \mathcal{R}^L(z)\right] , \end{aligned} \tag{6.29}$$

$$b(z) = \frac{\mathcal{N}^A(z)}{\mathcal{N}^{tot}(z)} b^A(z) + \frac{\mathcal{N}^E(z)}{\mathcal{N}^{tot}(z)}\, b^E(z) + \frac{\mathcal{N}^L(z)}{\mathcal{N}^{tot}(z)}\, b^L(z) , \tag{6.30}$$

where $c =$ is the speed of light, T_{obs} is the duration of the GW survey (which here we assume to be 3 yr), $\chi(z)$ is the comoving distance and $H(z)$ is the Hubble parameter (see chapter 2). The observed number of mergers per binary type $\mathcal{N}^{A,E,L}(z)$ in the redshift bin centered in z, is computed from the merger rates $\mathcal{R}^{A,E,L}(z)$ defined in eq. (6.20), eq. (6.23) and eq. (6.22). It is:

$$\mathcal{N}^{A,E,L}(z) = 4\pi \int_{z-\Delta z}^{z+\Delta z} dz' \, \frac{d^2N^{A,E,L}(z')}{dz'd\Omega} . \tag{6.31}$$

The quantities $\mathcal{R}^{A,E,L}(z)$, $d^2N/dzd\Omega$, $d^2N^{A,E,L}/dzd\Omega$ and $b(z)$, $b^{A,E,L}$, which are characterised in section 6.2.1 and section 6.2.2, are shown respectively in figure 6.7, figure 6.8, figure 6.6 for the different cases analysed in section 6.3. Note that early PBH binaries dominate the distribution mainly at $z > 1$, even when their local

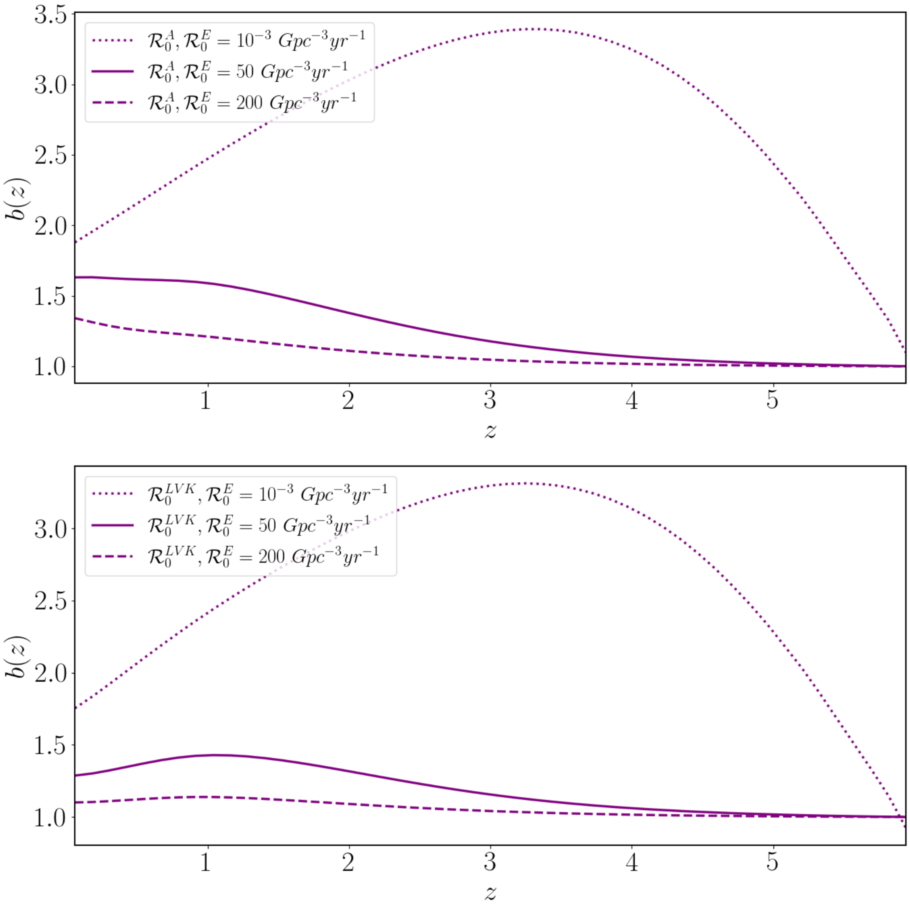

Figure 6.6: Bias $b(z)$ from eq. (6.30) in the cases of early PBH rate $\mathcal{R}_0^E = 10^{-1}\,\mathrm{Gpc}^{-3}\mathrm{yr}^{-1}$ (dotted line), $50\,\mathrm{Gpc}^{-3}\mathrm{yr}^{-1}$ (continuous line), and $200\,\mathrm{Gpc}^{-3}\mathrm{yr}^{-1}$ (dashed line). The ABH rate $\mathcal{R}_0^A = 133\,\mathrm{Gpc}^{-3}\mathrm{yr}^{-1}$ is assumed in the upper plot, while in the lower one $\mathcal{R}_0^{LVK} = 25\,\mathrm{Gpc}^{-3}\mathrm{yr}^{-1}$.

merger rate is smaller than the ABH one (compare the plots in the central lines of figure 6.7 and figure 6.8). In the case of figure 6.6, the drop that can be observed at $z > 4$ depends on the effect of the ET selection effect $F_{ET}(z)$ modelled in eq. (6.21).

6.3 Results

The models $\mathcal{M}_1$ = *only ABH contribute to GW emissions* and $\mathcal{M}_2$ = *both ABH and PBH contribute to the GW ET will observe* are compared by forecasting the Bayes factor. The $\mathcal{M}_2$ scenario assumes that a source exists that emits GW indistinguishable from the ones from ABH mergers, and that its progenitors have distribution and bias described by the relations in section 6.2.2. We interpret this GW source as PBH mergers.

Forecasts are made for the ET−like survey with specifications described in table 5.3: the full sky is observed with sky localization uncertainty $\Delta\Omega = 100\mathrm{deg}^2$, having the effect of smoothing out the smaller scales as in eq. (5.50). The detector horizon in this case, in agreement with [334] is pushed up to $z_{max} = 6$ while in chapter 5 we had assumed $z_{max} = 5$ since the number of ABH there is negligible. The conversion between z and D_L is made by assuming the fiducial cosmology in table 2.1 and the bins for the tomographic analysis are defined by the luminosity distance uncertainty $\Delta D_L/D_L = 0.1$. Angular power spectra are computed with `CAMB` [165] and used to compute the Fisher matrices $F_1,\ F_2$ for the two models $\mathcal{M}_1,\ \mathcal{M}_2$; the Fisher matrix

Figure 6.7: Merger rate $\mathcal{R}^i(z)$ computed for i = ABH+PBH (black) ABH (blue), late PBH (purple dotted), early PBH (purple dashed) with $\mathcal{R}_0^E = 10^{-1}\,\mathrm{Gpc}^{-3}\mathrm{yr}^{-1}$ (top), $\mathcal{R}_0^E = 50\,\mathrm{Gpc}^{-3}\mathrm{yr}^{-1}$ (central), $\mathcal{R}_0^E = 200\,\mathrm{Gpc}^{-3}\mathrm{yr}^{-1}$ (bottom). We assume $\mathcal{R}_0^A$ for left plots, $\mathcal{R}_0^{LVK}$ for right plots.

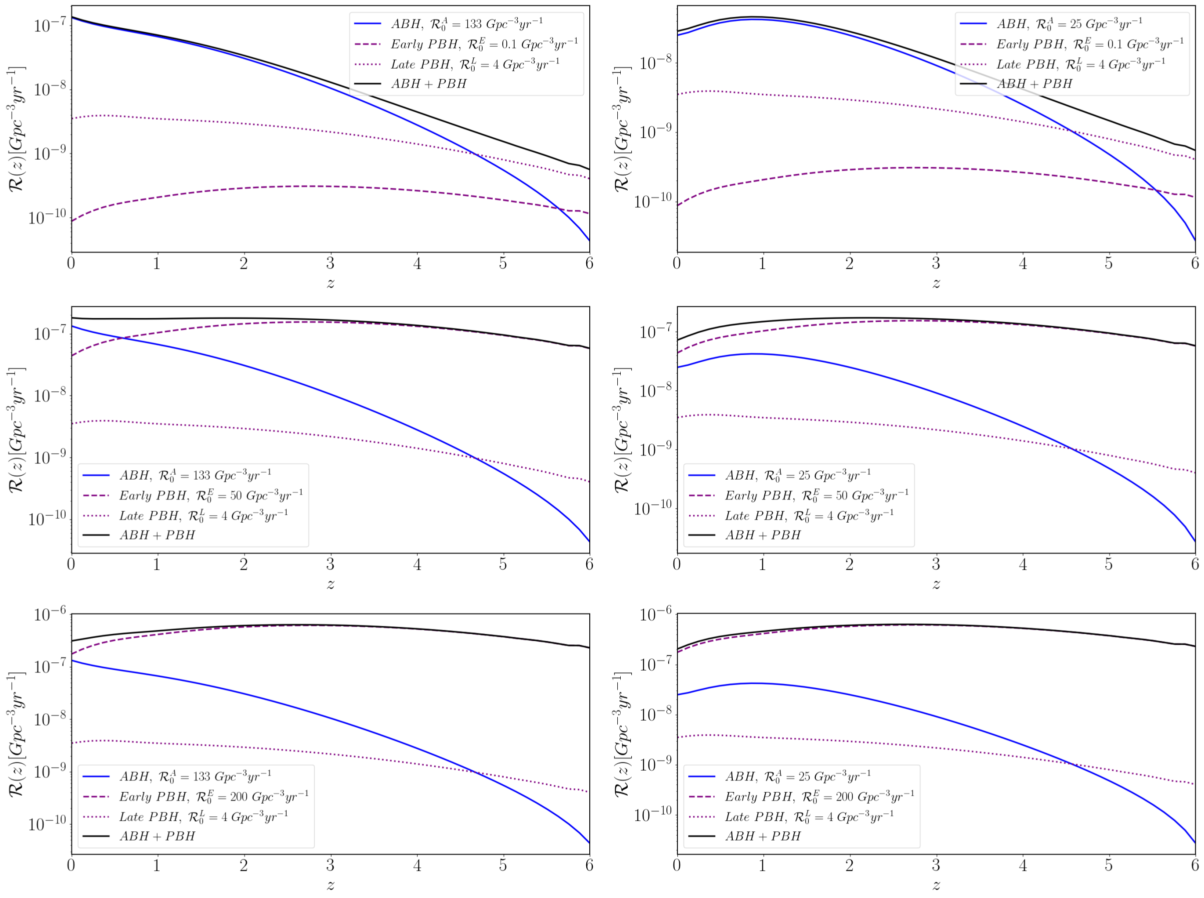

of the nested model $\mathcal{M}_1$, is computed by conditioning F_2 over all the parameters related with PBH.

Different configurations have been adopted and compared in this analysis. All the parameters with their fiducial values, are summarized in table 6.1: some of them are held fixed, while others propagate through the Fisher matrix computation as in eq. (5.58). The latter are then marginalized to compute the Bayes factor between $\mathcal{M}_1$ and $\mathcal{M}_2$ as eq. (6.5) describes. The shared parameters in the two models are $\boldsymbol{\theta}_1 = [A, D, \mathcal{R}_0^A]$; the extra−parameters instead are $\boldsymbol{\theta}_2^{rate} = [\mathcal{R}_0^E, \mathcal{R}_0^L]$ or $\boldsymbol{\theta}_2^{full} = [\mathcal{R}_0^E, \mathcal{R}_0^L, b^E, b^L]$. In the *rate* scenario we fixed the PBH bias parameters: the reason for this is both numerical and theoretical. On one side, holding them fixed we can probe separately different bias models, so to understand which of them could be detectable with ET. On the other side, the PBH bias parameters are degenerate with the PBH merger rates in the computation of the angular power spectra that make up the Fisher matrix: including them in the analysis, therefore, makes the results of our test less reliable. An alternative way to approach this problem is to consider Gaussian priors on the parameters and to compute the Bayes factor outside the Laplace approximation, by the means of eq. (6.19). We performed this analysis and we found that the Bayes factors computed by including a stringent Gaussian prior or by conditioning over some of the parameters converge. A detailed description of such results will be presented in the paper in preparation [4].

Figure 6.8: Observed number distribution $d^2N^i/dzd\Omega$. The legend is the same as figure 6.7.

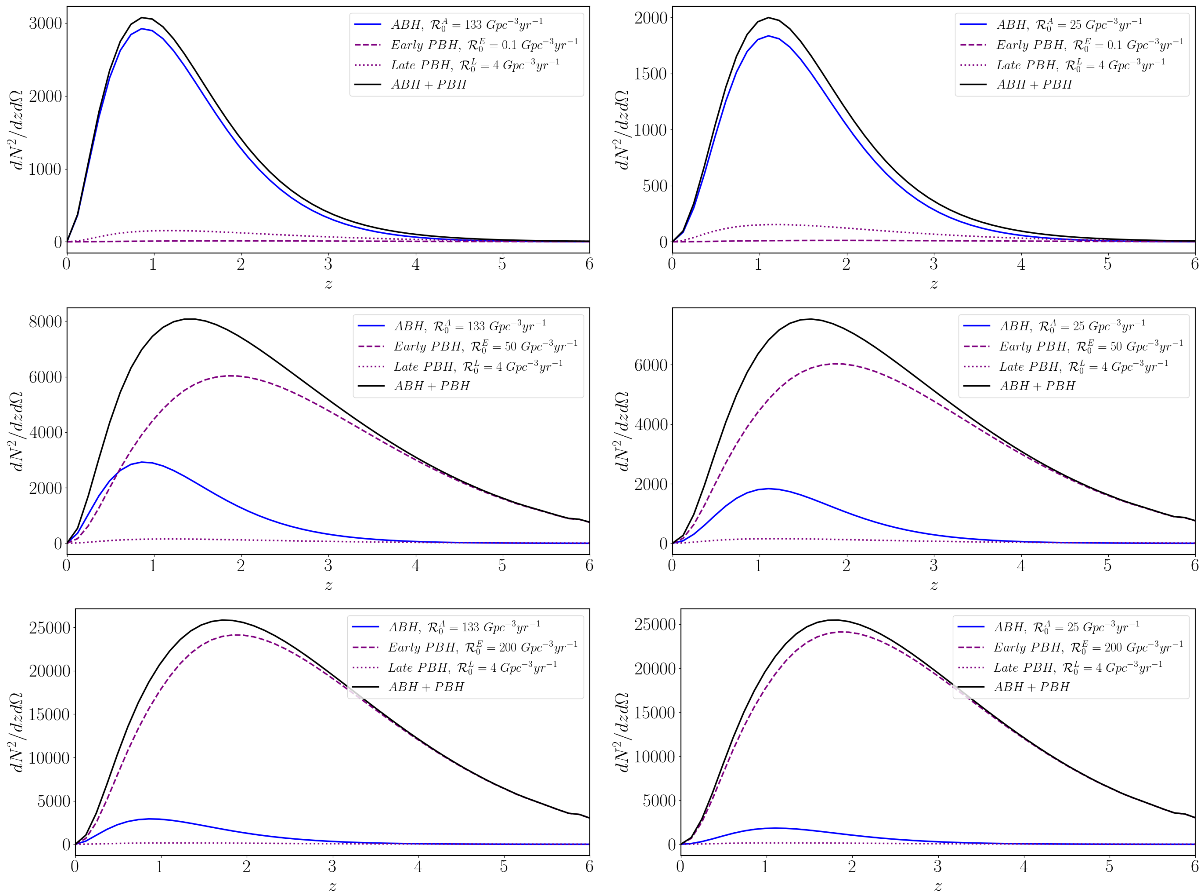

As table 6.1 shows, several other parameters should enter the Fisher matrix computation: these are the cosmological parameters required by `CAMB` and the α parameters describing the redshift evolution of ABH and PBH merger rates. We fixed these parameters after performing different tests to validate the robustness of the analysis.[2] In particular:

- The effect of the cosmological parameters on the final result can be neglected in favour of a smaller computational cost.
- Changing the fiducial values of the redshift evolution parameters for ABH or PBH only slightly affect the results.

To check the stability of the results, we also computed the Bayes factor through the Savage−Dickey ratio in eq. (6.7), where a single extra−parameter is needed. To do so, we fixed the PBH biases and we converted the parameters $\mathcal{R}_0^E$ and $\mathcal{R}_0^L$ into the PBH abundance Γ, defined in eq. (6.1). Finally, we marginalised over the distance:

$$\Gamma = \int_{z_{min}}^{z_{max}} dz\, \frac{\mathcal{N}^P(z)}{\mathcal{N}^{tot}(z)} = \int_{z_{min}}^{z_{max}} dz\, \frac{\mathcal{N}^E(z) + \mathcal{N}^L(z)}{\mathcal{N}^A(z) + \mathcal{N}^E(z) + \mathcal{N}^L(z)}\ . \tag{6.32}$$

In this simplified version of the $\mathcal{M}_2$ model, which we indicate as $\mathcal{M}_2^\Gamma$, the Fisher matrix for the complex model is computed by converting F_2 through:

$$F_\Gamma^{\gamma\delta} = \sum_{\alpha\beta} \frac{d\theta_2^\alpha}{d\theta_\Gamma^\gamma} F_2^{\alpha\beta} \frac{d\theta_2^\beta}{d\theta_\Gamma^\delta}\ , \tag{6.33}$$

[2] 2: A full description of the results obtained by varying the fiducial values of these parameters will be as well presented in the forthcoming paper [4]. We note, however, that in model selection studies it is preferable to have a small number of parameters: improving the parameter set, in fact, increases the degrees−of−freedom of the system and can provide over−fitting issues. The opposite instead holds for analyses aimed at parameter forecasts, where conditioning over some of the parameters can lead to optimistic estimates of the results.

Table 6.1: Parameters and fiducial values assumed in the computation; the values $\mathscr{R}_0^{E,L} = 0$ refer to the case in which the *true* model is $\mathscr{M}_1$. The ✓ indicates if the parameter is held fixed or marginalised in the computation of the Fisher matrix. As described in the text, we analysed both the cases in which b^L and b^E are either fixed or marginalised.

Parameter	Held fixed	Marginalized	Fiducial value
		Cosmology	
$[H_0, \Omega_c h^2, w_0, w_a, \Omega_b h^2, n_s, A_s]$	✓		*Planck 2018* [13]
		ET survey	
$[z_{min}, z_{max}]$	✓		$[0, 6]$
$\Delta D_L / D_L$	✓		10%
$\Delta\Omega$	✓		100 deg^2
T_{obs}	✓		3
$F(z)$	✓		$\mathcal{N}^A(z)/\mathcal{N}^A_{full}(z)$
		ABH distribution and bias	
$\mathscr{R}_0^{A,LVK}$		✓	$[133,\ 25]\,\mathrm{Gpc}^{-3}\mathrm{yr}^{-1}$
α^1	✓		$4.68 \cdot 10^{-8}$
α^2	✓		$1.34 \cdot 10^{-7}$
α^3	✓		$-2.29 \cdot 10^{-8}$
α^4	✓		1.47
A		✓	0.7
B	✓		2.68
P		✓	1
		PBH distribution and bias	
$\mathscr{R}_0^L$		✓	$[0,\ 4]\,\mathrm{Gpc}^{-3}\mathrm{yr}^{-1}$
α^P_L	✓		0
b^L	[✓]	[✓]	0.5
$\mathscr{R}_0^E$		✓	$[0,\ 10^{-1},\ 50,\ 200]\,\mathrm{Gpc}^{-3}\mathrm{yr}^{-1}$
α^E	✓		1.25
b^E	[✓]	[✓]	1

where $\boldsymbol{\theta}_\Gamma = [A, P, \mathscr{R}_0^A, \Gamma]$.[3] The fiducial value of Γ is computed from eq. (6.32) and its values are reported in table 6.2.

To reduce the computational cost of the code, the cosmological parameters are also fixed since, as we found in chapter 5, they do not affect too much the results. As in section 5.6, we fixed the B parameter of the ABH bias, since it is degenerate with the ones for A.

The analysis has been developed in several different scenarios:

Rate scenario: $\boldsymbol{\theta}_2 = [A, P, \mathscr{R}_0^{A/LVK}, \mathscr{R}_0^E, \mathscr{R}_0^L]$ ($b^{E,L}$ are fixed to their fiducial values;
Full scenario: $\boldsymbol{\theta}_2 = [A, P, \mathscr{R}_0^{A/LVK}, \mathscr{R}_0^E, \mathscr{R}_0^L, b^E, b^L]$.

For each scenario we consider six fiducial frameworks, which correspond to the different rates described in section 6.2.1 and section 6.2.2:

A×0.1P, LVK×0.1P: $\mathscr{R}_0^A = 133$ or $\mathscr{R}_0^{LVK} = 25\,\mathrm{Gpc}^{-3}\mathrm{yr}^{-1}$, $\mathscr{R}_0^E = 0.1\,\mathrm{Gpc}^{-3}\mathrm{yr}^{-1}$;
A×50P, LVK×50P: $\mathscr{R}_0^A = 133$ or $\mathscr{R}_0^{LVK} = 25\,\mathrm{Gpc}^{-3}\mathrm{yr}^{-1}$, $\mathscr{R}_0^E = 50\,\mathrm{Gpc}^{-3}\mathrm{yr}^{-1}$;
A×200P, LVK×200P: $\mathscr{R}_0^A = 133$ or $\mathscr{R}_0^{LVK} = 25\,\mathrm{Gpc}^{-3}\mathrm{yr}^{-1}$, $\mathscr{R}_0^E = 200\,\mathrm{Gpc}^{-3}\mathrm{yr}^{-1}$.

The baseline cases chosen for the analysis are the **Rate scenario, A×...** ones.

As for the priors, they are required to compute both the Bayes factor in eq. (6.5), in which $\Delta\theta_2^\alpha$ are the prior ranges of the extra−parameters, and the Savage−Dickey ratio in eq. (6.7). In particular, we assume the prior ranges in the upper part of

[3] The parameter set $\boldsymbol{\theta}_\Gamma = [A, P, \mathscr{R}_0^A, \Gamma, b^E, b^L]$ is also analysed by using the Bayes factor from eq. (6.5).

table 6.3 to account for the theoretical models uncertainties; in this case we consider uniform prior, therefore $p(\theta_2^\alpha) = (\Delta\theta_2^\alpha)^{-1}$.

Baseline case

The settings we choose as the baseline case are the **Rate scenario, A×...**. Here, the parameters entering the Fisher matrix of the model $\mathcal{M}_2$ are: $\boldsymbol{\theta}_2 = [A, P, \mathcal{R}_0^A, \mathcal{R}_0^E, \mathcal{R}_0^L]$, where $\mathcal{R}_0^i$ are the local ABH and PBH merger rates, while $A,\ P$ are the parameters that describe the ABH bias, defined such that $b(z) = A(z+B)^P$ and computed through the HOD/GOD technique described in section 5.3.2. Three frameworks were analysed, in which $\mathcal{R}_0^E$ is respectively $[0.1, 50, 200]\,\mathrm{Gpc^{-3}yr^{-1}}$.

We computed the Bayes factor as in eq. (6.5). Results are shown in figure 6.9, where the values of the Bayes factor $\langle B_{12}\rangle$ are compared with the limits defined in [353] to distinguish between tests that provide a *substantial*, *strong* or *decisive* evidence of one model with respect to the other.

According to figure 6.9, the model selection analysis states that ET will be able to confirm or disregard the contribution of PBH mergers to GW observed by ET in case their local rate is at least above $50\,\mathrm{Gpc^{-3}yr^{-1}}$. As described in section 6.2.2, this corresponds to $f_{PBH} \simeq 0.2\%$ and to $\Gamma = 0.810$. The result we obtained is in agreement with the fact that the ET observed volume will include high redshift regions, where the PBH have larger merger rate than ABH.

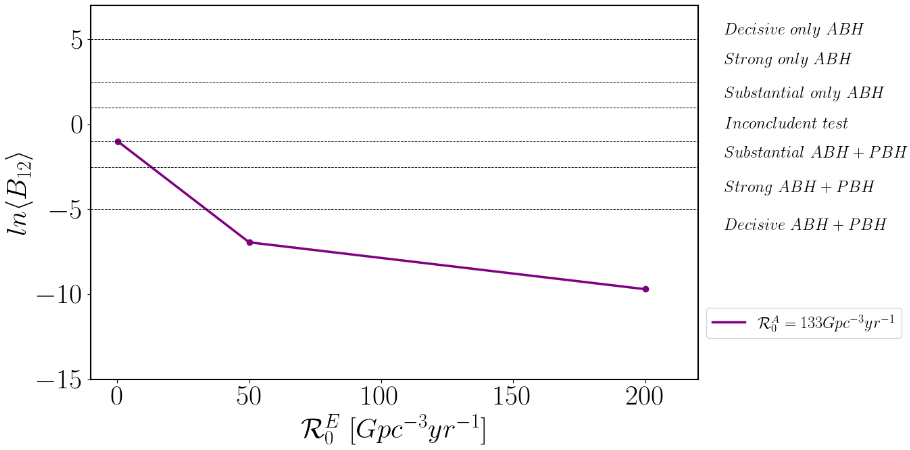

Figure 6.9: Bayes factor for the **Rate scenario, A×...**. This plot is analogous to the upper left one in figure 6.10.

Extended analysis

To verify the robustness of our forecast, we consider additional scenarios besides the baseline case. They are distinguished by the number and types of parameters entering the computation of the Fisher matrix.

Framework	Γ fiducial value	Framework	Γ fiducial value
A×0.1P	0.069	**LVK×0.1P**	0.101
A×50P	0.810	**LVK×50P**	0.867
A×200P	0.944	**LVK×200P**	0.963

Table 6.2: Γ fiducial values used in the analysis in the different frameworks. They are computed by integrating eq. (6.32) over all the redshift bin $z \in [0, 6]$.

Figure 6.10 shows the forecasts for the **Full scenario** and **Rate scenario** using $\mathcal{M}_1$, $\mathcal{M}_2$ in eq. (6.5), for all the frameworks; note that the correlations that exist between

Model	Parameter	Prior range $\Delta\theta_2^\alpha$
$\mathcal{M}_2$	$\mathcal{R}_0^E$	$500\,\mathrm{Gpc}^{-3}\mathrm{yr}^{-1}$
	$\mathcal{R}_0^L$	$100\,\mathrm{Gpc}^{-3}\mathrm{yr}^{-1}$
	b^E	0.3
	b^L	0.3
$\mathcal{M}_2^\Gamma$	Γ	1
	b^E	0.3
	b^L	0.3
$\mathcal{M}_1$	A	0.3
	P	0.3
	$\mathcal{R}_0^A$	$50\,\mathrm{Gpc}^{-3}\mathrm{yr}^{-1}$

Table 6.3: Uniform prior ranges for the extra parameters of $\mathcal{M}_2$, $\mathcal{M}_2^\Gamma$ (see eq. (6.33)) used to compute $\langle B \rangle$ from eq. (6.5). Note that we associate the largest uncertainties with the PBH rates. The prior ranges for $\mathcal{M}_1$ are instead used in the computation of the Savage–Dickey ratio in eq. (6.7) to define the boundaries between which the likelihood of the common parameters are integrated to be marginalised.

PBH rate and bias parameters in the **Full scenario** make the test less reliable; in this situation, the introduction of Gaussian priors would be needed to break the degeneracies. Our choice of prior is the one described in table 6.3.

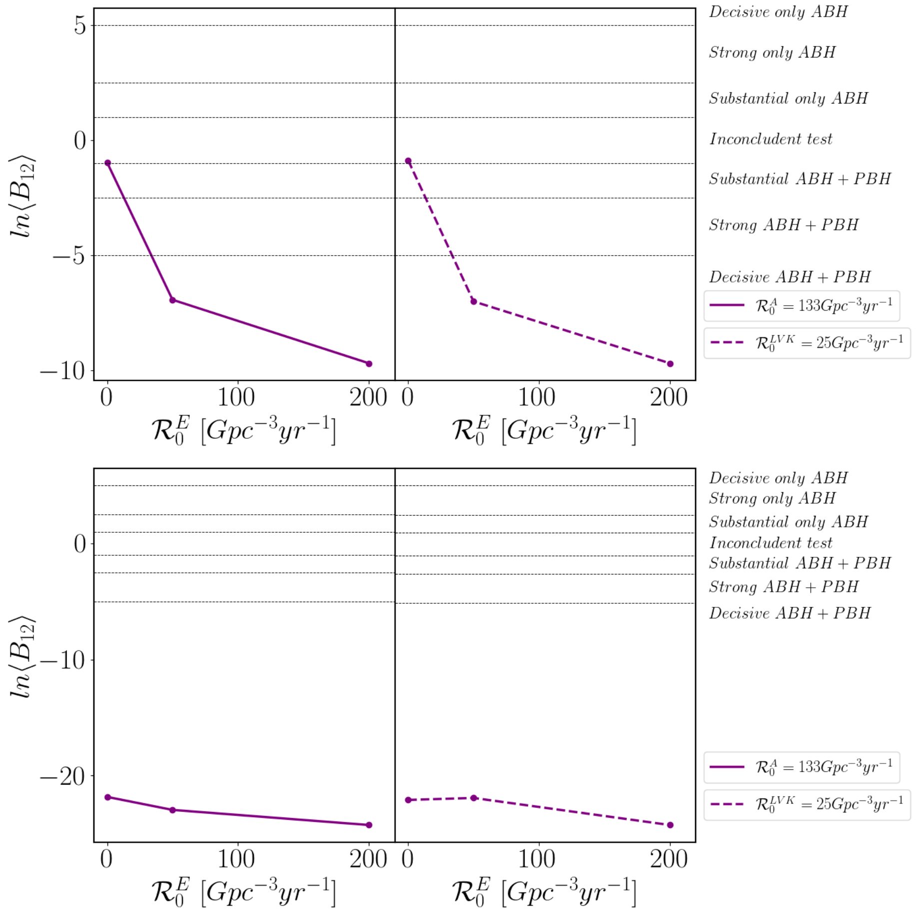

Figure 6.10: Bayes factor in the **Rate scenario** (top) and **Full scenario** (bottom) computed using $\mathcal{M}_1$, $\mathcal{M}_2$ in eq. (6.5) for the **A×[0.1,50,200]P** (left) and **LVK×[0.1,50,200]P** (right) frameworks.

Assuming $\mathcal{R}_0^A$ or $\mathcal{R}_0^{LVK}$ as the local ABH merger rate does not produce relevant differences when using $\mathcal{M}_2$ in the computation.

Figure 6.11 shows results obtained by using $\mathcal{M}_2^\Gamma$: the **Rate scenario** in this case considers one single extra–parameter Γ with respect to $\mathcal{M}_1$. For this reason, the Savage–Dickey ratio from eq. (6.7) is shown as well: the comparison between it and the Bayes factor shows that their results are compatible. The small deviation seen in the smaller value of $\mathscr{R}_0^E$ is due to the propagation of numerical uncertainties in the code.

The comparison between $\mathscr{M}_2$ and $\mathscr{M}_2^\Gamma$, instead, can be made by looking at figure 6.10 and figure 6.11. We note that in the second case the test on the PBH existence for $\mathscr{R}_0^E = 50\,\mathrm{Gpc^{-3}yr^{-1}}$ is not as much predictive as in the first case; by slightly increasing the threshold, however, the same results are recovered. This is due to the integration performed to compute Γ in eq. (6.32): in fact, in $\mathscr{M}_2^\Gamma$ we integrate the number of ABH and PBH over the full redshift interval: this collapses the redshift information, which is fundamental in the PBH detection. In $\mathscr{M}_2$, the Fisher matrix is obtained by summing the auto− and cross− tomographic contributions of all the bins. In $\mathscr{M}_2^\Gamma$ instead, the Fisher matrix is obtained as if it were computed over the full dataset, projected over the sky. Therefore, in the first case the relative abundances are considered bin by bin, while in the second only the total relative abundances are taken into account: this increases the ABH influence on the final result, making it affecting the results in a stronger way.

For the same reason, the variation in the number of ABH due to the use of $\mathscr{R}_0^A$ or $\mathscr{R}_0^{LVK}$ has in $\mathscr{M}_2^\Gamma$ a stronger effect. As shown by figure 6.11, the **LVK×200P** framework provides a value of $\langle B_{12}\rangle$ orders of magnitudes smaller than **A×200P**.

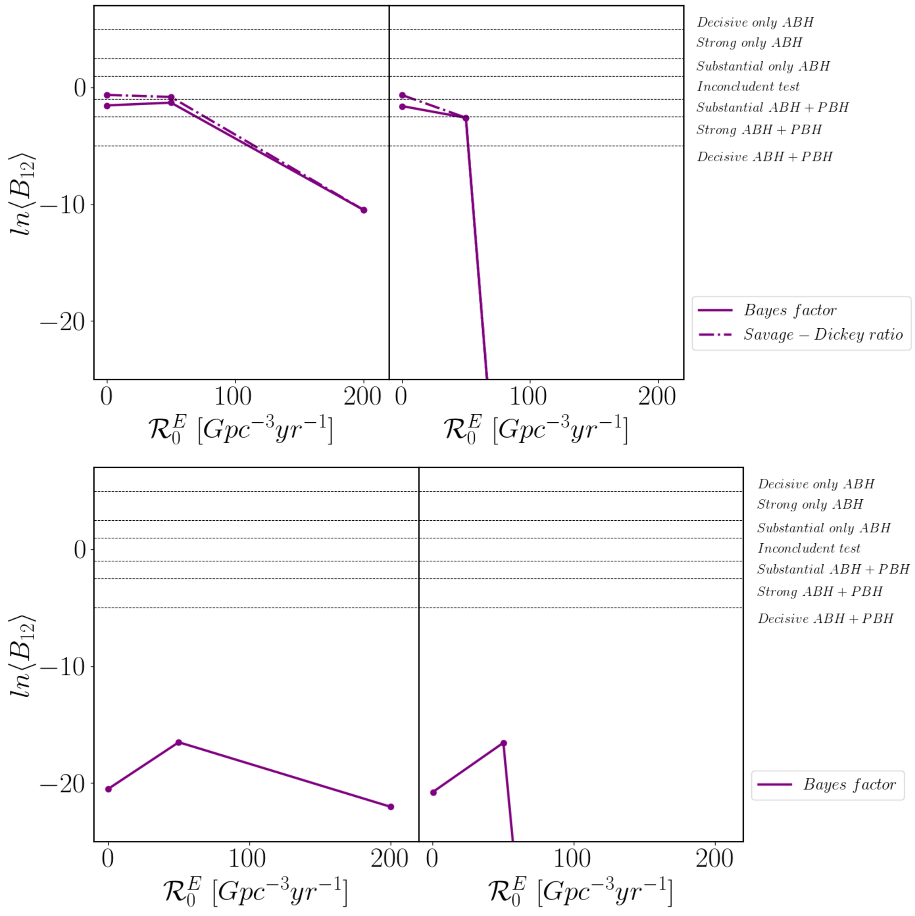

Figure 6.11: Bayes factor in the **Rate scenario** (top, continuous line) and **Full scenario** (bottom) computed using $\mathscr{M}_1$, $\mathscr{M}_2^\Gamma$ in eq. (6.5) for the **A×[0.1,50,200]P** (left) and **LVK×[0.1,50,200]P** (right) frameworks. The upper plot shows also the Savage−Dickey ratio from eq. (6.7) (dot−dashed line). The values of $ln\langle B_{12}\rangle$ for $\mathscr{R}_0^{LVK}$, $\mathscr{R}_0^E = 200\,\mathrm{Gpc^{-3}yr^{-1}}$ that exit the scale of the plot are $\simeq -205$.

Both figure 6.10 and figure 6.11 highlight the fact that the **Full scenario** would always give a decisive test for the $\mathscr{M}_2$ /$\mathscr{M}_2^\Gamma$ model i.e., for the existence of PBH.

This is related to the strong correlation between the PBH rates and biases, which increases the value of the evidence:

$$p(\mathfrak{S}) = \int d\boldsymbol{\theta}_2\, p(\mathfrak{S}|\boldsymbol{\theta}_2)p(\boldsymbol{\theta}_2)\,. \tag{6.34}$$

From eq. (6.5), this implies that the absolute value of $\ln\langle B_{12}\rangle$ becomes larger i.e., there is more evidence for the ABH+PBH detection. We tested that in all the frameworks the evidence in the **Full scenario** increases with respect to the **Rate scenario**; in particular in the case of $\mathcal{R}_0^E = 10^{-1}\,\mathrm{Gpc}^{-3}\mathrm{yr}^{-1}$ (which is the one whose predictions in figure 6.10 change the most in the two scenarios), $p(\mathfrak{S})$ increases of $\sim 80\%$. This enhance the plausibility of the complex model, beating the Occam's razor factor[4] that would instead favour the nested model.

In conclusion, the technique adopted suggests that future ET−like GW surveys:

- Will be sensitive to PBH existence thanks to the high distances probed by their horizon.
- Will be able to confirm or rule−out the existence of GW sources producing the same kind of signal as ABH mergers, but characterized by different spatial distribution and clustering properties i.e., bias. This will allow us to test different theories of PBH formation and evolution.

A crucial requirement for this to be effective is the possibility to perform a tomographic analysis. This translates in a requirement for the specifications of future GW surveys, namely a good luminosity distance uncertainty (we tested the case $\Delta D_L/D_L \simeq 10\%$, see table 5.3). Sky localization is instead not a crucial issue, since we need bias measurements on large scales. A $100\mathrm{deg}^2$ precision will suffice.

[4] The Occam's razor principle states that simple theories should be preferred with respect to more complex ones, where the number of parameters is larger, unless the data demand otherwise. In eq. (6.5), the factor describing this property is the product between $(2\pi)^{-n_e/2}\sqrt{\det F_2}/\sqrt{\det F_1}$ and the priors of the parameters [350].

Analysis of ABH simulations

7

7.1 Simulations and catalogues 124
N-body simulations . . . 125
Hydrodynamical simulations 127
The population-synthesis code MOBSE 129
7.2 Power spectrum estimator 130
Interlacing 133
FKP 134
7.3 Bias estimator . 135
7.4 Results 137

In chapter 5 and chapter 6 we demonstrated that future GW surveys, will have a strong constraining power on the clustering of binary black hole mergers in luminosity distance space. In order to verify our predictions (especially about bias) and to prepare tools for the actual data analysis in a more realistic context, we decided then to interface with simulations.

Clearly, this is a long−term project that must be implemented in steps. We start with the implementation of the estimators for the power spectrum and the bias. We apply them to the analysis of an idealized scenario, where the positions of all the BBH mergers are perfectly measured in comoving space. The simulated data are drawn from hydrodynamical N−body simulations [204, 205, 322], that model the astrophysical processes leading to their formation: therefore, in this chapter, only astrophysical black hole mergers are considered. In the future, to increase the level of realism and to implement the full pipeline for the data analysis, we will include also space distortions (see section 5.2), detector selection effects and measurement uncertainties.

The work described in this chapter will be published in a forthcoming paper [5]. In particular, in section 7.1 we give a brief review of the different kind of simulations used in the analysis (i.e., collision−less N−body, hydrodynamical, population synthesis based). In section 7.2 and section 7.3 we introduce the techniques that are commonly used in literature to estimate the power spectrum and bias of simulated datasets. Finally, in section 7.4, we describe how we implemented them and we present the results of our analysis.

7.1 Simulations and catalogues

In general, we can distinguish among two classes of simulations. The first type related with DM−only cosmological simulations, where DM is treated as a pressure−less, collision−less and non−interacting perfect fluid. In the Newtonian limit, its evolution is easily described by rewriting the Boltzmann eq. (2.22) for the DM distribution function $f(t, \boldsymbol{x}, \boldsymbol{v})$[1] in the collision−less limit i.e., in the form of the Vlasov equation:

$$\frac{df}{dt} = \frac{\partial f}{\partial t} + \boldsymbol{v}\frac{\partial f}{\partial \boldsymbol{x}} - \frac{\partial \phi}{\partial \boldsymbol{x}}\frac{\partial f}{\partial \boldsymbol{v}} = 0 \, . \tag{7.1}$$

This is coupled in the expanding Universe, with the Poisson eq. (2.30):[2]

$$\nabla^2_{\boldsymbol{x}}\phi = 4\pi G \int d\boldsymbol{v} \, f \, . \tag{7.2}$$

For the type of applications we have in mind, though, baryon evolution also has to be taken into account. In this case, highly non−linear physics makes the situation much more complicated. Typically, astrophysical gases are described by using the Euler eq. (2.28) and the conservation of mass and energy, through which the

[1] In chapter 2, the distribution function used for the Boltzmann equation was written in terms of the position $\boldsymbol{x}$ and of the proper momentum $\boldsymbol{p}$. Here, we converted $\boldsymbol{p}$ to velocity $\boldsymbol{v}$ and the gravitational potential ϕ.

[2] Note that the equation presented here is equivalent to the one in chapter 2, once that it is set: $\int d\boldsymbol{v} \, f = a^2\bar{\rho}\delta$.

hydrodynamics of the system is analysed. In [354] a review of this two approaches can be found, together with a description of the numerical techniques that have been developed to deal with them.

Another class of simulations exists, which is mostly used in astrophysics with respect to cosmology: these are the population−synthesis codes, in which models of stellar population and evolution are implementing by using a Monte Carlo approach.[3]

7.1.1 N-body simulations

When only DM is considered, the evolution of the Universe can be modelled as a set of N_p particles of mass m moving under the effect of gravity. In this case, instead of using the Bolzmann eq. (2.22) to describe the full DM field, it is possible to study the trajectory of each i−th particle through the Newton's law of motion. In this way, the particle ensemble can be interpreted as a coarse−grained discretization of the density field [354] i.e., $\langle f(t) \rangle \simeq \sum_i f(t, \boldsymbol{x}_i, \boldsymbol{v}_i)$. The velocity $\boldsymbol{v}_i$ and the position $\boldsymbol{x}_i$ of each particle depend on the other $N-1$, which are located at distances r_{ij}, through:

$$\begin{cases} \dot{\boldsymbol{v}}_i & = -G \sum_{j \neq i} \dfrac{m_j(\boldsymbol{x}_i - \boldsymbol{x}_j)}{r_{ij}^3} \\ \dot{\boldsymbol{x}}_i & = \boldsymbol{v}_i \end{cases} . \tag{7.3}$$

For $N = 2$ the analytical solutions of eq. (7.3) can easily be computed, while for systems with higher dimension this would require the use of a slowly convergent power series [355]. Integration particle−particle schemes have therefore to be developed to avoid this issue. These, starting from a set of initial condition, compute the trajectory of each particle through a series of time steps Δt in which, for each vector component:

$$\begin{cases} v_i(t + \Delta t) & \simeq v_i(t) + \dfrac{dv_i(t)}{dt} \Delta t \\ x_i(t + \Delta t) & \simeq x_i(t) + \dfrac{dx_i(t)}{dt} \Delta t \end{cases} . \tag{7.4}$$

The choice of the time steps, which can differ between x_i and v_i, identifies the integration scheme and leads to different levels of accuracy and to different computational costs [356].

Usually, if the particle are not too close one to the other i.e., if the density is not too high, approximation are used to speed up the computation and avoid the generation of unphysical effects and divergences. One of these is the **softening**: during close encounters, gravity is smoothed to a lower value to avoid the generation of spurious scatterings between the particles, leading to noise contributions [357].

Tree codes are used as well: to study the motion of the i−th particle, the cumulative effect exerted by the others is considered. Provided that these are far enough from i, their masses are summed together and their positions and velocities are reduced to the ones of the centre of mass. In this way, through the so called **Barnes−Hut algorithm** [358], only nearby particles are accounted directly, while the others are approximated. The number of required computational tasks is therefore reduced. Moreover, **particle mesh** algorithms [359] have be developed: the particle positions are re−mapped onto a discrete grid, over which the Poisson eq. (2.30) is solved, reducing the number of operations required.

[3] The name **Monte Carlo** identifies a large class of algorithms based on random samplings.

Cosmological $N-$body simulations are used mainly to study the large scale structure distribution of DM and DM halos, which are defined inside the simulations as regions of a certain radius that contain mass above a certain threshold.[4] To identify the halos, commonly the Friends−of−Friends algorithm (FoF) is used [360]: particles that are separated by less then the chosen **linking length** l_{FoF} form a group.[5] The number of particles forming a group determines its size: in the case of DM halos, usually, the smallest groups are disregarded. The mass of the halo is then computed as the sum of the DM particles forming the group.

The main advantages of $N-$body simulations are the linearity of the physical mechanisms involved and the relatively small computational cost required. These give the possibility of probing large volumes, running different realizations with various sets of initial conditions and cosmological parameters: by combining all of them, the local and peculiar effects are then averaged out and the cosmic variance (see section 2.2.2) is drastically reduced.

The QUIJOTE simulations

The QUIJOTE suite [361] contains 44100 $N-$body simulations, which have been realized assuming 7000 different sets of fiducial values for the cosmological parameters $[h,\ \Omega_c,\ \Omega_b,\ w_0, n_s,\ M_\nu,\ \sigma_8]$,[6] which are summarized in table 7.1. The simulations are realized within boxes having comoving side 1 h^{-1} Gpc and containing either 256^3, 512^3 or 1024^3 particles. These are evolved from $z = 127$, where the initial conditions are defined, up to $z = [3, 2, 1, 0.5, 0]$, where the snapshots are saved.

Figure 7.1 shows a slice of the QUIJOTE simulation box at $z = 0$ in the fiducial cosmology. The figure highlights the LSS created by the DM distribution.

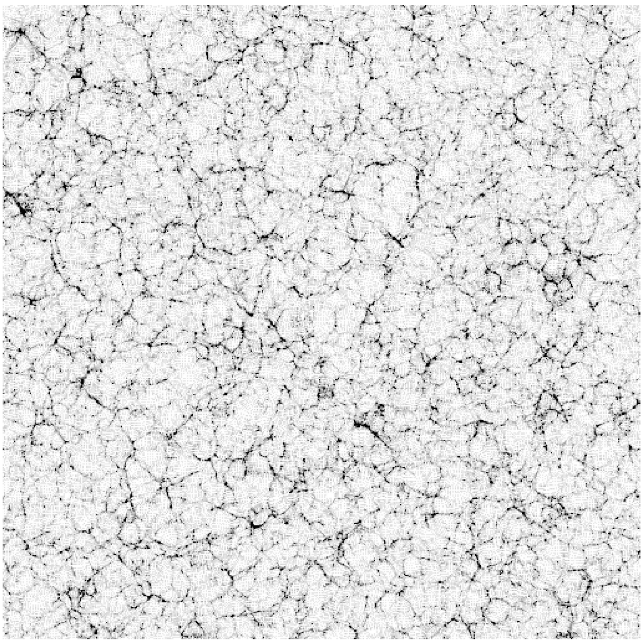

Figure 7.1: Slice of 5 h^{-1} Mpc side of the $z = 0$ snapshot in the fiducial cosmology of the QUIJOTE simulation. The black pixels highlight the DM distribution. *To appear in* [5].

For each snapshot and realization, QUIJOTE provides the catalogues of DM halos. These are identified by a linking length $l_{FoF} = 0.2\bar{l}$, being $\bar{l}$ the mean inter−particle separation; only halos containing at least 20 particles are considered.

[4] Typically, the density of the halos is set to be 200 times higher than the mean background density: this defines the halo mass m_{200}, which has to be enclosed inside a certain radius r_{200} [354].

[5] The name of the algorithm relates to the fact that each particle is linked to all the other within a distance l_{FoF}, which are indicated as its *friends*, and indirectly to all the particles linked to its friends, which are indicated as the *friends of friends*.

[6] $M_\nu \sim 0$eV is the sum of the neutrino masses, $\sigma_8 \sim 0.834$ is the present variance of the matter density fluctuations on a scale of 8 h^{-1} Mpc.

Figure 7.2 shows the DM halo mass distribution $n_h(m, z)$ (compare with section 3.1.1) we measured from the catalogues for the $z = [0, 1, 2]$ snapshots in the fiducial cosmology. This is compared with the Sheth–Mo–Tormen distribution [362] commonly used in the literature.

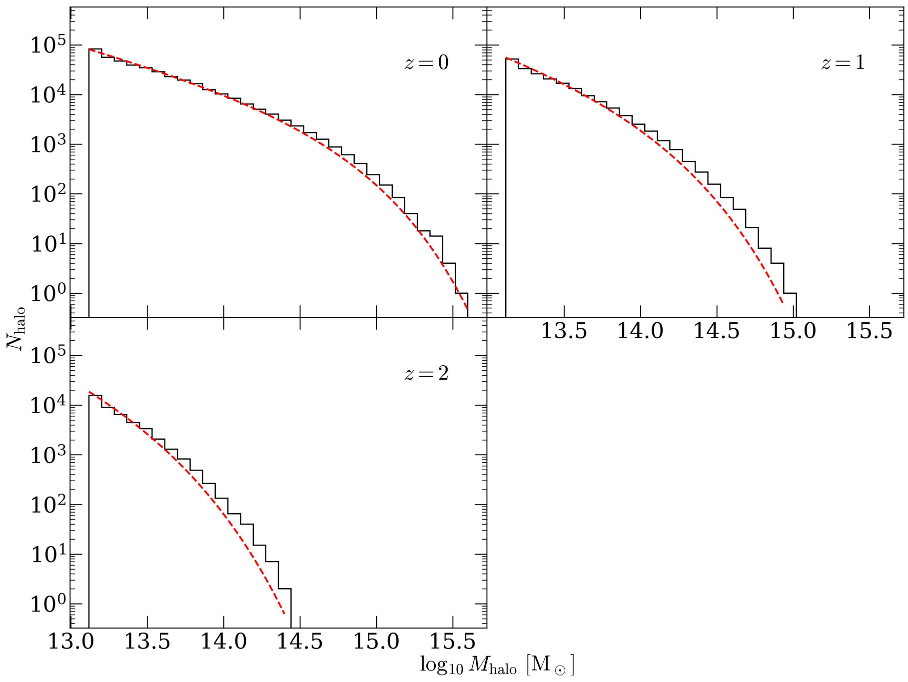

Figure 7.2: Mass distribution of DM halos in the QUIJOTE redshift snapshots used in the analysis in section 7.4 (black histogram) compared with the Sheth–Mo–Tormen halo mass function [362] (dashed red line). This has been normalized to the number of halos in the catalogs. *To appear in* [5].

7.1.2 Hydrodynamical simulations

The simulation of the baryon component is more difficult and computationally expensive, since it requires to take into account viscosity and processes such as radiative transfer, gas cooling or star formation. This is done through discretized solutions of the conservation and time evolution equations of the density, velocity and energy of the baryon fluid, complemented by the description of the astrophysical processes.

Such processes are included as **sub–grid** physics: numerical issues prevent from resolving them in the full simulation, therefore effective semi–analytical models are built to describe them. In these, particles below a certain relative distance are described through the density and pressure of the overall fluid, smoothed by a window function [363], on which the astrophysical processes depend.

Moreover, to reduce the dimension of the problem, usually the particle masses are chosen to be larger than the mass of the real bodies they represent e.g., to simulate a galaxy made by $\sim 10^{10}$ stars with $M \in [1, 100]\, M_\odot$, it is customary to use $\sim 10^5$ stellar particles having mass $M \in [10^6, 10^8]\, M_\odot$.

The EAGLE simulation

The EAGLE suite contains a set of cosmological simulations [206, 207] that track the evolution of gas, DM and stars across cosmic time. The simulations include sub–grid models for cooling, star formation, chemical enrichment, stellar and active galactic nucleus feedback. Galaxy catalogues are extracted from these simulations, considering different resolutions, which depend on the size of the box considered.

The box used in the EAGLE suite and adopted in this analysis, has comoving side $67.77\,h^{-1}$ Mpc and contains 1504^3 particles. Its resolution therefore is higher than the QUIJOTE one, but the probed volume is smaller. As it is evident by comparing figure 7.1 and figure 7.3, observed scales therefore are smaller as well: this has important consequences when analysing cosmological quantities, as section 7.4 will describe.

The fiducial cosmology used in the simulation is described in table 7.1. For the purpose of this work, only four snapshots were considered, specifically at $z = 0$, $z = 1$, $z = 2$ and $z = 6$.[7] Each of these epochs has been chosen since it has a particular significance in terms of astrophysical events:

- $z = 0$ corresponds to the current cosmic time, where the degree of non−linearity in the distribution of matter is at its highest.
- $z = 1$ is close to the detector horizon (see section 4.2) for binary black holes of the advanced LIGO interferometers [364].
- $z = 2$ is where the star formation rate (see section 3.3.1) peaks [365].
- $z = 6$ is close to the end of the reionisation epoch (see section 2.1.3) [6, 366].

[7] Each EAGLE snapshot has its own Δz width, but in the text they are indicated through their nearest integer, for clarity. In particular, the snapshots we adopted are: $z \in [0, 0.1]$, $z \in [0.93, 1.13]$, $z \in [1.87, 2.12]$ and $z \in [5.73, 6.51]$.

Figure 7.3 shows a slice of the simulation box at $z = 0$: DM is represented through the black dots.

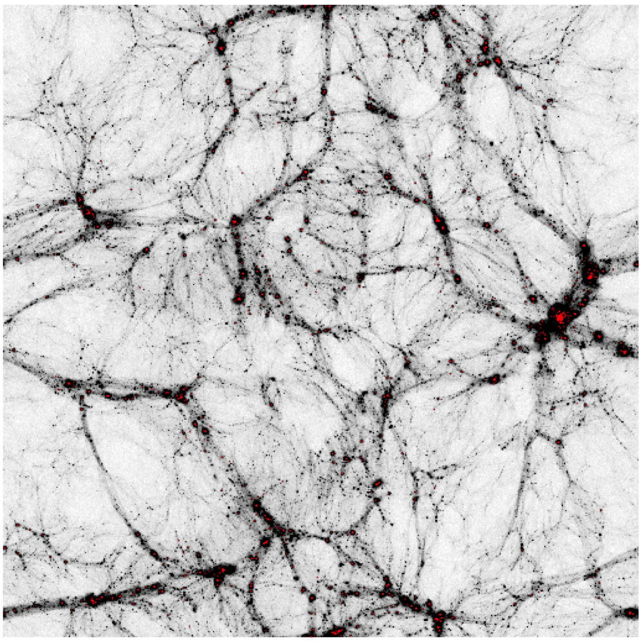

Figure 7.3: Slice of $5\,h^{-1}$ Mpc side of the EAGLE simulation in the $z = 0$ snapshot. The black pixels represent the DM distribution, while the red points represent a random sample of the binary black hole mergers generated from MOBSE described in section 7.1.3. By comparing this figure with figure 7.1 from the QUIJOTE simulation, the different resolution and scales probed are evident. *To appear in* [5].

The DM halos identified through the Friends−of−Friends algorithm are $\simeq (5.4 \cdot 10^5)$ at $z = 0$, $\simeq (6.8 \cdot 10^5)$ at $z = 1$, $\simeq (7.3 \cdot 10^5)$ at $z = 2$, and $\simeq (4.8 \cdot 10^5)$ at $z = 6$ [206, 207]. Figure 7.4 shows the halo mass distributions for each snapshot and compared to the Sheth−Mo−Tormen $n_h(m, z)$ [362]. Thanks to the higher resolution of the simulation, the mass of the halos in this case spans over a slightly different range with respect to the QUIJOTE ones, reaching smaller values. This is evident by comparing snapshots from figure 7.2 with the corresponding ones from figure 7.4.

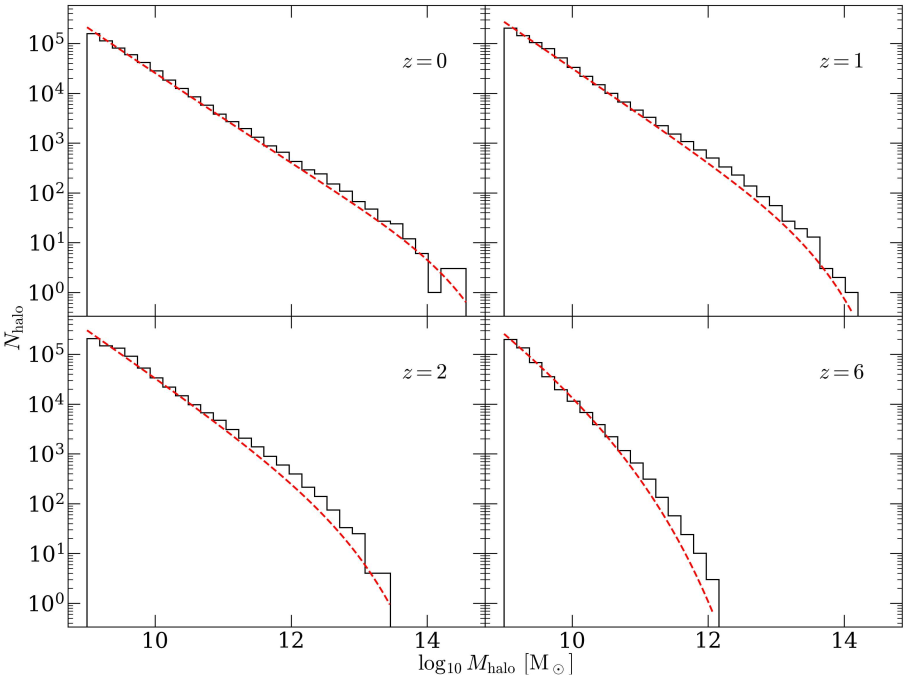

Figure 7.4: Mass distribution of DM halos in the EAGLE redshift snapshots adopted in the analysis in section 7.4 (black histogram) compared with the Sheth−Mo−Tormen halo mass function [362] (dashed red line). This has been normalized to the number of halos in the catalogues. By comparing this figure with figure 7.2, it is possible to note that DM halos identified in the EAGLE suite reach smaller masses. *To appear in* [5].

7.1.3 The population-synthesis code MOBSE

To perform studies of binary mergers on cosmological scales, the sub−grid physics described in section 7.1.2 and its limited mass resolution are not enough to yield accurate results. For this reason, the authors of [205, 322, 367] proposed to seed existing cosmological simulations with catalogues of stellar objects simulated through population−synthesis codes.

Population−synthesis codes are used in the study of structure and evolution of single stars or groups of them. These, depending on the goal of the simulation, use detailed models to characterize the properties of each simulated body and on the field where it is found. MOBSE [323, 367, 368] is one of them: it has been designed to simulate the formation and evolution of the progenitors of compact object binaries, which can eventually merge and produce GW.

MOBSE simulates stellar components that evolve to become compact remnants, such as neutron stars or black holes. It contains fitting formulas that describe the evolution of stellar properties as a function of metallicity and stellar mass. Up−to−date models for stellar wind mass loss [369] are included, together with state−of−the−art prescriptions for core collapse [370] and pair−instability supernovae [371]. The formalism for binary evolution processes from [368] is exploited in this code; the mass function and local merger rate density obtained are in agreement with results from [248, 250, 372].

The binary compact objects generated with MOBSE are randomly associated with stellar particles in the EAGLE simulation: they can be either binary black holes, binary neutron stars or black hole−neutron star systems. The link between the stellar particles and the presence of a binary inside them is based on the formation time, metallicity (see section 5.3.1) and total initial mass of the particles themselves [367]. Properties of the stellar progenitors of each binary and delay time between formation and merger of the binary are self−consistently taken into account.

In this way, catalogues of merger events in the EAGLE simulation are produced. As for BBH mergers, about $\simeq (\cdot 10^8)$ objects are found at $z = 0$, $\simeq (2.9 \cdot 10^8)$ at $z = 1$, $\simeq (2.0 \cdot 10^8)$ at $z = 2$, and $\simeq (1.3 \cdot 10^7)$ at $z = 6$. Figure 7.3 shows a subselection of the events at $z = 0$, comparing their distribution with the DM one. It is evident that mergers are mostly found where DM clusters the most i.e., in the high density peaks where also the most massive halos are found. This is coherent with the derivation in section 3.1.1.

At this level, the catalogues contain the full distribution of all the possible mergers produced in the simulated Universe. If the goal is to study their detectability with respect to a particular detector e.g., the Einstein Telescope, information regarding the signal−to−noise ratio[8] should be introduced to take into account its selection function. While this was done for the catalogues used for the analysis in chapter 5 and chapter 6, the ones used in this chapter have not been filtered.

All the results presented in section 7.4, therefore, refer to the full, intrinsic distribution of the mergers, without any detector selection effect.

7.2 Power spectrum estimator

The tool required to study the statistical properties of the simulated catalogues is the power spectrum $P(\boldsymbol{k})$, which was introduced in section 2.2.2 and characterized in section 3.2 in its formulation for point−like, Poisson distributed sources. To extract it from a data−set, it is necessary to build an estimator $\tilde{P}(\boldsymbol{k})$. In the following, we will present the standard procedure for the analysis of simulated catalogues. The extension to real data would introduce some complications:

- Simulated data are distributed inside regular boxes, inside which their coordinates are known with 100% precision, while real data cover irregular volumes and are affected by instrumental errors and systematics.
- The mean number density of simulated data is the same all over the box i.e., their average distribution is homogeneous and isotropic, while real data distribution can change from point to point and also be masked in some regions.
- In simulated catalogues contributions from different redshift snapshots come from independent outputs, while for real data all the information overlaps and need to be disentangled.
- Simulated catalogues are realized and analysed in comoving space, while real data are affected by the space distortions described in section 3.2.1 and section 5.2.

Let us consider a simulated catalogue made by N_p particles (as described in section 7.4, in our analysis they can be either DM, halos or mergers) distributed inside a cubic box having comoving size L.[9] The points are mapped through the $\boldsymbol{r} = (x, y, z)$ coordinates inside the box, where the $(0, 0, 0)$ point is fixed in one of the vertices; each point has the same mass m, therefore masses are simplified out in the following analysis.

The computation of the $\delta(\boldsymbol{r})$ overdensities in the particle distribution can not be directly performed on the discrete set but has to be weighted through the **Grid Assignment Scheme** (GAS). This is defined by a square grid made in each of the (x, y, z) directions by N_g cells of size $\mathcal{S} = L/N_g$, inside which the particle distribution is smoothed. On one side, in this way the structures on scales smaller

[8] As described in section 4.3.1, the merger detectability depends on the amplitude of the GW signal (which is related with intrinsic parameters, such as the progenitor masses, the spins and the distance from the observer), and on the antenna pattern of the detector (which is related to the binary position in the sky and its inclination with respect to the detector plane). When working with simulations, a rough selection can be performed, which only depends on the average SNR of the mergers and with the expected SNR lower limit of the detector.

[9] In the case of real data−sets, in order to perform the discrete Fast Fourier Transform (FFT) the survey has to be enclosed in a box [373–378]. For simulations, this is already taken into account.

than $\mathcal{S}$ are smeared; on the other, each particle point is used to assign a certain weight to a group of cells. Formally, per each grid cell in the position $\boldsymbol{r}_g$, this is equivalent to compute the density $\tilde{\delta}(\boldsymbol{r}_g)$ through the convolution:

$$\tilde{\delta}(\boldsymbol{r}_g) = \int d^3r' \, W(\boldsymbol{r}_g - \boldsymbol{r}')\delta(\boldsymbol{r}') = \sum_{i=1}^{N_p} W(\boldsymbol{r}_g - \boldsymbol{r}_i) \, . \tag{7.5}$$

The weight each point provides to the different cells depends on the particular GAS adopted. There are several possible choices [379]; usually, the top–hat function:

$$\mathcal{T}(s) = \begin{cases} 1 & \text{if } |s| < 1/2 \\ 0 & \text{otherwise} \end{cases} , \tag{7.6}$$

is convoluted p times to define the piece–wise GAS window function $W^{(p)}(s)$ with respect to the grid spacing in each direction:

$$\begin{aligned} s_x &= (x_g - x_i)/\mathcal{S} \, , \\ s_y &= (y_g - y_i)/\mathcal{S} \, , \\ s_z &= (z_g - z_i)/\mathcal{S} \, . \end{aligned} \tag{7.7}$$

Through this choice, the window function is a symmetric, positive–defined function, separable in its components (x, y, z). A widely–used choice for the GAS is the second order $p = 2$ piece–wise function. This is called the **Cloud–In–Cell** (CIC) and it is defined in each component by:

$$W^{(2)}(s) = (\mathcal{T} * \mathcal{T})(s) = \begin{cases} 1 - |s| & \text{if } |s| < 1/2 \\ 0 & \text{otherwise} \end{cases} . \tag{7.8}$$

The complete window function is therefore given by:

$$W(\boldsymbol{r}_g - \boldsymbol{r}_i) = \frac{1}{\mathcal{S}^3} \prod_{s=\{x,y,z\}} W^{(2)}\left(\frac{s_g - s_i}{\mathcal{S}}\right) , \tag{7.9}$$

where the $\mathcal{S}^3$ factor represents the cell volume, s_g represents the coordinates of the grid point and s_i the coordinates of the particle. In the CIC formulation, each point particle assigns a certain weight to the cell it belongs to (the *parental cell*) and to the seven *neighbouring cells* whose distance from the parental one is $< \mathcal{S}/2$. This is sketched in figure 7.5.

By introducing the GAS, the weighted overdensities are [373]:

$$\tilde{\delta}(\boldsymbol{r}_g) = W(\boldsymbol{r}_g - \boldsymbol{r})\delta(\boldsymbol{r}) \, . \tag{7.10}$$

The mean number density inside the box can be either computed by considering the contributions of all the cells or on the overall simulation:

$$\bar{n}(\boldsymbol{r}) = \sum_{g=1}^{N_g} \sum_{i=1}^{N_p} W(\boldsymbol{r}_g - \boldsymbol{r}_i) = \sum_{i=1}^{N_p} \delta^D(\boldsymbol{r} - \boldsymbol{r}_i) = \frac{N_p}{L^3} = \bar{n} \, . \tag{7.11}$$

To implement the algorithm for the estimate of the power spectrum, therefore, the weighted overdensities from eq. (7.10) has to be defined and Fourier transformed by applying the FFT.[10] This can be written as:

[10] We compute the FFT by using the `pyhton.scipy` library. This assumes that the grid spacing is unitary, therefore $\mathcal{S}$ has to be used to normalize its result: for this reason in eq. (7.12) the factor $\mathcal{S}$ is introduced. Moreover, note that the normalization adopted here is different with respect to the one used in chapter 2 and chapter 3; we did this choice to be coherent with the numerical libraries we made use of.

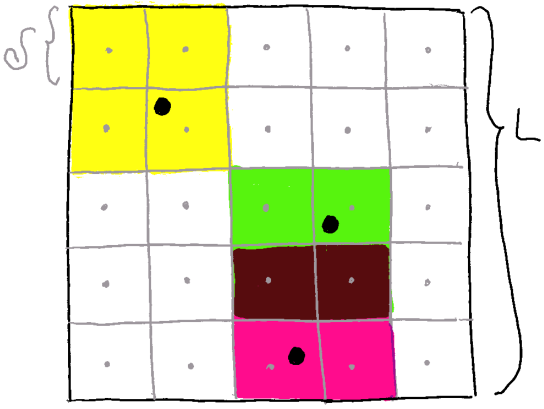

Figure 7.5: Sketch representation of how the CIC works; only two dimensions are considered, for clarity. L is the size of the box, $\mathcal{S}$ the size of the grid cells, which are represented with grey lines. Grey, small points are the N_g grid points, while black, big, points represent the N_p particles. The different colors indicate the cells to which each particle assigns weights through eq. (7.9). The darker, brown cells are the ones that receives weights from more than one particle.

$$\begin{aligned}\tilde{\delta}(\boldsymbol{k}) &= W(\boldsymbol{k})\left(\frac{FFT[\tilde{\delta}(\mathscr{x})]}{\mathcal{S}}, \frac{FFT[\tilde{\delta}(\mathscr{y})]}{\mathcal{S}}, \frac{FFT[\tilde{\delta}(\mathscr{z})]}{\mathcal{S}}\right) \\ &= W(\boldsymbol{k})\left(\frac{\tilde{\delta}(k_{\mathscr{x}})}{\mathcal{S}}, \frac{\tilde{\delta}(k_{\mathscr{y}})}{\mathcal{S}}, \frac{\tilde{\delta}(k_{\mathscr{z}})}{\mathcal{S}}\right).\end{aligned} \tag{7.12}$$

The values that $\boldsymbol{k}$ can assume are all and only the integer multiples of the **fundamental mode**, which is defined as:

$$k_f = \frac{2\pi}{L}\,. \tag{7.13}$$

The fundamental mode represents the smallest magnitude of the wavevector that can be sampled in Fourier space i.e., the maximum resolution that can be achieved.

In eq. (7.12), the Fourier transform of the CIC window from eq. (7.9) is:

$$W(\boldsymbol{k}) = \left[\frac{\sin(\mathcal{S}k_{\mathscr{x}}/2)}{\mathcal{S}k_{\mathscr{x}}/2} \cdot \frac{\sin(\mathcal{S}k_{\mathscr{y}}/2)}{\mathcal{S}k_{\mathscr{y}}/2} \cdot \frac{\sin(\mathcal{S}k_{\mathscr{z}}/2)}{\mathcal{S}k_{\mathscr{z}}/2}\right]^2. \tag{7.14}$$

The values $\mathcal{S}k_{\mathscr{x},\mathscr{y},\mathscr{z}}/2$ can be rewritten as $\pi k_{\mathscr{x},\mathscr{y},\mathscr{z}}/2k_{Ny}$, where:

$$k_{Ny} = \frac{\pi}{\mathcal{S}} = \frac{\pi N_g}{L}\,, \tag{7.15}$$

is the **Nyquist sampling frequency** i.e., the sampling resolution adopted.

To estimate the power spectrum, the covariance of the overdensities in eq. (7.12) is required. By applying eq. (2.36), this is:

$$\left\langle \delta(\boldsymbol{k}_1)\delta(\boldsymbol{k}_2)^* \right\rangle = (2\pi)^3\delta^D(\boldsymbol{k}_1+\boldsymbol{k}_2)P(\boldsymbol{k}_1) + \frac{1}{\bar{n}}\delta^D(\boldsymbol{k}_1+\boldsymbol{k}_2)\,. \tag{7.16}$$

The second contribution is due to the shot noise, described in section 3.2; eq. (7.12) and eq. (7.16) are combined to get:

$$\begin{aligned}\left\langle \tilde{\delta}(\boldsymbol{k}_1)\tilde{\delta}(\boldsymbol{k}_2)^* \right\rangle &= \int \frac{d^3k'}{(2\pi)^3} W(\boldsymbol{k}_1-\boldsymbol{k}')W(\boldsymbol{k}_2-\boldsymbol{k}')\left\langle \delta(\boldsymbol{k}_1)\delta(\boldsymbol{k}_2^*) \right\rangle \\ &= \delta^D(\boldsymbol{k}_1+\boldsymbol{k}_2)\int \frac{d^3k'}{(2\pi)^3}\left[W(\boldsymbol{k}_1-\boldsymbol{k}')W(\boldsymbol{k}_2-\boldsymbol{k}')P(\boldsymbol{k}')\right] + N(\boldsymbol{k}_1+\boldsymbol{k}_2)\,.\end{aligned} \tag{7.17}$$

The GAS window function introduced in eq. (7.10) and eq. (7.12) can here be interpreted as a smoothing effect, which makes $P(\boldsymbol{k}') = const$ in the narrow window around $\boldsymbol{k}'$ [373]. The expected value of the shot noise:

$$N(\boldsymbol{k}_1 + \boldsymbol{k}_2) = \int d^3\boldsymbol{r}\, \frac{W(\boldsymbol{r})}{\bar{n}(\boldsymbol{x})} \exp[i\boldsymbol{k}\cdot\boldsymbol{r}]\,, \tag{7.18}$$

has to be subtracted to the measured variance in order to properly estimate the power spectrum [373]. The presence of $\delta^D(\boldsymbol{k}_1 + \boldsymbol{k}_2)$, due to the uncorrelation between the different $\boldsymbol{k}$ modes, allows us to reduce the problem to:

$$\left\langle\tilde{\delta}(\boldsymbol{k})\tilde{\delta}(\boldsymbol{k})^*\right\rangle = \delta^D(\boldsymbol{k}) \int \frac{d^3k'}{(2\pi)^3} \left[W(\boldsymbol{k}-\boldsymbol{k}')^2 P(\boldsymbol{k}')\right] + N(0)\,, \tag{7.19}$$

from which the GAS window has to be deconvolved. By doing so and by subtracting the shot noise, the power spectrum estimator turns out to be:

$$\tilde{P}(\boldsymbol{k}) = \frac{\delta^D(\boldsymbol{k})}{W^2(\boldsymbol{k})} \int \frac{d^3k'}{(2\pi)^3} W(\boldsymbol{k}-\boldsymbol{k}')^2 P(\boldsymbol{k}')\,. \tag{7.20}$$

The estimator can finally be averaged over the different cells; moreover, because of the discreteness of the problem, the $\delta^D(\boldsymbol{k})$ is converted into a Kroenecker delta, which has to be normalized by the space in which $k = |\boldsymbol{k}|$ can spread i.e., the number of modes $N_k = k_f^{-3}$ [378] included inside $[k, k+k_f]$. Therefore eq. (7.20) becomes:

$$\tilde{P}(k) = \frac{k_f^3}{L^3} \sum_{k_i < k \leq k_i + k_f} \tilde{P}(k_i)\,. \tag{7.21}$$

The formulation introduced in eq. (7.20) represents the first approximation for the smooth power spectrum estimator. It can be refined by using different techniques, some of them are described in the following.

7.2.1 Interlacing

When computing the power spectrum, modes $k \geq 2k_{Ny}$ can be affected by the **aliasing** effect [376], which produces a spurious contribution and a systematic increase of power on the small scales. This is due to the finite resolution of the grid spacing: in fact, the unresolved small scales are sampled by the discrete FFT [378] and mistakenly identified as modes supported by the grid. This effect is formalised through:

$$\tilde{\delta}(\boldsymbol{k}) = \sum_{\mathsf{n}} \tilde{\delta}(\boldsymbol{k} - 2k_{Ny}\mathsf{n})\,, \tag{7.22}$$

where $\mathsf{n} = (\mathsf{n}_x, \mathsf{n}_y, \mathsf{n}_z)$ is an integer vector and $2k_{Ny}$ is the periodicity introduced by the discrete FFT. Only the $\mathsf{n} = 0$ terms are physical, while the following ones (whose contribution is dominant for $\mathsf{n} = 1$ and it decreases for higher n) are due to the aliasing.

To minimize this effect, one possible solution is to low−filter the data, removing all the modes above the Nyquist frequency. This however would make the GAS window non−local and the grid interpolation inefficient. Alternatively, the authors of [378] propose the **interlacing** technique. In this case, to interpolate the data two independent but equal grids are used, shifted one with respect to the other by $\mathcal{S}/2$

in all the directions. Therefore, $\tilde{\delta}(\boldsymbol{k})$ in eq. (7.12), is built by combining the two contributions $\tilde{\delta}^{G1}(\boldsymbol{k})$ and $\tilde{\delta}^{G2}(\boldsymbol{k})$ [378]:

$$\tilde{\delta}(\boldsymbol{k}) = \frac{\tilde{\delta}^{G1}(\boldsymbol{k}) + \tilde{\delta}^{G2}(\boldsymbol{k})}{2} = \frac{1}{2}\sum_{\mathbf{n}}\left[1 + (-1)^{\mathsf{n}_x+\mathsf{n}_y+\mathsf{n}_z}\right]\tilde{\delta}(\boldsymbol{k} + 2k_{Ny}\mathbf{n}) \,. \tag{7.23}$$

Since $1+(-1)^{\mathsf{n}_x+\mathsf{n}_y+\mathsf{n}_z} \neq 0$ only when $\mathsf{n}_x + \mathsf{n}_y + \mathsf{n}_z$ is even, the effect of the interlacing is to cancel some of the $\mathbf{n}$ contributions. In particular, the dominant $\mathbf{n} = 1$ is removed, therefore the aliasing effect is reduced.

This is analogous to doubling the sampling frequency: in this way, the aliasing effect starts to be relevant for $k \geq 4k_{Ny}$; however, since usually a cut–off scale due to physical motivations is introduced (see section 7.4), having the aliasing effect on such scales generally does not affect the results of the analysis.

7.2.2 FKP

A new weighting function $W(\boldsymbol{r})$ can be defined to minimize the variance of the quadratic estimator, so to optimize $\tilde{P}(k)$. In this sense, the Feldman–Kaiser–Peacock estimator (FKP, [374]) was firstly introduced. This approach is particularly effective for real surveys, where selection effects make the mean number density $\bar{n}(\boldsymbol{r})$ from eq. (7.11) position dependent. The FKP technique [374] introduces two new elements in the computation of the estimator: the synthetic random catalogue and the optimal weighting function.

The **synthetic random catalogue** $n_s(\boldsymbol{r})$ is defined as a spatially random field, which is filtered through the same selection function as the observed $n(\boldsymbol{r})$, but it does not contain the structures and overdensities of the latter, being in this way unclustered. It is generated as a Poisson point–like process whose mean number density is higher than the observed one, so to have:

$$n(\boldsymbol{r}) = \alpha n_s(\boldsymbol{r}) \,, \tag{7.24}$$

with $\alpha << 1$.

The **optimal weighting function**, instead, is defined as the weight through which the variance of the power spectrum estimator is minimized. This is defined through the inverse of the variance [373]:

$$W(\boldsymbol{r}) = \left[P(k) + \frac{1}{\bar{n}(\boldsymbol{r})}\right]^{-1} = \left[\bar{n}(\boldsymbol{r})P(k) + 1\right]^{-1} . \tag{7.25}$$

The effective overdensity field then is [377]:

$$F^{FKP}(\boldsymbol{r}) = \mathcal{N}\,\Theta(\boldsymbol{r})W(\boldsymbol{r})\left[n(\boldsymbol{r}) - \alpha n_s(\boldsymbol{r})\right] \,, \tag{7.26}$$

where $\Theta(\boldsymbol{r})$ describes the survey mask,[11] , α is the scaling factor introduced in eq. (7.24) and $\mathcal{N}$ is the normalization factor:

$$\mathcal{N} = \left[\int d^3x W(\boldsymbol{r})^2\bar{n}(\boldsymbol{r})^2\right]^{-1} . \tag{7.27}$$

$F^{FKP}(\boldsymbol{r})$ is used in the algorithm described in the previous section in place of $\tilde{\delta}(\boldsymbol{r})$. The expectation value $\langle F^{FKP}(\boldsymbol{k})F^{FKP}(\boldsymbol{k})^{*}\rangle$ enters then eq. (7.20) and eq. (7.21) to

[11] $\Theta(\boldsymbol{r}) = 1$ if the position $\boldsymbol{r}$ is included in the survey, 0 otherwise. For simulated catalogues where masks are not included, $\Theta(\boldsymbol{r}) \equiv 1$.

perform the computation of the power spectrum estimator. Using it to compute the variance:

$$\sigma^2(k) = \sum_{i=1}^{N_k} \frac{\left[|F(k_i)|^2 - \tilde{P}(k)\right]^2}{N_k - 1} , \tag{7.28}$$

it is possible to show that the weights in eq. (7.25) minimize $\sigma^2(k)$ when the synthetic sample is large i.e., $\alpha << 1$ [374]. Otherwise, the weights have to be corrected into $W(\boldsymbol{r}) = \left[1 + \alpha + P(\boldsymbol{k})\bar{n}(\boldsymbol{r})\right]^{-1}$.

The presence of $P(\boldsymbol{k})$ in eq. (7.25) implies that the algorithm developed to compute the power spectrum estimator through the FKP technique has to perform an iterative process. By starting from an initial guess $P_0(\boldsymbol{k})$, $W_0(\boldsymbol{r})$ are inferred and used to compute the field $F_0^{FKP}(\boldsymbol{r})$ as in eq. (7.26). From the variance of the Fourier transform of $F_0^{FKP}(\boldsymbol{r})$, the value of $\tilde{P}_0(\boldsymbol{k})$ is computed: this is used as a new estimate for the optimal weights in eq. (7.25) by defining $P_1(\boldsymbol{k}) = \tilde{P}_0(\boldsymbol{k})$. The procedure is then repeated until convergence, up to a desired precision.

7.3 Bias estimator

As described in section 3.1.2, the bias measures the relation between the clustering of a tracer and the underlying DM field. In the standard perturbation theory, when only local operators are taken into account, it relates the tracer overdensities $\delta_t(\boldsymbol{r})$ with the DM overdensities $\delta(\boldsymbol{r})$ through the expansion:

$$\delta_t(\boldsymbol{r}) = b(k)\delta(\boldsymbol{r}) \simeq \sum_{i=0}^{\infty} \frac{b_i(k)}{i!}\delta^i(\boldsymbol{r}) . \tag{7.29}$$

However, non−local operators have to be also included in the full bias computation e.g., the tidal contribution introduced in eq. (3.25) and the stochastic bias (see e.g., [154, 155]).

On the large scales, where the linear approximation holds, $b(k) \simeq b_1$ [154]. The linear bias then can be estimated through either of the following [380]:

$$\begin{aligned} \tilde{b}_1^{lin}(k) &\sim \sqrt{\frac{\tilde{P}_{tt}(k)}{\tilde{P}(k)}}, \\ \tilde{b}_1^{lin}(k) &\sim \frac{\tilde{P}_{tDM}(k)}{\tilde{P}(k)} , \end{aligned} \tag{7.30}$$

where $\tilde{P}_{tt}(k)$, $\tilde{P}(k)$ and $\tilde{P}_{tDM}$ are respectively the tracer auto−power spectrum, the DM auto−power spectrum and the tracer−DM cross−power spectrum estimated from the catalogues. All the estimators are computed by truncating the scales where first order perturbation theory is valid. When working with simulations, numerical fluctuations and systematics can break the scale−independence condition on $\tilde{b}_1^{lin}(k)$.

For small scales, higher order terms in the bias expansion are no longer negligible in the computation of $b(k)$. It is possible then to write at the second order expression as [381]:

$$b(k) = b_1(k) + b_2(k) + b_{K^2}(k) , \tag{7.31}$$

where $b_{K^2}(k) = -2/7(b_1(k) - 1)$, while $b_2(k)$ summarizes all the non−linear contributions; the value of b_1 and b_2 for DM halos, modelled through the models of [327] are shown in figure 7.6. In [327], the bias parameters are computed as:

$$b_1 = 1 + \frac{q\nu - 1}{\delta_c} + \frac{2p}{\delta_c\left[1 + (q\nu)^p\right]}\ , \tag{7.32}$$

which is slightly different than the value of eq. (5.35) adopted in chapter 5, and:

$$b_2 = q\nu\frac{q\nu - 3}{\delta_c^2} + \left[\frac{1 + 2p + 2(q\nu - 1)}{\delta_c} \cdot \frac{2p}{\delta_c\left[1 + (q\nu)^p\right]}\right]\ . \tag{7.33}$$

As defined in section 2.1, δ_c is the critical overdensity for the spherical collapse while ν is a parameter that depends on the halo mass m. This is assumed to be distributed following the standard Sheth−Mo−Tormen [212] halo mass function, computed through the `python.hmf` library. The values of the parameters are $p = 0.3$, $q = 0.707$.

Figure 7.6: Halo bias parameters b_1 (black continuous line) and b_2 (blue dashed line) computed using the prescription of [327] for $z = [0, 1, 2, 6]$, corresponding to the redshift snapshots in which the EAGLE simulation is analysed in section 7.4. The halo masses are assumed to be distributed following the standard Sheth−Mo−Tormen [212] halo mass function.

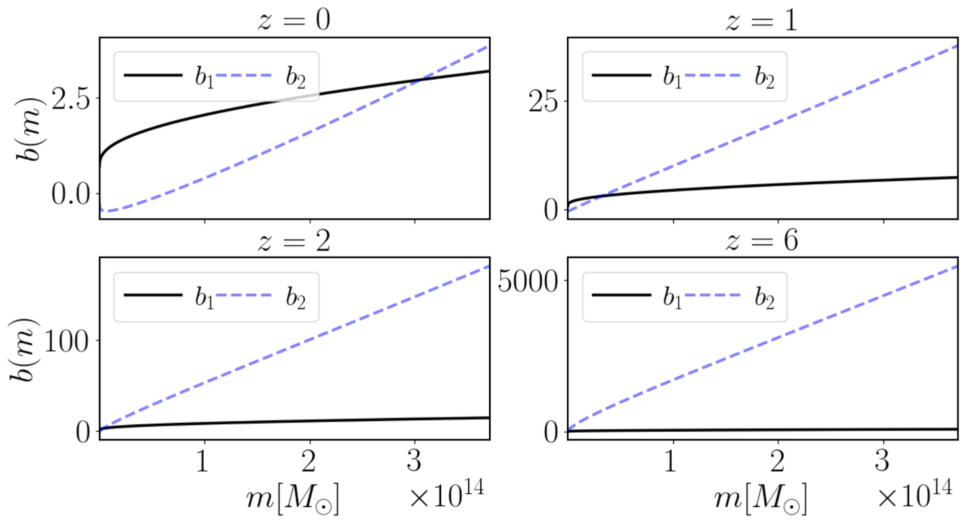

The parameter $b_2(k)$ can be treated as a nuisance parameter: marginalizing the overall estimator $\tilde{b}(k)$ over its value, the estimate of $\tilde{b}_1(k)$ can be obtained.

This is done by modelling the likelihood distribution (see section 6.1) of the two parameters as a multivariate normal distribution with N_k parameters, one for each of the k measured in the simulations:

$$p(\boldsymbol{d}|\,\boldsymbol{\theta},\,\Sigma) = \prod_{i=1}^{N} \frac{1}{\sqrt{2\pi}\sigma_i} \exp\left[-\frac{1}{2}\left(\frac{d_i - \theta_i}{\sigma_i}\right)^2\right]\ , \tag{7.34}$$

where $\boldsymbol{d} = (\tilde{P}_e(k_1),\ \ldots\ \tilde{P}_e(k_{N_k}))$ are the N_k independent estimates of the power spectrum (either auto- if $e = tt$ or cross- if $e = tDM$) at the different scales, $\boldsymbol{\theta} = (P_e(k_1),\ \ldots P_e(k_{N_k}))$ are their theoretical values and $\Sigma = \mathrm{diag}(\sigma_1^2,\ \ldots\sigma_{N_k}^2)$ is their diagonal covariance matrix.

The theoretical power spectra depend on the bias parameters $b(k)$. Therefore, they also contain the parameter we are interested in estimating i.e., the linear bias b_1, together with the other nuisance bias parameters $b_2(k),\ b_{K^2}(k)$. Since the latter depends on $b_1(k)$ [381], the posterior distribution (see section 6.1) depends only on $\boldsymbol{\theta} = (b_1,\, b_2)$.[12] Choosing uninformative uniform priors (see section 6.1) for both parameters inside the bins $[b_{1,2}^{min}, b_{1,2}^{max}]$, the logarithm of the posterior, either for the auto−power spectrum tt or the cross−power spectrum tDM, turns out to be:

$$
\begin{aligned}
\ln p(b_1,\, b_2|\, \boldsymbol{d}) &\propto \ln\left[p(\boldsymbol{d}|\, b_1,\, b_2) p(b_1,\, b_2)\right] \\
&= \begin{cases} \text{if } (b_1,\, b_2) \in [b_1^{min},\, b_1^{max}] \times [b_2^{min},\, b_2^{max}] : \\ \quad -\frac{1}{2}\,\sum_{i=1}^{N}\left[\frac{\left[\tilde{P}_{tt/tDM}(k_i) - P_{tt/tDM}(k_i,;\, b_1,\, b_2)\right]^2}{\sigma_i^2} + \ln 2\pi\sigma_i^2\right] . \\ \text{otherwise :} \\ \quad -\infty \end{cases}
\end{aligned}
\tag{7.35}
$$

The estimate $\tilde{b}_1(k)$ of the linear bias per each scale can be found by sampling[13] eq. (7.35) to get a set of vectors $(\tilde{b}_1(k),\, \tilde{b}_2(k))$ values distributed according to it. The value of $\tilde{b}_2(k)$ can then be marginalized to obtain a distribution for $\tilde{b}_1(k)$. Its central value is then used as the $\tilde{b}_1$ estimator.

7.4 Results

The main goal of this section is to estimate the bias of the black hole binary mergers in the hydrodynamical EAGLE+MOBSE simulations and to compare it with the HOD/GOD model introduced in chapter 5 [2, 3]. To do so, we developed our analysis through the following steps:

1. Build the power spectrum estimator in eq. (7.21) and extract $\tilde{P}(k)$ for the DM particles and halos in the QUIJOTE catalogue.
2. Implement the FKP estimator based on eq. (7.26) and compare its results with the previous point; this is done for future applications on actual data.
3. Build the linear bias estimator described in section 7.3 and compute $b_1(m, z)$ for the DM halos in the QUIJOTE catalogue.
4. Compare the results of the previous points with the theoretical expectations, to check the reliability of the implemented estimators.
5. Apply the power spectrum and bias estimators to the DM particles and halos of the EAGLE catalogue to assess similarities and differences with respect to the QUIJOTE case.
6. Estimate the power spectrum and bias of the mergers from the EAGLE+MOBSE catalogue.
7. Compare the estimation from the previous point with the semi−analytical prescriptions in chapter 5 [2, 3].

Since EAGLE+MOBSE simulations probe only small, non−linear scales, in point **6** we introduced higher order expansion terms in the estimation of both the power spectrum and the bias. This is described in detail in the following. The full pipeline is implemented in `python` and parallelized through the built−in `python.multiprocessing` package to speed up the computation.

[12] For clarity in the notation, we omit the $k-$ dependence.

[13] The sampling is done through the library `python.emcee` [382].

Table 7.1 summarizes the fiducial cosmologies in which the QUIJOTE and the EAGLE+MOBSE simulations are run, together with their properties used in the analysis, which are defined in section 7.1, section 7.2 and section 7.3.

Parameter	QUIJOTE	EAGLE+MOBSE	Unit
Cosmological parameters			
Ω_c	0.3175	0.3070	-
Ω_b	0.0490	0.0482	-
h	0.6711	0.6777	-
n_s	0.9624	0.9611	-
σ_8	0.8340	0.8288	-
Simulation properties			
L	1000	67.77	h^{-1} Mpc
$N_{DM}[z = 0, 1, 2]$	512^3	$\simeq 553^3$	-
$N_{DM}[z = 6]$	-	$\simeq 553^3$	
$N_h[z = 0]$	$\simeq 10^{5.61}$	$\simeq 10^{5.73}$	-
$N_h[z = 1]$	$\simeq 10^{5.29}$	$\simeq 10^{5.83}$	-
$N_h[z = 2]$	$\simeq 10^{4.64}$	$\simeq 10^{5.87}$	-
$N_h[z = 6]$	-	$\simeq 10^{5.68}$	-
$N_{BBH}[z = 0]$	-	$\simeq 10^{8.00}$	-
$N_{BBH}[z = 1]$	-	$\simeq 10^{8.46}$	-
$N_{BBH}[z = 2]$	-	$\simeq 10^{8.31}$	-
$N_{BBH}[z = 6]$	-	$\simeq 10^{7.11}$	-
Analysis parameters			
N_g	256	256	-
$\mathcal{S}$	3.9062	0.2647	h^{-1} Mpc
k_f	0.0063	0.0927	$h\,\mathrm{Mpc}^{-1}$
k_s	1.6085	23.735	$h\,\mathrm{Mpc}^{-1}$
k_{Nyq}	0.8042	11.867	$h\,\mathrm{Mpc}^{-1}$

Table 7.1: Summary of the simulation−related information of interested for the analysis. First of all, the fiducial cosmology adopted respectively in [361] for the QUIJOTE and in [206, 207] for the EAGLE simulations are introduced. Then, the simulation properties are provided: L is the comoving box size, $N_{DM}[z]$, $N_h[z]$, $N_{BBH}[z]$ are respectively the number of DM particles (as described in the text, only a subselection of the EAGLE DM catalogue is considered), DM halos and binary black hole mergers in each catalogue in the z snapshots used in the analysis. N_g and $\mathcal{S}$ are the number of grid points per side of the box and the grid spacing. k_f, k_s, k_{Nyq} respectively are the fundamental frequency, the sampling frequency and the Nyquist frequency; notice the different values they assume in the two simulated suits, which are related to the different size of the box: as described in the text, EAGLE+MOBSE only probes the smaller, quasi−linear scales.

1. QUIJOTE: DM and halo power spectrum estimators

Three snapshots of one QUIJOTE realization in the fiducial cosmology are analysed, for each of them two catalogues are considered: the first one contains the DM particle positions in the simulated box, while the second contains the positions and masses of the DM halos. In particular, the halo position is defined by the centre−of−mass of the n^{DM} particles identified as part of the halo itself by the FoF algorithm (see section 7.1.1), while its mass is given by the sum of the n^{DM} particle masses. Since each DM particle has the same mass m_i, the mass of the halo is simply $n^{DM} m_i$.

Each element of the two catalogues is weighted over the $N_g = 256$ points of the interpolation grid by using the CIC defined in eq. (7.9); the algorithm presented in section 7.2 is then applied. Both the single grid and the double grid required for the interlacing technique [378] are computed.

The DM power spectra estimated through eq. (7.21) for all the snapshots are shown in figure 7.9. Uncertainties for each value of $\tilde{P}(k)$ are assigned by computing the variance as in eq. (7.28) but using $\tilde{\delta}(\boldsymbol{k})$ instead of $F^{FKP}(\boldsymbol{k})$. The scatter observed at the largest scales is due to the fact that the analysis has been performed over a single realization of the QUIJOTE suite. Therefore, similarly to what happens with cosmic variance in real surveys, the large scales are sampled in only few configurations, leading to a larger uncertainty on their estimates. The smaller scales instead show a systematic increase in the measured power, which is due to the aliasing effect described in section 7.2; this however is relevant only on very high k.

2. QUIJOTE: FKP estimator

The FKP estimator described in section 7.2 has been implemented. Even if this tools is superfluous in the case of simulation analysis, being developed for cases in which survey masks or inhomogeneous field have to be faced [374, 376], its realization foresees the future necessities we will have when performing data analysis. Moreover, it is used as an internal check for the validity of the power spectrum estimation.

In this case, analogously to point **1**, a $N_g = 256$ grid and a CIC are considered. To check the performance of the two algorithms, we run them over a subset of the full DM catalogue, which is built random sampling 10^6 of the particles. The synthetic catalogue $n_s(\boldsymbol{r})$ required by eq. (7.26) to build the FKP estimator is created by sampling 5 points per grid cell i.e., $\alpha \simeq 0.012$.

Both the configurations without and with interlacing [378] are analysed and compared; the FKP estimator [374] is tested both including the weight optimization and by directly comparing the DM catalogue with the synthetic one.

In all the cases, the two estimators provide similar results and behaviours both on the large and small scales, as figure 7.7 shows in the case of the $z = 0$ snapshot. In terms of computational cost, however, they perform very differently and the FKP procedure requires a longer time to be completed. Similarly, also the use of the interlacing increases the time required to complete the procedure. Therefore, since the results provided are comparable, we decided to continue the analysis by using exclusively the more efficient estimator: from now on, we will always refer to the power spectrum estimator in eq. (7.21).

3. QUIJOTE: halo bias estimator

The halo bias $\tilde{b}_1$ is computed as described in section 7.3, by sampling the posterior of $b_1(k),\ b_2(k)$ in eq. (7.35) for both the auto− and cross− power spectrum. The number of modes considered is $N_{NL} < N$, the value of which is set by $k_{N_{NL}} < k_{cut-off}$ defined in point **4**, while the uninformative uniform priors are defined as $b_1 \in [0,\ 100], b_2 \in [-10,\ 5000]$. An example of the posterior sampling is provided in figure 7.8. The different shape obtained using the auto− and cross−power spectrum models is due to the fact that in the cross−model the posterior is linear with respect to b_1 and b_2, while in the auto−model it is quadratic in the bias parameters.

Since the QUIJOTE simulation probes large, linear scales, the value of b_1 can be estimated also through $\tilde{b}_1^{lin}(k)$, which are obtained from eq. (7.30), and by imposing the scale−independence condition through the average:

$$\tilde{b}_1^* = \sum_{i=1}^{N_{QL}} \frac{\tilde{b}_1^{lin}(k_i)/\sigma^2_{\tilde{b}_1^{lin},i}(k_i)}{1/\sigma^2_{\tilde{b}_1^{lin},i}(k_i)}\ , \tag{7.36}$$

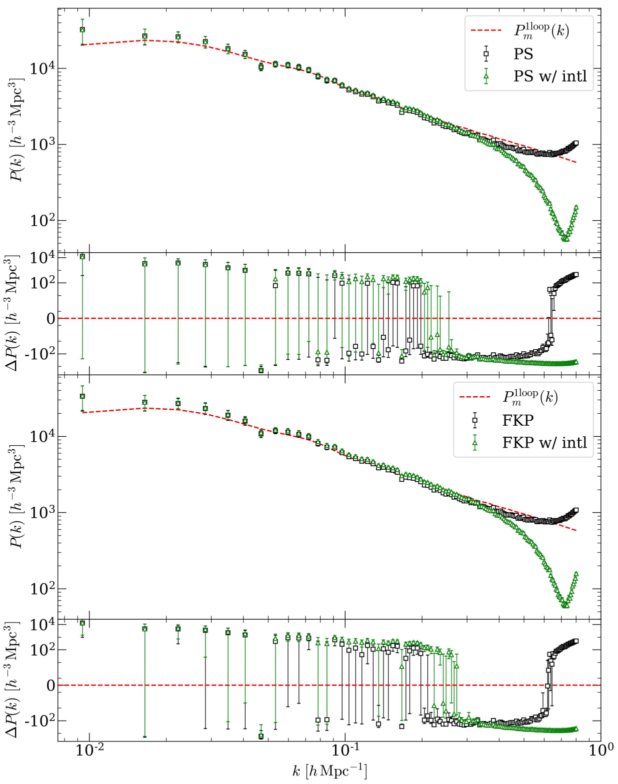

Figure 7.7: DM power spectra estimated for a random subset of 10^6 particles taken from the $z = 0$ snapshot of the QUIJOTE simulation and residuals with respect to the theoretical 1−loop matter power spectrum (see point **4**) which acquires the terms from eq. (3.10) (red dashed lines). On the top plot the power spectrum is estimated through eq. (7.21) (black squares), while on the bottom one FKP technique from section 7.2 is adopted. In all the plots, the green triangles estimate the power spectrum by including the interlacing technique. *To appear in* [5].

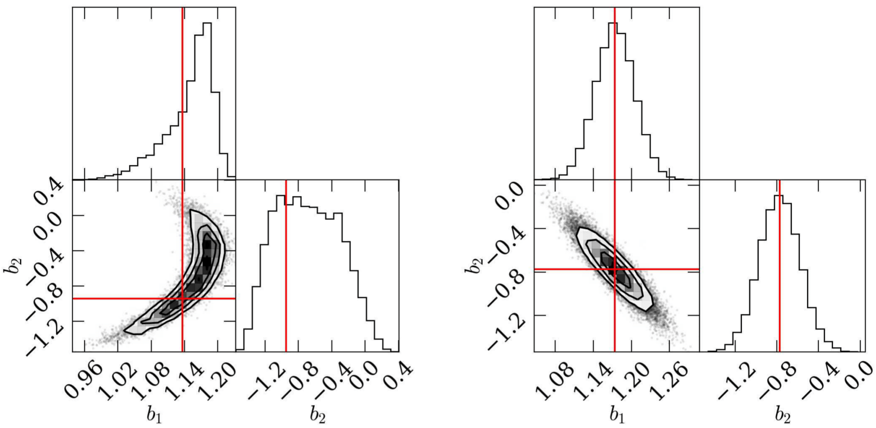

Figure 7.8: Examples of the posterior distributions for the dark matter halos with $\log_{10} \in [13.12, 13.20]$ of the QUIJOTE $z = 0$ snapshot obtained through the auto−power spectrum (left plot) and the cross−power spectrum (right plot). The red lines indicate the final estimates of $\tilde{b}_1$, chosen as the posterior maximum after $\tilde{b}_2$ is marginalized out. *To appear in* [5].

where $\sigma^2_{\tilde{b}_1^{lin}}(k_i)$ are the errors associated to the bias estimates and computed by propagating the variances σ^2_{DM} and σ^2_{hh} of the DM and halo auto−power spectra estimated in **1**:

$$\begin{aligned}\sigma_{\tilde{b}_1^{lin}}(k) &= \sqrt{\left(\frac{\partial \tilde{b}_1^{lin}(k)}{\partial \tilde{P}_{hh}(k)}\sigma_{hh}(k)\right)^2 + \left(\frac{\partial \tilde{b}_1^{lin}(k)}{\partial \tilde{P}(k)}\sigma_{DM}(k)\right)^2}\Bigg|_{k_i} \\ &= \frac{\tilde{b}_1^{lin}(k_i)}{2}\sqrt{\left(\frac{\sigma_{hh,i}}{\tilde{P}_{hh}(k_i)}\right)^2 + \left(\frac{\sigma_{DM,i}}{\tilde{P}(k_i)}\right)^2}\,.\end{aligned} \tag{7.37}$$

All the bias estimates are reported in table 7.2 and shown in figure 7.10. The error bars on the posterior estimate $\tilde{b}_1$ are given by the 16th and 84th percentiles on the marginalized distribution, while on the estimate $\tilde{b}_1^*$ they are computed through:

$$\sigma_{\tilde{b}_1^*} = \sqrt{\frac{1}{N_{QL}-1}\sum_{i=1}^{N_{QL}}\left[\tilde{b}_1^* - \tilde{b}_1^{lin}(k_i)\right]^2}\,. \tag{7.38}$$

The halo bias is here computed in different mass bins,[14] each defined to contain a similar number of halos. Per each mass bin, the bias error only takes into account the variance of the power spectrum inside the bin itself, while other contributions are neglected. For example, the masses of the halos defined through the FoF algorithm [361] are perfectly known in each catalogue and we assume that there is no error associated with them (i.e., the variance of the mass distribution between different realizations of the simulation or in dependence to different cosmology setups is not taken into account in the error propagation). Both table 7.2 and figure 7.10 provide therefore an optimistic measurement of the bias error bars.

[14] The halo mass distribution is extracted from the simulations by counting the halos belonging to each mass bin (see figure 7.2) and then it is compared with the standard Sheth−Mo−Tormen halo mass function [212].

4. Consistency check with theoretical models

The DM power spectrum $\tilde{P}(k)$ estimated from the QUIJOTE simulation can be compared with the theoretically modelled $P(k)$ introduced in section 3.1. In the standard perturbation theory, the evolution of the DM overdensities gives rise to a theoretical power spectrum which includes both linear and non−linear terms, as it is described by eq. (3.9).

The linearity is preserved when $\delta << 1$, i.e, on the large scales $\tilde{P}(k)$ is well described by the linear power spectrum $P^{lin}(k)$ from eq. (2.36). According to [383, 384], the cut−off scale k_{NL} below which non−linear corrections can be neglected, is:

$$k_{NL}(z) = k_{NL}^0(1+z)^{2/(2+n_s)}, \tag{7.39}$$

where $k_{NL}^0 \sim 0.2\,h\,\mathrm{Mpc}^{-1}$ is the local value of the cut−off scale. For the other snapshots of the QUIJOTE simulation used in the analysis, the cut−off scales are: $k_{NL}(z=1) = 0.32\,h\,\mathrm{Mpc}^{-1}$ and $k_{NL}(z=2) = 0.42\,h\,\mathrm{Mpc}^{-1}$; these are indicated through the vertical black lines in figure 7.9.

For $k > k_{NL}$, higher order terms have to be included in the theoretical computation of the power spectrum: following [139], the first expansion to account for is the 1−loop power spectrum $P^{1-loop}(k) = P^{lin}(k) + P^{NLO}(k) = P^{lin}(k) + 2P^{(13)}(k) + P^{(22)}(k)$ (compare with eq. (3.10)).

The 1−loop expression is then used to check the accuracy of the estimation of the QUIJOTE power spectrum in figure 7.9. All the contributions can be numerically computed through publicly available codes: $P^{lin}(k)$ is obtained with `CAMB` [165], while the $P^{NLO}(k)$ terms are build from `FAST−PT` [385, 386]; they are then summed and interpolated to the measured Fourier modes k by using cubic splines.

Figure 7.9 shows that the DM power spectra estimated from the QUIJOTE simulation are compatible with $P^{1-loop}(k)$ for all the snapshots up to a certain scale, which for $z = 0$ is $k \simeq 0.2 - 0.3\,h\,\mathrm{Mpc}^{-1}$, while for higher redshifts it moves to smaller scales and higher k. As k increases, the estimated and theoretical power spectra diverge, while staying in the 1% compatible region up to very high k. At this scales, to improve the compatibility between the two, $\tilde{P}(k)$ should be corrected by the aliasing effect described in section 7.2 and the theoretical $P(k)$ should be computed by including higher order terms.

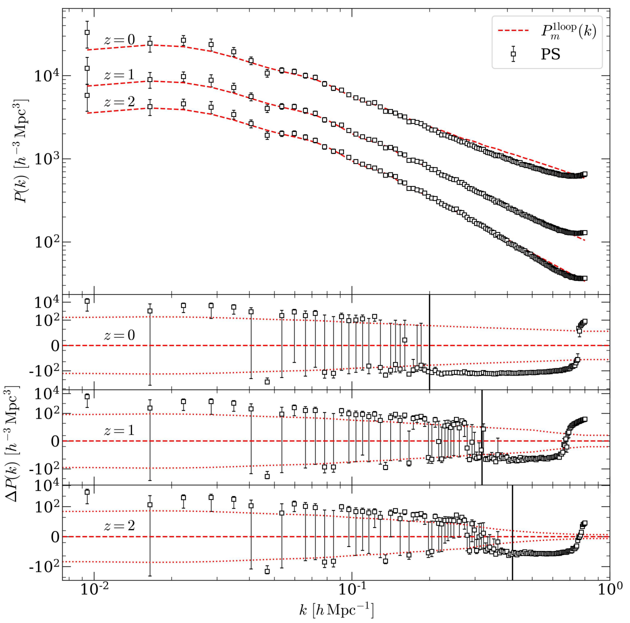

Figure 7.9: Upper plot: estimated DM power spectra (black dots) of the full DM catalogues of QUIJOTE simulation in the $z = [0,\ 1,\ 2]$ redshift snapshots compared with the the theoretical 1−loop DM power spectrum (dashed red line) from eq. (3.10). The other plots show for each snapshot the residuals between the estimated and theoretical DM power spectra. The dotted red lines indicate the 1% bounds with respect to the theoretical model, while the solid black lines show the wave number $\tilde{k}_{\rm NL}$ at which the perturbative description breaks down. *To appear in* [5].

Given these considerations, to provide a reliable estimate of the DM power spectra, we decided to cut all the scales above $k_{cut-off} \simeq 0.3\,h\,{\rm Mpc}^{-1}$.

As for the bias estimates, both $\tilde{b}_1$ from eq. (7.35) and $\tilde{b}_1^*$ from eq. (7.36) are compared in table 7.2 and figure 7.10 with the linear bias computed through the model from eq. (7.32), which was shown in figure 5.8. The mass and redshift dependence of the halo bias depend on how DM particles move and cluster inside the simulations under the effect of gravity: the halo formation and evolution of can be related with the hierarchical framework described in section 3.1

Table 7.2: Linear halo bias estimates $\tilde{b}_1$ (with both auto− and cross−power spectra, see eq. (7.35)) and $\tilde{b}_1^*$ (see eq. (7.36)) obtained with the different methods described in the text for DM halos in the QUIJOTE simulations. The halos are grouped in five mass bins, defined such that each bin has almost the same number of halo.

$\log(m\ [M_\odot]) \in$	$[13.12, 13.20]$	$[13.20, 13.29]$	$[13.29, 13.44]$	$[13.44, 13.67]$	$[13.67, 15.60]$
$z = 0$					
Bias from eq. (7.32)	1.03	1.12	1.32	1.44	1.92
$\tilde{b}_1^*$	$1.17^{+0.07}_{-0.07}$	$1.19^{+0.08}_{-0.08}$	$1.27^{+0.11}_{-0.11}$	$1.39^{+0.07}_{-0.07}$	$1.87^{+0.08}_{-0.08}$
$\tilde{b}_1$ (auto-)	$1.14^{+0.05}_{-0.03}$	$1.20^{+0.01}_{-0.05}$	$1.26^{+0.01}_{-0.06}$	$1.36^{+0.01}_{-0.04}$	$1.81^{+0.02}_{-0.04}$
$\tilde{b}_1$ (cross-)	$1.17^{+0.03}_{-0.03}$	$1.23^{+0.03}_{-0.03}$	$1.26^{+0.03}_{-0.03}$	$1.40^{+0.03}_{-0.03}$	$2.02^{+0.04}_{-0.04}$
$z = 1$					
Bias from eq. (7.32)	1.91	2.13	2.57	2.91	3.72
$\tilde{b}_1^*$	$2.35^{+0.19}_{-0.19}$	$2.43^{+0.28}_{-0.28}$	$2.62^{+0.29}_{-0.29}$	$2.99^{+0.21}_{-0.21}$	$4.03^{+0.23}_{-0.23}$
$\tilde{b}_1$ (auto-)	$2.35^{+0.05}_{-0.05}$	$2.42^{+0.07}_{-0.06}$	$2.63^{+0.06}_{-0.04}$	$3.04^{+0.06}_{-0.05}$	$4.14^{+0.06}_{-0.05}$
$\tilde{b}_1$ (cross-)	$2.42^{+0.04}_{-0.04}$	$2.54^{+0.05}_{-0.05}$	$2.75^{+0.05}_{-0.05}$	$3.15^{+0.05}_{-0.05}$	$4.21^{+0.07}_{-0.07}$
$z = 2$					
Bias from eq. (7.32)	3.48	3.90	4.80	5.50	6.61
$\tilde{b}_1^*$	$4.69^{+0.58}_{-0.58}$	$5.24^{+0.84}_{-0.84}$	$5.58^{+0.73}_{-0.73}$	$6.83^{+0.89}_{-0.89}$	$9.25^{+2.20}_{-2.20}$
$\tilde{b}_1$ (auto-)	$4.43^{+0.19}_{-0.20}$	$4.77^{+0.23}_{-0.23}$	$5.03^{+0.23}_{-0.24}$	$6.34^{+0.28}_{-0.29}$	$8.03^{+0.55}_{-0.64}$
$\tilde{b}_1$ (cross-)	$4.58^{+0.10}_{-0.10}$	$4.99^{+0.11}_{-0.12}$	$5.41^{+0.12}_{-0.11}$	$6.24^{+0.14}_{-0.14}$	$7.82^{+0.22}_{-0.23}$

The $\tilde{b}_1$ estimates agree within margin of error with $\tilde{b}_1^*$. All the estimated values

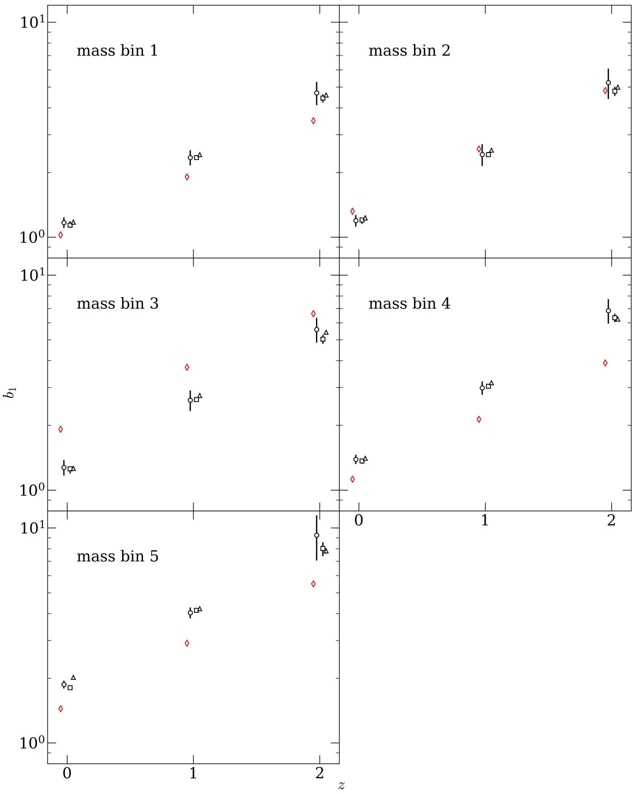

Figure 7.10: Linear halo bias as a function of redshift estimated from the QUIJOTE simulation. The estimates from eq. (7.32) (red diamonds) are compared with the linear estimator $\tilde{b}_1^*$ from eq. (7.36) (black circles) and with the estimates $\tilde{b}_1$ related with the posterior sampling of the auto− (black squares) and cross− (black triangles) power spectra. *To appear in* [5].

slightly deviate from the halo bias predictions of eq. (7.32) [327].

5. EAGLE+MOBSE: DM and halo estimators

The analysis performed on the QUIJOTE catalogues in the previous points showed that both the power spectrum and the bias estimators are reliable. After this validation test, the same estimators were applied to the study of the EAGLE+MOBSE catalogues of DM particles and halos.

However, these simulations present some peculiarities. First of all, the number of simulated DM particles is much larger: therefore, because of the computational cost of the procedure, only a subset of them is taken into account. This is built by random sampling 5% of the total 1504^3 DM particles. Moreover, the side of the simulated box is very small (see table 7.1) because of the high computational cost: therefore measurements on large scales are not possible. Still due to computational cost, only one realization of the simulation has been obtained, therefore our estimate will be affected by cosmic variance. Finally, halos in this case have lower mass than in the QUIJOTE case.

The small size of the box largely reduces the number of modes that can be considered in the analysis: keeping the same values as before for k_{NL} and $k_{cut-off}$, the fundamental frequency in the EAGLE box is such that only three large scale modes are included in the parameter estimation for the catalogs at $z > 0$, while for $z = 0$ only two points can be taken into account. Linear scales, therefore are not available: for this reason, we did not estimate $\tilde{b}_1^*$ from eq. (7.36) but we only rely on the estimate from the posterior sampling in eq. (7.35).

One example of the posterior sampling is shown in figure 7.11. As expected, the variance is larger with respect to figure 7.8.

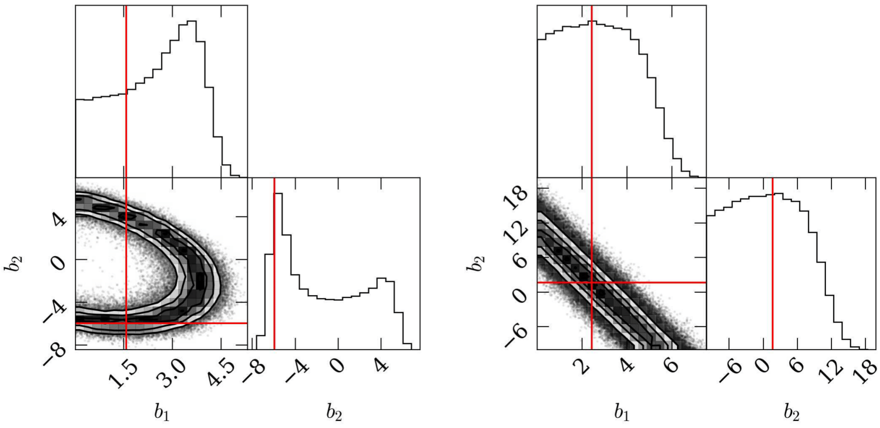

Figure 7.11: Examples of the posterior distributions for the DM halos with $\log_{10}(m\,[M_\odot]) \in [9, 9.11]$ of the EAGLE $z = 0$ snapshot obtained through the auto−power spectrum (left plot) and the cross−power spectrum (right plot). The red line indicate the final estimate of $\tilde{b}_1$, chosen as the posterior maximum after b_2 is marginalized out. *To appear in* [5].

Results for the halo bias estimates are reported in table 7.3 and showed in figure 7.12 compared to expectations from eq. (7.32).

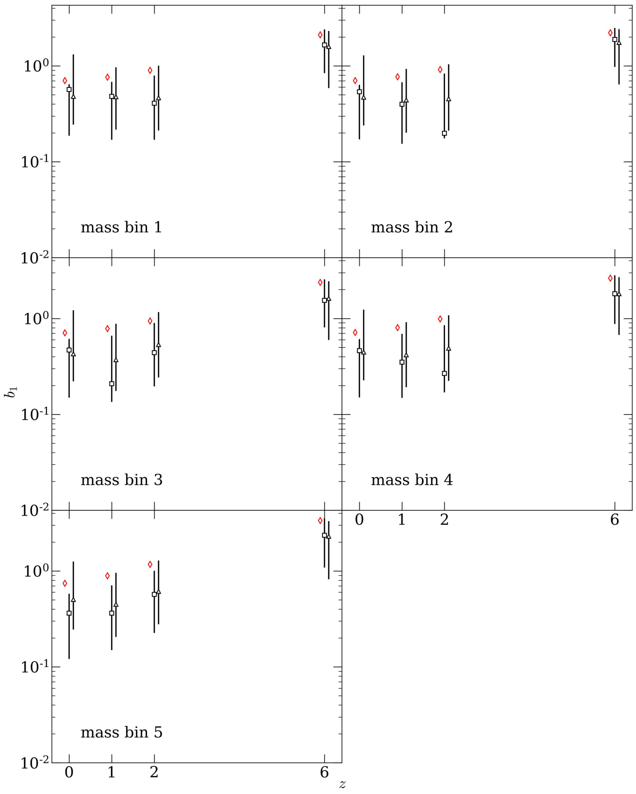

Figure 7.12: Halo bias $\tilde{b}_1$ as a function of redshift estimated from the EAGLE simulation. The estimates from eq. (7.32) (red diamonds) are compared with the $\tilde{b}_1$ related with the posterior sampling of the auto− (black squares) and cross− (black triangles) power spectra. *To appear in* [5].

Estimates of the halo bias $\tilde{b}_1$ are partially consistent with the expectations from eq. (7.32) [327]; the error bars in this case are larger than ones in the QUIJOTE analysis because of the smaller number of modes introduced in the computation.

The small discrepancy observed for halo bias in both figure 7.10 and figure 7.12 between our estimator and the expression from [327] could be related to the fact that this model does not accurately represent our data. Referring to figure 7.2 and

$\log(m\,[M_\odot]) \in$	$[9, 9.11]$	$[9.11, 9.25]$	$[9.25, 9.44]$	$[9.44, 9.74]$	$[9.74, 14.57]$
$z = 0$					
Bias from eq. (7.32)	0.70	0.70	0.71	0.71	0.74
$\tilde{b}_1$ (auto-)	$0.57^{+0.08}_{-0.38}$	$0.54^{+0.10}_{-0.37}$	$0.47^{+0.14}_{-0.32}$	$0.46^{+0.15}_{-0.31}$	$0.36^{+0.22}_{-0.24}$
$\tilde{b}_1$ (cross-)	$0.48^{+0.83}_{-0.24}$	$0.47^{+0.81}_{-0.23}$	$0.43^{+0.79}_{-0.21}$	$0.45^{+0.79}_{-0.22}$	$0.50^{+0.75}_{-0.26}$
$z = 1$					
Bias from eq. (7.32)	0.76	0.77	0.78	0.80	0.89
$\tilde{b}_1$ (auto-)	$0.48^{+0.20}_{-0.31}$	$0.40^{+0.28}_{-0.24}$	$0.21^{+0.45}_{-0.07}$	$0.35^{+0.34}_{-0.20}$	$0.36^{+0.35}_{-0.21}$
$\tilde{b}_1$ (cross-)	$0.48^{+0.49}_{-0.26}$	$0.44^{+0.49}_{-0.24}$	$0.37^{+0.51}_{-0.20}$	$0.42^{+0.50}_{-0.23}$	$0.45^{+0.51}_{-0.24}$
$z = 2$					
Bias from eq. (7.32)	0.90	0.92	0.94	0.99	1.17
$\tilde{b}_1$ (auto-)	$0.41^{+0.39}_{-0.24}$	$0.20^{+0.63}_{-0.02}$	$0.44^{+0.46}_{-0.24}$	$0.27^{+0.58}_{-0.10}$	$0.57^{+0.44}_{-0.34}$
$\tilde{b}_1$ (cross-)	$0.46^{+0.54}_{-0.25}$	$0.45^{+0.59}_{-0.24}$	$0.53^{+0.63}_{-0.29}$	$0.49^{+0.59}_{-0.27}$	$0.61^{+0.67}_{-0.34}$
$z = 6$					
Bias from eq. (7.32)	2.11	2.22	2.37	2.63	3.35
$\tilde{b}_1$ (auto-)	$1.66^{+0.74}_{-0.82}$	$1.89^{+0.60}_{-0.91}$	$1.54^{+1.01}_{-0.74}$	$1.81^{+1.01}_{-0.93}$	$2.36^{+1.17}_{-1.28}$
$\tilde{b}_1$ (cross-)	$1.59^{+0.72}_{-1.00}$	$1.75^{+0.66}_{-1.11}$	$1.62^{+0.83}_{-1.02}$	$1.81^{+0.88}_{-1.13}$	$2.30^{+1.01}_{-1.48}$

Table 7.3: Halo bias estimates $\tilde{b}_1$ (with both auto– and cross–power spectra, see eq. (7.35)) obtained with the different methods described in the text for DM halos in the EAGLE simulations. The halos are grouped in five mass bins, defined such that each bin has almost the same number of halo.

figure 7.4, it is possible to notice that the Sheth–Mo–Tormen halo mass function [212] (which enters the computation of the bias from eq. (7.32)) describes the simulated halo mass distribution only as a first approximation. It is possible then that this difference propagates in the bias estimators as well.

6. EAGLE+MOBSE: merger power spectrum and bias

The BBH merger catalogues in the four snapshots include information on the positions of the events, on the characteristics of their host halos and galaxies (e.g., the star formation rate or metallicity) and on their astrophysical nature (e.g., the progenitor masses). For the analysis developed in this work, only the positions are taken into account.

Also in this case, catalogues present a peculiarity: because of the limited mass resolution of the EAGLE simulation (see section 7.1.2), it is possible for a single stellar particle to host several mergers. The points in the catalogues, therefore, present a multiplicity, leading to the fact that in the same position (which depends on a given stellar particle) several mergers can be found.

We estimate the BBH merger power spectrum and bias analogously to the DM halo case. Results are in this case shown in figure 7.13: the model used for comparison is the HOD/GOD semi–analytical description introduced in section 5.3.2, the parameters of which were updated for consistency with the halo bias model used in **5**, as described in detail in **7**.

7. Comparison with the semi-analytical model

In section 5.3.2, we introduced the HOD/GOD model to estimate the merger bias. This, as well as the standard HOD technique used for galaxy surveys and described in section 3.3.1, is based on a weighted average of the bias of the host i.e., of galaxies. The weight depends on the conditioned number distribution of the binary mergers depending on the properties of their hosts e.g., $\langle N_{BBH}^{SIM} | M_*, SFR \rangle$ using the stellar mass M_* and the star formation rate SFR (compare with section 5.3.2).

As described in detail in section 5.3.2, once that such distribution is extracted from the simulation, the HOD/GOD technique provides a semi−analytical way to estimate the bias, without the need of any initial assumption on its value or shape. The analysis carried on in chapter 5 shows that the merger bias is well described by a linear dependence on redshift:

$$b(z) = A_{BBH}z + q_{BBH} \ , \tag{7.40}$$

where the fiducial values of $[A_{BBH}, q_{BBH}]$ are estimated from the simulations. In section 5.3.2, we reported as values for these parameters $A_{BBH} = 0.7$, $q_{BBH} = 1.88$. These directly depended on the catalogues from which $\langle N_{BBH}^{SIM} | M_*, SFR \rangle$ was extracted and have to be updated if the simulations change.

The EAGLE+MOBSE catalogues analysed in this chapter are indeed an updated version of the ones used in chapter 5. The main differences are:

- The new catalogues are computed inside a 100 Mpc side box, while the old ones were realized inside a 25 Mpc box.
- The new catalogues refer to the full distribution of BBH, while the old ones included selection effects from ET.
- Upgrades have been introduced in the description of the astrophysical processes.

Therefore, we expect $\langle N_{BBH}^{SIM} | M_*, SFR \rangle$ to slightly change when recomputed using the new catalogues; this kind of analysis is currently under development and our results will be updated soon.

Moreover, the fiducial values of $[A_{BBH},\ q_{BBH}]$ depend on the halo mass function and bias prescriptions that enter in eq. (5.32) and eq. (5.34). While in section 5.3.2 we adopted the b_1 prescription from [326], results from this chapter refers to the higher order expansion described in [327]. For this reason, the parameters of eq. (5.32) has been recomputed and interpolated again on the old catalogues. The updated version of the HOD/GOD bias estimation therefore is:

$$b_1(z) = 0.29z + 1.51 \ . \tag{7.41}$$

Finally, we investigated the multiplicity of the merger catalogues described in point **6**, to check whether having more than one BBH assigned to the same stellar particle (and therefore to the same position) can give rise to a *super−clustering* effect. To do so, we re−normalized the catalogues in order to neglect this effect and we recomputed the bias estimator from eq. (7.35). Our results showed that no relevant modifications are introduced by the multiplicity term.

As figure 7.13 shows, the bias estimates $\tilde{b}_1(z)$ can be well approximated by a linear model: in fact, performing a linear fit on both the estimates obtained by using the auto− and cross−power spectra, the correlation coefficient obtained is very high.[15]

We defined therefore the family of linear functions from eq. (7.40) within $1-\sigma$ uncertainty from the best fit values that describe $\tilde{b}_1(z)$. In particular, these are $\tilde{b}_1(z) = (0.29 \pm 0.01)z + 1.03 \pm 0.05$ for the auto−model. The compatibility between the estimated bias and the HOD/GOD model is verified.

[15] The correlation coefficient is $r = 0.998$ for estimates from auto−spectra; the value $r = 1$ indicates that the points are perfectly described by a linear function.

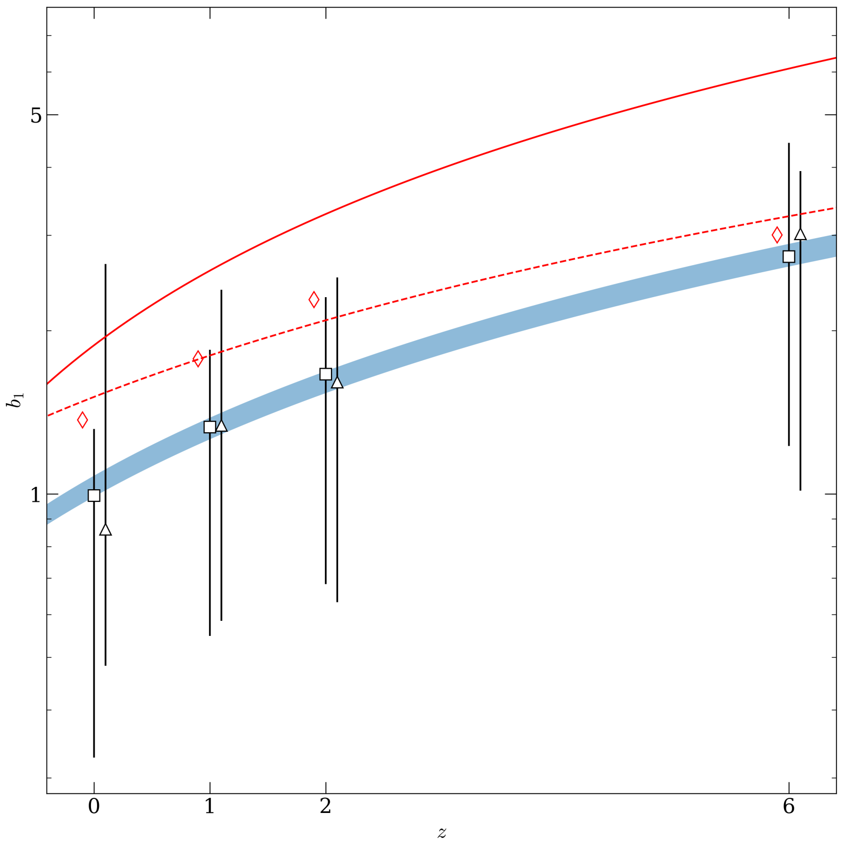

Figure 7.13: Comparison of $\tilde{b}_1$ values as a function of redshift for binary black hole mergers from the EAGLE+MOBSE simulation. The red diamonds are the HOD/GOD estimates, whose best fit from eq. (7.41) is showed by the red dashed line, while the solid red line shows the model from section 5.3.2 adopted in chapter 5 [2, 3]. The black squares and the triangles are the $\tilde{b}_1$ estimates obtained with the posterior sampling from eq. (7.35) for the auto−power and cross−power spectrum models. The blue band bounds the linear functions from eq. (7.40) in the $1-\sigma$ uncertainty interval around the best fit for the auto−power spectrum model i.e., $\tilde{b}_1(z) = (0.29 \pm 0.01)z + 1.03 \pm 0.05$. *To appear in* [5].

Conclusions 8

8.1 Future prospects 149

The main goal of this work was to develop a framework for the analysis and interpretation of future gravitational wave surveys in a cosmological context. We focused both on cosmological parameters and on the cosmological bias of gravitational wave merger events. We showed in particular that the latter can be a powerful tool to discriminate between different merger formation channels.

After the presentation of some background material in chapter 2, chapter 3, chapter 4, the discussion of the original scientific work and of the main results was carried on in chapter 5, chapter 6, chapter 7.

Chapter 5 presented the original points that we introduced to study future gravitational wave surveys from third generation ground−based detectors such as the Einstein Telescope. These can be summarized as follows:

- We need to map the survey in luminosity distance space, since the redshift can not be extracted from the waveform; this implies that the space distortions are different with respect to the standard redshift space (see section 5.2).
- Survey are full sky and their horizon reaches very high distances, allowing us to probe very large cosmic volumes.
- The sky localization uncertainty is very large and it prevents the observation of the small scales.
- To model the bias of the gravitational wave sources i.e., the compact binary mergers, a semi−analytical HOD/GOD model can be used; this is related with the formation channel of the merger progenitors (see section 5.3).

The chapter also included the results from [2, 3], where the constraining power on cosmological and bias parameters were analysed by means of the Fisher matrix technique in different configurations. These mainly distinguished between Einstein Telescope−only surveys (see section 5.5), future gravitational wave detector networks and multi−tracer techniques involving supernovae IA (see section 5.6).

The take−home−messages of this analysis are the following:

- Luminosity distance space distortions behaves differently than redshift space distortions; mapping different tracers in the two spaces and comparing them will therefore set−up a new tool to probe the large scale structures.
- The constraining power with respect to cosmological parameters is worsened by the absence of the small scales in the analysis. If a single detector is adopted and no electromagnetic counterpart is observed, gravitational wave surveys will not be competitive with future galaxy surveys.
- For the bias parameters, small scales and sky localization precision turned out to be not so relevant. Therefore, as soon as the Einstein Telescope will be operational and catalogues of these sources will be available, we will be able to put very good constraints on the bias of gravitational wave events from binary mergers.

The last point opens up a very interesting perspective: having a good measurement of the bias will enable us to constrain the origin and the formation channel of the tracers. A first application of this was given in **chapter 6**, which is based on [4]. Here, by using a model selection approach, we showed that the Einstein Telescope will be able to confirm or disregard the existence of sources whose gravitational wave signal is identical to astrophysical binary black hole mergers but which have a different number distribution and bias. Provided that these sources are primordial black hole mergers, they closely follow the DM distribution and therefore they introduce in the bias of the blind survey a deviation respect to the astrophysical−only black hole scenario. The amplitude of such deviation depends on the merger rate of the primordial black hole mergers relatively to the astrophysical ones (see section 6.2).

We showed that the accuracy of the model selection technique depends on the number of parameters introduced in the analysis and on the level of degeneracies between them. We stated that the best test is obtained when the primordial bias parameters can be fixed i.e., different theoretical models are tested separately (see section 6.3).

The application of this methodology on the analysis on actual datasets will require the implementation of estimators for both the tracer power spectrum and bias. For this reason and to test the results of the previous chapters, in **chapter 7** we decided to interface with simulated catalogues of binary black hole mergers. As proposed in [5], we developed our power spectrum and bias estimators following the techniques usually applied in literature for galaxy surveys (see section 7.2 and section 7.3). First of all, we tested our tools on the DM and DM halo catalogues of the cosmological N−body QUIJOTE simulation suite. After this validation step, we extended the analysis to the EAGLE+MOBSE catalogues of binary black hole mergers (see section 7.4). The peculiarities of these with respect to the QUIJOTE case are related to the fact that the EAGLE suite is made of hydrodynamical simulations, while MOBSE is a population−synthesis code: their computational cost, therefore, is enormous with respect to a DM−only simulation. In particular:

- The number of DM particles adopted is very large and the computational cost of the analysis of the full catalogue is prohibitive.
- The mass resolution of stellar mass particles is such that more than one merger is located in the same position, introducing a multiplicity in the catalogue.
- The size of the simulation box is very small, therefore large, linear scales can not be probed.

While the first and second point relate with numerical issues and were easily solved in the implementation procedure, the last one introduces a *conceptual* issue. In fact, since we had to deal with very small scales, we had to include higher order expansion terms in both the power spectrum and bias estimators. When considering the bias, in particular, a second parameter was introduced in the analysis and then marginalized out in order to constrain the linear bias contribution. This was then compared with the HOD/GOD result from the previous chapters: since the two showed good agreement, we asserted the reliability of the semi−analytical model we developed.

8.1 Future prospects

The work we developed in this thesis opens up many possible extensions and follow−up projects, both on the theoretical and on the numerical side. Some are already under development; in particular:

- Gravitational wave surveys can be a powerful tool to study **primordial non−Gaussianity**. This does not require to access the small scales as the other cosmological parameters, since it can be constrained by using scale−dependent halo bias measurements on the largest accessible scales. For this reason, the low−angular resolution of future gravitational wave catalogues will not be a problem. At the same time, the very large volumes and high redshifts they probe should provide a significant advantage over galaxy surveys. We will provide forecasts on this in the future.
- To develop a fully self−consistent analysis, all the **luminosity distance space distortions** have to be theoretically modelled. Due to the large scales probed by the gravitational wave surveys, also wide angle effects will then be required. We will complete the analysis in this sense and implement these effects in one of the publicly available cosmological codes e.g., `CAMB` or `CLASS`, so to make them accessible by the community.
- In contrast with the large scales that future surveys will probe, currently existing simulations of binary mergers are limited to small volumes because of their computational cost. Despite being fundamental for astrophysical studies, when dealing with cosmology they are affected by cosmic variance and provide measurements only on non−linear scales. Nevertheless, they can be used to extract an essential information i.e., the HOD/GOD of the mergers. We plan to extract and use such HOD/GOD in order to **populate large, N−body simulations with mergers**. Also by using machine learning techniques, we will be able to create catalogues on large scales, where the estimators will be implemented and tested, so to develop a full pipeline through which future datasets will be analysed.

To conclude, this thesis studied new promising approaches to exploit the new window on the Universe that was opened by gravitational wave observations. The main tool that we explored was the clustering of gravitational wave sources both as a cosmological and an astrophysical probe. We showed that this clustering analysis will allow us both to constrain cosmological parameters and to investigate different channels for gravitational wave merger formation, thus opening exciting prospects for a large number of future applications.

> *It has been said that astronomy is a humbling and character−building experience. There is perhaps no better demonstration of the folly of human conceits than this distant image of our tiny world. To me, it underscores our responsibility to deal more kindly with one another, and to preserve and cherish the pale blue dot, the only home we've ever known.*
>
> Carl Sagan
> *A Pale Blue Dot* [1]

Bibliography

Here are the references in citation order.

[1] Carl Sagan. *Pale blue dot: a vision of the human future in space*. The Random House Publishing Group, 1996 (cited on pages 1, 150).

[2] S. Libanore et al. 'Gravitational Wave mergers as tracers of Large Scale Structures'. In: *Journal of Cosmology and Astroparticle Physics* 2021.02 (Feb. 2021), pp. 035–035. DOI: `10.1088/1475-7516/2021/02/035` (cited on pages 2, 3, 71, 73, 74, 80, 88–90, 94, 95, 98, 100, 137, 147, 148).

[3] S. Libanore et al. 'Clustering of Gravitational Wave and Supernovae events: a multitracer analysis in Luminosity Distance Space'. In: *Journal of Cosmology and Astroparticle Physics* 2022.02 (Feb. 2022), p. 003. DOI: `10.1088/1475-7516/2022/02/003` (cited on pages 2, 3, 71, 73, 74, 80, 86, 88, 90, 94, 98, 137, 147, 148).

[4] Sarah Libanore, Michele Liguori, and Alvise Raccanelli. *To appear*. 2022 (cited on pages 2, 4, 107, 117, 118, 149).

[5] M. Peron, S. Libanore, M. Liguori, M. C. Artale, and D. Karagiannis. *To appear*. 2022 (cited on pages 2, 4, 124, 126–129, 140, 142–144, 147, 149).

[6] Planck Collaboration. 'Planck 2018 results - I. Overview and the cosmological legacy of Planck'. In: *Astronomy & Astrophysics* 641 (2020). DOI: `10.1051/0004-6361/201833880` (cited on pages 7, 10, 21, 26, 128).

[7] E. A. Milne. *Relativity, Gravitation and World Structure*. Oxford: Clarendon Press, 1935 (cited on page 7).

[8] J. Bernstein, G. Feinberg, and J. Kleczek. 'Book-Review - Cosmological Constants'. In: *Astrophysics and Space Science* 134 (June 1987), p. 422 (cited on page 7).

[9] Edmund Bertschinger. 'Cosmic structure formation'. In: *Physica D: Nonlinear Phenomena* 77.1 (1994). Special Issue Originating from the 13th Annual International Conference of the Center for Nonlinear Studies Los Alamos, NM, USA, 17–21 May 1993, pp. 354–379. DOI: `https://doi.org/10.1016/0167-2789(94)90145-7` (cited on pages 8, 14, 21).

[10] Edwin Hubble. 'A Relation between Distance and Radial Velocity among Extra-Galactic Nebulae'. In: *Proceedings of the National Academy of Science* 15.3 (Mar. 1929), pp. 168–173. DOI: `10.1073/pnas.15.3.168` (cited on page 8).

[11] James B. Hartle. *Gravity: An Introduction to Einstein's General Relativity*. Benjamin Cummings, Jan. 2003 (cited on pages 8, 54, 55, 58).

[12] Scott Dodelson. *Modern Cosmology*. Academic Press, Elsevier Science, 2003 (cited on pages 9, 11, 12, 18–20, 27, 92).

[13] Planck Collaboration. 'Planck 2018 results - VI. Cosmological parameters'. In: *Astronomy & Astrophysics* 641 (2020). DOI: `10.1051/0004-6361/201833910` (cited on pages 9, 11, 12, 14, 20, 22, 48, 76, 95–99, 107, 119).

[14] S. Aiola et al. 'The Atacama Cosmology Telescope: DR4 maps and cosmological parameters'. In: *Journal of Cosmology and Astroparticle Physics* 2020.12 (Dec. 2020), p. 047. DOI: `10.1088/1475-7516/2020/12/047` (cited on page 9).

[15] Adam G. Riess et al. 'A redetermination of the Hubble constant with the Hubble Space Telescope from a differential distance ladder'. In: *The Astrophysical Journal* 699.1 (June 2009), pp. 539–563. DOI: `10.1088/0004-637x/699/1/539` (cited on pages 10, 48).

[16] Adam G. Riess et al. 'A 3% solution: determination of the Hubble constant with the Hubble space telescope and wide field camera 3'. In: *The Astrophysical Journal* 730.2 (Mar. 2011), p. 119. DOI: `10.1088/0004-637x/730/2/119` (cited on pages 10, 48).

[17] A. G. Riess et al. 'A 2.4% determination of the local value of the Hubble constant'. In: *The Astrophysical Journal* 826.1 (July 2016), p. 56. DOI: `10.3847/0004-637x/826/1/56` (cited on pages 10, 48).

[18] Efstathiou G. *A Lockdown Perspective on the Hubble Tension (with comments from the SH0ES team)*. 2020 (cited on page 10).

[19] Kenneth C. Wong et al. 'H0LiCOW – XIII. A 2.4 per cent measurement of H0 from lensed quasars: 5.3σ tension between early- and late-Universe probes'. In: *Monthly Notices of the Royal Astronomical Society* 498.1 (Sept. 2019), pp. 1420–1439. DOI: `10.1093/mnras/stz3094` (cited on page 10).

[20] George Efstathiou. 'H0 revisited'. In: *Monthly Notices of the Royal Astronomical Society* 440.2 (Mar. 2014), pp. 1138–1152. DOI: `10.1093/mnras/stu278` (cited on page 10).

[21] Wenlong Yuan, Adam G. Riess, Lucas M. Macri, Stefano Casertano, and Daniel M. Scolnic. 'Consistent Calibration of the Tip of the Red Giant Branch in the Large Magellanic Cloud on the Hubble Space Telescope Photometric System and a Redetermination of the Hubble Constant'. In: *The Astrophysical Journal* 886.1 (Nov. 2019), p. 61. DOI: `10.3847/1538-4357/ab4bc9` (cited on page 10).

[22] Gong-Bo Zhao et al. 'Dynamical dark energy in light of the latest observations'. In: *Nature Astronomy* 1.9 (Aug. 2017), pp. 627–632. DOI: `10.1038/s41550-017-0216-z` (cited on page 10).

[23] Kyriakos Vattis, Savvas M. Koushiappas, and Abraham Loeb. 'Dark matter decaying in the late Universe can relieve the H0 tension'. In: *Physical Review D* 99.12 (June 2019). DOI: `10.1103/physrevd.99.121302` (cited on page 10).

[24] Adam G. Riess et al. *A Comprehensive Measurement of the Local Value of the Hubble Constant with 1 km/s/Mpc Uncertainty from the Hubble Space Telescope and the SH0ES Team*. 2021 (cited on page 10).

[25] B. F. Schutz. 'Determining the Hubble constant from gravitational wave observations'. In: *Nature* 323.6086 (Sept. 1986), pp. 310–311. DOI: `10.1038/323310a0` (cited on pages 10, 68, 72).

[26] B. P. Abbott et al. 'A gravitational-wave standard siren measurement of the Hubble constant'. In: *Nature* 551.7678 (Oct. 2017), pp. 85–88. DOI: `10.1038/nature24471` (cited on pages 10, 68, 72).

[27] H. Y. Chen, M. Fishbach, and D. E. Holz. 'A two per cent Hubble constant measurement from standard sirens within five years'. In: *Nature* 562.7728 (2018). DOI: `10.1038/s41586-018-0606-0` (cited on pages 10, 68).

[28] G. Gamow. 'Expanding Universe and the Origin of Elements'. In: *Physical Review* 70.7-8 (Oct. 1946), pp. 572–573. DOI: `10.1103/PhysRev.70.572.2` (cited on page 10).

[29] Ralph A. Alpher and Robert C. Herman. 'Theory of the Origin and Relative Abundance Distribution of the Elements'. In: *Reviews of Modern Physics* 22.2 (Apr. 1950), pp. 153–212. DOI: `10.1103/RevModPhys.22.153` (cited on page 10).

[30] Craig J. Copi, David N. Schramm, and Michael S. Turner. 'Big-Bang Nucleosynthesis and the Baryon Density of the Universe'. In: *Science* 267.5195 (1995), pp. 192–199. DOI: `10.1126/science.7809624` (cited on page 10).

[31] E. Margaret Burbidge, G. R. Burbidge, William A. Fowler, and F. Hoyle. 'Synthesis of the Elements in Stars'. In: *Reviews of Modern Physics* 29 (4 Oct. 1957), pp. 547–650. DOI: `10.1103/RevModPhys.29.547` (cited on page 10).

[32] T. Rauscher, A. Heger, R. D. Hoffman, and S. E. Woosley. 'Nucleosynthesis in Massive Stars with Improved Nuclear and Stellar Physics'. In: *The Astrophysical Journal* 576.1 (Sept. 2002), pp. 323–348. DOI: `10.1086/341728` (cited on page 10).

[33] S. J. Smartt et al. 'A kilonova as the electromagnetic counterpart to a gravitational-wave source'. In: *Nature* 551.7678 (Nov. 2017), pp. 75–79. DOI: `10.1038/nature24303` (cited on page 10).

[34] F. Zwicky. 'Republication of: The redshift of extragalactic nebulae'. In: *General Relativity and Gravitation* 41.1 (Jan. 2009), pp. 207–224. DOI: `10.1007/s10714-008-0707-4` (cited on page 10).

[35] V. C. Rubin, Jr. Ford W. K., and N. Thonnard. 'Rotational properties of 21 SC galaxies with a large range of luminosities and radii, from NGC 4605 (R=4kpc) to UGC 2885 (R=122kpc).' In: *The Astrophysical Journal* 238 (June 1980), pp. 471–487. DOI: `10.1086/158003` (cited on page 10).

[36] A. Arbey and F. Mahmoudi. 'Dark matter and the early Universe: A review'. In: *Progress in Particle and Nuclear Physics* (Apr. 2021), p. 103865. DOI: `10.1016/j.ppnp.2021.103865` (cited on page 10).

[37] Gerard Jungman, Marc Kamionkowski, and Kim Griest. 'Supersymmetric dark matter'. In: *Physics Reports* 267.5-6 (Mar. 1996), pp. 195–373. DOI: `10.1016/0370-1573(95)00058-5` (cited on page 10).

[38] John Preskill, Mark B. Wise, and Frank Wilczek. 'Cosmology of the invisible axion'. In: *Physics Letters B* 120.1 (1983), pp. 127–132. DOI: `https://doi.org/10.1016/0370-2693(83)90637-8` (cited on page 10).

[39] Bernard Carr and Florian Kühnel. 'Primordial Black Holes as Dark Matter: Recent Developments'. In: *Annual Review of Nuclear and Particle Science* 70.1 (2020), pp. 355–394. DOI: `10.1146/annurev-nucl-050520-125911` (cited on page 10).

[40] Julien Lesgourgues and Sergio Pastor. 'Neutrino cosmology and Planck'. In: *New Journal of Physics* 16.6 (June 2014), p. 065002. DOI: `10.1088/1367-2630/16/6/065002` (cited on page 10).

[41] Adam G. Riess et al. 'Observational Evidence from Supernovae for an Accelerating Universe and a Cosmological Constant'. In: *The Astrophysical Journal* 116.3 (Sept. 1998), pp. 1009–1038. DOI: `10.1086/300499` (cited on pages 10, 21).

[42] S. Perlmutter et al. 'Measurements of Ω and Λ from 42 High-Redshift Supernovae'. In: *The Astrophysical Journal* 517.2 (June 1999), pp. 565–586. DOI: `10.1086/307221` (cited on page 10).

[43] P. J. E. Peebles and Bharat Ratra. 'The cosmological constant and dark energy'. In: *Reviews of Modern Physics* 75.2 (Apr. 2003), pp. 559–606. DOI: `10.1103/revmodphys.75.559` (cited on page 10).

[44] Michael J. Mortonson, David H. Weinberg, and Martin White. *Dark Energy: A Short Review*. 2013 (cited on page 10).

[45] M. Chevallier and D. Polarski. 'Accelerating Universes with scaling Dark Matter'. In: *International Journal of Modern Physics D* 10.02 (Apr. 2001), pp. 213–223. DOI: `10.1142/s0218271801000822` (cited on page 10).

[46] Eric V. Linder. 'Exploring the Expansion History of the Universe'. In: *Physical Review Letter* 90.9 (Mar. 2003), p. 091301. DOI: `10.1103/PhysRevLett.90.091301` (cited on page 10).

[47] Timothy Clifton, Pedro G. Ferreira, Antonio Padilla, and Constantinos Skordis. 'Modified gravity and cosmology'. In: *Physics Reports* 513.1-3 (Mar. 2012), pp. 1–189. DOI: `10.1016/j.physrep.2012.01.001` (cited on page 11).

[48] Noemi Frusciante and Louis Perenon. 'Effective field theory of dark energy: A review'. In: *Physics Reports* 857 (May 2020), pp. 1–63. DOI: `10.1016/j.physrep.2020.02.004` (cited on page 11).

[49] Austin Joyce, Lucas Lombriser, and Fabian Schmidt. 'Dark Energy Versus Modified Gravity'. In: *Annual Review of Nuclear and Particle Science* 66.1 (Oct. 2016), pp. 95–122. DOI: `10.1146/annurev-nucl-102115-044553` (cited on page 11).

[50] Oliver Piattella. 'Lecture Notes in Cosmology'. In: *UNITEXT for Physics* (2018). DOI: `10.1007/978-3-319-95570-4` (cited on pages 13, 21).

[51] David H. Lyth and Andrew R. Liddle. *The primordial density perturbation: cosmology, inflation and the origin of structure; rev. version*. Cambridge: Cambridge University Press, 2009 (cited on pages 13, 15, 27).

[52] Mary K. Gaillard, Paul D. Grannis, and Frank J. Sciulli. 'The standard model of particle physics'. In: *Reviews of Modern Physics* 71.2 (Mar. 1999), S96–S111. DOI: `10.1103/revmodphys.71.s96` (cited on page 13).

[53] P. Coles. *Large-scale Structure, Theory and Statistics*. 2001 (cited on page 15).

[54] P. J. E. Peebles. *The large-scale structure of the universe*. Princeton University Press, 1980 (cited on page 16).

[55] A. J. S. Hamilton. 'Linear Redshift Distortions: A Review'. In: *The Evolving Universe* (1998), pp. 185–275. DOI: `10.1007/978-94-011-4960-0_17` (cited on pages 17, 37).

[56] P. J. E. Peebles. 'Large-scale background temperature and mass fluctuations due to scale-invariant primeval perturbations'. In: *Astrophysical Journal, Letters* 263 (Dec. 1982), pp. L1–L5. DOI: `10.1086/183911` (cited on page 17).

[57] G. R. Blumenthal, S. M. Faber, J. R. Primack, and M. J. Rees. 'Formation of galaxies and large-scale structure with cold dark matter.' In: *Nature* 311 (Oct. 1984), pp. 517–525. DOI: `10.1038/311517a0` (cited on page 17).

[58] Sadri H. *Mathematical Physics - A modern introduction to its foundations*. Springer, 1999 (cited on page 18).

[59] P. Coles and F. Lucchin. *Cosmology - The origin and evolution of cosmic structure*. John Wiley & Sons, Ltd, 2002 (cited on page 19).

[60] T. Padmanabhan. 'Cosmological constant-the weight of the vacuum'. In: *Physical report* 380.5-6 (July 2003), pp. 235–320. DOI: `10.1016/S0370-1573(03)00120-0` (cited on page 20).

[61] A. A. Starobinskiĭ. 'Spectrum of relict gravitational radiation and the early state of the universe'. In: *Soviet Journal of Experimental and Theoretical Physics Letters* 30 (Dec. 1979), p. 682 (cited on page 21).

[62] Alan H. Guth. 'Inflationary universe: A possible solution to the horizon and flatness problems'. In: *Physical Review D* 23.2 (Jan. 1981), pp. 347–356. DOI: `10.1103/PhysRevD.23.347` (cited on page 21).

[63] A. D. Linde. 'A new inflationary universe scenario: A possible solution of the horizon, flatness, homogeneity, isotropy and primordial monopole problems'. In: *Physics Letters B* 108.6 (1982), pp. 389–393. DOI: `https://doi.org/10.1016/0370-2693(82)91219-9` (cited on page 21).

[64] Andreas Albrecht and Paul J. Steinhardt. 'Cosmology for Grand Unified Theories with Radiatively Induced Symmetry Breaking'. In: *Physical Review Letter* 48.17 (Apr. 1982), pp. 1220–1223. DOI: `10.1103/PhysRevLett.48.1220` (cited on page 21).

[65] Jérôme Martin, Christophe Ringeval, Roberto Trotta, and Vincent Vennin. 'The best inflationary models after Planck'. In: *Journal of Cosmology and Astroparticle Physics* 2014.03 (Mar. 2014), pp. 039–039. DOI: `10.1088/1475-7516/2014/03/039` (cited on page 22).

[66] P. A. R. Ade et al. 'Planck2013 results. XXII. Constraints on inflation'. In: *Astronomy & Astrophysics* 571 (Oct. 2014), A22. DOI: `10.1051/0004-6361/201321569` (cited on page 22).

[67] E. R. Harrison. 'Fluctuations at the Threshold of Classical Cosmology'. In: *Physical Review D* 1.10 (May 1970), pp. 2726–2730. DOI: `10.1103/PhysRevD.1.2726` (cited on page 22).

[68] Ya. B. Zeldovich. 'A Hypothesis, Unifying the Structure and the Entropy of the Universe'. In: *Monthly Notices of the Royal Astronomical Society* 160.1 (Oct. 1972), 1P–3P. DOI: `10.1093/mnras/160.1.1P` (cited on page 22).

[69] S. W. Hawking. 'Gravitational Radiation from Colliding Black Holes'. In: *Physical Review Letter* 26.21 (May 1971), pp. 1344–1346. DOI: `10.1103/PhysRevLett.26.1344` (cited on page 22).

[70] B. J. Carr and S. W. Hawking. 'Black Holes in the Early Universe'. In: *Monthly Notices of the Royal Astronomical Society* 168.2 (Aug. 1974), pp. 399–415. DOI: `10.1093/mnras/168.2.399` (cited on page 22).

[71] Bernard Carr, Florian Kühnel, and Marit Sandstad. 'Primordial black holes as dark matter'. In: *Physical Review D* 94.8 (Oct. 2016). DOI: `10.1103/physrevd.94.083504` (cited on pages 22–24).

[72] Misao Sasaki, Teruaki Suyama, Takahiro Tanaka, and Shuichiro Yokoyama. 'Primordial black holes—perspectives in gravitational wave astronomy'. In: *Classical and Quantum Gravity* 35.6 (Feb. 2018), p. 063001. DOI: `10.1088/1361-6382/aaa7b4` (cited on pages 22–25).

[73] B. J. Carr and James E. Lidsey. 'Primordial black holes and generalized constraints on chaotic inflation'. In: *Physical Review D* 48.2 (July 1993), pp. 543–553. DOI: `10.1103/PhysRevD.48.543` (cited on page 23).

[74] B. J. Carr, J. H. Gilbert, and James E. Lidsey. 'Black hole relics and inflation: Limits on blue perturbation spectra'. In: *Physical Review D* 50.8 (Oct. 1994), pp. 4853–4867. DOI: `10.1103/physrevd.50.4853` (cited on page 23).

[75] Kazunori Kohri, Chia-Min Lin, and David H Lyth. 'More hilltop inflation models'. In: *Journal of Cosmology and Astroparticle Physics* 2007.12 (Dec. 2007), pp. 004–004. DOI: `10.1088/1475-7516/2007/12/004` (cited on page 23).

[76] Jun'ichi Yokoyama. 'Chaotic new inflation and formation of primordial black holes'. In: *Physical Review D* 58.8 (Sept. 1998). DOI: `10.1103/physrevd.58.083510` (cited on page 23).

[77] David H. Lyth, Carlo Ungarelli, and David Wands. 'Primordial density perturbation in the curvaton scenario'. In: *Physical Review D* 67.2 (Jan. 2003). DOI: `10.1103/physrevd.67.023503` (cited on page 23).

[78] Samuel M. Leach, Ian J. Grivell, and Andrew R. Liddle. 'Black hole constraints on the running-mass inflation model'. In: *Physical Review D* 62.4 (July 2000). DOI: `10.1103/physrevd.62.043516` (cited on page 23).

[79] S. W. Hawking, I. G. Moss, and J. M. Stewart. 'Bubble collisions in the very early universe'. In: *Physical Review D* 26.10 (Nov. 1982), pp. 2681–2693. DOI: `10.1103/PhysRevD.26.2681` (cited on page 23).

[80] I. G. Moss. 'Black-hole bubbles'. In: *Physical Review D* 32.6 (Sept. 1985), pp. 1333–1344. DOI: `10.1103/PhysRevD.32.1333` (cited on page 23).

[81] S. W. Hawking. 'Black holes from cosmic strings'. In: *Physics Letters B* 231.3 (Nov. 1989), pp. 237–239. DOI: `10.1016/0370-2693(89)90206-2` (cited on page 23).

[82] Jaume Garriga and Maria Sakellariadou. 'Effects of friction on cosmic strings'. In: *Physical Review D* 48.6 (Sept. 1993), pp. 2502–2515. DOI: `10.1103/physrevd.48.2502` (cited on page 23).

[83] Florian Kühnel and Marit Sandstad. 'Ellipsoidal collapse and primordial black hole formation'. In: *Physical Review D* 94.6 (Sept. 2016). DOI: `10.1103/physrevd.94.063514` (cited on page 23).

[84] James Hopwood Jeans. 'I. The stability of a spherical nebula'. In: *Philosophical Transactions of the Royal Society of London* Series A (1902), pp. 1–53. DOI: `https://doi.org/10.1098/rsta.1902.0012` (cited on pages 23, 27).

[85] R. J. Bontz and M. P. Haugan. 'A Diffraction Limit on the Gravitational Lens Effect'. In: *Astrophysics and Space Science* 78.1 (Aug. 1981), pp. 199–210. DOI: `10.1007/BF00654034` (cited on page 24).

[86] Andrey Katz, Joachim Kopp, Sergey Sibiryakov, and Wei Xue. 'Femtolensing by dark matter revisited'. In: *Journal of Cosmology and Astroparticle Physics* 2018.12 (Dec. 2018), pp. 005–005. DOI: `10.1088/1475-7516/2018/12/005` (cited on page 24).

[87] Fabio Capela, Maxim Pshirkov, and Peter Tinyakov. 'Constraints on primordial black holes as dark matter candidates from capture by neutron stars'. In: *Physical Review D* 87.12 (June 2013). DOI: `10.1103/physrevd.87.123524` (cited on page 24).

[88] Chris Kouvaris and Peter Tinyakov. 'Growth of black holes in the interior of rotating neutron stars'. In: *Physical Review D* 90.4 (Aug. 2014). DOI: `10.1103/physrevd.90.043512` (cited on page 24).

[89] S. W. Hawking. 'Black hole explosions?' In: *Nature* 248.5443 (Mar. 1974), pp. 30–31. DOI: `10.1038/248030a0` (cited on page 24).

[90] Amandeep S. Josan, Anne M. Green, and Karim A. Malik. 'Generalized constraints on the curvature perturbation from primordial black holes'. In: *Physical Review D* 79.10 (May 2009). DOI: `10.1103/physrevd.79.103520` (cited on page 24).

[91] B. J. Carr, Kazunori Kohri, Yuuiti Sendouda, and Jun'ichi Yokoyama. 'New cosmological constraints on primordial black holes'. In: *Physical Review D* 81.10 (May 2010). DOI: `10.1103/physrevd.81.104019` (cited on page 24).

[92] Planck Collaboration. *Planck 2018 results. IX. Constraints on primordial non-Gaussianity*. 2019 (cited on page 24).

[93] U. Seljak and Holz D. E. *Limits on the Density of Compact Objects from High Redshift Supernovae*. 1999 (cited on page 24).

[94] R. Benton Metcalf and Joseph Silk. ‘New Constraints on Macroscopic Compact Objects as Dark Matter Candidates from Gravitational Lensing of Type Ia Supernovae’. In: *Physical Review Letter* 98 (7 Feb. 2007), p. 071302. DOI: `10.1103/PhysRevLett.98.071302` (cited on page 24).

[95] M. Zumalacárregui and U. Seljak. ‘Limits on Stellar-Mass Compact Objects as Dark Matter from Gravitational Lensing of Type Ia Supernovae’. In: *Physical Review Letter* 121.14 (Oct. 2018). DOI: `10.1103/physrevlett.121.141101` (cited on page 24).

[96] Peter W. Graham, Surjeet Rajendran, and Jaime Varela. ‘Dark matter triggers of supernovae’. In: *Physical Review D* 92.6 (Sept. 2015). DOI: `10.1103/physrevd.92.063007` (cited on page 24).

[97] Jaiyul Yoo, Julio Chaname, and Andrew Gould. ‘The End of the MACHO Era: Limits on Halo Dark Matter from Stellar Halo Wide Binaries’. In: *The Astrophysical Journal* 601.1 (Jan. 2004), pp. 311–318. DOI: `10.1086/380562` (cited on page 24).

[98] B. J. Carr and M. Sakellariadou. ‘Dynamical Constraints on Dark Matter in Compact Objects’. In: *The Astrophysical Journal* 516.1 (May 1999), pp. 195–220. DOI: `10.1086/307071` (cited on page 24).

[99] Timothy D. Brandt. ‘Constraints on MACHO Dark Matter from compact stellar systems in Ultra-Faint Dwarf galaxies’. In: *The Astrophysical Journal* 824.2 (June 2016), p. L31. DOI: `10.3847/2041-8205/824/2/l31` (cited on page 24).

[100] C. G. Lacey and J. P. Ostriker. ‘Massive black holes in galactic halos?’ In: *The Astrophysical Journal* 299 (Dec. 1985), pp. 633–652. DOI: `10.1086/163729` (cited on page 24).

[101] B. Nordström et al. ‘The Geneva-Copenhagen survey of the Solar neighbourhood’. In: *Astronomy & Astrophysics* 418.3 (Apr. 2004), pp. 989–1019. DOI: `10.1051/0004-6361:20035959` (cited on page 24).

[102] Yacine Ali-Haïmoud and Marc Kamionkowski. ‘Cosmic microwave background limits on accreting primordial black holes’. In: *Physical Review D* 95.4 (Feb. 2017). DOI: `10.1103/physrevd.95.043534` (cited on page 24).

[103] Yutaka Fujita, Susumu Inoue, Takashi Nakamura, Tadahiro Manmoto, and Kenji E. Nakamura. ‘Emission from Isolated Black Holes and MACHO[CLC]s[/CLC] Accreting from the Interstellar Medium’. In: *The Astrophysical Journal* 495.2 (Mar. 1998), pp. L85–L89. DOI: `10.1086/311220` (cited on page 25).

[104] Daniele Gaggero et al. ‘Searching for Primordial Black Holes in the Radio and X-Ray Sky’. In: *Physical Review Letter* 118.24 (June 2017). DOI: `10.1103/physrevlett.118.241101` (cited on page 25).

[105] Yoshiyuki Inoue and Alexander Kusenko. ‘New X-ray bound on density of primordial black holes’. In: *Journal of Cosmology and Astroparticle Physics* 2017.10 (Oct. 2017), pp. 034–034. DOI: `10.1088/1475-7516/2017/10/034` (cited on page 25).

[106] P. Meszaros. ‘Primeval black holes and galaxy formation.’ In: *Astronomy & Astrophysics* 38.1 (Jan. 1975), pp. 5–13 (cited on page 25).

[107] N. Afshordi, P. McDonald, and D. N. Spergel. ‘Primordial Black Holes as Dark Matter: The Power Spectrum and Evaporation of Early Structures’. In: *The Astrophysical Journal* 594.2 (Aug. 2003), pp. L71–L74. DOI: `10.1086/378763` (cited on page 25).

[108] Ryo Saito and Jun’ichi Yokoyama. ‘Gravitational-Wave Background as a Probe of the Primordial Black-Hole Abundance’. In: *Physical Review Letter* 102.16 (Apr. 2009), p. 161101. DOI: `10.1103/PhysRevLett.102.161101` (cited on page 25).

[109] Andrea N Lommen. ‘Pulsar timing arrays: the promise of gravitational wave detection’. In: *Reports on Progress in Physics* 78.12 (Nov. 2015), p. 124901. DOI: `10.1088/0034-4885/78/12/124901` (cited on page 25).

[110] George Hobbs and Shi Dai. ‘Gravitational wave research using pulsar timing arrays’. In: *National Science Review* 4.5 (Dec. 2017), pp. 707–717. DOI: `10.1093/nsr/nwx126` (cited on page 25).

[111] R. N. Manchester et al. ‘The Parkes Pulsar Timing Array Project’. In: *Publications of the Astronomical Society of Australia* 30 (2013). DOI: `10.1017/pasa.2012.017` (cited on page 25).

[112] M. A. McLaughlin. ‘The North American Nanohertz Observatory for Gravitational Waves’. In: *Classical and Quantum Gravity* 30.22 (Nov. 2013), p. 224008. DOI: `10.1088/0264-9381/30/22/224008` (cited on page 25).

[113] Michael Kramer and David J. Champion. ‘The European Pulsar Timing Array and the Large European Array for Pulsars’. In: *Classical and Quantum Gravity* 30.22 (Nov. 2013), p. 224009. DOI: `10.1088/0264-9381/30/22/224009` (cited on page 25).

[114] Yacine Ali-Haïmoud, Ely D. Kovetz, and Marc Kamionkowski. ‘Merger rate of primordial black-hole binaries’. In: *Physical Review D* 96.12 (Dec. 2017). DOI: `10.1103/physrevd.96.123523` (cited on pages 25, 51, 114).

[115] Martti Raidal, Christian Spethmann, Ville Vaskonen, and Hardi Veermäe. ‘Formation and evolution of primordial black hole binaries in the early universe’. In: *Journal of Cosmology and Astroparticle Physics* 2019.02 (Feb. 2019), pp. 018–018. DOI: `10.1088/1475-7516/2019/02/018` (cited on pages 25, 51, 114).

[116] Zu-Cheng Chen and Qing-Guo Huang. ‘Merger Rate Distribution of Primordial Black Hole Binaries’. In: *The Astrophysical Journal* 864.1 (Aug. 2018), p. 61. DOI: `10.3847/1538-4357/aad6e2` (cited on page 25).

[117] Alvise Raccanelli, Ely D. Kovetz, Simeon Bird, Ilias Cholis, and Julian B. Muñoz. ‘Determining the progenitors of merging black-hole binaries’. In: *Physical Review D* 94.2 (July 2016). DOI: `10.1103/physrevd.94.023516` (cited on pages 25, 52, 69, 106).

[118] Bernard Carr and Florian Kuhnel. *Primordial Black Holes as Dark Matter Candidates*. 2021 (cited on pages 25, 51, 114).

[119] Simeon Bird et al. ‘Did LIGO Detect Dark Matter?’ In: *Physical Review Letter* 116.20 (May 2016). DOI: `10.1103/physrevlett.116.201301` (cited on pages 25, 52, 113, 114).

[120] V. De Luca, G. Franciolini, and A. Riotto. ‘NANOGrav Data Hints at Primordial Black Holes as Dark Matter’. In: *Physical Review Letter* 126.4 (Jan. 2021). DOI: `10.1103/physrevlett.126.041303` (cited on page 25).

[121] Wayne Hu and Scott Dodelson. ‘Cosmic Microwave Background Anisotropies’. In: *Annual Review of Astronomy and Astrophysics* 40.1 (2002), pp. 171–216. DOI: `10.1146/annurev.astro.40.060401.093926` (cited on page 26).

[122] Douglas Scott and George F. Smoot. *Cosmic Microwave Background Mini-review*. 2010 (cited on page 26).

[123] Anthony Challinor. ‘CMB anisotropy science: a review’. In: *Proceedings of the International Astronomical Union* 8.S288 (Aug. 2012), pp. 42–52. DOI: `10.1017/s1743921312016663` (cited on page 26).

[124] Mario G. Santos et al. *Cosmology with a SKA HI intensity mapping survey*. 2015 (cited on page 26).

[125] Ely D. Kovetz et al. *Line-Intensity Mapping: 2017 Status Report*. 2017 (cited on page 26).

[126] Hao Liu, James Creswell, Sebastian von Hausegger, Andrew D. Jackson, and Pavel Naselsky. ‘A blind search for a common signal in gravitational wave detectors’. In: *Journal of Cosmology and Astroparticle Physics* 2018.02 (Feb. 2018), pp. 013–013. DOI: `10.1088/1475-7516/2018/02/013` (cited on pages 26, 58).

[127] S. Planelles, D. R. G. Schleicher, and A. M. Bykov. ‘Large-Scale Structure Formation: From the First Non-linear Objects to Massive Galaxy Clusters’. In: *Space Science Reviews* 188.1-4 (Apr. 2014), pp. 93–139. DOI: `10.1007/s11214-014-0045-7` (cited on page 27).

[128] James M. Bardeen. ‘Gauge-invariant cosmological perturbations’. In: *Physical Review D* 22.8 (Oct. 1980), pp. 1882–1905. DOI: `10.1103/PhysRevD.22.1882` (cited on page 27).

[129] Hideo Kodama and Misao Sasaki. ‘Cosmological Perturbation Theory’. In: *Progress of Theoretical Physics Supplement* 78 (1984), pp. 1–166. DOI: `10.1143/PTPS.78.1` (cited on page 27).

[130] E. Lifshitz. ‘Republication of: On the gravitational stability of the expanding universe’. In: *General Relativity and Gravitation* 49.2 (Feb. 2017), p. 18. DOI: `10.1007/s10714-016-2165-8` (cited on page 27).

[131] Edmund Bertschinger. ‘Cosmological Dynamics’. In: 1995 (cited on pages 27, 28).

[132] V. F. Mukhanov, H. A. Feldman, and R. H. Brandenberger. ‘Theory of cosmological perturbations’. In: *Physical report* 215.5-6 (June 1992), pp. 203–333. DOI: `10.1016/0370-1573(92)90044-Z` (cited on page 28).

[133] Chung-Pei Ma and Edmund Bertschinger. 'Cosmological Perturbation Theory in the Synchronous and Conformal Newtonian Gauges'. In: *The Astrophysical Journal* 455 (Dec. 1995), p. 7. DOI: 10.1086/176550 (cited on page 28).

[134] M. Maggiore. *Gravitational Waves - Volume 1: theory and experiments*. Oxford University Press, 2008 (cited on pages 28, 49, 54–59, 62, 68).

[135] Kenji Tomita. 'Non-Linear Theory of Gravitational Instability in the Expanding Universe'. In: *Progress of Theoretical Physics* 37.5 (May 1967), pp. 831–846. DOI: 10.1143/PTP.37.831 (cited on page 28).

[136] Sabino Matarrese, Silvia Mollerach, and Marco Bruni. 'Relativistic second-order perturbations of the Einstein–de Sitter universe'. In: *Physical Review D* 58.4 (July 1998). DOI: 10.1103/physrevd.58.043504 (cited on page 28).

[137] Pritha Bari, Angelo Ricciardone, Nicola Bartolo, Daniele Bertacca, and Sabino Matarrese. *Signatures of Primordial Gravitational Waves on the Large-Scale Structure of the Universe*. 2021 (cited on page 28).

[138] Chiara Caprini and Daniel G. Figueroa. 'Cosmological backgrounds of gravitational waves'. In: *Classical and Quantum Gravity* 35.16 (July 2018), p. 163001. DOI: 10.1088/1361-6382/aac608 (cited on pages 28, 61).

[139] Hyerim Noh and Jai-Chan Hwang. 'Nonlinear cosmological power spectrum in Einstein's gravity'. In: *Physical Review D* 77.12 (June 2008), p. 123533. DOI: 10.1103/PhysRevD.77.123533 (cited on pages 29, 141).

[140] William H. Press and Paul Schechter. 'Formation of Galaxies and Clusters of Galaxies by Self-Similar Gravitational Condensation'. In: *The Astrophysical Journal* 187 (Feb. 1974), pp. 425–438. DOI: 10.1086/152650 (cited on pages 29–31).

[141] A. Cooray and R. Sheth. 'Halo models of large scale structure'. In: *Physics Reports* 372.1 (Dec. 2002), pp. 1–129. DOI: 10.1016/s0370-1573(02)00276-4 (cited on pages 29–33, 44, 46, 47).

[142] James E. Gunn and III Gott J. Richard. 'On the Infall of Matter Into Clusters of Galaxies and Some Effects on Their Evolution'. In: *The Astrophysical Journal* 176 (Aug. 1972), p. 1. DOI: 10.1086/151605 (cited on page 29).

[143] J. A. Fillmore and P. Goldreich. 'Self-similar gravitational collapse in an expanding universe'. In: *The Astrophysical Journal* 281 (June 1984), pp. 1–8. DOI: 10.1086/162070 (cited on pages 29, 30).

[144] E. Bertschinger. 'Self-similar secondary infall and accretion in an Einstein-de Sitter universe'. In: *Astrophysical Journal, Supplement* 58 (May 1985), pp. 39–65. DOI: 10.1086/191028 (cited on page 29).

[145] Julio F. Navarro, Carlos S. Frenk, and Simon D. M. White. 'The Structure of Cold Dark Matter Halos'. In: *The Astrophysical Journal* 462 (May 1996), p. 563. DOI: 10.1086/177173 (cited on page 30).

[146] Jürg Diemand and Ben Moore. 'The Structure and Evolution of Cold Dark Matter Halos'. In: *Advanced Science Letters* 4.2 (Feb. 2011), pp. 297–310. DOI: 10.1166/asl.2011.1211 (cited on page 30).

[147] Ravi K. Sheth and Giuseppe Tormen. 'Large-scale bias and the peak background split'. In: *Monthly Notices of the Royal Astronomical Society* 308.1 (Sept. 1999), pp. 119–126. DOI: 10.1046/j.1365-8711.1999.02692.x (cited on pages 31, 32).

[148] Jeremy Tinker et al. 'Toward a Halo Mass Function for Precision Cosmology: The Limits of Universality'. In: *The Astrophysical Journal* 688.2 (Dec. 2008), pp. 709–728. DOI: 10.1086/591439 (cited on pages 31, 84).

[149] Steven Murray, Chris Power, and Aaron Robotham. *HMFcalc: An Online Tool for Calculating Dark Matter Halo Mass Functions*. 2013 (cited on pages 31, 83, 84).

[150] J. Neyman and E. L. Scott. 'A Theory of the Spatial Distribution of Galaxies.' In: *The Astrophysical Journal* 116 (July 1952), p. 144. DOI: 10.1086/145599 (cited on page 32).

[151] Robert J. Scherrer and Edmund Bertschinger. 'Statistics of Primordial Density Perturbations from Discrete Seed Masses'. In: *The Astrophysical Journal* 381 (Nov. 1991), p. 349. DOI: 10.1086/170658 (cited on page 32).

[152] J. M. Bardeen, J. R. Bond, N. Kaiser, and A. S. Szalay. 'The Statistics of Peaks of Gaussian Random Fields'. In: *The Astrophysical Journal* 304 (May 1986), p. 15. DOI: 10.1086/164143 (cited on pages 32, 47).

[153] Neal Dalal, Olivier Doré, Dragan Huterer, and Alexander Shirokov. 'Imprints of primordial non-Gaussianities on large-scale structure: Scale-dependent bias and abundance of virialized objects'. In: *Physical Review D* 77.12 (June 2008), p. 123514. DOI: `10.1103/PhysRevD.77.123514` (cited on pages 32, 68).

[154] Vincent Desjacques, Donghui Jeong, and Fabian Schmidt. 'Large-scale galaxy bias'. In: *Physics Reports* 733 (Feb. 2018), pp. 1–193. DOI: `10.1016/j.physrep.2017.12.002` (cited on pages 32, 33, 135).

[155] Titouan Lazeyras, Marcello Musso, and Fabian Schmidt. 'Large-scale assembly bias of dark matter halos'. In: *Journal of Cosmology and Astroparticle Physics* 2017.3 (Mar. 2017), p. 059. DOI: `10.1088/1475-7516/2017/03/059` (cited on pages 33, 135).

[156] D. N. Limber. 'The Analysis of Counts of the Extragalactic Nebulae in Terms of a Fluctuating Density Field'. In: *The Astrophysical Journal* 117 (1953). DOI: `10.1086/145672` (cited on page 36).

[157] Nick Kaiser. 'Weak Gravitational Lensing of Distant Galaxies'. In: *The Astrophysical Journal* 388 (Apr. 1992), p. 272. DOI: `10.1086/171151` (cited on page 36).

[158] Marilena LoVerde and Niayesh Afshordi. 'Extended Limber approximation'. In: *Physical Review D* 78.12 (Dec. 2008). DOI: `10.1103/physrevd.78.123506` (cited on page 36).

[159] Niayesh Afshordi, Yeong-Shang Loh, and Michael A. Strauss. 'Cross-correlation of the cosmic microwave background with the 2MASS galaxy survey: Signatures of dark energy, hot gas, and point sources'. In: *Physical Review D* 69.8 (Apr. 2004). DOI: `10.1103/physrevd.69.083524` (cited on page 37).

[160] P. Simon. 'How accurate is Limber's equation?' In: *Astronomy & Astrophysics* 473.3 (Aug. 2007), pp. 711–714. DOI: `10.1051/0004-6361:20066352` (cited on page 37).

[161] Marilena LoVerde, Lam Hui, and Enrique Gaztañaga. 'Lensing corrections to features in the angular two-point correlation function and power spectrum'. In: *Physical Review D* 77 (2 Jan. 2008), p. 023512. DOI: `10.1103/PhysRevD.77.023512` (cited on pages 37, 38, 42).

[162] Xiao Fang, Elisabeth Krause, Tim Eifler, and Niall MacCrann. 'Beyond Limber: efficient computation of angular power spectra for galaxy clustering and weak lensing'. In: *Journal of Cosmology and Astroparticle Physics* 2020.05 (May 2020), pp. 010–010. DOI: `10.1088/1475-7516/2020/05/010` (cited on page 37).

[163] N. Kaiser. 'Clustering in real space and in redshift space'. In: *Monthly Notices of the Royal Astronomical Society* 227.1 (1987). DOI: `10.1093/mnras/227.1.1` (cited on pages 37–39, 75, 77).

[164] Jaiyul Yoo, A. Liam Fitzpatrick, and Matias Zaldarriaga. 'New perspective on galaxy clustering as a cosmological probe: General relativistic effects'. In: *Physical Review D* 80.8 (Oct. 2009). DOI: `10.1103/physrevd.80.083514` (cited on page 37).

[165] A. Challinor and A. Lewis. 'Linear power spectrum of observed source number counts'. In: *Physical Review D* 84.4 (2011). DOI: `10.1103/PhysRevD.84.043516` (cited on pages 37, 43, 44, 74, 78, 79, 94, 112, 116, 141).

[166] Donghui Jeong, Fabian Schmidt, and Christopher M. Hirata. 'Large-scale clustering of galaxies in general relativity'. In: *Physical Review D* 85.2 (Jan. 2012), p. 023504. DOI: `10.1103/PhysRevD.85.023504` (cited on pages 37, 39).

[167] Donghui Jeong and Fabian Schmidt. 'Large-scale structure with gravitational waves. I. Galaxy clustering'. In: *Physical Review D* 86.8 (Oct. 2012), p. 083512. DOI: `10.1103/PhysRevD.86.083512` (cited on pages 37, 39).

[168] Vera C. Rubin, Jr. Ford W. Kent, and Judith S. Rubin. 'A Curious Distribution of Radial Velocities of SC i Galaxies with 14.0 <= M <= 15.0'. In: *Astrophysical Journal, Letters* 183 (Aug. 1973), p. L111. DOI: `10.1086/181265` (cited on page 38).

[169] A. Sandage and G. A. Tammann. 'Steps toward the Hubble constant. V. The Hubble constant from nearby galaxies and the regularity of the local velocity field.' In: *The Astrophysical Journal* 196 (Mar. 1975), pp. 313–328. DOI: `10.1086/153413` (cited on page 38).

[170] A. Yahil, A. Sandage, and G. A. Tammann. 'The velocity field of bright nearby galaxies. III - The distribution in space of galaxies within 80 megaparsecs - The north galactic density anomaly'. In: *The Astrophysical Journal* 242 (Dec. 1980), pp. 448–468. DOI: `10.1086/158479` (cited on page 38).

[171] M. Davis and J. Huchra. 'A survey of galaxy redshifts. III. The density field and the induced gravity field.' In: *The Astrophysical Journal* 254 (Mar. 1982), pp. 437–450. DOI: `10.1086/159751` (cited on page 38).

[172] M. Davis and P. J. E. Peebles. 'A survey of galaxy redshifts. V. The two-point position and velocity correlations.' In: *The Astrophysical Journal* 267 (Apr. 1983), pp. 465–482. DOI: `10.1086/160884` (cited on page 38).

[173] N. Kaiser. 'A sparse-sampling strategy for the estimation of large-scale clustering from redshift surveys'. In: *Monthly Notices of the Royal Astronomical Society* 219 (Apr. 1986), pp. 785–790. DOI: `10.1093/mnras/219.4.785` (cited on page 38).

[174] C. Alcock and B. Paczyński. 'An evolution free test for non-zero cosmological constant'. In: *Nature* 281 (1979). DOI: `https://doi.org/10.1038/281358a0` (cited on page 38).

[175] M. López-Corredoira. 'Alcock-Paczyński Cosmolocial test'. In: *The Astrophysical Journal* 781.2 (Jan. 2014), p. 96. DOI: `10.1088/0004-637x/781/2/96` (cited on page 38).

[176] J. C. Jackson. 'A Critique of Rees's Theory of Primordial Gravitational Radiation'. In: *Monthly Notices of the Royal Astronomical Society* 156.1 (Feb. 1972), 1P–5P. DOI: `10.1093/mnras/156.1.1P` (cited on page 38).

[177] Jens V. Villumsen, Wolfram Freudling, and Luiz N. da Costa. 'Clustering of Galaxies in the Hubble Deep Field'. In: *The Astrophysical Journal* 481.2 (May 1997), pp. 578–586. DOI: `10.1086/304072` (cited on pages 38, 42).

[178] Nick Kaiser. 'Weak Lensing and Cosmology'. In: *The Astrophysical Journal* 498.1 (May 1998), pp. 26–42. DOI: `10.1086/305515` (cited on pages 38, 42).

[179] Takahiko Matsubara. 'The Gravitational Lensing in Redshift-Space Correlation Functions of Galaxies and Quasars'. In: *The Astrophysical Journal* 537.2 (July 2000), pp. L77–L80. DOI: `10.1086/312762` (cited on pages 38, 42).

[180] Lam Hui, Enrique Gaztañaga, and Marilena LoVerde. 'Anisotropic magnification distortion of the 3D galaxy correlation. I. Real space'. In: *Physical Review D* 76 (10 Nov. 2007), p. 103502. DOI: `10.1103/PhysRevD.76.103502` (cited on pages 38, 42).

[181] R. K. Sachs and A. M. Wolfe. 'Perturbations of a Cosmological Model and Angular Variations of the Microwave Background'. In: *The Astrophysical Journal* 147 (Jan. 1967), p. 73. DOI: `10.1086/148982` (cited on page 38).

[182] Saleem Zaroubi and Yehuda Hoffman. *Clustering in Redshift Space: Linear Theory*. 1994 (cited on page 39).

[183] Alexander S. Szalay, Takahiko Matsubara, and Stephen D. Landy. In: 498.1 (May 1998), pp. L1–L4. DOI: `10.1086/311293` (cited on page 39).

[184] Takahiko Matsubara. 'Correlation Function in Deep Redshift Space as a Cosmological Probe'. In: *The Astrophysical Journal* 615.2 (Nov. 2004), pp. 573–585. DOI: `10.1086/424561` (cited on page 39).

[185] Péter Pápai and István Szapudi. 'Non-perturbative effects of geometry in wide-angle redshift distortions'. In: *Monthly Notices of the Royal Astronomical Society* 389.1 (Aug. 2008), pp. 292–296. DOI: `10.1111/j.1365-2966.2008.13572.x` (cited on pages 39, 40, 74).

[186] Alvise Raccanelli, Lado Samushia, and Will J. Percival. 'Simulating redshift-space distortions for galaxy pairs with wide angular separation'. In: *Monthly Notices of the Royal Astronomical Society* 409.4 (Sept. 2010), pp. 1525–1533. DOI: `10.1111/j.1365-2966.2010.17388.x` (cited on pages 39, 40, 74).

[187] Francesco Montanari and Ruth Durrer. 'New method for the Alcock-Paczyński test'. In: *Physical Review D* 86.6 (Sept. 2012). DOI: `10.1103/physrevd.86.063503` (cited on pages 40, 74).

[188] Malcolm S. Longair. *Galaxy formation*. Springer, Berlin, Heidelberg, 1999 (cited on page 42).

[189] Martin Kilbinger. 'Cosmology with cosmic shear observations: a review'. In: *Reports on Progress in Physics* 78.8 (July 2015), p. 086901. DOI: `10.1088/0034-4885/78/8/086901` (cited on pages 42, 43).

[190] Andrew J. Barber and A. N. Taylor. 'Shear and magnification angular power spectra and higher-order moments from weak gravitational lensing'. In: *Monthly Notices of the Royal Astronomical Society* 344.3 (Sept. 2003), pp. 789–797. DOI: `10.1046/j.1365-8711.2003.06872.x` (cited on page 43).

[191] Matthias Bartelmann and Peter Schneider. 'Weak gravitational lensing'. In: *Physics Reports* 340.4-5 (Jan. 2001), pp. 291–472. DOI: `10.1016/s0370-1573(00)00082-x` (cited on page 43).

[192] S. D. M. White and M. J. Rees. 'Core condensation in heavy halos: a two-stage theory for galaxy formation and clustering'. In: *Monthly Notices of the Royal Astronomical Society* 183 (1978). DOI: `10.1093/mnras/183.3.341` (cited on pages 44, 71).

[193] Andreas A. Berlind and David H. Weinberg. 'The Halo Occupation Distribution: Toward an Empirical Determination of the Relation between Galaxies and Mass'. In: *The Astrophysical Journal* 575.2 (Aug. 2002), pp. 587–616. DOI: `10.1086/341469` (cited on pages 44, 46, 47).

[194] Jeremy L. Tinker, David H. Weinberg, Zheng Zheng, and Idit Zehavi. 'On the Mass-to-Light Ratio of Large-Scale Structure'. In: *The Astrophysical Journal* 631.1 (Dec. 2005), pp. 41–58. DOI: `10.1086/432084` (cited on pages 45, 47).

[195] U. Seljak. 'Analytic model for galaxy and dark matter clustering'. In: *Monthly Notices of the Royal Astronomical Society* 318.1 (Oct. 2000), pp. 203–213. DOI: `10.1046/j.1365-8711.2000.03715.x` (cited on pages 45, 46).

[196] Kohji Yoshikawa, Atsushi Taruya, Y. P. Jing, and Yasushi Suto. 'Nonlinear Stochastic Biasing of Galaxies and Dark Halos in Cosmological Hydrodynamic Simulations'. In: *The Astrophysical Journal* 558.2 (Sept. 2001), pp. 520–534. DOI: `10.1086/322445` (cited on pages 45, 46).

[197] A. J. Benson, S. Cole, C. S. Frenk, C. M. Baugh, and C. G. Lacey. 'The nature of galaxy bias and clustering'. In: *Monthly Notices of the Royal Astronomical Society* 311.4 (Feb. 2000), pp. 793–808. DOI: `10.1046/j.1365-8711.2000.03101.x` (cited on pages 45, 46).

[198] P. Schechter. 'An analytic expression for the luminosity function for galaxies.' In: *The Astrophysical Journal* 203 (Jan. 1976), pp. 297–306. DOI: `10.1086/154079` (cited on page 45).

[199] Bruno Binggeli, Allan Sandage, and G. A. Tammann. 'The luminosity function of galaxies.' In: *Annual Review of Astronomy and Astrophysics* 26 (Jan. 1988), pp. 509–560. DOI: `10.1146/annurev.aa.26.090188.002453` (cited on page 45).

[200] Michael R. Blanton and John Moustakas. 'Physical Properties and Environments of Nearby Galaxies'. In: *Annual Review of Astronomy and Astrophysics* 47.1 (Sept. 2009), pp. 159–210. DOI: `10.1146/annurev-astro-082708-101734` (cited on page 45).

[201] Robert C. Kennicutt and Neal J. Evans. 'Star Formation in the Milky Way and Nearby Galaxies'. In: *Annual Review of Astronomy and Astrophysics* 50 (Sept. 2012), pp. 531–608. DOI: `10.1146/annurev-astro-081811-125610` (cited on page 45).

[202] Pavel Kroupa. 'The Initial Mass Function of Stars: Evidence for Uniformity in Variable Systems'. In: *Science* 295.5552 (Jan. 2002), pp. 82–91. DOI: `10.1126/science.1067524` (cited on page 45).

[203] L. Portinari, J. Sommer-Larsen, and R. Tantalo. 'On the mass-to-light ratio and the initial mass function in disc galaxies'. In: *Monthly Notices of the Royal Astronomical Society* 347.3 (Jan. 2004), pp. 691–719. DOI: `10.1111/j.1365-2966.2004.07207.x` (cited on page 45).

[204] M. C. Artale et al. 'The impact of assembly bias on the halo occupation in hydrodynamical simulations'. In: *Monthly Notices of the Royal Astronomical Society* 480.3 (2018), pp. 3978–3992. DOI: `10.1093/mnras/sty2110` (cited on pages 45, 80, 84–86, 104, 112, 113, 124).

[205] M. C. Artale et al. 'Mass and star formation rate of the host galaxies of compact binary mergers across cosmic time'. In: *Monthly Notices of the Royal Astronomical Society* 491.3 (2019), pp. 3419–3434. DOI: `10.1093/mnras/stz3190` (cited on pages 45, 80, 86, 104, 112, 113, 124, 129).

[206] Robert A. Crain et al. 'The EAGLE simulations of galaxy formation: calibration of subgrid physics and model variations'. In: *Monthly Notices of the Royal Astronomical Society* 450.2 (June 2015), pp. 1937–1961. DOI: `10.1093/mnras/stv725` (cited on pages 45, 80, 127, 128, 138).

[207] J. Schaye et al. 'The EAGLE project: simulating the evolution and assembly of galaxies and their environments'. In: *Monthly Notices of the Royal Astronomical Society* 446.1 (2015). DOI: `10.1093/mnras/stu2058` (cited on pages 45, 80, 127, 128, 138).

[208] J. A. Peacock and R. E. Smith. 'Halo occupation numbers and galaxy bias'. In: *Monthly Notices of the Royal Astronomical Society* 318.4 (Nov. 2000), pp. 1144–1156. DOI: `10.1046/j.1365-8711.2000.03779.x` (cited on page 46).

[209] Roman Scoccimarro, Ravi K. Sheth, Lam Hui, and Bhuvnesh Jain. 'How Many Galaxies Fit in a Halo? Constraints on Galaxy Formation Efficiency from Spatial Clustering'. In: *The Astrophysical Journal* 546.1 (Jan. 2001), pp. 20–34. DOI: `10.1086/318261` (cited on page 46).

[210] Guinevere Kauffmann, Adi Nusser, and Matthias Steinmetz. 'Galaxy formation and large-scale bias'. In: *Monthly Notices of the Royal Astronomical Society* 286.4 (Apr. 1997), pp. 795–811. DOI: `10.1093/mnras/286.4.795` (cited on page 46).

[211] Chung-Pei Ma and J. N. Fry. 'Deriving the Nonlinear Cosmological Power Spectrum and Bispectrum from Analytic Dark Matter Halo Profiles and Mass Functions'. In: *The Astrophysical Journal* 543.2 (Nov. 2000), pp. 503–513. DOI: `10.1086/317146` (cited on page 46).

[212] R. K. Sheth, L. Hui, A. Diaferio, and R. Scoccimarro. 'Linear and non-linear contributions to pairwise peculiar velocities'. In: *Monthly Notices of the Royal Astronomical Society* 325.4 (Aug. 2001), pp. 1288–1302. DOI: `10.1046/j.1365-8711.2001.04222.x` (cited on pages 46, 136, 141, 145).

[213] M. Magliocchetti and C. Porciani. 'The halo distribution of 2dF galaxies'. In: *Monthly Notices of the Royal Astronomical Society* 346.1 (Nov. 2003), pp. 186–198. DOI: `10.1046/j.1365-2966.2003.07094.x` (cited on page 47).

[214] M. Colless et al. 'The 2dF Galaxy Redshift Survey: spectra and redshifts'. In: *Monthly Notices of the Royal Astronomical Society* 328.4 (Dec. 2001), pp. 1039–1063. DOI: `10.1046/j.1365-8711.2001.04902.x` (cited on page 47).

[215] S. Chandrasekhar. 'The Maximum Mass of Ideal White Dwarfs'. In: *The Astrophysical Journal* 74 (July 1931), p. 81. DOI: `10.1086/143324` (cited on pages 48, 50).

[216] K. Nomoto. 'Accreting white dwarf models for type I supernovae. I - Presupernova evolution and triggering mechanisms'. In: *The Astrophysical Journal* 253 (Feb. 1982), pp. 798–810. DOI: `10.1086/159682` (cited on page 48).

[217] J. C. Wheeler and R. P. Harkness. 'Type I supernovae'. In: *Reports on Progress in Physics* 53.12 (Dec. 1990), pp. 1467–1557. DOI: `10.1088/0034-4885/53/12/001` (cited on page 48).

[218] A. Khokhlov, E. Mueller, and P. Hoeflich. 'Light curves of type IA supernova models with different explosion mechanisms.' In: *Astronomy & Astrophysics* 270 (Feb. 1993), pp. 223–248 (cited on page 48).

[219] J. Craig Wheeler, Peter Höflich, Robert P. Harkness, and Jason Spyromilio. 'Explosion Diagnostics of Type IA Supernovae from Early Infrared Spectra'. In: *The Astrophysical Journal* 496.2 (Mar. 1998), pp. 908–914. DOI: `10.1086/305427` (cited on page 48).

[220] David Branch and G. A. Tammann. 'Type Ia Supernovae as Standard Candles'. In: *Annual Review of Astronomy and Astrophysics* 30.1 (1992), pp. 359–389. DOI: `10.1146/annurev.aa.30.090192.002043` (cited on page 48).

[221] Yu. P. Pskovskii. 'The Photometric Properties of Supernovae'. In: *Astronomicheskii Zhurnal* 44 (Jan. 1967), p. 82 (cited on page 48).

[222] C. T. Kowal. 'Absolute magnitudes of supernovae'. In: *Astronomical Journal* 73 (Dec. 1968), pp. 1021–1024. DOI: `10.1086/110763` (cited on page 48).

[223] Adam G. Riess, William H. Press, and Robert P. Kirshner. 'A Precise Distance Indicator: Type IA Supernova Multicolor Light-Curve Shapes'. In: *The Astrophysical Journal* 473 (Dec. 1996), p. 88. DOI: `10.1086/178129` (cited on page 48).

[224] G. Altavilla et al. 'Cepheid calibration of Type Ia supernovae and the Hubble constant'. In: *Monthly Notices of the Royal Astronomical Society* 349.4 (Apr. 2004), pp. 1344–1352. DOI: `10.1111/j.1365-2966.2004.07616.x` (cited on page 48).

[225] Charles L. Steinhardt, Albert Sneppen, and Bidisha Sen. 'Effects of Supernova Redshift Uncertainties on the Determination of Cosmological Parameters'. In: *The Astrophysical Journal* 902.1 (Oct. 2020), p. 14. DOI: `10.3847/1538-4357/abb140` (cited on page 48).

[226] K. A. Postnov and L. R. Yungelson. 'The Evolution of Compact Binary Star Systems'. In: *Living Reviews in Relativity* 17 (Mar. 2014). DOI: `https://doi.org/10.12942/lrr-2014-3` (cited on page 49).

[227] Luc Blanchet. 'Gravitational Radiation from Post-Newtonian Sources and Inspiralling Compact Binaries'. In: *Living Reviews in Relativity* 17.1 (Feb. 2014). DOI: `10.12942/lrr-2014-2` (cited on page 49).

[228] Koester D. and Chanmugam G. 'Physics of white dwarf stars'. In: *Reports on Progress in Physics* 53.7 (July 1990), pp. 837–915. DOI: `10.1088/0034-4885/53/7/001` (cited on page 50).

[229] Rudolf Kippenhahn, Alfred Weigert, and Achim Weiss. *Stellar Structure and Evolution*. Springer-Verlag, 2012 (cited on page 50).

[230] Stirling A. Colgate and Richard H. White. 'The Hydrodynamic Behavior of Supernovae Explosions'. In: *The Astrophysical Journal* 143 (Mar. 1966), p. 626. DOI: `10.1086/148549` (cited on page 50).

[231] J. R. Oppenheimer and G. M. Volkoff. 'On Massive Neutron Cores'. In: *Physical Review* 55.4 (Feb. 1939), pp. 374–381. DOI: `10.1103/PhysRev.55.374` (cited on page 50).

[232] F. Zwicky. 'On Collapsed Neutron Stars'. In: *The Astrophysical Journal* 88 (Nov. 1938), pp. 522–525. DOI: `10.1086/144003` (cited on page 50).

[233] Leor Barack et al. 'Black holes, gravitational waves and fundamental physics: a roadmap'. In: *Classical and Quantum Gravity* 36.14 (June 2019), p. 143001. DOI: `10.1088/1361-6382/ab0587` (cited on page 50).

[234] H. Sana et al. 'Binary Interaction Dominates the Evolution of Massive Stars'. In: *Science* 337.6093 (July 2012), p. 444. DOI: `10.1126/science.1223344` (cited on page 50).

[235] N. Ivanova et al. 'Common envelope evolution: where we stand and how we can move forward'. In: *Astronomy and Astrophysics Reviews* 21 (Feb. 2013), p. 59. DOI: `10.1007/s00159-013-0059-2` (cited on page 50).

[236] Peter Eggleton. *Evolutionary Processes in Binary and Multiple Stars*. Cambridge University Press, 2009 (cited on page 50).

[237] Takashi Nakamura, Misao Sasaki, Takahiro Tanaka, and Kip S. Thorne. 'Gravitational Waves from Coalescing Black Hole MACHO Binaries'. In: *The Astrophysical Journal* 487.2 (Oct. 1997), pp. L139–L142. DOI: `10.1086/310886` (cited on page 51).

[238] Kunihito Ioka, Takeshi Chiba, Takahiro Tanaka, and Takashi Nakamura. 'Black hole binary formation in the expanding universe: Three body problem approximation'. In: *Physical Review D* 58.6 (Aug. 1998). DOI: `10.1103/physrevd.58.063003` (cited on page 51).

[239] Gerald D. Quinlan and Stuart L. Shapiro. 'Dynamical Evolution of Dense Clusters of Compact Stars'. In: *The Astrophysical Journal* 343 (Aug. 1989), p. 725. DOI: `10.1086/167745` (cited on page 52).

[240] Hideaki Mouri and Yoshiaki Taniguchi. 'Runaway Merging of Black Holes: Analytical Constraint on the Timescale'. In: *The Astrophysical Journal* 566.1 (Feb. 2002), pp. L17–L20. DOI: `10.1086/339472` (cited on page 52).

[241] Martti Raidal, Ville Vaskonen, and Hardi Veermäe. 'Gravitational waves from primordial black hole mergers'. In: *Journal of Cosmology and Astroparticle Physics* 2017.09 (Sept. 2017), pp. 037–037. DOI: `10.1088/1475-7516/2017/09/037` (cited on page 52).

[242] S. Libanore, L. Valbusa Dall'Armi, E. Vanzan, and A. Raccanelli. *In preparation*. 2022 (cited on page 53).

[243] K. Kritos, V. De Luca, G. Franciolini, A. Kehagias, and A. Riotto. 'The astro-primordial black hole merger rates: a reappraisal'. In: *Journal of Cosmology and Astroparticle Physics* 2021.05 (May 2021), p. 039. DOI: `10.1088/1475-7516/2021/05/039` (cited on page 53).

[244] L. Valbusa Dall'Armi, S. Libanore, E. Vanzan, N. Bellomo, and Raccanelli A. *To appear*. 2022 (cited on page 53).

[245] B. P. Abbott et al. 'Observation of Gravitational Waves from a Binary Black Hole Merger'. In: *Physical Review Letter* 116.6 (Feb. 2016), p. 061102. DOI: 10.1103/PhysRevLett.116.061102 (cited on page 54).

[246] B. P. Abbott et al. 'Binary Black Hole Mergers in the First Advanced LIGO Observing Run'. In: *Physical Review X* 6.4 (Oct. 2016). DOI: 10.1103/physrevx.6.041015 (cited on pages 54, 71).

[247] J. Aasi et al. 'Advanced LIGO'. In: *Classical and Quantum Gravity* 32.7 (Mar. 2015), p. 074001. DOI: 10.1088/0264-9381/32/7/074001 (cited on pages 54, 64).

[248] B. P. Abbott et al. 'GWTC-1: A Gravitational-Wave Transient Catalog of Compact Binary Mergers Observed by LIGO and Virgo during the First and Second Observing Runs'. In: *Physical Review X* 9.3 (Sept. 2019). DOI: 10.1103/physrevx.9.031040 (cited on pages 54, 69, 71, 129).

[249] R. Abbott et al. 'Population Properties of Compact Objects from the Second LIGO-Virgo Gravitational-Wave Transient Catalog'. In: *Astrophysical Journal, Letters* 913.1 (May 2021), p. L7. DOI: 10.3847/2041-8213/abe949 (cited on page 54).

[250] The LIGO Scientific Collaboration and the Virgo Collaboration. *GWTC-2.1: Deep Extended Catalog of Compact Binary Coalescences Observed by LIGO and Virgo During the First Half of the Third Observing Run*. 2021 (cited on pages 54, 65, 69, 71, 129).

[251] LIGO Scientific Collaboration and Virgo Collaboration. 'GWTC-2: Compact Binary Coalescences Observed by LIGO and Virgo during the First Half of the Third Observing Run'. In: *Physical Review X* 11.2 (June 2021), p. 021053. DOI: 10.1103/PhysRevX.11.021053 (cited on pages 54, 65, 69, 71, 113).

[252] F. Acernese et al. 'Advanced Virgo: a second-generation interferometric gravitational wave detector'. In: *Classical and Quantum Gravity* 32.2 (Dec. 2014), p. 024001. DOI: 10.1088/0264-9381/32/2/024001 (cited on pages 54, 64).

[253] Kentaro Somiya. 'Detector configuration of KAGRA–the Japanese cryogenic gravitational-wave detector'. In: *Classical and Quantum Gravity* 29.12 (June 2012), p. 124007. DOI: 10.1088/0264-9381/29/12/124007 (cited on pages 54, 64).

[254] T. Akutsu et al. 'KAGRA: 2.5 generation interferometric gravitational wave detector'. In: *Nature* 3.1 (Jan. 2019), pp. 35–40. DOI: 10.1038/s41550-018-0658-y (cited on pages 54, 64).

[255] M. Punturo et al. 'The Einstein Telescope: a third-generation gravitational wave observatory'. In: *Classical and Quantum Gravity* 27.19 (Sept. 2010), p. 194002. DOI: 10.1088/0264-9381/27/19/194002 (cited on pages 54, 65, 69, 71, 106).

[256] B. Sathyaprakash et al. 'Scientific objectives of Einstein Telescope'. In: *Classical and Quantum Gravity* 29.12 (June 2012), p. 124013. DOI: 10.1088/0264-9381/29/12/124013 (cited on pages 54, 65, 69, 71, 106).

[257] Michele Maggiore et al. 'Science case for the Einstein telescope'. In: *Journal of Cosmology and Astroparticle Physics* 2020.03 (Mar. 2020), pp. 050–050. DOI: 10.1088/1475-7516/2020/03/050 (cited on pages 54, 60, 61, 65, 66, 69, 71, 88, 106).

[258] K. Riles. 'Gravitational waves: Sources, detectors and searches'. In: *Progress in Particle and Nuclear Physics* 68 (Jan. 2013), pp. 1–54. DOI: 10.1016/j.ppnp.2012.08.001 (cited on pages 58, 60).

[259] T. J. Sejnowski. 'Sources of gravity waves'. In: *Physics Today* 27.1 (1974). DOI: 10.1063/1.3128396 (cited on page 58).

[260] Christian D. Ott. 'The gravitational-wave signature of core-collapse supernovae'. In: *Classical and Quantum Gravity* 26.6 (Feb. 2009), p. 063001. DOI: 10.1088/0264-9381/26/6/063001 (cited on page 58).

[261] Alessandra Corsi and Benjamin J. Owen. 'Maximum gravitational-wave energy emissible in magnetar flares'. In: *Physical Review D* 83.10 (May 2011), p. 104014. DOI: 10.1103/PhysRevD.83.104014 (cited on page 58).

[262] Thibault Damour and Alexander Vilenkin. 'Gravitational Wave Bursts from Cosmic Strings'. In: *Physical Review Letter* 85.18 (Oct. 2000), pp. 3761–3764. DOI: 10.1103/PhysRevLett.85.3761 (cited on page 58).

[263] Benjamin J. Owen. 'Search templates for gravitational waves from inspiraling binaries: Choice of template spacing'. In: *Physical Review D* 53.12 (June 1996), pp. 6749–6761. DOI: `10.1103/physrevd.53.6749` (cited on pages 59, 60).

[264] Curt Cutler and Éanna E. Flanagan. 'Gravitational waves from merging compact binaries: How accurately can one extract the binary's parameters from the inspiral waveform?' In: *Physical Review D* 49.6 (Mar. 1994), pp. 2658–2697. DOI: `10.1103/physrevd.49.2658` (cited on pages 59, 63, 66, 67).

[265] Tania Regimbau. 'The astrophysical gravitational wave stochastic background'. In: *Research in Astronomy and Astrophysics* 11.4 (Mar. 2011), pp. 369–390. DOI: `10.1088/1674-4527/11/4/001` (cited on page 60).

[266] E. S. Phinney. *A Practical theorem on gravitational wave backgrounds*. July 2001 (cited on page 60).

[267] Joseph D. Romano and Neil. J. Cornish. 'Detection methods for stochastic gravitational-wave backgrounds: a unified treatment'. In: *Living Reviews in Relativity* 20.1 (Apr. 2017). DOI: `10.1007/s41114-017-0004-1` (cited on page 60).

[268] Bruce Allen and Joseph D. Romano. 'Detecting a stochastic background of gravitational radiation: Signal processing strategies and sensitivities'. In: *Physical Review D* 59.10 (Mar. 1999). DOI: `10.1103/physrevd.59.102001` (cited on page 60).

[269] Chiara Caprini. 'Stochastic background of gravitational waves from cosmological sources'. In: *Journal of Physics: Conference Series* 610 (May 2015), p. 012004. DOI: `10.1088/1742-6596/610/1/012004` (cited on page 61).

[270] Nicola Bartolo et al. 'Science with the space-based interferometer LISA. IV: probing inflation with gravitational waves'. In: *Journal of Cosmology and Astroparticle Physics* 2016.12 (Dec. 2016), pp. 026–026. DOI: `10.1088/1475-7516/2016/12/026` (cited on page 61).

[271] Angelo Ricciardone. 'Primordial Gravitational Waves with LISA'. In: *Journal of Physics: Conference Series* 840 (May 2017), p. 012030. DOI: `10.1088/1742-6596/840/1/012030` (cited on page 61).

[272] B. P. Abbott et al. 'GW170817: Implications for the Stochastic Gravitational-Wave Background from Compact Binary Coalescences'. In: *Physical Review Letter* 120.9 (Feb. 2018), p. 091101. DOI: `10.1103/PhysRevLett.120.091101` (cited on page 61).

[273] B. P. Abbott et al. 'Prospects for observing and localizing gravitational-wave transients with Advanced LIGO, Advanced Virgo and KAGRA'. In: *Living Reviews in Relativity* 23.1 (Sept. 2020). DOI: `10.1007/s41114-020-00026-9` (cited on pages 61, 64, 65, 67).

[274] C. Bond, D. Brown, and A. Freise et al. 'Interferometer techniques for gravitational-wave detection'. In: *Living Reviews in Relativity* 19 (Mar. 2016). DOI: `10.1007/s41114-016-0002-8` (cited on page 61).

[275] B. P. Abbott et al. 'LIGO: the Laser Interferometer Gravitational-Wave Observatory'. In: *Reports on Progress in Physics* 72.7 (June 2009), p. 076901. DOI: `10.1088/0034-4885/72/7/076901` (cited on page 63).

[276] B. P. Abbott et al. 'GW150914: The Advanced LIGO Detectors in the Era of First Discoveries'. In: *Physical Review Letter* 116.13 (Mar. 2016). DOI: `10.1103/physrevlett.116.131103` (cited on page 63).

[277] D. V. Martynov et al. 'Sensitivity of the Advanced LIGO detectors at the beginning of gravitational wave astronomy'. In: *Physical Review D* 93.11 (June 2016), p. 112004. DOI: `10.1103/PhysRevD.93.112004` (cited on page 63).

[278] C. J. Moore, R. H Cole, and C. P. L. Berry. 'Gravitational-wave sensitivity curves'. In: *Classical and Quantum Gravity* 32.1 (Dec. 2014), p. 015014. DOI: `10.1088/0264-9381/32/1/015014` (cited on pages 63, 64).

[279] Pau Amaro-Seoane et al. *eLISA: Astrophysics and cosmology in the millihertz regime*. 2012 (cited on pages 65, 66).

[280] The eLISA Consortium. *The Gravitational Universe*. 2013 (cited on pages 65, 66).

[281] Alberto Sesana. 'Multi-band gravitational wave astronomy: science with joint space- and ground-based observations of black hole binaries'. In: *Journal of Physics: Conference Series* 840 (May 2017), p. 012018. DOI: `10.1088/1742-6596/840/1/012018` (cited on page 66).

[282] Massimo Tinto and Sanjeev V. Dhurandhar. 'Time-Delay Interferometry'. In: *Living Reviews in Relativity* 8.1 (July 2005). DOI: 10.12942/lrr-2005-4 (cited on page 66).

[283] Jeff Crowder and Neil J. Cornish. 'Beyond LISA: Exploring future gravitational wave missions'. In: *Physical Review D* 72.8 (Oct. 2005), p. 083005. DOI: 10.1103/PhysRevD.72.083005 (cited on page 66).

[284] Curt Cutler and Daniel E. Holz. 'Ultrahigh precision cosmology from gravitational waves'. In: *Physical Review D* 80.10 (Nov. 2009), p. 104009. DOI: 10.1103/PhysRevD.80.104009 (cited on pages 66, 72).

[285] K. S. Thorne. 'Gravitational Waves'. In: *300 Years of Gravitation*. Ed. by S. W. Hawking and W. Israel. Cambridge: Cambridge University Press, 1987, pp. 330–458 (cited on page 66).

[286] Bernard F. Schutz. 'Networks of gravitational wave detectors and three figures of merit'. In: *Classical and Quantum Gravity* 28.12 (May 2011), p. 125023. DOI: 10.1088/0264-9381/28/12/125023 (cited on page 67).

[287] Stephen Fairhurst. 'Triangulation of gravitational wave sources with a network of detectors'. In: *New Journal of Physics* 13.6 (June 2011), p. 069602. DOI: 10.1088/1367-2630/13/6/069602 (cited on page 67).

[288] Stephen Fairhurst. 'Localization of transient gravitational wave sources: beyond triangulation'. In: *Classical and Quantum Gravity* 35.10 (Apr. 2018), p. 105002. DOI: 10.1088/1361-6382/aab675 (cited on page 67).

[289] L. M. Burko. 'Gravitational Wave Detection in the Introductory Lab'. In: *The Physics Teacher* 55 (2017). DOI: 10.1119/1.4981036 (cited on page 68).

[290] Daniel E. Holz and Scott A. Hughes. 'Using Gravitational-Wave Standard Sirens'. In: *The Astrophysical Journal* 629.1 (Aug. 2005), pp. 15–22. DOI: 10.1086/431341 (cited on pages 68, 72).

[291] Samaya Nissanke et al. *Determining the Hubble constant from gravitational wave observations of merging compact binaries*. 2013 (cited on page 68).

[292] B. P. Abbott et al. 'Multi-messenger Observations of a Binary Neutron Star Merger'. In: *The Astrophysical Journal* 848.2 (Oct. 2017), p. L12. DOI: 10.3847/2041-8213/aa91c9 (cited on page 68).

[293] B. P. Abbott et al. 'GW170817: Observation of Gravitational Waves from a Binary Neutron Star Inspiral'. In: *Physical Review Letter* 119.16 (Oct. 2017), p. 161101. DOI: 10.1103/PhysRevLett.119.161101 (cited on page 68).

[294] B. P. Abbott et al. 'Gravitational Waves and Gamma-Rays from a Binary Neutron Star Merger: GW170817 and GRB 170817A'. In: *The Astrophysical Journal* 848.2 (Oct. 2017), p. L13. DOI: 10.3847/2041-8213/aa920c (cited on page 68).

[295] A. Blanchard et al. 'Euclid preparation: VII. Forecast validation for Euclid cosmological probes'. In: *Astronomy & Astrophysics* 642 (Oct. 2020), A191. DOI: 10.1051/0004-6361/202038071 (cited on pages 69, 101).

[296] Walter Del Pozzo. 'Inference of cosmological parameters from gravitational waves: Applications to second generation interferometers'. In: *Physical Review D* 86.4 (Aug. 2012). DOI: 10.1103/physrevd.86.043011 (cited on pages 69, 73).

[297] Suvodip Mukherjee, Benjamin D. Wandelt, Samaya M. Nissanke, and Alessandra Silvestri. 'Accurate precision cosmology with redshift unknown gravitational wave sources'. In: *Physical Review D* 103.4 (Feb. 2021). DOI: 10.1103/physrevd.103.043520 (cited on pages 69, 73, 100, 104, 106).

[298] P. Zhang. *The large scale structure in the 3D luminosity-distance space and its cosmological applications*. 2018 (cited on pages 69, 73–76).

[299] Suvodip Mukherjee and Benjamin D. Wandelt. *Beyond the classical distance-redshift test: cross-correlating redshift-free standard candles and sirens with redshift surveys*. 2018 (cited on page 69).

[300] G. Scelfo et al. 'GW×LSS: chasing the progenitors of merging binary black holes'. In: *Journal of Cosmology and Astroparticle Physics* 2018.09 (2018) (cited on pages 69, 106, 113, 114).

[301] G. Scelfo et al. 'Exploring galaxies-gravitational waves cross-correlations as an astrophysical probe'. In: *Journal of Cosmology and Astroparticle Physics* 2020.10 (2020) (cited on pages 69, 104, 106).

[302] The LIGO Scientific Collaboration, The Virgo Collaboration, and The KAGRA Scientific Collaboration. *The population of merging compact binaries inferred using gravitational waves through GWTC-3*. 2021 (cited on pages 71, 72).

[303] E. Belgacem et al. 'Gravitational-wave luminosity distance in modified gravity theories'. In: *Physical Review D* 97.10 (2018). DOI: `10.1103/PhysRevD.97.104066` (cited on page 72).

[304] E. Belgacem et al. 'Modified gravitational-wave propagation and standard sirens'. In: *Physical Review D* 98.2 (2018). DOI: `10.1103/physrevd.98.023510` (cited on page 72).

[305] A. Garoffolo et al. 'Gravitational waves and geometrical optics in scalar-tensor theories'. In: *Journal of Cosmology and Astroparticle Physics* 2020.11 (2020). DOI: `10.1088/1475-7516/2020/11/040` (cited on page 72).

[306] C. Dalang et al. 'Horndeski gravity and standard sirens'. In: *Physical Review D* 102.4 (2020). DOI: `10.1103/physrevd.102.044036` (cited on page 72).

[307] A. Garoffolo et al. 'Detecting dark energy fluctuations with gravitational waves'. In: *Physical Review D* 103.8 (2021). DOI: `10.1103/physrevd.103.083506` (cited on page 72).

[308] B. P. Abbott et al. 'A Gravitational-wave Measurement of the Hubble Constant Following the Second Observing Run of Advanced LIGO and Virgo'. In: *The Astrophysical Journal* 909.2 (Mar. 2021), p. 218. DOI: `10.3847/1538-4357/abdcb7` (cited on page 72).

[309] M. J. Graham et al. 'Candidate Electromagnetic Counterpart to the Binary Black Hole Merger Gravitational-Wave Event S190521g'. In: *Physical Review Letter* 124.25 (June 2020). DOI: `10.1103/physrevlett.124.251102` (cited on page 72).

[310] M. Fishbach et al. 'A Standard Siren Measurement of the Hubble Constant from GW170817 without the Electromagnetic Counterpart'. In: *The Astrophysical Journal* 871.1 (Jan. 2019), p. L13. DOI: `10.3847/2041-8213/aaf96e` (cited on page 73).

[311] Brice Ménard et al. *Clustering-based redshift estimation: method and application to data*. 2014 (cited on page 73).

[312] Mubdi Rahman, Brice Ménard, Ryan Scranton, Samuel J. Schmidt, and Christopher B. Morrison. 'Clustering-based redshift estimation: comparison to spectroscopic redshifts'. In: *Monthly Notices of the Royal Astronomical Society* 447.4 (Jan. 2015), pp. 3500–3511. DOI: `10.1093/mnras/stu2636` (cited on page 73).

[313] Ely D. Kovetz, Alvise Raccanelli, and Mubdi Rahman. 'Cosmological constraints with clustering-based redshifts'. In: *Monthly Notices of the Royal Astronomical Society* 468.3 (Mar. 2017), pp. 3650–3656. DOI: `10.1093/mnras/stx691` (cited on page 73).

[314] T. Pyne and M. Birkinshaw. 'The luminosity distance in perturbed FLRW space-times'. In: *Monthly Notices of the Royal Astronomical Society* 348.2 (Feb. 2004), pp. 581–588. DOI: `10.1111/j.1365-2966.2004.07362.x` (cited on page 73).

[315] T. Namikawa. 'Analyzing clustering of astrophysical gravitational-wave sources: luminosity-distance space distortions'. In: *Journal of Cosmology and Astroparticle Physics* 2021.01 (2021). DOI: `10.1088/1475-7516/2021/01/036` (cited on pages 73, 74, 77–79, 94).

[316] D. Bertacca et al. 'Cosmological perturbation effects on gravitational-wave luminosity distance estimates'. In: *Physics of the Dark Universe* 20 (June 2018), pp. 32–40. DOI: `10.1016/j.dark.2018.03.001` (cited on pages 73, 74, 77, 89).

[317] D. Bertacca and A. et al. Begnoni. *In preparation*. 2022 (cited on page 73).

[318] M. Sasaki. 'The magnitude-redshift relation in a perturbed Friedmann universe'. In: *Monthly Notices of the Royal Astronomical Society* 228 (1987). DOI: `10.1093/mnras/228.3.653` (cited on page 74).

[319] L. Hui and P. B. Greene. 'Correlated fluctuations in luminosity distance and the importance of peculiar motion in supernova surveys'. In: *Physical Review D* 73.12 (2006). DOI: `10.1103/physrevd.73.123526` (cited on page 74).

[320] E. Baird. *Aberration and Special Relativity*. arXiv:physics/9806037. 1998 (cited on page 74).

[321] Camille Bonvin, Ruth Durrer, and M. Alice Gasparini. 'Fluctuations of the luminosity distance'. In: *Physical Review D* 73.2 (Jan. 2006), p. 023523. DOI: `10.1103/PhysRevD.73.023523` (cited on page 77).

[322] M Celeste Artale et al. 'An astrophysically motivated ranking criterion for low-latency electromagnetic follow-up of gravitational wave events'. In: *Monthly Notices of the Royal Astronomical Society* 495.2 (May 2020), pp. 1841–1852. DOI: `10.1093/mnras/staa1252` (cited on pages 80, 86, 104, 112, 113, 124, 129).

[323] N. Giacobbo and M. Mapelli. 'The progenitors of compact-object binaries: impact of metallicity, common envelope and natal kicks'. In: *Monthly Notices of the Royal Astronomical Society* 480 (2018). DOI: `10.1093/mnras/sty1999` (cited on pages 80, 129).

[324] M. Mapelli and N. Giacobbo. 'The cosmic merger rate of neutron stars and black holes'. In: *Monthly Notices of the Royal Astronomical Society* 479.4 (2018). DOI: `10.1093/mnras/sty1613` (cited on page 80).

[325] Giulio Scelfo, Lumen Boco, Andrea Lapi, and Matteo Viel. 'Exploring galaxies-gravitational waves cross-correlations as an astrophysical probe'. In: *Journal of Cosmology and Astroparticle Physics* 2020.10 (Oct. 2020), pp. 045–045. DOI: `10.1088/1475-7516/2020/10/045` (cited on pages 82, 86).

[326] J. L. Tinker et al. 'The Large-Scale bias of Dark Matter halos: numerical calibration and model tests'. In: *The Astrophysical Journal* 724.2 (2010). DOI: `10.1088/0004-637x/724/2/878` (cited on pages 84, 146).

[327] D. Karagiannis et al. 'Constraining primordial non-Gaussianity with bispectrum and power spectrum from upcoming optical and radio surveys'. In: *Monthly Notices of the Royal Astronomical Society* 478.1 (2018). DOI: `10.1093/mnras/sty1029` (cited on pages 85, 136, 143, 144, 146).

[328] F. Calore et al. 'Cross-correlating galaxy catalogs and gravitational waves: A tomographic approach'. In: *Physical Review Research* 2.2 (2020). DOI: `10.1103/PhysRevResearch.2.023314` (cited on page 86).

[329] LSST Science Collaboration. *LSST Science Book, Version 2.0*. 2009 (cited on page 86).

[330] K. Garcia et al. 'On the amount of peculiar velocity field information in supernovae from LSST and beyond'. In: *Physics of the Dark Universe* 29 (2020), p. 100519 (cited on pages 86, 87).

[331] H. Cullan et al. 'Measuring the Growth Rate of Structure with Type IA Supernovae from LSST'. In: *The Astrophysical Journal* 847.2 (Sept. 2017). DOI: `10.3847/1538-4357/aa88c8` (cited on pages 87, 88).

[332] S. Mukherjee and B. D. Wandelt. 'Beyond the classical distance-redshift test: cross-correlating redshift-free standard candles and sirens with redshift surveys'. In: *arXiv:1808.06615* (Aug. 2018) (cited on page 87).

[333] W. Zhao and L. Wen. 'Localization accuracy of compact binary coalescences detected by the third-generation gravitational-wave detectors and implication for cosmology'. In: *Physical Review D* 97.6 (2018). DOI: `10.1103/physrevd.97.064031` (cited on pages 88, 89).

[334] S. Vitale and M. Evans. 'Parameter estimation for binary black holes with networks of third-generation gravitational-wave detectors'. In: *Physical Review D* 95 (6 2017). DOI: `10.1103/physrevd.95.064052` (cited on pages 88, 116).

[335] R. Takahashi et al. 'Revising the halofit model for the non linear power spectrum'. In: *The Astrophysical Journal* 761 (2012). DOI: `10.1088/0004-637x/761/2/152` (cited on page 90).

[336] Alan Heavens. *Statistical techniques in cosmology*. 2010 (cited on pages 91, 108, 109).

[337] L. Verde. 'Statistical Methods in Cosmology'. In: *Lecture Notes in Physics* (2010), pp. 147–177. DOI: `10.1007/978-3-642-10598-2_4` (cited on pages 91, 92, 108, 109).

[338] Dan Coe. *Fisher Matrices and Confidence Ellipses: A Quick-Start Guide and Software*. 2009 (cited on page 93).

[339] U. Seljak. 'Extracting Primordial Non-Gaussianity without Cosmic Variance'. In: *Physical Review Letter* 102.2 (2009). DOI: `10.1103/PhysRevLett.102.021302` (cited on pages 93, 100).

[340] P. McDonald and U. Seljak. 'How to evade the sample variance limit on measurements of redshift-space distortions'. In: *Journal of Cosmology and Astroparticle Physics* 2009.10 (2009) (cited on pages 93, 100).

[341] N. Hamaus et al. 'Optimal constraints on local primordial non-Gaussianity from the two-point statistics of large-scale structure'. In: *Physical Review D* 84 (2011) (cited on pages 93, 100).

[342] L. Abramo et al. 'Fourier analysis of multitracer cosmological surveys'. In: *Monthly Notices of the Royal Astronomical Society* 455.4 (2016). DOI: `10.1093/mnras/stv2588` (cited on pages 93, 100, 101).

[343] A. Witzemann et al. 'Simulated multitracer analyses with HI intensity mapping'. In: *Monthly Notices of the Royal Astronomical Society* 485.4 (2019). DOI: `10.1093/mnras/stz778` (cited on page 93).

[344] Zheng Zheng and David H. Weinberg. 'Breaking the Degeneracies between Cosmology and Galaxy Bias'. In: *The Astrophysical Journal* 659.1 (Apr. 2007), pp. 1–28. DOI: `10.1086/512151` (cited on pages 93, 101).

[345] Z. Cheng et al. *The completed SDSS-IV extended Baryon Oscillation Spectroscopic Survey: Cosmological implications from multi-tracer BAO analysis with galaxies and voids*. 2021 (cited on pages 93, 101).

[346] L. R. Abramo and K. E. Leonard. 'Why multitracer surveys beat cosmic variance'. In: *Monthly Notices of the Royal Astronomical Society* 432.1 (Apr. 2013), pp. 318–326. DOI: `10.1093/mnras/stt465` (cited on pages 93, 101).

[347] Antony Lewis and Sarah Bridle. 'Cosmological parameters from CMB and other data: A Monte Carlo approach'. In: *Physical Review D* 66.10 (Nov. 2002), p. 103511. DOI: `10.1103/PhysRevD.66.103511` (cited on page 94).

[348] Alvise Raccanelli. 'Gravitational wave astronomy with radio galaxy surveys'. In: *Monthly Notices of the Royal Astronomical Society* (Apr. 2017). DOI: `10.1093/mnras/stx835` (cited on page 106).

[349] D. S. Sivia and J. Skilling. *Data Analysis, A Bayesian Tutorial. Second Edition*. Oxford Science Publications, 2006 (cited on pages 108, 109).

[350] A. F. Heavens, T. D. Kitching, and L. Verde. 'On model selection forecasting, dark energy and modified gravity'. In: *Monthly Notices of the Royal Astronomical Society* 380.3 (Aug. 2007), pp. 1029–1035. DOI: `10.1111/j.1365-2966.2007.12134.x` (cited on pages 108, 109, 123).

[351] Roberto Trotta. 'Forecasting the Bayes factor of a future observation'. In: *Monthly Notices of the Royal Astronomical Society* 378.3 (June 2007), pp. 819–824. DOI: `10.1111/j.1365-2966.2007.11861.x` (cited on page 109).

[352] S. Mukherjee and J. Silk. 'Can we distinguish astrophysical from primordial black holes via the stochastic gravitational wave background?' In: *Monthly Notices of the Royal Astronomical Society* 506.3 (July 2021), pp. 3977–3985. DOI: `10.1093/mnras/stab1932` (cited on page 113).

[353] H. Jeffreys. *Theory of Probability*. Third. Oxford, England: Oxford, 1961 (cited on page 120).

[354] Mark Vogelsberger, Federico Marinacci, Paul Torrey, and Ewald Puchwein. *Cosmological Simulations of Galaxy Formation*. 2019 (cited on pages 125, 126).

[355] Qiu-Dong Wang. 'The global solution of the N-body problem'. In: *Celestial Mechanics and Dynamical Astronomy* 50.1 (Mar. 1990), pp. 73–88. DOI: `10.1007/BF00048987` (cited on page 125).

[356] Sverre J. Aarseth. *Gravitational N-Body Simulations*. Cambridge University press, 2003 (cited on page 125).

[357] Walter Dehnen. 'Towards optimal softening in three-dimensional N-body codes - I. Minimizing the force error'. In: *Monthly Notices of the Royal Astronomical Society* 324.2 (June 2001), pp. 273–291. DOI: `10.1046/j.1365-8711.2001.04237.x` (cited on page 125).

[358] Josh Barnes and Piet Hut. 'A hierarchical O(N log N) force-calculation algorithm'. In: *Nature* 324.6096 (Dec. 1986), pp. 446–449. DOI: `10.1038/324446a0` (cited on page 125).

[359] *Computer Simulation Using Particles*. CRC Press, 1988 (cited on page 125).

[360] M. Davis, G. Efstathiou, C. S. Frenk, and S. D. M. White. 'The evolution of large-scale structure in a universe dominated by cold dark matter'. In: *The Astrophysical Journal* 292 (May 1985), pp. 371–394. DOI: `10.1086/163168` (cited on page 126).

[361] Francisco Villaescusa-Navarro et al. 'The Quijote Simulations'. In: *The Astrophysical Journal Supplement Series* 250.1 (Aug. 2020), p. 2. DOI: `10.3847/1538-4365/ab9d82` (cited on pages 126, 138, 141).

[362] Ravi K. Sheth, H. J. Mo, and Giuseppe Tormen. 'Ellipsoidal collapse and an improved model for the number and spatial distribution of dark matter haloes'. In: *Monthly Notices of the Royal Astronomical Society* 323.1 (May 2001), pp. 1–12. DOI: `10.1046/j.1365-8711.2001.04006.x` (cited on pages 127–129).

[363] R. A. Gingold and J. J. Monaghan. 'Smoothed particle hydrodynamics: theory and application to non-spherical stars'. In: *Monthly Notices of the Royal Astronomical Society* 181 (Nov. 1977), pp. 375–389. DOI: `10.1093/mnras/181.3.375` (cited on page 127).

[364] LIGO Scientific Collaboration. 'Advanced LIGO'. In: *Classical and Quantum Gravity* 32.7 (Apr. 2015), p. 074001. DOI: `10.1088/0264-9381/32/7/074001` (cited on page 128).

[365] Michael Rowan-Robinson et al. 'The star formation rate density from z = 1 to 6'. In: *Monthly Notices of the Royal Astronomical Society* 461.1 (Sept. 2016), pp. 1100–1111. DOI: `10.1093/mnras/stw1169` (cited on page 128).

[366] Robert H. Becker et al. 'Evidence for Reionization at [ITAL][CLC]z[/CLC][/ITAL]≃6: Detection of a Gunn-Peterson Trough in a [ITAL][CLC]z[/CLC][/ITAL]=6.28 Quasar'. In: *Astronomical Journal* 122.6 (Dec. 2001), pp. 2850–2857. DOI: `10.1086/324231` (cited on page 128).

[367] M. Mapelli et al. 'The cosmic merger rate of stellar black hole binaries from the Illustris simulation'. In: *Monthly Notices of the Royal Astronomical Society* 472.2 (2017). DOI: `10.1093/mnras/stx2123` (cited on page 129).

[368] Jarrod R. Hurley, Christopher A. Tout, and Onno R. Pols. 'Evolution of binary stars and the effect of tides on binary populations'. In: *Monthly Notices of the Royal Astronomical Society* 329.4 (Feb. 2002), pp. 897–928. DOI: `10.1046/j.1365-8711.2002.05038.x` (cited on page 129).

[369] N. Giacobbo, M. Mapelli, and M. Spera. 'Merging black hole binaries: the effects of progenitor's metallicity, mass-loss rate and Eddington factor'. In: *Monthly Notices of the Royal Astronomical Society* 474 (2018). DOI: `10.1093/mnras/stx2933` (cited on page 129).

[370] C. L. Fryer et al. 'Compact Remnant Mass Function: Dependence on the Explosion Mechanism and Metallicity'. In: *Astronomical Journal* 749.1 (2012). DOI: `10.1088/0004-637X/749/1/91` (cited on page 129).

[371] M. Mapelli et al. 'Impact of the Rotation and Compactness of Progenitors on the Mass of Black Holes'. In: *Astronomical Journal* 888.2 (2020). DOI: `10.3847/1538-4357/ab584d` (cited on page 129).

[372] LIGO Scientific Collaboration and Virgo Collaboration. 'Binary Black Hole Population Properties Inferred from the First and Second Observing Runs of Advanced LIGO and Advanced Virgo'. In: *The Astrophysical Journal* 882.2 (2019). DOI: `10.3847/2041-8213/ab3800` (cited on page 129).

[373] David J. Baumgart and J. N. Fry. 'Fourier Spectra of Three-dimensional Data'. In: *The Astrophysical Journal* 375 (July 1991), p. 25. DOI: `10.1086/170166` (cited on pages 130, 131, 133, 134).

[374] Hume A. Feldman, Nick Kaiser, and John A. Peacock. 'Power-spectrum analysis of three-dimensional redshift surveys'. In: *The Astrophysical Journal* 426 (May 1994), p. 23. DOI: `10.1086/174036` (cited on pages 130, 134, 135, 139).

[375] Y. P. Jing. 'Correcting for the Alias Effect When Measuring the Power Spectrum Using a Fast Fourier Transform'. In: *The Astrophysical Journal* 620.2 (Feb. 2005), pp. 559–563. DOI: `10.1086/427087` (cited on page 130).

[376] Stéphane Colombi, Andrew Jaffe, Dmitri Novikov, and Christophe Pichon. 'Accurate estimators of power spectra in N-body simulations'. In: *Monthly Notices of the Royal Astronomical Society* 393.2 (Feb. 2009), pp. 511–526. DOI: `10.1111/j.1365-2966.2008.14176.x` (cited on pages 130, 133, 139).

[377] Robert E. Smith and Laura Marian. 'What is the optimal way to measure the galaxy power spectrum?' In: *Monthly Notices of the Royal Astronomical Society* 457.4 (Feb. 2016), pp. 4285–4290. DOI: `10.1093/mnras/stw282` (cited on pages 130, 134).

[378] E. Sefusatti, M. Crocce, R. Scoccimarro, and H. M. P. Couchman. 'Accurate estimators of correlation functions in Fourier space'. In: *Monthly Notices of the Royal Astronomical Society* 460.4 (May 2016), pp. 3624–3636. DOI: `10.1093/mnras/stw1229` (cited on pages 130, 133, 134, 138, 139).

[379] Max Tegmark, Andrew J. S. Hamilton, Michael A. Strauss, Michael S. Vogeley, and Alexander S. Szalay. 'Measuring the Galaxy Power Spectrum with Future Redshift Surveys'. In: *The Astrophysical Journal* 499.2 (May 1998), pp. 555–576. DOI: `10.1086/305663` (cited on page 131).

[380] David Valcin, Francisco Villaescusa-Navarro, Licia Verde, and Alvise Raccanelli. 'BE-HaPPY: bias emulator for halo power spectrum including massive neutrinos'. In: *Journal of Cosmology and Astroparticle Physics* 2019.12 (Dec. 2019), pp. 057–057. DOI: `10.1088/1475-7516/2019/12/057` (cited on page 135).

[381] Tobias Baldauf, Uroš Seljak, Vincent Desjacques, and Patrick McDonald. 'Evidence for quadratic tidal tensor bias from the halo bispectrum'. In: *Physical Review D* 86.8 (Oct. 2012), p. 083540. DOI: `10.1103/PhysRevD.86.083540` (cited on pages 135, 137).

[382] Daniel Foreman-Mackey, David W. Hogg, Dustin Lang, and Jonathan Goodman. 'emcee: The MCMC Hammer'. In: *Publications of the Astronomical Society of the Pacific* 125.925 (Mar. 2013), p. 306. DOI: `10.1086/670067` (cited on page 137).

[383] R. E. Smith et al. 'Stable clustering, the halo model and non-linear cosmological power spectra'. In: *Monthly Notices of the Royal Astronomical Society* 341.4 (June 2003), pp. 1311–1332. DOI: `10.1046/j.1365-8711.2003.06503.x` (cited on page 141).

[384] José Fonseca, Jan-Albert Viljoen, and Roy Maartens. 'Constraints on the growth rate using the observed galaxy power spectrum'. In: *Journal of Cosmology and Astroparticle Physics* 2019.12 (Dec. 2019), p. 028. DOI: `10.1088/1475-7516/2019/12/028` (cited on page 141).

[385] Joseph E. McEwen, Xiao Fang, Christopher M. Hirata, and Jonathan A. Blazek. 'FAST-PT: a novel algorithm to calculate convolution integrals in cosmological perturbation theory'. In: *Journal of Cosmology and Astroparticle Physics* 2016.9 (Sept. 2016), p. 015. DOI: `10.1088/1475-7516/2016/09/015` (cited on page 141).

[386] Xiao Fang, Jonathan A. Blazek, Joseph E. McEwen, and Christopher M. Hirata. 'FAST-PT II: an algorithm to calculate convolution integrals of general tensor quantities in cosmological perturbation theory'. In: *Journal of Cosmology and Astroparticle Physics* 2017.2 (Feb. 2017), p. 030. DOI: `10.1088/1475-7516/2017/02/030` (cited on page 141).